A new Method for the Reconstruction of Very-High-Energy Gamma-Ray Spectra and Application to Galactic Cosmic-Ray Accelerators

Dissertation
zur Erlangung des Doktorgrades
des Fachbereichs Physik
der Universität Hamburg

vorgelegt von

Milton Virgílio Fernandes
aus Hamburg

Hamburg
2014

Gutachter der Dissertation:	Prof. Dr. Dieter Horns[1] Dr. Gavin Rowell[2]
Gutachter der Disputation:	Prof. Dr. Dieter Horns[1] Prof. Dr. Caren Hagner[1]
Vorsitzender des Prüfungsausschusses:	Dr. Georg Steinbrück[1]
Vorsitzender des Promotionsausschusses:	Prof. Dr. Daniela Pfannkuche[1]
Dekan der Fakultät für Mathematik, Informatik und Naturwissenschaften:	Prof. Dr. Heinrich Graener[1]
Termin der Disputation:	20.06.2014

[1] Universität Hamburg
[2] Universität Adelaide (Australien)

There is a fundamental reason why we look at the sky with wonder and longing – for the same reason that we stand, hour after hour, gazing at the distant swell of the open ocean.

There is something like an ancient wisdom, encoded and tucked away in our DNA, that knows its point of origin as surely as a salmonid knows its creek. Intellectually, we may not want to return there, but the genes know, and long for their origins – their home in the salty depths. But if the seas are our immediate source, the penultimate source is certainly the heavens.

The spectacular truth is – and this is something that your DNA has known all along – the very atoms of your body – the iron, calcium, phosphorus, carbon, nitrogen, oxygen, and on and on – were initially forged in long-dead stars.

This is why, when you stand outside under a moonless, country sky, you feel some ineffable tugging at your innards.

We are star stuff. Keep looking up.

Gerald D. Waxman, *Astronomical Tidbits: A Layperson's Guide to Astronomy*

KURZFASSUNG

In dieser Arbeit wurde auf Basis hochenergetischer ($E > 0.1\,\mathrm{GeV}$) und sehr hochenergetischer (SHE; $E > 0.1\,\mathrm{TeV}$) γ-Strahlung untersucht, ob in galaktischen Sternhaufen (SH) und Sternentstehungsgebieten (SEGen) die Hadronen der galaktischen kosmischen Strahlung (GKS) beschleunigt werden können. Im Prinzip sollte dies an der Schockfront des kollektiven Sternhaufenwindes, der von den massereichen Sternen getrieben wird, möglich sein. Die so produzierten SHE γ-Photonen lassen sich mit abbildenden Luft-Cherenkov-Teleskopen (aLCT) detektieren. Einige galaktische SHE γ-Photonquellen, darunter auch potentiell durch SH erzeugte, füllen einen Großteil des aLCT-Gesichtsfelds (GFs) aus und bedürfen der Nachbeobachtung quellfreier Regionen, um den dominanten Untergrund in einer spektralen Rekonstruktion zu ermitteln.

Eine neue Methode wurde daher entwickelt, um Spektren ausgedehnter Quellen ohne solche Nachbeobachtungen rekonstruieren zu können: das Template Background Spectrum (TBS). Sie basiert auf der Methode zur Erstellung von Himmelskarten, bei der der Untergrund im Parameterraum bestimmt wird. Die Idee ist nun, dass eine Nachschlagetabelle der Untergrundnormalisierung in Energie, Zenitwinkel und Winkelabstand erstellt wird und mögliche Systematiken berücksichtigt werden. Die mit TBS und gängigen modernen Untergrundbestimmungsmethoden rekonstruierten Spektren aus H.E.S.S. -Daten sind kompatibel; es wurden auch jene Spektren mit TBS rekonstruiert, die sonst der Nachbeobachtung bedürfen. Somit ist TBS die dritte allgemeine Methode, um SHE γ-Photonspektren zu rekonstruieren; jedoch die erste, die keiner Nachbeobachtung in der Analyse ausgedehnter Quellen bedarf.

Die Entdeckung der bislang größten SHE γ-Photonquelle HESS J1646–458 (Durchmesser: 2.2°) mit H.E.S.S. in Richtung des SHs Westerlund 1 lässt sich plausibel durch das SH-Wind-Szenario erklären. Aufgrund der Größe der Quelle befinden sich weitere mögliche Gegenstücke zur TeV-Emission (Pulsar, Binärsystem, Magnetar) im GF. Die Assoziation der SHE γ-Photonquelle HESS J1646–458 mit dem SH ist favorisiert, kann aber nicht bestätigt werden.

Der SH Pismis 22 befindet sich inmitten der bereits detektierten und bislang unidentifizierten ausgedehnten TeV-γ-Photonquelle HESS J1614–518. Neue H.E.S.S.-Daten und öffentlich verfügbare Multiwellenlängen(MWL)-Daten (im Radio-, Röntgen- und HE-Bereich) sowie im GF vorhandene potentielle Gegenstücke wurden analysiert. Die energieabhängige TeV-Morphologie (mit mindestens zwei Quellkomponenten) und die MWL-Beobachtungen lassen sich nur schwer in Einklang bringen. Ein SH-Wind-Szenario scheint unwahrscheinlich, andere plausible Gegenstücke gibt es nicht, doch könnte ein Relikt eines Pulsarwindnebels das Fehlen prominenter Röntgenemission erklären. HESS J1614–518 bleibt somit unidentifiziert.

Die Analyse bislang unveröffentlichter H.E.S.S.-Daten des SEGes Gould'scher Gürtel (GG) lieferte keinen sicheren Anhaltspunkt für SHE γ-Strahlungsquellen. Es wurden daher Obergrenzen auf den Photonfluss und die Erhöhung der Dichte der GKS berechnet. Der GG mit den vielen hellen Sternen und womöglich signalschwacher großskalig ausgedehnter SHE γ-Strahlung scheint die unterschiedlichen Untergrundbestimmungsmethoden zu beeinträchtigen und könnte daher eine Limitierung moderner aLCTe(-Datenanalyse) darstellen. Die mit TBS mögliche Entdeckung einer ausgedehnten Emissionsregion um Orion A mit einem Photonfluss von 10.8 % des Krebsnebels kann nicht bestätigt werden und ist eventuell ein Artefakt der Analyse dieser Region.

Beobachtungen mit den H.E.S.S.-Teleskopen legen nahe, dass SH Beschleuniger der GKS sein könnten, doch bedarf es weiterer SHE Beobachtungen für detailliertere morphologische und spektrale Studien. Auch wären weitere Daten im Röntgenbereich (im Falle von HESS J1614–518) als auch Studien zu Untergrundsystematiken (im Falle des GGs) nötig.

Abstract

In this thesis, high-energy (HE; $E > 0.1\,\mathrm{GeV}$) and very-high-energy (VHE; $E > 0.1\,\mathrm{TeV}$) γ-ray data were investigated to probe Galactic stellar clusters (SCs) and star-forming regions (SFRs) as sites of hadronic Galactic cosmic-ray (GCR) acceleration. In principle, massive SCs and SFRs could accelerate GCRs at the shock front of the collective SC wind fed by the individual high-mass stars. The subsequently produced VHE γ rays would be measured with imaging air-Cherenkov telescopes (IACTs). A couple of the Galactic VHE γ-ray sources, including those potentially produced by SCs, fill a large fraction of the field-of-view (FoV) and require additional observations of source-free regions to determine the dominant background for a spectral reconstruction.

A new method of reconstructing spectra for such extended sources without the need of further observations is developed: the Template Background Spectrum (TBS). This methods is based on a method to generate skymaps, which determines background in parameter space. The idea is the creation of a look-up of the background normalisation in energy, zenith angle, and angular separation and to account for possible systematics. The results obtained with TBS and state-of-the-art background-estimation methods on H.E.S.S. data are in good agreement. With TBS even those sources could be reconstructed that normally would need further observations. Therefore, TBS is the third method to reconstruct VHE γ-ray spectra, but the first one to not need additional observations in the analysis of extended sources.

The discovery of the largest VHE γ-ray source HESS J1646–458 (2.2° in size) towards the SC Westerlund 1 (Wd1) can be plausibly explained by the SC-wind scenario. But owing to its size, other alternative counterparts to the TeV emission (pulsar, binary system, magnetar) were found in the FoV. Therefore, an association of HESS J1646–458 with the SC is favoured, but cannot be confirmed.

The SC Pismis 22 is located in the centre of the previously reported, but unidentified extended TeV γ-ray source HESS J1614–518. Unpublished H.E.S.S. data and archival multi-wavelength (MWL) data (radio, X-ray, and HE data) as well various astrophysical objects in the FoV were investigated in search of a counterpart. The energy-dependent TeV morphology (with at least two source regions) can hardly be reconciled with the MWL data. A SC-wind scenario appears unlikely and the FoV lacks plausible counterparts, but a relic pulsar wind nebula could explain the lack of prominent X-ray emission. The VHE γ-ray source remains unidentified.

The analysis of unpublished H.E.S.S. data on the SFR the Gould Belt (GB) did not provide any firm evidence of VHE γ-ray emission, and upper limits on the flux and the cosmic-ray enhancement were derived. The analyses appeared to be affected by the many bright stars and a hypothetically faint large-scale extended emission, possibly posing a limitation in observations and data analysis of current IACTs. Towards Orion A, a possible discovery of extended VHE γ rays with a flux of 10.8 % of the Crab Nebula is found with TBS, but cannot be confirmed and could be an artifact of the analysis of this region.

Observations with the H.E.S.S. telescope system motivate that SCs and SFRs can accelerate GCRs. However, further H.E.S.S. observations are needed for further morphological and spectral studies. Also, more X-ray observations (in the case of HESS J1614–518) and further studies on the background-estimation methods and their systematics (in the case of the GB) are required.

silent gratitude isn't much use to anyone
Gladys B. Stern

ACKNOWLEDGEMENTS

I would like to take the opportunity and acknowledge the following things.

TECHNICAL ACKNOWLEDGEMENTS

A large part of the work presented in this thesis is based on results produced with *python* along with its modules *numpy*, *matplotlib*, *pyfits*, *pyminuit*, and *scipy*. Especially, the development of TBS and the analysis framework has benefited from this powerful programming language. I therefore deeply thank the many unsung authors, developers, and maintainers of the respective websites. In this matter, I acknowledge the use of the `FITS` data format (Wells et al., 1981). The text editors of choice were `kate` and `vim`.

The websites `Google` and `wikipedia.org` were always good starting points when being in doubt or uncertain. Language issues were mostly solved with the help of `dict.cc` and `dict.leo.org`. I acknowledge the very frequent use of `NASA ADS`, `arXiv`, `SIMBAD`, and `TeVCat`.

I acknowledge the use of the `BIRD` cluster at DESY for the *Fermi*–LAT results presented in Chapter 6. In this matter, a thank you to the UCO and the *Fermi* HelpDesk, especially Dave Davis, Elizabeth Ferrara, and Jeremy Perkins.

I thank Jan Eike von Seggern for providing his python code to perform the upper-limit calculations (PhD thesis; von Seggern, 2014). I acknowledge being provided with the H.E.S.S. muon data by Raquel de los Reyes.

I thank the H.E.S.S. chairman Prof. Christian Stegmann for allowing me to use and show the H.E.S.S. data in Chapter 4.

This thesis was written using `kile` and `LaTex`.

FINANCIAL SUPPORT

This thesis has been funded by the University of Hamburg and the German Ministry for Education and Research (BMBF, grant no. 05A11GU2). I acknowledge funding of the business trips and conferences attendances. I thank the School of Chemistry and Physics in Adelaide for funding the travelling costs and hosting my stay in Adelaide.

Personal Acknowledgements

First of all, I'd like to thank my supervisor Prof. Dieter Horns for giving me the opportunity to work in his group and on the various tasks and topics. Especially, the freedom given to pursue the goals and to tackle the challenges was important to me in so many ways.

I owe Martin Tluczykont a big thank you for all the time he made to answer my big and small questions and for our enlightening discussions on nearly every topic in γ-ray astronomy, sports, and politics. I thank Martin Raue (out of science) for all the fruitful discussions and tips, especially on H.E.S.S. data analysis (I hereby acknowledge using his catch phrase *Das Ding ist ...*). I'd like to thank the entire Hamburg Astroteilchengruppe for the good time over the past years. A special thank you goes to my office mates Max-Anton Kastendieck and Manuel Enrico Meyer (now in Stockholm) for the good working atmosphere. Also, work and leisure wouldn't have been the same without the (scientific and personal) discussions and the chit-chat with Alexander Gewering-Peine, Andrei Lobanov (I enjoyed our coffee battle), Nelly Nguyen (out of science), Franziska Spies, Hannes-Sebastian Zechlin (now Turin), and – of course, Helena Kaufmann, Jagdev Bains, Henrike Meiss, Siawosch Schewa, and Friederike Albrecht.

The seven weeks in Adelaide as a visiting scientist were about the best and a very memorable time during my PhD. I am very grateful to Gavin Rowell for giving me this opportunity and being able to work with him and in the HEAG. It was a heaps good and productive time and I'd like to thank everyone in the HEAG, but especially Prof. Bruce Dawson (for our discussions on CRs), Phoebe Claire de Wilt (especially for being the first person I could ask whenever I had questions about Adelaide and stuff at the uni), Gail Higginbottom (for the chit-chat and the coffee & chocolate breaks), Maximus Malacari & Steven Saffi (for being awesome *tourist* guides and the various trips), and Nigel Maxted (for the prank battle; now in Montpellier). A special thank you goes to Barry Lord.

I also thank the entire H.E.S.S. A&R and Galactic working groups for providing advice and information; in particular: Raquel de los Reyes (for all the information on the muon efficiencies), Christoph Deil (for discussions on H.E.S.S. background systematics), Karl Kosack (for discussions on H.E.S.S. data analysis and for maintaining the `fits` module in HAP), and Stefan Ohm (for our discussions on H.E.S.S. data analysis). I thank Prof. Christopher van Eldik and Ryan Chaves for valuable comments on the TBS paper draft; and Konrad Bernlöhr and Henning Gast for information on the H.E.S.S. MC simulations.

I thank the local IT staff, but especially Rainer-Peter Feller (in his everlasting state of *cheerful grumpiness*) for always helping in IT problems. The atmosphere at the DESY campus was a pleasure to work in; therefore, I thank all my friends and colleagues who were *responsible* for this.

I am grateful that Gavin Rowell and Caren Hagner agreed to be the second referees of my thesis and of my thesis defence, respectively. I also thank Georg Steinbrück for being the chairman in my thesis defence. I owe my gratitude to the following people for carefully proofreading this manuscript and providing valuable comments: Daniela Hadasch, Steffen Krakau, Andrei Lobanov, Nigel Maxted, Manuel Meyer, Stefan Ohm, Franziska Spies, and Martin Tluczykont.

Last, but surely not least I'd like to thank my family for their never-ending support in so many ways and at all times.

Milton (May 2014).

Table of Contents

List of Figures xiii

List of Tables xvii

List of Abbreviations xix

Frequently used Constants, Units, and Prefices xx

1 Introduction 1

2 Cosmic-Ray Acceleration in Stellar Clusters and Star-Forming Regions 9
2.1 Acceleration of cosmic rays . . . 9
2.1.1 Second-order Fermi acceleration . . . 9
2.1.2 First-order Fermi acceleration . . . 10
2.1.3 Supernova remnants . . . 10
2.1.4 Other Galactic VHE gamma-ray sources . . . 12
2.2 Particle acceleration in massive stellar clusters . . . 14
2.2.1 High-mass stars and their winds . . . 14
2.2.2 Collective cluster wind . . . 15

3 Gamma-Rays, the *Fermi* Satellite, and the H.E.S.S. Telescope Array 19
3.1 *Fermi* Gamma-ray space telescope . . . 21
3.1.1 The Large Area Telescope . . . 21
3.1.2 Instrument response . . . 24
3.1.3 Data analysis . . . 25
3.1.4 Limitations of spaceborne gamma-ray observations . . . 27
3.2 Air Showers and Cherenkov Light . . . 28
3.2.1 Electromagnetic air showers . . . 28
3.2.2 Hadronic air showers . . . 30
3.2.3 Cherenkov light . . . 31
3.2.4 Comparison between electromagnetic and hadronic air showers . . . 32
3.2.5 Detection methods of extensive air showers . . . 34
3.3 High Energy Stereoscopic System . . . 37
3.3.1 Cherenkov telescopes . . . 38
3.3.2 Data taking . . . 39
3.3.3 Coincidence trigger . . . 40

3.3.4 Event reconstruction . . . 40
3.3.5 Gamma/hadron separation . . . 43
3.3.6 Optical-efficiency correction . . . 45
3.3.7 Camera acceptance . . . 47
3.3.8 Background estimation . . . 48
3.3.9 Spectral reconstruction . . . 54

4 Template Background Spectrum 55
4.1 The concept . . . 56
4.2 Look-up table . . . 57
4.2.1 Loss in optical efficiency . . . 58
4.2.2 Bright stars . . . 59
4.2.3 Template correction vs. energy, zenith angle, and camera offset . . . 59
4.3 TBS correction . . . 61
4.3.1 Interpolation . . . 61
4.3.2 Extrapolation . . . 63
4.3.3 Effective TBS Correction . . . 65
4.3.4 Excess events . . . 67
4.4 Spectral reconstruction . . . 68
4.4.1 Forward folding . . . 68
4.4.2 Chi-square minimisation . . . 68
4.4.3 Maximum likelihood . . . 69
4.4.4 Butterfly plots . . . 70
4.5 Application to H.E.S.S. data . . . 71
4.5.1 Instrument response . . . 71
4.5.2 Analysis of H.E.S.S. data . . . 76
4.6 Discussion . . . 90
4.6.1 Contribution of TBS to the total uncertainty . . . 90
4.6.2 Choice of parameters . . . 92
4.7 Summary & Conclusions . . . 93
4.8 Outlook . . . 94

5 Discovery of Extended VHE Gamma-Ray Emission from the Vicinity of the Young Massive Stellar Cluster Westerlund 1 97

6 The Unidentified VHE Gamma-Ray Source HESS J1614–518 109
6.1 H.E.S.S. observations and data analysis . . . 110
6.1.1 Morphology . . . 111
6.1.2 Spectral studies . . . 118
6.2 Multi-wavelength data . . . 122
6.2.1 *Fermi*–LAT data . . . 123
6.2.2 X-ray data . . . 126
6.2.3 Radio data . . . 128
6.3 Counterpart scenarios . . . 130
6.3.1 The stellar cluster Pismis 22 . . . 131

6.3.2 The Wolf-Rayet star WR 74 . . . 133
6.3.3 The low-mass X-ray binary 4U 1608–52 . . . 133
6.3.4 The Ant Nebula . . . 134
6.3.5 Pulsars and pulsar-wind nebulae . . . 134
6.3.6 Undetected SNR . . . 137
6.4 Summary and conclusions . . . 137
6.5 Outlook . . . 138

7 Search for very-high-energy Gamma-Rays from the Gould Belt 139
7.1 *Fermi*–LAT observations . . . 142
7.2 H.E.S.S. observations and data analysis . . . 143
7.3 Search for VHE gamma-ray emission . . . 145
7.3.1 Lupus 3 . . . 146
7.3.2 Lynds 1495A . . . 148
7.3.3 Orion A . . . 150
7.3.4 Perseus cloud . . . 152
7.3.5 ρ–Ophiuchus B . . . 154
7.4 Results obtained with extra-Galactic look-ups . . . 156
7.5 Spectral analysis . . . 157
7.5.1 Orion A . . . 157
7.6 Cosmic-ray enhancement factor . . . 160
7.7 Summary and Outlook . . . 161

8 Concluding Remarks 163

9 Publication List 167

A Auxiliary Information to Chapter 4 171
A.1 Histograms . . . 171
A.2 TBS framework . . . 173
A.3 Bilinear interpolation . . . 175
A.4 Alternative definitions of the energy threshold . . . 176
A.5 Correlation plots . . . 177
A.5.1 Crab Nebula . . . 178
A.5.2 Centaurus A . . . 179
A.5.3 HESS J1745–290 . . . 180
A.5.4 HESS J1507–622 . . . 181
A.5.5 Vela X . . . 182
A.5.6 Vela Junior . . . 183

B Auxiliary Information to Chapter 6 185
B.1 Differential energy spectra . . . 185
B.2 Radial velocities . . . 187
B.3 Starburst 99 parameters . . . 188

C AUXILIARY INFORMATION TO CHAPTER 7 191
C.1 *Fermi*–LAT VIEW ON THE GOULD BELT . . . 191
C.1.1 Lupus 3 cloud . . . 192
C.1.2 Taurus region (Lynds 1495A) . . . 193
C.1.3 Orion A . . . 194
C.1.4 Perseus cloud . . . 195
C.1.5 ρ–Ophiuchus B . . . 196
C.2 ANALYSIS OF CENTAURUS A WITH EXTRA-GALACTIC LOOK-UPS OF THE CAMERA ACCEPTANCE . . . 197
C.3 CROSS-CHECK ANALYSES . . . 200
C.3.1 Lupus 3 . . . 200
C.3.2 Lynds 1495A . . . 201
C.3.3 Orion A . . . 202
C.3.4 Perseus cloud . . . 204
C.3.5 ρ–Ophiuchus B . . . 205
C.4 RESULTS OF THE SPECTRAL RECONSTRUCTION USED TO DETERMINE THE EXCESS UPPER LIMITS . . . 206

BIBLIOGRAPHY 207

List of Figures

1.1 The measured cosmic-ray flux . . . 2
1.2 The Hillas diagram . . . 3

2.1 Evidence of hadronic cosmic-ray acceleration in supernova remnants . . . 12
2.2 Collective cluster-wind model . . . 16

3.1 The first γ-ray skymap of the Milky Way as observed with COS–B . . . 20
3.2 Schematic display of the *Fermi* satellite . . . 21
3.3 The point-spread function and the energy resolution of the *Fermi*–LAT . . . 24
3.4 The effective area and the FoV of the *Fermi*–LAT . . . 25
3.5 Illustration of γ-ray induced air shower . . . 29
3.6 Illustration of hadron-induced air shower . . . 30
3.7 Cherenkov-light distribution on ground level . . . 32
3.8 Monte Carlo simulation of a 300 GeV γ-ray and 1 TeV proton air shower . . . 33
3.9 Number of particles in γ-ray induced air showers vs. radiation length . . . 34
3.10 Image of H.E.S.S. phase 2 . . . 37
3.11 The H.E.S.S. telescopes and the Cherenkov camera. . . . 38
3.12 Cleaned camera image of a simulated γ-ray and a hadron shower . . . 41
3.13 Stereoscopic reconstruction of the event direction. . . . 43
3.14 Correlation between core distance and angular . . . 44
3.15 Relative distributions of the MRSW and MRSL parameters . . . 45
3.16 Muon ring and optical efficiency . . . 46
3.17 The camera acceptance for VHE γ rays. . . . 47
3.18 The ring-background method and the reflected-region background method 50
3.19 The template background model . . . 52

4.1 Example of the calculation of α . . . 58
4.2 The template correction vs. energy and zenith angle . . . 60
4.3 Exemplary template correction $\alpha(\theta)$ for TBS . . . 62
4.4 Example of an extrapolation for TBS . . . 64
4.5 Sample of β from H.E.S.S. data on Vela X . . . 66
4.6 The energy-resolution matrix . . . 73
4.7 The effective area . . . 74
4.8 The energy bias . . . 75
4.9 Forward-folded spectrum of the Crab Nebula . . . 79
4.10 Forward-folded spectrum of Centaurus A . . . 80
4.11 Forward-folded spectrum of HESS J1745–290 . . . 82

4.12 Forward-folded spectrum of HESS J1507–622 84
4.13 Forward-folded spectrum of Vela X 86
4.14 Forward-folded spectrum of Vela Junior 88
4.15 Normalised error contribution to the overall excess error in TBS for the Crab Nebula, Centaurus A, HESS J1745–290, and HESS J1507–622 . . . 91
4.16 Normalised error contribution to the overall excess error in TBS for Vela X and Vela Junior 92

6.1 The VHE γ-ray excess counts map of HESS J1614–518 111
6.2 Slice along HESS J1614–518 and the subregions 112
6.3 The VHE γ-ray excess counts maps of HESS J1614–518 for reconstructed energies below and above 1 TeV 117
6.4 Forward-folded spectra of HESS J1614–518 and the subregions 121
6.5 Reported keV and GeV sources in the vicinity of HESS J1614–518 122
6.6 Energy spectra of 1FHL J1615.3–5146e and HESS J1614–518 125
6.7 XMM–*Newton* count image of the centre of HESS J1614–518 127
6.8 MOST 843 MHz and SGPS HI radio images towards HESS J1614–518 . . 129
6.9 Possible astrophysical counterparts in the FoV of HESS J1614–518 130

7.1 The Gould Belt depicted on the 100 μm emission map 139
7.2 Schematic display of the Gould Belt 140
7.3 CO(1-0) radio maps of the Gould Belt source regions 141
7.4 The VHE γ-ray significance skymaps of the Lupus 3 cloud with the template background model and the ring-background method 147
7.5 The VHE γ-ray significance skymaps of Lynds 1495A with the template background model and the ring-background method 149
7.6 The VHE γ-ray significance skymaps of the Orion A cloud with the template background model and the ring-background method 151
7.7 The VHE γ-ray significance skymaps of the Perseus cloud with the template background model and the ring-background method 153
7.8 The VHE γ-ray significance skymaps of ρ–Oph B with the template background model and the ring-background method 155
7.9 Forward-folded spectrum of Orion A 158

A.1 Example of the calculation of α (histograms, 1) 171
A.2 Example of the calculation of α (histograms, 2) 172
A.3 Framework of TBS 174
A.4 Correlation plots for the TBS analysis of the Crab Nebula 178
A.5 Correlation plots for the TBS analysis of Centaurus A 179
A.6 Correlation plots for the TBS analysis of HESS J1745–290 180
A.7 Correlation plots for the TBS analysis of HESS J1507–622 181
A.8 Correlation plots for the TBS analysis of Vela X 182
A.9 Correlation plots for the TBS analysis of Vela Junior 183

B.1 Forward-folded spectra of HESS J1614–518 assuming a power law and a power law with exponential cutoff 186
B.2 Determination of the radial velocity and the distance 187

C.1 The HE γ-ray counts maps of the Lupus 3 region 192
C.2 The HE γ-ray counts maps of the Taurus region (Lynds 1495A) 193
C.3 The HE γ-ray counts map of the Orion A region 194
C.4 The HE γ-ray counts map of the Perseus region 195
C.5 The HE γ-ray counts map of the ρ–Oph B region 196
C.6 The VHE γ-ray significance skymaps of the Centaurus A FoV with the template background model and the ring-background method using the acceptance correction from extra-Galactic data 197
C.7 The VHE γ-ray significance skymaps of the Lupus 3 cloud with the template background model and the ring-background method using the acceptance correction from extra-Galactic data 200
C.8 The VHE γ-ray significance skymaps of Lynds 1495A with the template background model and the ring-background method using the acceptance correction from extra-Galactic data 201
C.9 The VHE γ-ray significance skymaps of the Orion A cloud with the template background model and the ring-background method using the acceptance correction from extra-Galactic data 202
C.10 The VHE γ-ray significance skymaps of the Orion A cloud with the template background model and the ring-background method using the ζ_{hard} cuts 203
C.11 The VHE γ-ray significance skymaps of the Orion A cloud with the template background model and the ring-background method using the acceptance correction from extra-Galactic data and the ζ_{hard} cuts 203
C.12 The VHE γ-ray significance skymaps of the Perseus cloud with the template background model and the ring-background method using the acceptance correction from extra-Galactic data 204
C.13 The VHE γ-ray significance skymaps of ρ–Oph B with the template background model and the ring-background method using the acceptance correction from extra-Galactic data 205

List of Tables

4.1 Observation properties of re-analysed H.E.S.S. data sets 77
4.2 Analysis results with the standard template background model 78
4.3 Results of the analysis with TBS 78
4.4 Spectral results on the Crab Nebula and Centaurus A 81
4.5 Spectral results on HESS J1745–290 and HESS J1507–622 85
4.6 Spectral results on Vela X and Vela Junior 89

6.1 Available high-quality H.E.S.S. data on HESS J1614–518 110
6.2 The different source hypotheses for the slice along HESS J1614–518 . . . 114
6.3 Results of the χ^2 fits and the F–test to the slice 115
6.4 Best-fit parameters for the models ii., v., and vii. 116
6.5 Locations of HESS J1614–518 and its subregions 118
6.6 Analysis results on HESS J1614–518 and the tested subregions with TBS 119
6.7 Spectral results on HESS J1614–518 and its subregions 120
6.8 Spectral properties of the reported HE γ-ray sources in the vicinity of HESS J1614–518 123
6.9 Results of the extended-source analysis of 1FHL J1615.3–5146e 125
6.10 Properties of the pulsars in the FoV of HESS J1614–518 135
6.11 Expected X-ray and γ-ray luminosities for the pulsars in the vicinity of HESS J1614–518 135

7.1 Integral fluxes between 0.3 GeV and 300 GeV of the Gould Belt clouds . . 142
7.2 The Gould Belt cloud complexes observed with H.E.S.S. 143
7.3 The extrapolated TeV fluxes for the Gould Belt regions 144
7.4 Available high-quality H.E.S.S. data on the Gould Belt 144
7.5 Analysis results of the Gould Belt regions with TBS 158
7.6 Spectral properties Orion A derived with TBS 159
7.7 Analysis results of the cross checks on ζ–Tauri and an empty region in the Orion A FoV 159
7.8 Spectral results of the cross checks on ζ–Tauri and an empty region in the Orion A FoV 159
7.9 The cosmic-ray enhancement factor for the Gould Belt sources 161
7.10 Summary of the results on the Gould Belt clouds 162

C.1 Spectral parameters for the five Gould Belt regions as obtained with TBS 206

List of Abbreviations

ACD : *Anti-Coincidence Detector*
CCD : *Charge-coupled device*
CMB : *Cosmic microwave background*
CR : *Cosmic ray*
CT : *Cherenkov telescope*
Dec : *Declination*
DSA : *Diffusive shock acceleration*
DST : *Data summary tape*
EAS : *Extensive air shower*
EB : *Excess to background*
FoV : *Field of view*
FSRQ : *Flat-spectrum radio quasar*
GB : *Gould Belt*
GCR : *Galactic cosmic ray*
HAP : *H.E.S.S. analysis package*
HE : *High-energy*
HMXB : *High-mass X-ray binary*
IACT : *Imaging air-Cherenkov telescope*
IR : *Instrument response*
IRF : *Instrument response function*
ISM : *Interstellar medium*
LuT : *Look-up table*
MC : *Monte Carlo*
MET : *Mission-elapsed time*
MWL : *Multi-wavelength*
NSB : *Night-sky background*
LBV : *Luminous blue variable*
LMXB : *Low-mass X-ray binary*
MHD : *Magneto-hydrodynamic*
MOST : *Molonglo Observatory Synthesis Telescope*
nIACT : *Non-imaging air-Cherenkov telescope*
p.e. : *photo-electron*
PCT : *Precision-Converter Tracker*
PMT : *Photo-multiplier tube*
PWN : *Pulsar wind nebula*
RA : *Right ascension*
RingBg : *Ring background*
RMS : *Root mean square*
ROI : *Region of interest*
RrBg : *Reflected-region background*
RSG : *Red supergiant*
SC : *Stellar cluster*
SFR : *Star-forming region*
SGPS : *South Galactic Plane Survey*
SN : *Supernova*
SNR : *Supernova remnant*
SSD : *Silicon-strip detector*
TBg : *Template background*
TBS : *Template Background Spectrum*
VHE : *Very-high-energy*
vs. : *versus*
w.r.t. : *with respect to*
Wd1 : *Westerlund 1*
WR : *Wolf-Rayet*
1FHL : *First Fermi–LAT catalogue of sources above 10 GeV*
2FGL : *Second Fermi–LAT source catalogue*

FREQUENTLY USED CONSTANTS, UNITS, AND PREFICES

Constant	Meaning	Value
c	speed of light (vacuum)	2.998×10^{8} m
h	Planck constant	6.626×10^{-34} J s
k_{B}	Boltzmann constant	1.381×10^{-23} J/K
π	ratio of circumference to diameter of a circle	3.142 . . .

Quantity	Variable	Units (used)	Units (SI)
Energy	E	electron volt (eV)	1.602×10^{-19} J
		ergon (erg)	1.0×10^{-7} J
Magnetic flux density	B	Gauss (G)	1.0×10^{-4} T
Length	d	parsec (pc)	3.086×10^{16} m
Time	t, T	year (yr)	3.153×10^{7} s
Mass	M, m	Solar mass ($M_{\odot}$)	1.989×10^{30} kg
Luminosity	L	Solar luminosity ($L_{\odot}$)	3.846×10^{26} J s^{-1}

Integral fluxes are in units of m^{-2} s^{-1}.
Differential fluxes are in units of (MeV, GeV, or TeV)$^{-1}$m^{-2} s^{-1}.
Energy fluxes are in units of erg cm^{-2} s^{-1}.

Prefix	Name	Factor
n	nano	10^{-9}
μ	micro	10^{-6}
m	milli	10^{-3}
c	centi	10^{-2}
k	kilo	10^{3}
M	mega	10^{6}
G	giga	10^{9}
T	tera	10^{12}
P	peta	10^{15}
E	exa	10^{18}

Chapter 1

Introduction

It was in 1912 that Victor Franz Hess discovered the cosmic rays (CRs) during one of his (now) famous balloon ascensions and flights, mostly accompanied by W. Hoffory (in charge of the balloon) and sometimes also by E. Wolf (a meteorologist to keep track of the atmospheric conditions). Back then, the rate of events of the so-called *ionising radiation* was expected to drop with increasing distance from the Earth's surface. After all, the radiation was supposed to originate from within the Earth. Instead, Hess found out that the radiation level increased the higher he ascended with the balloon. Since the ascensions were also done at night-time, the measured radiation was unlikely to be coming from the Sun.[i] For this discovery, its correct interpretation, and the follow-up studies made over the following years, Hess was awarded the Nobel prize in physics 1936.

Now, over a century later, we know that CRs mainly consist of protons and heavier nuclei – about 99% are hydrogen and helium nuclei and the remaining $\sim 1\,\%$ are electrons and positrons (e.g. Nakamura, 2010).[ii] The CRs approach the Earth from virtually every direction and exhibit energies from 10^9 eV (GeV)[iii] up to ~ 300 EeV (1 EeV = 10^{18} eV) as reported in Bird et al. (1995). Particles with lower energies are in general not observable, which is mainly a consequence of the solar wind preventing the sub-GeV CR particles from reaching the Earth. On the other hand, the upper end of the energy range is defined by the so-called *GZK cutoff* resulting from the strong CR attenuation due to proton interaction with the cosmic microwave background (Greisen, 1966; Zatsepin & Kuz'min, 1966).

These energies are not achievable in man-made particle accelerators.[iv] For example, a kinetic energy of 10^{20} eV represents that of a 5 kg-heavy bowling ball rolling with a speed of $\sim \mathbf{3}\,\mathrm{m\,s^{-1}}$, but stored in only one nucleus. The observed flux of CRs at GeV energies is roughly one CR particle per hand palm within two minutes. From this, it follows that the Earth is downright bombarded by CR particles. Obviously, there must exist some powerful astrophysical objects outside the Earth capable of accelerating particles onto such high energies.

---

[i] A detailed documentation of the balloon ascensions can be found in Federmann (2003), for example.

[ii] It is not uncommon that also photons and cosmic neutrinos are considered cosmic rays as well. However, throughout this thesis *cosmic rays* always refers to the charged particles.

[iii] See list of frequently used units and prefixes on Page xx.

[iv] Currently, the Large Hadron Collider reaches proton energies around 7×10^{12} eV.

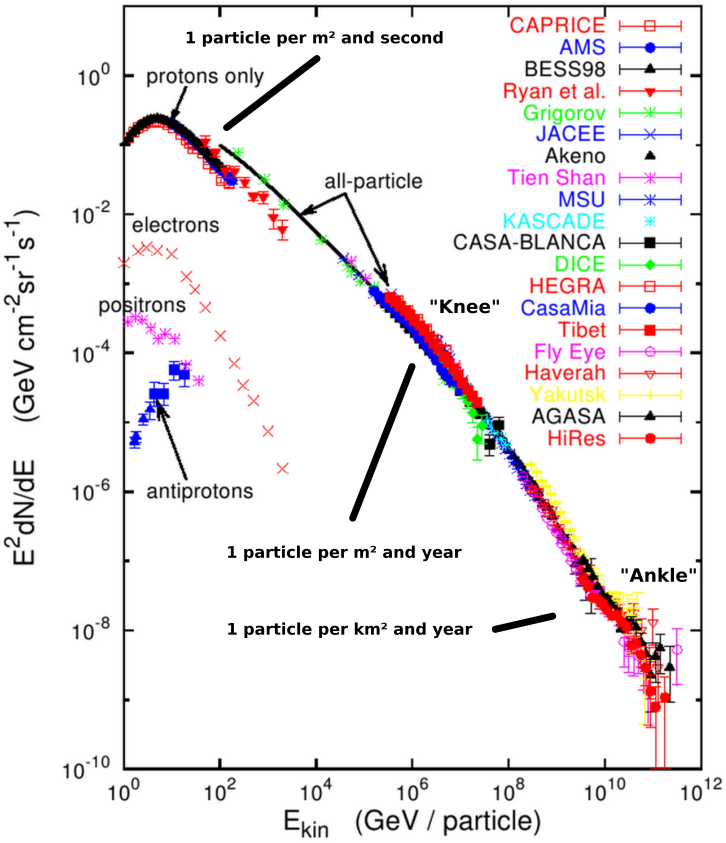

FIGURE 1.1 The measured cosmic-ray flux measured with different experiments covering nearly twelve decades in logarithmic energy scale. Depicted are the different experiments (different colours and markers), and the characteristic *knee* and *ankle* of the CR spectrum. In addition, exemplary fluxes at certain energies are indicated. For references to the individual data points and experiments, see Hillas (2006). The yellow reference reads Yakutsk. An updated spectrum around the ankle can be found in Gaisser (2012), for example. Image adapted from Hillas (2006).

In a combination of various observations with spaceborne and ground-based experiments sensitive to different energy ranges, the differential energy spectrum of cosmic rays is measured almost completely within the aforementioned energy range (see Figure 1.1). At first glance, the entire spectrum appears to follow a single power law in energy $dN/dE \propto E^{-\Gamma}$ with $\Gamma \approx 2.7$. At second glance, the spectrum shows distinct features, which indicate a modification of the spectral shape at certain energies: the *knee* around 10^{15} eV and the *ankle* around 10^{19} eV. At the knee, the spectrum steepens from $\Gamma \approx 2.7$ to $\Gamma \approx 3.0 \ldots 3.2$ and at the ankle, the spectral behaviour hardens ($\Gamma \approx 2.7$) before it strongly steepens to $\Gamma < -4$ at energies above 10^{19} eV (e.g. Reynolds, 2008; Blasi, 2013).

Thus, there are two conclusions that can be drawn. First, the underlying power-law behaviour over the measured energy range suggests a simple universal mechanism that accelerates the CRs. Second, the knee and the ankle might be an indication of different source contributions present in the CR spectrum. Thus, it is suggested and commonly

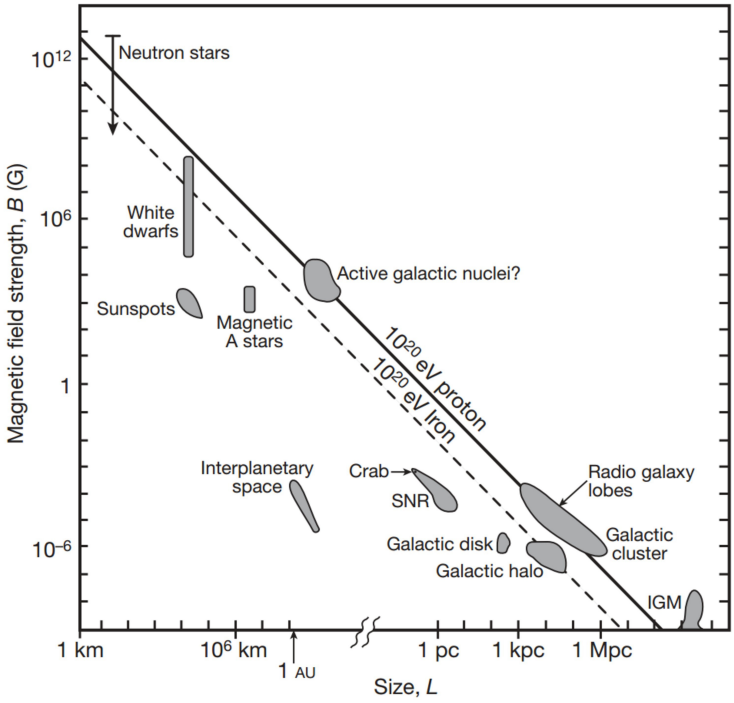

FIGURE 1.2 The Hillas diagram relating the physical size of a CR accelerator to its magnetic field strength (depicted are various astrophysical objects). Here, Crab stands for the Crab Nebula (a pulsar wind nebula), SNR for supernova remnant (both introduced in Chapter 2), and IGM for intergalactic magnetic field. The maximum energy of a 10^{20} eV proton and a iron nucleus are indicated by a solid and a dashed lined, respectively. Image adopted from Bauleo & Rodríguez Martino (2009).

believed that the CRs up to the knee are dominantly accelerated within the Galaxy, but that higher energies are only achievable in processes of extra-Galactic origin. This is also supported from the work done by Hillas (1984).

Hillas (1984) derived constraints on the physical sizes of astrophysical objects that can possibly accelerate CRs. This was motivated by the fact that accelerated particles leave their acceleration sites after reaching the maximum energy, thus there are two possibilities how the accelerator can confine the charged particle population. This is either done by the size of the CR accelerator or by its magnetic field strength. The relation linking both quantities to the maximum energy is

$$E_{\mathrm{max}} \approx L\,B\,, \tag{1.1}$$

for a highly-relativistic proton where L is the size of the accelerator and B its magnetic field strength. Therefore, as long as the Larmor radius ($r_{\mathrm{Larmor}} \propto B^{-1}$) of the proton is smaller than the size of the accelerator L, the particle is confined. The famous *Hillas diagram* illustrates this dependency and is shown in Figure 1.2. This diagram indicates that CR accelerators exhibit very strong magnetic field strengths or are preferably large objects to accelerate particles up to the end of the observed CR spectrum (Fig. 1.1).

Despite the extensive efforts and a considerable progress in the studies of CRs so far, there are still questions yet to be answered:

Where do these particles come from? and *What objects accelerate them?*

A fundamental physical property of the CRs has successfully hampered an answer to these questions. Because CRs are charged, they are deflected in magnetic fields present in the Milky Way, outside the Galaxy, and in other galaxies. Therefore, these particles may not point back towards their origin, which makes it difficult to identify the site(s) of acceleration.

However, in addition to this, CRs interact with matter to produce photons and neutrinos (present in interactions involving CR hadrons), which are not deflected in magnetic fields. These photons are therefore non-thermal and called γ rays. Because these interactions mostly occur within or close to the cosmic particle accelerator, observations of γ rays make it possible to search for the acceleration sites of CRs.[v] Therefore, the γ rays offer an observing tool to probe objects where the most powerful processes take place.

The rather young discipline in astronomy devoted to the detection of γ rays is called γ-ray astronomy. This field in astronomy is split into spaceborne and ground-based observations and has quickly established itself as an important tool to understand processes present at various objects of Galactic and extra-Galactic origin.

Spaceborne experiments provide a direct detection of γ rays, but are limited by their small detection area (around 1 m^2) and the low γ-ray fluxes at higher energies. Currently, the *Fermi* satellite covers an energy range from low MeV energies up to roughly 300 GeV and more (Atwood et al., 2009).

Since the Earth's atmosphere is opaque to γ rays, direct observations of γ rays are not possible on Earth. Among the ground-based detectors of γ rays that indirectly detect γ rays, the imaging air-Cherenkov telescopes (IACTs) have proven to be successful in terms of energy coverage and angular resolution. These IACTs make use of the fact that γ rays initiate particle cascades (air showers) in the atmosphere that emit Cherenkov light that can be measured on ground level and therefore allow for large detection areas. This light pool is imaged onto the camera of the IACT and allows for a complete reconstruction of the incident γ ray. Cherenkov telescope systems like H.E.S.S., MAGIC, and VERITAS cover an energy range from $\sim$ 50 GeV up to almost 100 TeV (e.g. reviewed in Hillas, 2013). The sensitivity is mainly constrained by the mirrors of the telescopes (sparse amount of light at low energies) and the size of the area covered by the telescopes, in which the Cherenkov light is detectable (the larger the covered area, the higher the maximum energies of observable air showers). It is the first time and just about six years ago, that satellite and ground-based detectors together have started to provide a seamless coverage of γ-ray photons from low MeV energies up to almost 100 TeV.

Since CRs up to the knee of the CR spectrum (around PeV energies) are believed to be accelerated within the Galaxy, data from the *Fermi* satellite and the IACTs are valuable in the search of these Galactic CR accelerators. At these energies, supernova remnants

[v] In principle, observations of neutrinos can also be conducted once sufficiently sensitive detectors are available.

(SNRs; discussed in more detail in Chapter 2) constitute the paradigm of Galactic CR acceleration for various reasons. For example, SNRs provide a sufficient kinetic energy that is needed to explain the observed Galactic energy density of $1\,\mathrm{eV\,cm^{-3}}$; here, one supernova event every 30 to 40 years in the Milky Way would be sufficient. Moreover, since the SNR expands at a supersonic velocity and collides with matter in the ambient medium, efficient particle acceleration up to at least 100 TeV is predicted in theory. Therefore, a possible and rather efficient Galactic CR accelerator should provide a sufficient amount of kinetic energy – ideally in processes at supersonic velocities.

However, SNRs are not the only place in the Galaxy where particle acceleration to TeV and perhaps PeV energies can take place. High-mass stars lose a large amount of matter during their lifetime through supersonic outflows (stellar winds). These stars are mostly found in associations or, at larger scales, in stellar clusters (SCs). Interactions of the individual supersonic winds and the development of a collective cluster wind should in principle allow for particle acceleration onto very-high-energies (VHE; energies $E > 100\,\mathrm{GeV}$). Therefore, young star-forming regions (SFRs) and especially massive SCs known to harbour many high-mass stars are perfect study objects to probe such a scenario.

In this thesis, data from the H.E.S.S. telescope system and the *Fermi* satellite were analysed to search for HE (high-energy; $0.1\,\mathrm{GeV} < E < 100\,\mathrm{GeV}$) and VHE γ rays originating from CRs accelerated within SCs and SFRs. For this, H.E.S.S. data on the SCs Westerlund 1 (Wd1; Westerlund, 1961) and Pismis 22 (Piatti et al., 2000) and the SFR known as the Gould Belt (Gould & Galle, 1874) were analysed.

Amongst known SCs, Wd1 is the most-massive one and harbours a unique amount of high-mass stars in the Galaxy. Therefore, this SC was the best candidate to probe acceleration processes in SCs linked to high-mass stars. Indeed, one of the largest VHE γ-ray sources was discovered towards Wd1: the TeV source HESS J1646–458 with a diameter of $\sim 2^\circ$. This source and the investigation of a possible SC origin are presented in Chapter 5.

However, this source together with a couple of other sources pose a challenge to the spectral reconstruction of IACT data. Since CRs induce an overwhelming amount of air showers in the atmosphere that are recorded by the cameras, too, they constitute a dominant background to every measurement. Thus, this background has to be determined before the γ rays from the source of interest are accessible. Usually, it is always possible to produce skymaps with different methods to determine the background. However, in the standard method used in the spectral reconstruction background, test regions are placed in the FoV to determine the background. Their placement is constrained by the geometry of the FoV and the source. Since the FoV of the camera is physically limited, sources with angular extents comparable to the size of the FoV cannot be spectrally reconstructed. Prior to this thesis, the only alternative were observations of source-free regions at the expense of limited dark-time or using previously observed source-free regions with matching observation conditions. For HESS J1646–458, the first option would have meant further $\sim$ 45 hrs of observations, which was not feasible. Therefore, the second option was chosen and only $\sim$ 20 hours of the data on HESS J1646–458 were used to reconstruct the spectrum because more than half of the data remained without a background estimate (no match of archival source-free regions with the Wd1 observations).

Therefore, a new analysis method has been successfully developed that enables the spectral analysis of very extended VHE γ-ray sources without the need for further observations of source-free regions. This method is named *Template Background Spectrum* (TBS) and based on an established method to produce skymaps (the template background model; Rowell, 2003). The template ansatz is the determination of the background in air-shower parameter space. For example, the parameter used to separate γ rays from the background can be the width of the shower image in the camera. Apart from the source itself, no placement of further regions in the FoV is required. No additional data of source-free regions are needed. The TBS method introduces an energy-dependent application of the template background model. In addition, systematic effects of the camera response in combination with the measured γ rays and the background are accounted for. This method has been tested on published H.E.S.S. data and provided compatible results. Moreover, very extended sources like Vela X (Abramowski et al., 2012b) and Vela Junior (Aharonian et al., 2005b) for which normally additional observations of source-free regions are required, were spectrally reconstructed with the TBS method. The development and testing of the TBS method is presented in Chapter 4.

In the following, TBS was used to reconstruct spectra of the other studied objects in this work. The detection of the TeV source HESS J1614–518 towards Pismis 22 was reported in Aharonian et al. (2005a, 2006b) where an association of the VHE γ-ray emission with the SC could not be established. The lack of other possible counterparts made this source one of the largest and TeV-brightest sources to remain unidentified. In this thesis, new H.E.S.S. data were investigated together with an extensive study of archival multi-wavelength (MWL) data (GeV, X-ray and radio data) to shed light on the nature of this source. This study that also involved a detailed discussion of other potential counterparts is presented in Chapter 6.

A discovery of VHE γ-ray emission from young SFRs would be a clear indication that SCs and regions of on-going star formation are CR accelerators. The Gould Belt (GB) is a large-scale elliptical structure (major axis of about 354 pc and minor axis of about 232 pc) in the Galaxy traced by giant molecular clouds (sites of possible future star formation) and young SFRs with high-mass stars. Observations with the *Fermi* satellite reported by Yang et al. (2013) motivate the presence of γ-ray emission at TeV energies that, albeit most probably faint, could be degree-scale extended. These regions are larger than the FoV of H.E.S.S. and therefore pose an unprecedented challenge to the analysis of these VHE γ-ray data. In addition, many bright stars associated with these cloud structures affect the IACT performance. In Chapter 7, unpublished H.E.S.S. data on the GB clouds Lupus Orion, Perseus, and ρ–Ophiuchus and Taurus were analysed in search for VHE γ-ray emission. For this, different analysis methods were applied and investigated, but led to different results. Among these, the possible discovery of VHE γ-ray emission towards Orion is discussed.

The structure of this thesis is as follows. The next chapter provides an introduction to CR acceleration and motivates why SCs are considered possible CR accelerators (Chapter 2). Then, in Chapter 3, the detection methods of HE and VHE γ rays with emphasis on the *Fermi* satellite and the H.E.S.S. telescope system are presented. In Chapter 4, the

development of the TBS method is presented. The following three Chapters present and discuss the results of the studies on the SCs Wd1 (Chapter 5), Pismis 22 (Chapter 6, and on the GB (Chapter 7). This thesis concludes in Chapter 8 with final remarks summarising the results on the different source regions in the light of SCs being CR accelerators. This chapter is succeeded by the list of publications (Chapter 9), the Appendix, and the bibliography.

Chapter 2

Acceleration of Galactic Cosmic Rays in Massive Stellar Clusters and Star-Forming Regions

The question of what accelerates CRs and what astrophysical processes are involved in doing so is still not fully and satisfactorily answered. It is believed that the observed CRs up to the *knee* of the CR energy spectrum (about 3 PeV) are of Galactic origin, whereas CRs of higher energies are accelerated outside the Milky Way (in other galaxies) and traverse the intergalactic medium. As CRs are subject to constant deflection in magnetic fields, they do not point back at their origin. Therefore, a direct access to their site of acceleration is hampered. Measurements of CRs led to the observations that their energy spectrum is fairly well described by a single power law. Therefore, acceleration processes and mechanisms should ideally result in a power-law behaviour thus allowing for (possible) multiple contributions of different sources to add up the to observed spectrum.

2.1 Acceleration of cosmic rays

The acceleration of the particles onto relativistic energies was proposed more than a half century ago by Fermi (1949) and was later on named after him. In the following, the basic principle is explained.[i]

2.1.1 Second-order Fermi acceleration

Fermi (1949) proposed a stochastic process, in which particles could be accelerated onto very-high energies by randomly scattering off magnetised clouds and thereby on average gain energy per collision:

$$\left\langle \frac{\Delta E}{E} \right\rangle \propto \beta^2 \,, \tag{2.1}$$

where $\beta = v/c$ with v being the particle velocity and c the speed of light. This process was later on named 2$^{\text{nd}}$ order Fermi acceleration because the relative energy gain goes with

[i] For this, it is referred to a lecture of Regis Terrier at the NPAC 2012.

the power of 2 in β.

Since low velocities of the order of 1 to 10 km s^{-1} are involved, the efficiency of this process is low (see also Hillas, 1984). For example, with $v = 10\,\mathrm{km\,s^{-1}}$, one achieves $\langle \Delta E/E \rangle \approx 10^{-8}$ per collision, thus the average gain is low. Particles can also lose energy in this stochastic scattering process. The particle spectrum of this process is a simple power law $N \propto E^{-\alpha}$, where the rather unconstrained index α depends on β and the cloud density.

2.1.2 First-order Fermi acceleration

A similar acceleration scenario was proposed by Krymskii (1977); Axford et al. (1977); Bell (1978); Blandford & Ostriker (1978) independently within a short period of time. In the blast wave of a supernova (SN), particles are accelerated at the boundaries of a supersonic expanding shock wave. By crossing the shock front the particles gain energy every time they cross the shock back and forth:

$$\left\langle \frac{\Delta E}{E} \right\rangle \propto \beta\,. \tag{2.2}$$

This process is linear in β and therefore named 1$^{\mathrm{st}}$ order Fermi acceleration. In a simplified scheme, particles gain energy ΔE every time they cross the shock front and are isotropised. After every crossing the gain in energy is $\Delta E = kE$ with a fraction k; and after n crossings, the particle with initial energy E_0 has gained $E_n = (k+1)^n E_0$. At the same time, the escape probability increases (depending on the compression ratio r of the shock and the velocity of the medium ahead of the shock) that the particle leaves the shocked region.

As a result, the differential energy spectrum of this *diffuse shock acceleration* (DSA) process is proportional to $E^{-\alpha}$, where $\alpha = (r+2)\,/\,(r-1)$. In the case of a strong shock ($r = 4$), a simple power law with $\alpha = 2$ is found. This theoretical result is close to the observed value of $E^{-2.7}$ up to the knee for the CR spectrum. Slight modifications of this acceleration scenario can lead to an even better agreement (e.g. discussed in Hillas, 2005).

Comparing both acceleration processes, the efficiency through a 1$^{\mathrm{st}}$ order Fermi acceleration is higher as the energy gain is linear in β (as $\beta < 1$). Moreover, because the DSA process predicts a *universal* power-law behaviour, different accelerators are possible and therefore can add up to the observed CR spectrum without resulting in a feature below the knee. This is not necessarily the case for the 2$^{\mathrm{nd}}$ order Fermi acceleration, which also predicts a power-law shape, but, then again, is strongly dependent on the ambient conditions (cloud density and β).

2.1.3 Supernova remnants

The earliest evidence that CRs are accelerated in the Milky Way came from observations at radio wavelengths, which showed extended emission. In 1953, Shklovskii proposed that this emission was due to synchrotron radiation of non-thermal electrons and should

be considered remnants of yet undetected SNe. Thus, these electrons implied efficient acceleration onto (at least) GeV energies, and later on, this acceleration could be explained plausibly via the 1st order Fermi-acceleration process (e.g. reviewed in Reynolds, 2008).

In addition, the 1st order Fermi-acceleration process provides a mechanism to accelerate particles to multi-TeV and PeV energies. Since then, it is commonly believed that also the hadronic component of the CRs can be accelerated in SNRs. SNRs are mainly discovered in observations at radio wavelengths and there is indication that the oldest SNRs are only visible in these wavelengths ranges (Koo et al., 2006).

2.1.3.1 SUPERNOVA REMNANTS AS HADRONIC COSMIC-RAY ACCELERATORS

The acceleration of GCRs up to PeV energies via the 1nd order Fermi-acceleration process requires the presence of a large energy reservoir that can be tapped. The main reasons why SNRs are considered viable acceleration sites of GCRs is the average energy release of $\sim 10^{51}$ erg per SN. Assuming that around 10 % of the energy are mechanically available for particle acceleration[ii] (in form of an expanding shock wave with velocities around 10^4 km s^{-1}), the observed GCR energy density can be explained: to contain the observed particle population within the Milky Way at the observed energy density of about 1 eV cm^{-3} (e.g. Webber, 1998) for at least 10 Myrs (energy and element-dependent) about 10^{41} erg s^{-1} are required. Thus, a SN every 30 to 40 yrs would be sufficient and moreover, is expected from observations of other galaxies. This idea goes back to the work of Ginzburg & Syrovatskii (1964) and we refer the reader also to Klapdor-Kleingrothaus & Zuber (1997); Hillas (2005); Drury (2012).

Additionally, the chemical composition of the CRs can be explained in this scenario as well as the overabundances of specific elements like ^{22}Ne (Higdon & Lingenfelter, 2003). Also, the aforementioned match of the power laws of the CR spectrum and the DSA prediction support the SNR scenario.

2.1.3.2 GAMMA-RAYS FROM SUPERNOVA REMNANTS

The presence of relativistic particles (protons and electrons) can be indirectly confirmed by the detection of γ rays. Relativistic electrons may produce γ rays (of roughly one third of the electron energy) through synchrotron radiation. Additionally, γ rays can also be produced through inverse-Compton upscattering of photons present in a seed photon field, e.g. the cosmic microwave background (CMB) or a stellar radiation field. In collisions of the relativistic protons with the matter in the interstellar medium (ISM), π^0 mesons are produced, which decay into γ rays. Moreover, the same process can also take place more distant from the SNR when escaping relativistic protons interact with nearby clouds and again subsequently produce γ rays from π^0 decay. These γ rays are then detectable with satellites or ground-based detectors sensitive to this energy regime (discussed later on in Chapter 3). Prominent examples are the historic shell-type SNRs SN 1006 (Acero et al., 2010) and W 28 (Aharonian et al., 2008).

[ii] The major part of the SN energy is *lost* through neutrinos and therefore not available for further particle acceleration.

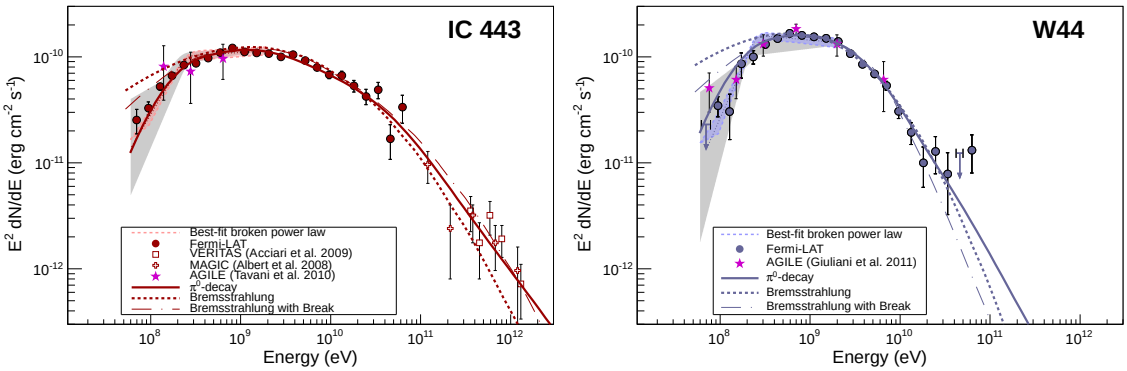

FIGURE 2.1 Evidence of hadronic CR acceleration in SNRs from *Fermi*–LAT observations. Depicted are the MeV-to-TeV spectra of two SNRs which both show the characteristic low-energy cutoff attributed to the decay of π^0 mesons produced in interactions of hadronic CRs. **LEFT:** The spectrum of the SNR IC 443. **RIGHT:** The spectrum of the SNR W 44. Images adopted from Ackermann et al. (2013b).

It is just a year ago that observations in the MeV to GeV energy band with the *Fermi* satellite[iii] resulted in the first direct evidence that protons are accelerated onto the VHE regime. In the HE spectra of the SNRs IC 443 and W 44, the characteristic π^0 decay was clearly identified through a low-energy cut-off around 100 MeV (the so-called π^0 *bump*; Ackermann et al., 2013b). The reported MeV-to-TeV spectra of both SNRs are illustrated in Figure 2.1.

2.1.4 OTHER GALACTIC VHE GAMMA-RAY SOURCES

Currently, 147 TeV sources are listed in `TeVCat` with 22 additional source candidates (Galactic and extra-Galactic sources).[iv] Almost all extra-Galactic sources are linked to the presence and activity of supermassive black holes in the centre of distant galaxies (e.g. Hinton & Hofmann, 2009). Apart from the Galactic VHE γ-ray sources for which no plausible counterparts in other wavelengths have been found (these *dark* or unidentified sources constitute about a third of all detected TeV γ-ray sources), all firmly associated TeV sources of Galactic origin are linked to some stage of stellar evolution. These sources are (of course) SNRs, but also pulsar-wind nebulae (PWNe) and binaries.

PULSAR-WIND NEBULAE A PWN is a system comprised of a rotating pulsar powering a magnetised wind of electrons and positrons. The source of power is the spin-down power of the pulsar. The γ-ray emission is due to an inverse-Compton process where photons resulting from synchrotron radiation (of the $e^{\pm}$ in the wind) and from the CMB are upscattered (a detailed description is given in Gaensler & Slane, 2006). Most prominent members of this most-abundant TeV source class are the Crab Nebula and the Vela X PWN (Aharonian et al., 2006a; Abramowski et al., 2012b).

[iii] Introduced and discussed in Section 3.1.
[iv] URL: *tevcat.uchicago.edu* as of March 2014.

BINARY SYSTEMS Binary systems are comprised of a compact object (a neutron or a stellar black hole) and a stellar companion. Binary systems detected in VHE γ rays consist of a high-mass star as the stellar companion and are bright in X-rays. Therefore, they are named high-mass X-ray binaries (HMXBs). A possible scenario is the inverse-Compton scattering of the photons from the stellar companion with the leptons present in the pulsar wind. See for example the binary LS 5039 (Aharonian et al., 2006c).

GAMMA RAYS FROM STELLAR CLUSTERS? Naturally, high-mass stars provide a large amount of kinetic energy through dense supersonic winds, especially at later stages of their evolution. The available energy reservoir can be considerably large because most high-mass stars are found in associations and (massive[v]) stellar clusters that can add up to an enormous amount of energy and eventually exceed the kinetic energy provided by a single SN. Thus, it is striking that a clear confirmation of TeV emission directly linked to SCs has not been established so far.

There are (at least) four TeV sources, where a SC poses a viable counterpart: the TeV γ-ray source HESS J1848–018 and possibly the SFR W 43, HESS J1023–575 and the young massive SC Westerlund 2, HESS J1646–458 and the currently most-massive SC in the Galaxy Wd1, and HESS J1614–518 and the old SC Pismis 22 (Chaves et al., 2008; Abramowski et al., 2011, 2012c; Rowell et al., 2008).

But because these sources are extended, alternative/additional (possible) counterparts are found in the VHE γ-ray emission regions. For example, the TeV sources around W 43 and Westerlund 2 might be a PWNe, which is motivated by the analysis of GeV data from the *Fermi* satellite (Acero et al., 2013). The Wd1 source is the largest TeV source and a couple of alternative counterparts (e.g. pulsars and a binary system) are located in this VHE γ-ray source. The counterpart discussion is to be found in Chapter 5. The TeV source around Pismis 22 is one of the TeV-brightest sources to remain unidentified (Rowell et al., 2008; Ohm et al., 2010). For this source, a SC scenario is motivated also because of the apparent lack of other alternative counterparts. In Chapter 6, new H.E.S.S. and available MWL data have been investigated to shed light on the nature of this source.

In the TeV γ-ray energy range, emission towards the SCs of interest appeared extended, therefore the emphasis is on collective effects and scenarios that explain a large source region and not single or few-stars scenarios, which are expected to lead to more compact emission regions. Possible scenarios (other than the ones already mentioned above and not directly related to SCs as such) are that of colliding wind binaries. Here, binary system of the high-mass stars drive strong winds and at their wind-wind interaction zones particle acceleration at least up to GeV energies is possible (Eichler & Usov, 1993). Both leptonic (inverse-Compton upscattering of the stellar-radiation photons) and hadronic processes (through nuclei present in both winds) are possible and the interested reader is referred to e.g. Mücke & Pohl (2002); Benaglia & Romero (2003). A colliding-wind binary candidate has been detected at GeV energies with the *Fermi* satellite (Abdo et al., 2010b), but remained undetected in the TeV regime (Abramowski et al., 2012d).

[v] In this sense *massive* cluster refers to a high initial cluster mass, e.g. $> 10^3\ M_\odot$.

2.2 Particle acceleration in massive stellar clusters

In this section, it is motivated why massive SCs are considered possible particle accelerators. For this, high-mass stars and their properties, which make them the powerhouse of SCs, are introduced.

2.2.1 High-mass stars and their winds

Stars are formed when (giant) molecular clouds collapse due to gravitational instabilities, e.g. triggered by an external event such as a nearby SN. This leads to condensation of cloud matter to clumps, which grow larger by gravitationally accreting matter. These clumps grow and become denser and continuously heat up. Eventually, after passing an evolutionary phase as protostar (*T-Tauri* stars), nuclear fusion sets in and the star is born. A very detailed and recommendable review on (high-mass) star formation and evolution is given in Woosley et al. (2002).

The mass of the parent cloud determines the amount of stars will be formed and their distribution of masses. In general, a large parent cloud leads to a more massive SC with more high-mass stars towards the upper mass range ($\geq 100\,M_\odot$). This dependence is described by the initial-mass function, which predicts the distribution of stellar masses for a given initial cluster mass (Salpeter, 1955; Kroupa, 2001).

The emphasis is put on the high-mass stars of the spectral class O ($M > 16\,M_\odot$). These stars drive strong and dense winds, which make them interesting objects for particle acceleration. Moreover, during their lifetime, they pass evolutionary stages, in which an enhanced mass loss is observed.

In general, there are three different processes, which can explain the observed mass loss of stars through stellar winds (Conti, 1978). The mass loss can be driven by the radiation pressure (strong emission lines) of the star and is coupled to the stellar luminosity. Alternatively, the stellar winds may be the result of some non-thermal process (turbulence, vibration, rotation) leading to an enhancement of matter towards the stellar surface, which would result in an outflow into the ISM because of the density gradient. Also, a rapid rotation of the high-mass star could lead to a mass loss and thus to a stellar-wind outflow.

Conti scenario The evolution of an O star can be described by the so-called *Conti scenario*, which has been modified by Crowther (2007) to account for the observations of high-mass stars in their later stages. For O stars with initial masses M_O, the evolutionary stages and transitions are

$$\begin{aligned}
25 < M_\mathrm{O}/M_\odot < 40 \;&:\; \mathrm{O} \rightarrow \mathrm{LBV/RSG} \rightarrow \mathrm{WN_{H-}} \rightarrow \mathrm{SN\,Ib} \\
40 < M_\mathrm{O}/M_\odot < 75 \;&:\; \mathrm{O} \rightarrow \mathrm{LBV} \rightarrow \mathrm{WN_{H-}} \rightarrow \mathrm{WC} \rightarrow \mathrm{SN\,Ic} \\
M_\mathrm{O}/M_\odot > 75 \;&:\; \mathrm{O} \rightarrow \mathrm{WN_{H+}} \rightarrow \mathrm{LBV} \rightarrow \mathrm{WN_{H-}} \rightarrow \mathrm{WC} \rightarrow \mathrm{SN\,Ic}\,.
\end{aligned}$$

Here, LBV (luminous blue variable) and RSG (red supergiant) stars are short-lived stages in the stellar evolution with an enhanced mass loss, the WN and WC stars are Wolf–Rayet (WR) stars, where N and C refer to the dominant emission lines visible in the stellar spectra, i.e. nitrogen and helium in the case of WN stars and carbon and oxygen lines for WC stars, respectively. The H+ and H− indicate WR atmospheres with strong or weak/depleted hydrogen lines. The evolution is highly dependent on the metallicity of the stars, but, in general, the presented tracks are a sufficiently well description of the evolutionary phases of O stars. The last stage in the evolution of O stars is a core-collapse SN. The nomenclature is based on the presence and absence of specific lines, e.g. hydrogen and helium and also depends on how the light curve evolves with time (see e.g. Woosley & Weaver, 1986; Smith, 2014, and references therein). O stars with masses $\lesssim 20\,M_\odot$ evolve into various blue/red supergiant stages before they end as SN IIp (Meynet et al., 2011). The high-mass O stars have a mass-dependent lifetime of 3 to 5 Myrs before they evolve into LBVs/RSGs and WR stars.

KINETIC WIND ENERGY OF HIGH-MASS STARS The determination of how long the star spends its lifetime in these later stages is model-dependent. O stars exhibit mass losses in the range of $10^{-7}\,M_\odot\,\mathrm{yr}^{-1}$ to $10^{-5}\,M_\odot\,\mathrm{yr}^{-1}$, which flow with terminal velocities between $1000\,\mathrm{km\,s}^{-1}$ and $3000\,\mathrm{km\,s}^{-1}$ (Vink et al., 2001; Prinja et al., 1990). The short phases as RSG and LBV stars ($O(10^3 \ldots 10^4\,\mathrm{yrs})$) are characterised by periods of a high mass loss (up to $10^{-4}\,M_\odot\,\mathrm{yr}^{-1}$), but rather low velocities of $O(10 - 100\,\mathrm{km\,s}^{-1})$ as estimated in Parizot et al. (2004). Thus over typical RSG and LBV lifetimes, the contribution to the total kinetic energy budget is negligible. WR stars exhibit mass losses of $10^{-4.8}\,M_\odot\,\mathrm{yr}^{-1}$ to $10^{-5.3}\,M_\odot\,\mathrm{yr}^{-1}$, which are transported in stellar winds with velocities in the range of $1000\,\mathrm{km\,s}^{-1}$ to $4000\,\mathrm{km\,s}^{-1}$. Since their lifetime can span about 0.5 Myrs, their output in mechanical wind energy is large. Thus, in a massive SC, O and WR stars provide a sufficiently large mechanical energy reservoir and supersonic winds, which could in principle be used to accelerate particles. On the other hand, contributions of RSG and LBV stars are negligible w.r.t. (with respect to) the total stellar lifetime. For example, the kinetic wind luminosities of ten O and ten WR stars are calculated for representative values:

$$L_w(\mathrm{O}) \approx 10^{38} \left(\frac{\dot{M}}{10^{-6}\,M_\odot\,\mathrm{yr}^{-1}}\right) \left(\frac{v_\infty}{1700\,\mathrm{km\,s}^{-1}}\right)^2 \left(\frac{N_\star}{10}\right) \mathrm{erg\,s}^{-1}\,, \tag{2.3}$$

$$L_w(\mathrm{WR}) \approx 10^{39} \left(\frac{\dot{M}}{10^{-5}\,M_\odot\,\mathrm{yr}^{-1}}\right) \left(\frac{v_\infty}{2000\,\mathrm{km\,s}^{-1}}\right)^2 \left(\frac{N_\star}{10}\right) \mathrm{erg\,s}^{-1}\,. \tag{2.4}$$

Thus, ten O-type stars will enhance their kinetic wind luminosity output by a factor of 10 when evolving into the WR phase. This leads to a comparable amount of kinetic energy $E = L\,t$ for O stars with lifetimes of $t \approx 5$ Myrs and WR stars with $t \approx 0.5$ Myrs.

2.2.2 COLLECTIVE CLUSTER WIND

Weaver et al. (1977) presented a detailed model showing that a single high-mass star with a strong stellar wind leads to the formation of a so-called *bubble*, i.e. a void driven by the

stellar outflow and resulting in shock-like structure at the boundaries of the wind and the ISM. Since then, many works were put forward to apply this single-star model to massive SCs, in which collective effects of the single stars are considered. In the following, it is referred to the works of Parizot et al. (2004); Oskinova (2005); Silich et al. (2005).

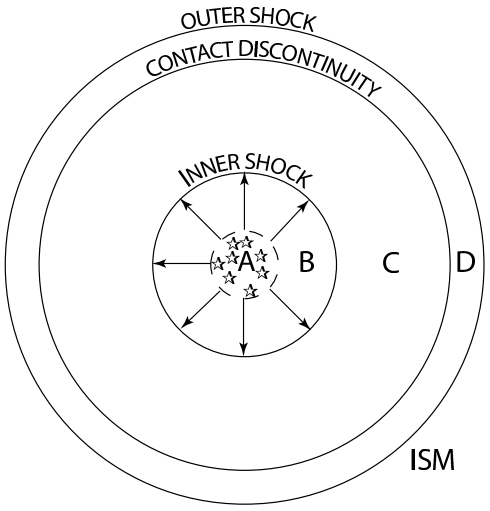

FIGURE 2.2 The collective cluster-wind model from Silich et al. (2005). Region A is the SC volume with its high-mass stars driving the collective stellar winds. Region B is the free-wind zone. Region C is the hot superbubble, which is formed between the inner shock and the thin shell of swept-up matter. Region D is the shell of swept-up matter expanding into the ISM.

In Figure 2.2, a sketch of the model of a collective cluster wind from Silich et al. (2005) is presented. As for the single-star scenario, the winds (and occurred SNe) within the SC (region A) add up to a collective cluster wind, which blows out matter in the SC in form of a hot and tenuous plasma. This cluster wind is highly turbulent as the mean distance between two high-mass stars is smaller than the respective single-star bubble making them interact with each other, potentially increasing the existing magneto-hydrodynamic (MHD) turbulences present in the winds of high-mass stars (Dwarkadas, 2008). The SC itself is X-ray bright due to its stellar content. Region B is called the free-wind region, where the wind flows with the terminal velocity v_∞. However, in the case of very massive SCs, the winds radiate efficiently to cool before reaching the inner shock. From there on, the winds form the superbubble (C). The boundaries of this superbubble is the shell structure (the outer shock) consisting of the swept-up matter (D) separating the superbubble interior from the ISM and the inner shock, which is built when the reverse shock meets the SC outflow. The superbubble therefore persists as long as the SC can provide its strong cluster wind. Similar as in the case for the shock front of SNRs, the outer shock is bright in X-rays. The regions A and B emit X-rays because of the radiative cooling of the hot plasma wind.

Following Silich et al. (2005), the properties of the collective cluster-wind model are

determined:

$$
\begin{aligned}
v_\infty &= 1700 \left(\frac{L_{\rm SC}}{10^{39}\,{\rm erg\,s^{-1}}}\right)^{1/2} \left(\frac{\dot{M}_{\rm SC}}{M_\odot\,{\rm yr^{-1}}}\right)^{-1/2} {\rm km\,s^{-1}}\,, \\
R_{\rm in} &= 20 \left(\frac{L_{\rm SC}}{10^{39}\,{\rm erg\,s^{-1}}}\right)^{3/10} \left(\frac{n}{1\,{\rm cm^{-3}}}\right)^{-3/10} \left(\frac{t}{10^5\,{\rm yrs}}\right)^{2/5} \left(\frac{v_\infty}{10^3\,{\rm km\,s^{-1}}}\right)^{-1/2} {\rm pc}\,, \\
R_{\rm out} &= 30 \left(\frac{L_{\rm SC}}{10^{39}\,{\rm erg\,s^{-1}}}\right)^{1/5} \left(\frac{n}{1\,{\rm cm^{-3}}}\right)^{-1/5} \left(\frac{t}{10^5\,{\rm yrs}}\right)^{3/5} {\rm pc}\,, \\
v_{\rm out} &= 6 \left(\frac{R_{\rm out}}{\rm pc}\right) \left(\frac{t}{10^5\,{\rm yrs}}\right)^{-1} {\rm km\,s^{-1}}\,,
\end{aligned}
\tag{2.5}
$$

where $L_{\rm SC}$ is the kinetic cluster luminosity from winds and SNe, $\dot{M}_{\rm SC}$ the total mass loss of the SC, $R_{\rm in}$ the radius of the inner shock, and $R_{\rm out}$ that of the outer shock that expands with the velocity $v_{\rm out}$; n is the density of the ambient medium in units of particle per cm^3.

This cluster model includes potential acceleration sites of particles. Already in the cluster itself, wind-wind interactions of high-mass stars are possible. In Dwarkadas (2008), it was shown in two-dimensional MHD simulations of a high-mass star that these non-radial motions (i.e. eddies and turbulences) merge and grow and can consume about 20 % of the stellar kinetic wind energy in total.[i] It is suggestive that combined winds of the various stars can lead to stronger turbulences and thereby giving rise to 2$^{\rm nd}$ order Fermi acceleration. The outer shock may give rise to particle acceleration through 1$^{\rm st}$ order Fermi acceleration similar as in the common SNR scenario, but may be not that efficient as the winds are slower than in the SNR paradigm. Additionally, SNe within the superbubble will amplify existing shocks and turbulences. However, the SNRs of SNe to occur within the cluster will not reach the boundary of the superbubble and moreover, the SNR will become subsonic before entering the radiative phase and *die* in the superbubble interior (Parizot et al., 2004).

Oskinova (2005) showed that massive SCs are likely to be very bright in X-rays and exhibit diffuse emission. For a simulated SC with an initial mass of $10^6\,M_\odot$, the X-rays from the stellar winds should dominate the X-ray luminosity of the SC up to an age about 6 Myrs. At later stages, the X-ray brightness is determined by SNe of the high-mass stars. After 40 Myrs, no significant (diffuse) X-ray emission is expected as the contribution of SNe to the X-ray emission rapidly declines. The phases when the different contributions set in and dominate depend on the initial cluster mass. In general, the diffuse X-ray emission $L_{\rm diff,X}$ can be downscaled to smaller SC sizes as it scales with the number of high-mass stars $N_\star$ or their mass loss, respectively: $L_{\rm diff,X} \propto \dot{M}^3 \propto N_\star^3$.

Summary The more massive a SC is the more high-mass stars it harbours. Therefore, the most massive SCs are the most promising candidates w.r.t. particle acceleration onto TeV energies.

[i] In a three-dimensional MHD simulation of a single star, the percentage of kinetic energy going into turbulences has certainly to be downscaled because of the additional degree of freedom.

The SC Wd1 is currently the most massive stellar cluster in the Milky Way with an estimated mass of about $10^5\,M_\odot$ and is supposed to harbour about 150 high-mass OB[ii] stars and at least 24 WR stars (Clark et al., 2005). In terms of cluster mass and high-mass stars, this SC is the good candidate for the above-presented scenario and was therefore target of H.E.S.S. observations. The results of the H.E.S.S. observations are presented in Chapter 5. Current models as presented above, do not only motivate CR acceleration onto VHE γ-ray energies, but also predict observable X-ray emission from these sites .

However, as all identified Galactic TeV sources are linked to phases of stellar evolution, a very young massive SC, in which no SNe have yet occurred, or a young SFR could give insights to the question if SCs can accelerate GCRs onto TeV and PeV energies and therefore contribute to the observed energy density of GCRs. Results on the GB, a large-scale SFR are presented in Chapter 7.

[ii]Stars of the spectral type B have masses above $2\,M_\odot$ and up to $16\,M_\odot$.

Chapter 3

Gamma-Rays, the *Fermi* Satellite, and the H.E.S.S. Telescope Array

On the next pages, a very brief overview of γ-ray observations is given. The emphasis is on the early days and the spaceborne experiments leading to observations of HE γ-rays above 100 MeV with the *Fermi* satellite. Current satellites are not sensitive enough to explore the γ-ray energy regime at TeV energies (and beyond), but because γ-ray photons induce particle cascades in the Earth's atmosphere, these cascades (called *extensive air showers*) provide sufficient information to reconstruct the incident γ-ray photon. In Section 3.2, these air showers and their implications for ground-based observations of γ-rays in the VHE γ-ray regime above 100 GeV are laid out. Subsequently, the basic methods of ground-based observations are described. Among the instruments and experiments dedicated to the detection of VHE γ-rays, the main focus is on the H.E.S.S. telescope array. Data from the *Fermi* satellite and from the H.E.S.S. telescope array are used and discussed throughout this work; therefore, these experiments are described in more detail.

The first evidence for gamma rays Following the tradition of spaceborne experiments throughout a large wavelength range, the first γ rays were directly observed with satellites. Since the Earth's atmosphere is opaque to photons with energies beyond 10 eV (e.g. Weekes, 1988), this was a straight-forward approach.

The first telescope to observe γ rays was *Explorer 11* (Kraushaar & Clark, 1962; Kraushaar et al., 1965). However, because the 22 γ-ray candidates within a CR background of 22000 events were not clustered, these events could not be attributed to a source nor to the Galactic Plane. These observations were considered upper limits on the true γ-ray flux. In 1967, two Vela satellites of the Project *Vela*[i] serendipitously detected the first γ-ray bursts[ii]. Between 1969 and 1973, in total 16 of such burst events lasting between 0.1 and 30 s in the energy range between 0.2 to 1.5 MeV were observed and reported in Klebesadel et al. (1973).

[i] The purpose of these altogether 12 satellites were to monitor the Soviet compliance with the Partial Test Ban Treaty of 1963 (*state.gov/t/isn/4797.htm*).

[ii] Short γ-ray light flashes from large (extra-Galactic) distances indicating a high output in energy of unknown nature within a short time.

FOLLOW-UP EXPERIMENTS Motivated by the results of Explorer 11, the first γ rays from the Galactic Plane were detected with the OSO 3 (Orbiting Solar Observatory 3) satellite with its *High Energy Gamma-Ray* instrument (Kraushaar et al., 1972). With the satellites SAS–2 (the Small Astronomy Satellite 2, Derdeyn et al., 1972) and COS–B (The Cosmic-Ray Satellite B, Bignami et al., 1975) the first γ-ray observations were conducted in similar energy bands from about 20 MeV to $\sim$ 1 GeV and 30 MeV to $\sim$ 5 GeV and resulted in the first high-energy γ-ray images of the Galaxy (see Figure 3.1).

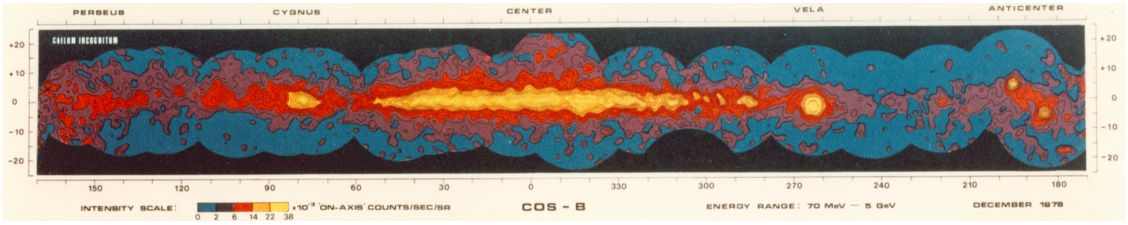

FIGURE 3.1 The γ-ray emission from the Milky Way measured with COS–B in units of on-axis counts s^{-1} sr^{-1} in the energy range between 70 MeV and 5 GeV. The black areas (denoted as *caelum incognitum*, unknown sky) were not observed. Image adopted from *ESA*, the European Space Agency.

A few years later, the *Compton Gamma-Ray Observatory* (CGRO) with its on-board experiments BATSE (the Burst And Transient Source Experiment, Fishman, 1992), OSSE (the Oriented Scintillation Spectrometer Experiment, Cameron et al., 1992), COMPTEL (The imaging Compton Telescope Denherder et al., 1992), and EGRET (the Energetic Gamma Ray Experiment Telescope, Kanbach et al., 1988) was launched. The EGRET had a FoV of 0.5 sr and was sensitive to γ rays in an energy band of 20 MeV to about 30 GeV with a hard-spectrum[iii] point-source sensitivity of 10^{-3} m^{-2} s^{-1} for an exposure of 1 year above 100 MeV. Thus, EGRET is considered a breakthrough in γ-ray astronomy (for a review on the impact and legacy of EGRET see Thompson, 2008). With EGRET, the first all-sky observations above 100 MeV were conducted and altogether 271 γ-ray sources were detected with 170 of them being unidentified (Hartman et al., 1999).

In the recent past, the satellites AGILE (in 2007) and *Fermi* (in 2008) were launched. The satellite AGILE is sensitive to a higher energy range of 30 MeV to 50 GeV (the Gamma-Ray Imaging Detector) and a lower one of 350 keV to 100 MeV with MCAL (the Mini Calorimeter). Additionally, it is sensitive to hard X-rays from 16 to about 60 keV (the SuperAGILE detector, see Tavani et al., 2009, and references therein for more information).

The Large Area Telescope on board the *Fermi* γ-ray satellite is the successor to EGRET and was designed to exceed in performance.[iv]

[iii] Hard refers to a differential energy spectrum proportional to $E^{-\Gamma}$, where $\Gamma \lesssim 2$.

[iv] See fermi.gsfc.nasa.gov/science/instruments/table1-1.html for a head-to-head comparison.

3.1 *Fermi* GAMMA-RAY SPACE TELESCOPE

The *Fermi* satellite (formerly GLAST: the *Gamma-ray Large Area Space Telescope*) was launched in June 2008 and was brought into a circular orbit in 565 km altitude. The satellite is equipped with two instruments: the Gamma-ray Burst Monitor (GBM) and the Large Area Telescope (LAT). The GBM consists of two detectors covering a combined energy range of about 150 keV to nearly 30 MeV and its science objective is to search the sky for transient phenomena, e.g. γ-ray bursts. As the GBM and its data are not within the scope of this work, the interested reader is referred to Meegan et al. (2009) for further information. In the following, the LAT is introduced and described, mainly on the basis of Atwood et al. (2009); Ackermann et al. (2012), *www-glast.stanford.edu/Instrument.html* and the *Cicerone*[i].

3.1.1 THE LARGE AREA TELESCOPE

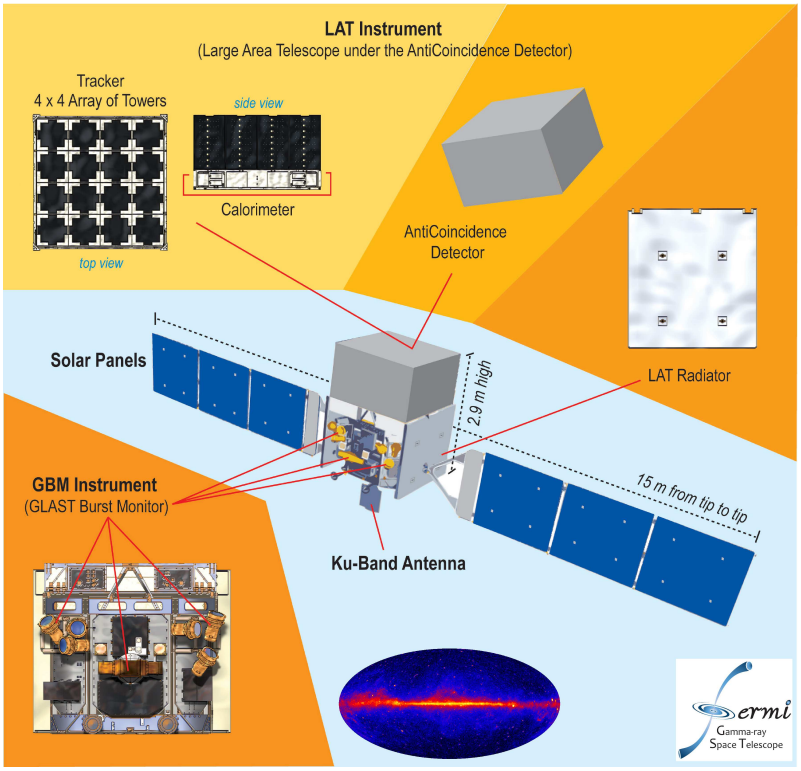

FIGURE 3.2 Schematic display of the *Fermi* Gamma-ray Space Telescope and its relevant parts with focus on the LAT. Image adapted from Winstein & Zurek (2009).

The LAT is a pair-conversion telescope comprised of a precision converter-tracker (PCT) and a calorimeter; both enclosed by the anti-coincidence detector (ACD; see Figure 3.2). Its FoV of about 2.4 sr (discussed later) allows for a simultaneous observation of a

[i] fermi.gsfc.nasa.gov/ssc/data/analysis/documentation/Cicerone (January 2014).

large part of the sky. After two orbits (each one in about 1.5 hrs), the entire sky is surveyed with an average exposure of 30 mins on every given position in the sky. Its nominal energy range is 20 MeV up to 300 GeV and more. The sensitivity of the *Fermi*–LAT is better than $6 \times 10^{-5}\,\mathrm{m^{-2}\,s^{-1}}$ for a hard-spectrum point source with one year of exposure above 100 MeV.

3.1.1.1 DETECTION OF GAMMA RAYS

A HE or VHE γ ray enters the LAT detector uninhibited by the ACD, i.e. a layer of scintillators around the PCT. In the tracker module, the γ ray undergoes a pair-production process creating an electron/positron pair. On its way through the PCT module, the lepton pair causes ionisation within the thin particle-tracking detectors and ultimately deposits its energy in a calorimeter directly attached to the end of the tracker module. Thus with the tracker module and the calorimeter, the direction and the energy of the primary γ ray can be determined. In the following paragraphs, the LAT and its modules are explained.

PRECISION CONVERTER-TRACKER The PCT (see also Atwood et al., 2007) consists of 16 tracker modules ordered in a 4×4 scheme (see Figure 3.2). Each module is made out of 18 layers. Except the last two, each layer is comprised of a tungsten conversion foil (to trigger the pair production of the incident γ ray) followed by two single-sided silicon-strip detectors (SSDs), which track the electron/positron pair. The radiation length in matter is given by

$$X_0 = \frac{1432.8\,A}{Z(Z+1)(11.319 - \ln Z)}\,\mathrm{g\,cm^{-2}}\,, \tag{3.1}$$

where A is the mass number and Z the atomic number of the matter involved (e.g. Eidelman et al., 2004). In tungsten with $A = 183.84$ and $Z = 74$, the radiation length is $X_0 = 6.8\,\mathrm{g\,cm^{-2}}$.

Thus based on the recorded track, the direction of the incident γ-ray photon is reconstructed and the 68 % containment radius of the spread in reconstructed directions of a simulated point source defines the point-spread function (PSF) of the LAT. The simulated PSF has also been validated with observation data on the pulsars Vela and Geminga (Ackermann et al., 2013a).

Scattering of the electron and the positron and bremsstrahlung lead to a deterioration of the best-achievable angular resolution. Moreover, if the conversion of the incident γ ray does not already occur in the first conversion foil, the best-obtainable PSF becomes larger by a factor of about 2.

The first 12 layers are equipped with a thin tungsten foil of 0.1 mm (0.03 radiation lengths) thickness, whereas the next four are six times thicker.[ii] This setup is a trade-off between a desirably small PSF at low energies (thin tungsten foils) and a large effective detection area at highest (LAT-accessible) energies needing a thick conversion foil (thus losing precision of the PSF). Depending on where the conversion of the incident γ ray took place, events are flagged *front* (first twelve layers) and *back*-converted (next four layers). The strongly energy-dependent PSF and its implications are discussed later on.

[ii] In total, the LAT detector has a radiation length of 10.1 X_0 at nominal incidence.

The PCT enables a background rejection. Geometrically, the electron/positron pair ought to point back at the incident particle to ascertain the candidate particle being a γ ray. Consequently, events are discarded that an association with the trajectory of the incident γ-ray candidate and its conversion into the lepton pair.

CALORIMETER A calorimeter is mounted at the end of every tracker module. It is made out of 8 layers times 12 CsI(Tl) crystals and is used to measure the energy of the electron/positron pair, each of which is deposited by means of air showers[iii]. Each crystal is equipped with two different photodiodes that in combination are sensitive to an energy range of 2 MeV to 70 GeV. The calorimeter has a depth of 8.6 radiation lengths at nominal incidence.

Besides the energy determination, the calorimeter is used as an additional back-ground-suppression means as electron/positron-induced air showers are well-known and their profile can be used to identify background events.[iv] Further information on the calorimeter can be found in Grove & Johnson (2010).

ANTI-COINCIDENCE DETECTOR The ACD is required to reject the overwhelming amount of charged CRs hitting the LAT.[v] For this, the ACD is made out of plastic scintillator tiles and scintillating ribbons that cover the gaps between the tiles. Each tile is connected via wavelength shifting fibres to two photo-multiplier tubes (PMTs) creating a redundant system. Hence, a CR leads to a measurable light yield and triggers a *veto* by the ACD meaning a rejection of this event. The average efficiency for rejecting CRs is better than 99.97 %.

In the calorimeter, the electron/positron-induced air shower creates high-keV photons that can Compton-upscatter electrons in the ACD and thus lead to a false veto, called *self-veto*. To avoid this, only the ACD segments in the vicinity of the incident γ-ray photon (candidate) are able to send out a veto.

Additionally, the ACD is covered by a thin golden thermal blanket to shield the LAT interior from any light pollution through micro-meteoroids or space debris. The total thickness of the ACD is 10 mm, representing 0.06 radiation lengths.

Details on the reconstruction of the energy and the direction of the incident γ ray can be found in the aforementioned references. Information on the calibration procedure (not mentioned here) is discussed, e.g. in Ackermann et al. (2012). The focus in the remainder of the *Fermi*–LAT section is on the performance of the LAT w.r.t. the high-level analysis used in Chapter 6.

[iii] Air showers are particle cascades and in the case of electromagnetic ones, they are driven by bremsstrahlung (of the leptons) and pair production (of the photons). Air showers are in detail described in Section 3.3.8.

[iv] Hadronic CRs induce air showers containing hadrons and muons and thus leave a different imprint in the calorimeter.

[v] The flux of these CRs is 10^5 times larger than that of the γ rays and therefore constitutes an enormous background to be dealt with.

3.1.2 INSTRUMENT RESPONSE

Depending on the desired LAT data products and aspects (e.g. skymaps, energy spectra, light curves, diffuse analysis) different quality and selection cuts can be applied to the data. The observed events are sorted into hierarchically ordered classes. The classification scheme consists of four event types: *transient*, *source*, *clean*, and *ultraclean*. The respective cuts are based on the information from the tracker module, the calorimeter, the ACD, and thus on the overall reconstruction quality. They are chosen such as to reduce the fraction of background events and thereby events in higher event classes exhibit higher probabilities of being a *real* γ ray, e.g. at least 10 % (*transient*) to about almost 99.6 % (*ultraclean*). As a drawback, a higher quality of the data set implies lower event statistics. These sets of selection cuts and criteria are constantly updated and stored as set of instrument-response functions (IRFs) based on Monte Carlo (MC) simulations. In this work (here and later), the recommended `P7SOURCE_V6` IRFs were used.

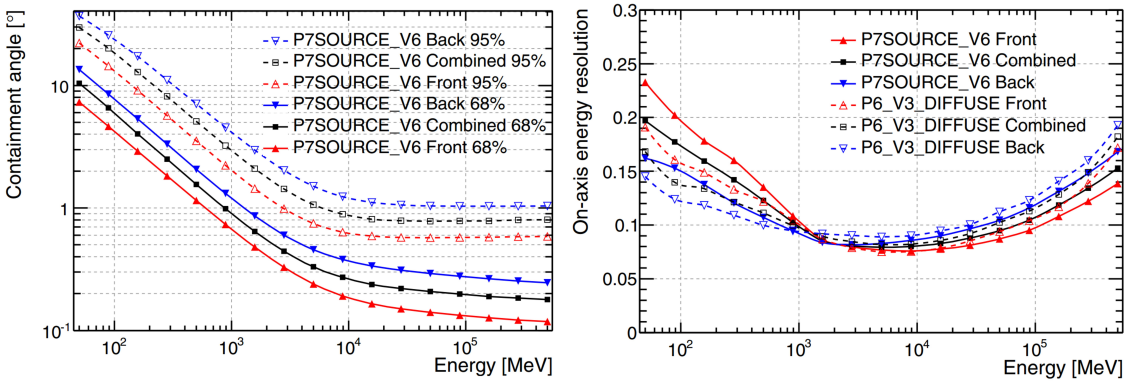

FIGURE 3.3 The point-spread function (denoted as containment angle) and the energy resolution vs. energy for the `P7SOURCE_V6` IRFs at small inclination angles ($\cos(\theta) > 0.975$). **LEFT:** The PSF indicated for all events of the *source* class (named total, black) and the subsets of front (red) and back-converted (blue) events for a 68 % (solid lines) and a 95 % (dashed lines) containment radius. **RIGHT:** Energy resolution for the total (black), the front (red) and back-converted (blue) events; for comparison the previous IRF (`P6_V3_DIFFUSE`) are indicated. Image adopted from Ackermann et al. (2012).

3.1.2.1 POINT-SPREAD FUNCTION

As mentioned above, the PSF is limited at lower energies by multiple scattering implying a E^{-1} dependence of the PSF. Smaller contributions to the uncertainty of the PSF are through the incomplete coverage of the SSDs and the bremsstrahlung of the electron/positron pairs. As a result, the PSF improves with $E^{-0.78}$. However, at higher energies the PSF flattens out with energy caused by the limited resolution of the SSDs. In Figure 3.3, the PSF versus (vs.) energy is shown for a 68 % and a 95 % containment radius for the *source* classification and its subsets of front and back-converted events. The combined PSF (68 % containment) has a dynamical range of ~ 100 as the PSF is around 10° at low MeV energies and improves to $\sim 0.1°$ at energies beyond 10 GeV.

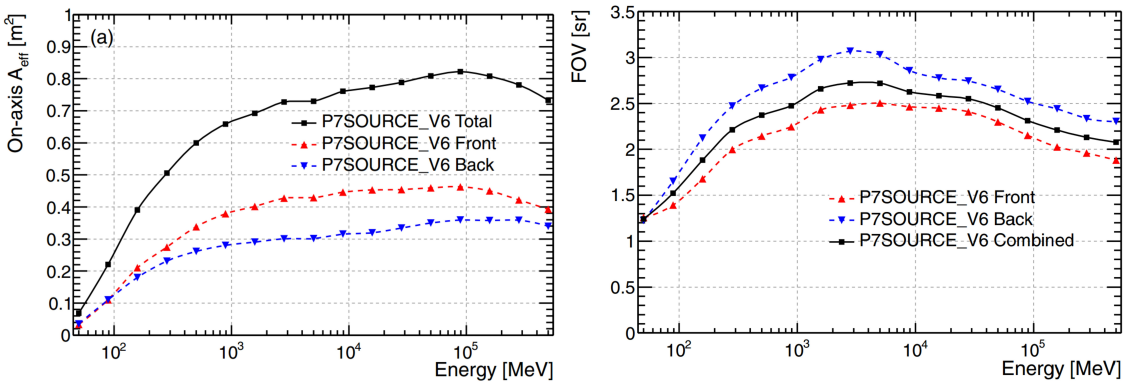

FIGURE 3.4 Effective area and FoV for *Fermi*–LAT for the `P7SOURCE_V6` IRFs. **LEFT:** The total effective area for `P7SOURCE_V6` IRF (black) and the front (red) and back-converted (blue) subsets for small inclinations. **RIGHT:** The FoV calculated for $\theta = 0°$ for the total data set (combined) and separately for front and back-converted events. Image adopted from Ackermann et al. (2012).

3.1.2.2 ENERGY RESOLUTION

The energy resolution is a measure for the precision of the energy reconstruction. Overall, it is than 15 % (see Figure 3.3) and approaches values smaller than 10 % depending on the conversion type. For computing reasons, the energy resolution is per default not accounted for in the analysis of LAT data.

3.1.2.3 EFFECTIVE AREA

The effective area A_{eff} of the LAT is the detection area usable at a given energy E_i and depends also on the solid angle $d\Omega(\theta, \phi)$ with θ being the inclination angle and ϕ the azimuth angle of *Fermi*–LAT. It is calculated through the fraction of simulated N and observed events n at a given energy E_i and angles θ_j and ϕ_k (Ackermann et al., 2012):

$$A_{\text{eff}}(E_i, \theta_j, \phi_k) = 6 \frac{n_{i,j,k}}{N} \frac{2\pi}{\Delta\Omega_{i,j}} \frac{\Delta E}{\Delta E_i} \text{m}^2 , \tag{3.2}$$

where ΔE and ΔE_i are the respective energy ranges of the simulated and observed γ-ray counts. The energy-dependent FoV is defined as the ratio of the integral of A_{eff} over the solid angle (called the *acceptance*) and the *on-axis* A_{eff}:

$$\text{FoV}(E) = \frac{\int A_{\text{eff}}(E, \theta, \phi)\, d\Omega}{A_{\text{eff}}(E, \theta = 0°)} \text{sr} . \tag{3.3}$$

In Figure 3.4, the effective area and the FoV of the *Fermi*–LAT are depicted.

3.1.3 DATA ANALYSIS

The *Fermi*–LAT is in survey mode in about 90 % of the time. This means that a source (of interest) is observed under various observing conditions. In the analysis of the data,

these changing conditions have to be accounted for in combination with the large changes of the effective area and the PSF with energy. As a consequence of the broad PSF (Fig. 3.3), especially at lower energies, a photon reconstructed at a given source position could still be possibly coming from another source or from the diffuse Galactic or extra-Galactic background. Thus not only the source of interest, but also nearby sources within a radius of 5° to 30° (called region-of-interest, ROI and depends on the energy range) and the respective backgrounds have to be modelled at the same time. This is done in a maximum-likelihood analysis based on the approach previously used for the analysis of EGRET data (Mattox et al., 1996). In this analysis, the observed photons are assigned to the most likely source such that the individual fits (source-wise) and the overall fit (the complete set of all sources within the ROI) are best-modelled.

3.1.3.1 LIKELIHOOD ANALYSIS

[vi]The observed γ-ray counts n are usually *binned*[vii] in k bins (e.g. energy, sky position and time) and underlie Poissonian statistics. The measured events have to pass the same quality cuts as defined for the specific IRFs. Events are discarded if they were observed (a) during periods where the LAT was not in observation mode, (b) when the LAT passed over the south-Atlantic anomaly[viii] or (c) too close towards the rim of the Earth[ix]. The likelihood expression used to describe the observed counts w.r.t. the modelled counts per bin m_k is the product of the respective probabilities

$$\mathfrak{L} = \prod_k \frac{m_k^{n_k} \exp(-m_k)}{n_k!} \tag{3.4}$$

$$= \exp\left(-N_{\mathrm{pred}}\right) \prod_k \frac{m_k^{n_k}}{n_k!}\,, \tag{3.5}$$

because $\prod_k \exp(-m_k) = \exp\left(-N_{\mathrm{pred}}\right)$. The challenge of this analysis is to find the set of predicted counts that maximises $\log \mathfrak{L}$:

$$\log \mathfrak{L} = -N_{\mathrm{pred}} + \sum_k n_k \log(m_k) - \log(n_k!)\,, \tag{3.6}$$

for which the constant term $\log(n_k!)$ can be left out, and thus:

$$\log \mathfrak{L} = -N_{\mathrm{pred}} + \sum_k n_k \log(m_k)\,. \tag{3.7}$$

[vi]This section mainly refers to Abdo et al. (2010a); Mattox et al. (1996) and additional slides presented at the SciNeGHE 2010 workshop by Tosti (2010).

[vii]In the *unbinned* likelihood analysis, every event is considered separately and the final likelihood runs of over all i events: $\mathfrak{L} = \exp\left(-N_{\mathrm{pred}}\right) \prod_i m_i$.

[viii]The Earth exhibits are weak multipole moment, which leads to a higher CR flux above the south Atlantic close to the Brazilian coast.

[ix]The Earth's atmosphere is a CR-induced GeV source (Abdo et al., 2009) and thus considered a background.

If ϵ is the true energy and $\hat{p}$ the true position in the sky and ϵ',$\hat{p}'$ the respective observed values, then the modelled counts per bin k within an observation time t are determined through

$$m_k = \int dt \int_k d\epsilon' \, d\hat{p}' \, M(\epsilon', \hat{p}', t) \,, \tag{3.8}$$

where $M(\epsilon', \hat{p}', t)$ is the distribution of the expected γ-ray counts. It is a function of the source model S and the IRFs R:

$$M(\epsilon', \hat{p}', t) = \int_{\mathrm{ROI}} d\epsilon \, d\hat{p} \, S(\epsilon, \hat{p}) \, R(\epsilon, \hat{p}, \epsilon', \hat{p}', t) \,. \tag{3.9}$$

The source model includes all reported point and diffuse sources (e.g. reported in Nolan et al., 2012), further assumed or tested point sources and diffuse sources, and the Galactic and extra-Galactic diffuse background. The Galactic diffuse model is an all-sky map finely binned in energy containing the expected γ-ray background along the Galactic Plane. The extra-Galactic diffuse model is an isotropic and energy-dependent flux contribution over the entire sky. In the source model, point sources are described by their nominal (or assumed) position and a spectral shape (e.g. a power law with $dN/dE \propto E^{-\Gamma}$), diffuse sources (e.g. including the Galactic diffuse model) are described by a spectral shape and template file accounting for their position, the expected photon counts, and the morphology. Additionally, diffuse sources can be included by only stating energy bins and the respective flux estimate (e.g. as done for the extra-Galactic diffuse model).

Given $M(\epsilon', \hat{p}', t)$, the sum of the predicted counts within the ROI can be calculated:

$$N_{\mathrm{pred}} = \int dt \int_{\epsilon_{\mathrm{min}}}^{\epsilon_{\mathrm{max}}} d\epsilon' \int_{\mathrm{ROI}} d\hat{p}' \, M(\epsilon', \hat{p}', t) \,. \tag{3.10}$$

Thus the analysis is time consuming as the best fit that maximises Equation 3.7 has to consider every source in the source model with its specific properties and has to account for all γ-ray photons in the ROI.

The test statistic TS is defined as likelihood ratio of the maximum likelihood value of the model excluding a specific source (model 0) and the likelihood including a specific source (model 1) at a given position:

$$\mathrm{TS} = -2 \log \left(\frac{\mathfrak{L}_{\mathrm{max},0}}{\mathfrak{L}_{\mathrm{max},1}} \right) . \tag{3.11}$$

For large TS values, the TS values for the null hypothesis are distributed as a χ^2 with n degrees of freedom and where n are the additional parameters of model 1 (*Wilks theorem*, see Wilks, 1938). The TS value is used for source detection, but can also be used to test different nested spectral shapes.

3.1.4 LIMITATIONS OF SPACEBORNE GAMMA-RAY OBSERVATIONS

After 5 years of constant data taking, events with energies above 300 GeV were observed with the *Fermi*–LAT. However, satisfying statistics approaching TeV energies are virtually impossible to achieve with current spaceborne instruments (given the limited detection area and observed source spectra). This was realised much before the launch of the

satellites AGILE and *Fermi*. It is known that the observed γ-ray fluxes follow a power law; the event rates drop with increasing energy and result in a (too) low likelihood of a direct measurement.

Even for a strong source like the Crab Nebula[x], just 12 γ-ray photons per m^2 and year are expected at 1 TeV based on the spectral results in Aharonian et al. (2006a). Thus *meaningful* science approaching TeV energies cannot be addressed with current space telescopes. The required larger detection areas could and can only be realised on Earth. On Earth, however, direct observations of HE and VHE γ-rays are not possible because the Earth's atmosphere is opaque to photons of these energies.

But γ-ray photons initiate particle cascades in the atmosphere that produce a detectable amount of light on the ground. These particles and especially the light pool provide an indirect access to the incident γ-ray and its properties. This indirect observation method has allowed a comparatively young field in the astronomy to successfully and quickly rise over the past thirty years. In the following section, the particle cascades are introduced and discussed before the principle of their detection and analysis is explained on the example of the H.E.S.S. telescope system (Sect. 3.3).

3.2 AIR SHOWERS AND CHERENKOV LIGHT

[i]When very-high-energetic particles reach the Earth and enter the upper layers of the atmosphere, they initiate so-called extensive air showers (EAS, or simply air showers). An air shower is a particle cascade traversing the atmosphere in about 10 μs. One distinguishes the two types of air showers by the primary interaction: hadronic (strong interaction) and electromagnetic air showers. In the VHE γ-ray regime, hadronic air showers are mainly induced by CR protons, whereas electromagnetic showers can be initiated by either γ rays or CR electrons.

3.2.1 ELECTROMAGNETIC AIR SHOWERS

The first interaction of a primary γ-ray photon is the production of an electron-positron ($e^{\pm}$) pair in the Coulomb field of a nucleus in the atmosphere. These secondary electrons then radiate bremsstrahlung and thereby produce a photon each. Hence, after every process the number of particles has doubled. In the simple[ii] model of Heitler (1954), these two processes alternately drive the particle cascade as long as the energy of the particles is sufficiently high to produce further particles. The mean free path (or radiation length) through the atmosphere the photon has travelled before losing $1/e$ of its energy is $X_0(\gamma) = 47.8\,\mathrm{g\,cm^{-2}}$. For electrons (meaning positrons as well), the mean free path is

[x]The Crab Nebula is the strongest stable point source in the TeV sky and therefore considered a *standard candle* (e.g. discussed in Meyer et al., 2010).

[i]A review of particle physics including air-shower physics can be found in Eidelman et al. (2004) and references therein. This references has been used in this section when referring to numbers and values.

[ii]Simple refers to the model of Heitler (1954) assuming identical radiation lengths of γ-rays and electrons.

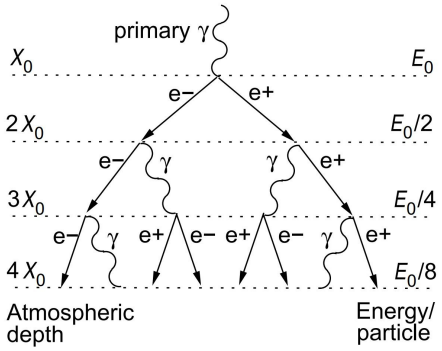

FIGURE 3.5 Illustration of γ-ray induced air shower according to the simple model of Heitler (1954). In addition, the atmospheric depth and the energy per particle after every step in the shower development are denoted. Image adopted from Carrigan (2007).

slightly smaller: $X_0(e^{\pm}) = 7/9\, X_0(\gamma)$. In Figure 3.5, the Heitler model of an electromagnetic air shower is depicted.

The particles lose energy through ionisation of molecules in the atmosphere[iii], through Compton scattering (at keV energies), and through the photoelectric effect (at eV energies). The number of particles in the air shower does not increase.

At early stages of the shower development, bremsstrahlung and pair production are the dominant processes driving the air shower by constantly increasing the number of particles. At a certain energy, the *critical* energy, energy losses through ionisation are comparable to those of bremsstrahlung and pair production and the air shower has reached its maximum number of produced particles. The critical energy in the atmosphere is

$$E_{\mathrm{crit}} \approx \frac{710}{Z + 0.92}\,\mathrm{MeV}\,, \tag{3.12}$$

where Z is the atomic number. For nitrogen with $Z = 7$, $E_{\mathrm{crit}} \approx 90\,\mathrm{MeV}$. Given the number of particles at the shower maximum N_{max}, the Earth's atmosphere can be considered a giant calorimeter to derive the primary particle's energy $E_0 = N_{\mathrm{max}}\, E_{\mathrm{crit}}$. The shower maximum X_{max} is determined through

$$X_{\mathrm{max}} = \left(\ln\left(\frac{E_{\mathrm{crit}}}{E_0}\right) - \ln 2\right) X_0\,. \tag{3.13}$$

Typically, a TeV γ-ray interacting at 25 km above sea level produces an EAS that reaches its maximum at about 10 km. Past this shower maximum, the particles are on average not energetic enough to produce new particles via bremsstrahlung and pair production; the shower begins to abate.

For a primary electron, the air shower begins with a bremsstrahlung process followed by a pair production thus entering the above-described air-shower development. It is not possible to distinguish air showers induced by photons and electrons. However, as the

[iii] Fluorescence telescopes measure the light emitted in the recombination, e.g. in the AUGER experiment (Zavrtanik, 2000).

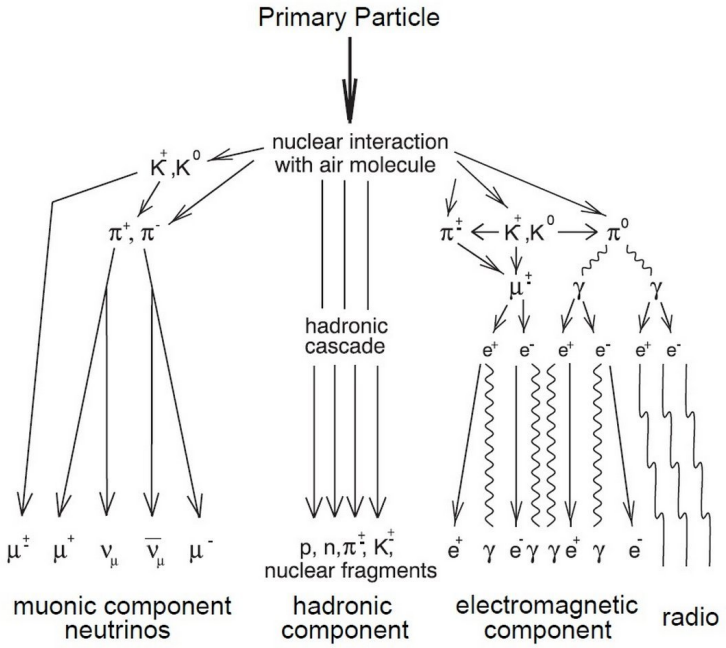

FIGURE 3.6 Illustration of a hadron-induced air shower and its different components. Image adopted from *lip.pt/ jespada/Research/PhysPAO.php*.

first interaction of the primary electron takes place a bit earlier (i.e. slightly higher in the atmosphere) and because the Cherenkov light (introduced in Section 3.2.3) of this primary electron (*direct* Cherenkov light) could be visible for sensitive enough instruments, there is discrimination potential that can perhaps be exploited to separate γ-ray from $e^{\pm}$-induced air showers.

3.2.2 HADRONIC AIR SHOWERS

The primary particles of hadronic air showers at TeV energies are mainly CR protons, but also heavier nuclei. The mean free path for a TeV proton is $X_0(\mathrm{p}) \approx 80\,\mathrm{g\,cm^{-2}}$. The first interaction is the inelastic scattering of the VHE proton with a nucleus in the atmosphere. The nucleus is fractured and as a result of this strong interaction, various nucleus fragments, and mesons are produced. Important for the shower evolution are the π mesons and their weak decay modes. The neutral pion π^0 decays into two photons (the next-probable decay mode is into a photon and an electron/positron pair with a probability of $\sim 1\,\%$) and therefore initiates an electromagnetic sub-shower. The charged pions decay into muons and neutrinos ($\pi^+ \rightarrow \mu^+ + \nu_\mu$ and $\pi^- \rightarrow \mu^- + \bar{\nu}_\mu$); the respective electronic decay modes are helicity-suppressed. The neutrinos do not contribute to the shower development, which is also the case for the relativistic muons as they mostly traverse the atmosphere before decaying into electrons and neutrinos ($\mu^- \rightarrow \mathrm{e}^- + \bar{\nu}_\mathrm{e} + \nu_\mu$ and $\mu^+ \rightarrow \mathrm{e}^+ + \nu_\mathrm{e} + \bar{\nu}_\mu$).

In Figure 3.6, a hadronic shower with its different particles and decay modes is depicted. The differences between electromagnetic and hadronic showers will be discussed in Section 3.2.4, but before that the Cherenkov-light emission is introduced.

3.2.3 CHERENKOV LIGHT

When charged particles in a dielectric medium of a refractive index n move with a velocity v, which is larger than the speed of light in this medium, i.e. $v > c/n$, they radiate Cherenkov light (Čerenkov, 1937). This Cherenkov light is emitted in a very narrow cone under an angle θ_C, the Cherenkov angle:

$$\cos\theta_C = \frac{1}{n\beta} \overset{!}{<} 1\,, \tag{3.14}$$

where $\beta = v/c \approx 1$ for relativistic particles. Typical values for the Cherenkov angle around 25 km above sea level are around $\theta_C \lesssim 0.4°$; around the shower maximum at 10 km altitude, it is around 0.6° to 0.8° (e.g. Kosack, 2005). The Cherenkov angle increases with decreasing height and is around 1.4° for a standard refractive index of $n = 1.0003$.

The minimum energy requirement for the relativistic particle of mass m_0 to emit Cherenkov radiation is

$$\begin{aligned} E_{\min} &= \frac{m_0 c^2}{\sqrt{1-\beta^2}} \\ &= \frac{m_0 c^2}{\sqrt{1-(1/n)^2}}\,. \end{aligned} \tag{3.15}$$

Through Equation 3.15 and $n = 1.0003$, the minimum energy to emit Cherenkov light is ~ 38 GeV for a proton, ~ 4.3 GeV for a muon, and about 21 MeV for an electron.

The number of Cherenkov photons N_C emitted per path dx and wavelength interval $d\lambda$ of the Cherenkov emission is

$$\frac{d^2 N_C}{dx\,d\lambda} \propto \left(1 - (\beta n_\lambda)^{-2}\right) \lambda^{-2}\,, \tag{3.16}$$

where λ is the wavelength and $n_\lambda = n(\lambda)$ is the wavelength-dependent refractive index of the medium. The spectrum of the Cherenkov light increases for decreasing wavelengths, but suffers from different processes: (*a*) In the atmosphere, short wavelengths suffer stronger from the elastic *Rayleigh* scattering (λ^{-4} dependence) off molecules, e.g. nitrogen and ozone. (*b*) At extreme UV wavelengths ($\lambda \lesssim 300$ nm) the condition in Equation 3.14 is not met as the absorption of the Cherenkov photons in ozone leads to $n < 1$ and to the generation and fission of ozone, e.g. $3O_2 \rightarrow 2O_3$ and $O_3 \rightarrow O_2 + O$, respectively. (*c*) Scattering off particles of similar size as the wavelengths, such as water vapour or simply aerosols is called *Mie* scattering and affects all wavelengths equally strong. Moreover, the Cherenkov photons are subject to Compton scattering as well (*d*). All these processes lead to a peak towards the blue optical wavelengths, to a reduced amount of light, and to a smearing-out of the Cherenkov-light distribution on ground level.

The showers on ground level exhibit the highest light yield within a distance of $\sim$ 120 m from the core position, from which on a rapid decrease in photons per m^2 is observed (Fig. 3.7). Geometrically, these 120 m are a consequence of the Cherenkov light from the particles in the shower measured on ground at about 2 km above sea level.

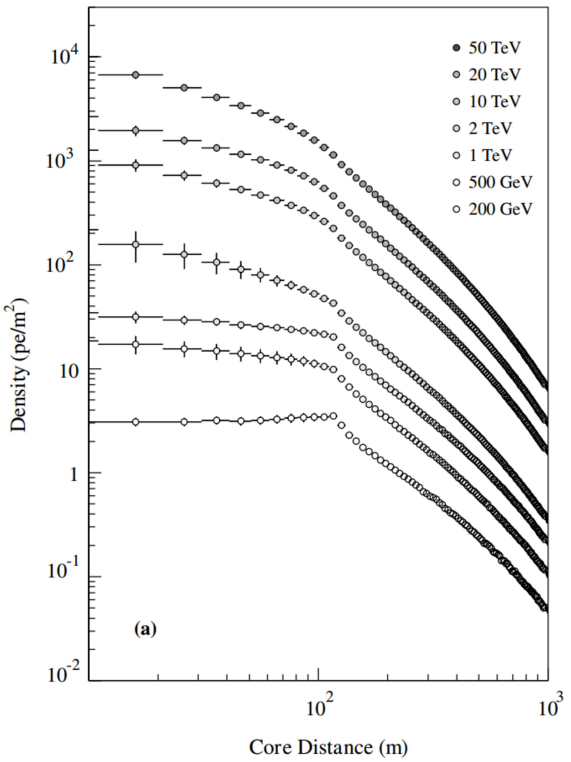

FIGURE 3.7 The Cherenkov-light density on ground level (2.4 km above sea level) for fixed γ-ray energies between 0.2 TeV and 50 TeV. Image adopted from de la Calle Pérez & Biller (2006).

3.2.4 COMPARISON BETWEEN ELECTROMAGNETIC AND HADRONIC AIR SHOWERS

The shower development of γ-ray air showers is based only on electromagnetic interactions, whereas hadronic air showers are subject to the strong interaction as well. Electrons are the main source of Cherenkov light in the shower development of electromagnetic and hadronic air showers. For example, at around 1 TeV, only a third of the primary proton's energy goes into the electromagnetic sub-showers and as a result, the light yield of the hadronic air shower is comparable to that of electromagnetic air shower induced by a γ-ray photon of 300 GeV.

In Figure 3.8, an air shower induced by a 300 GeV γ ray and one by a 1 TeV proton are illustrated based on MC simulations. In the top panel, a projection along the shower axis depicts the tracks of the shower particles (a and b). For the on-axis γ-ray shower, scattering processes in the atmosphere lead to a slight broadening (a) and to a smearing-out of the light distribution on ground level (c), but the characteristic circle is clearly visible. In contrast to this, the hadronic shower exhibits a much broader shower development and a wider light distribution on ground level (b and d). This is because of the strong interactions and the transverse momentum, which is conserved throughout the shower development. On ground level, the electromagnetic sub-showers are visible (ring in d). As

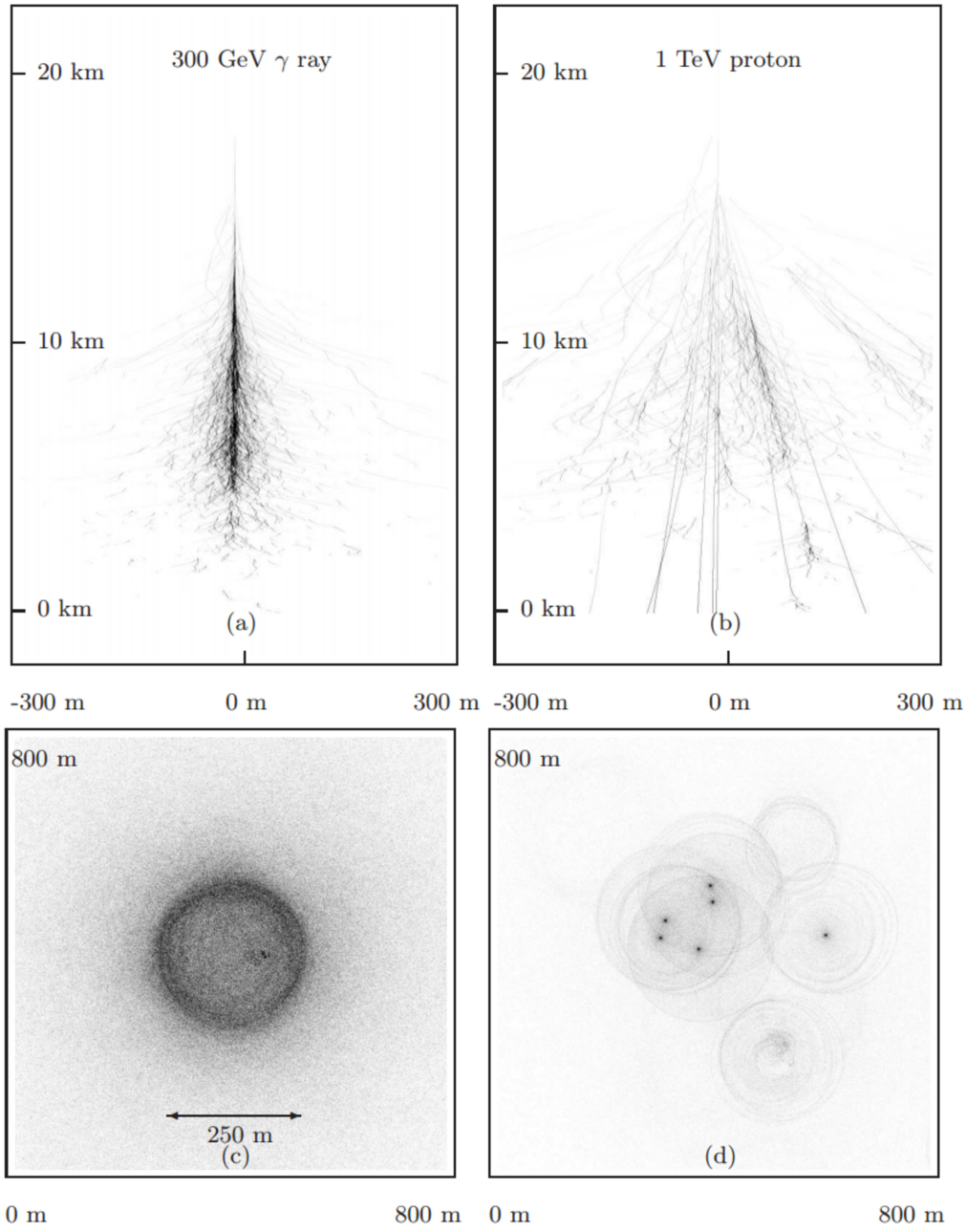

FIGURE 3.8 Monte Carlo simulation of a 300 GeV γ-ray induced air shower (a,c) compared to that induced by an 1 TeV proton (b,d). The top panel depicts a longitudinal slice through the respective air showers from 20 km down to ground level. The lower panel illustrates the lateral light distribution on ground level. Image adopted from Ohm (2010).

a result of the different interactions and the particle population, hadronic showers are not symmetric like the electromagnetic showers in general.

As the atmosphere has an average depth of $\sim 1000\,\mathrm{g\,cm^{-2}}$ (depending on the altitude above sea level), it takes around $13\,X_0$ for a hadronic air shower to reach the ground level,

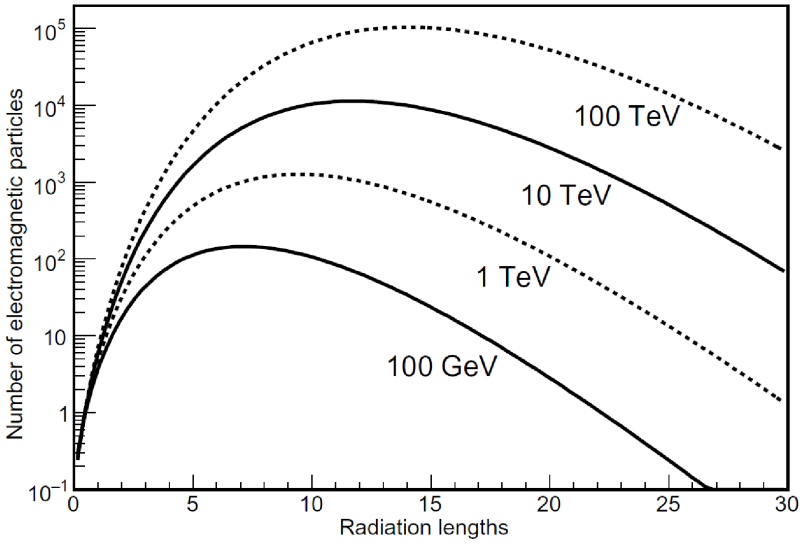

FIGURE 3.9 Number of particles in γ-ray induced air showers of different primary energies versus radiation length. A radiation length of 15 corresponds to an altitude of 5 km above sea level and 28 to 4 km above sea level. Image adopted from Sinnis (2009).

but 20 (γ-ray) to 30 (electron) X_0 for the electromagnetic EASs. Hence, hadronic air showers penetrate the atmosphere deeper than their electromagnetic counterparts of same energy.

3.2.5 DETECTION METHODS OF EXTENSIVE AIR SHOWERS

In general, the sensitivity of Cherenkov detectors is determined by the measurable amount of Cherenkov light. On the one hand, low-energy events exhibit only a few Cherenkov photons per square metre of measurable light (Fig. 3.7), thus large mirrors are needed to collect the sparse photons. On the other hand, the event rate of high-energy events is rather low, which requires the detectors to cover a large area.[iv] The closer the detectors are built to the shower maximum, the larger measurable amount of light and particles (see Figure 3.9). Therefore, for a given Cherenkov detector, a higher altitude leads to a lower energy threshold. The detector site does play a role as locations with less light pollution (less noise in the detector) and clear (less absorption and scattering in the atmosphere) and dry nights (more observation time and less scattering off water vapour) affect the detector performance.

The ground-based detection of atmospheric Cherenkov light from air showers is split into two disciplines: the imaging and the non-imaging technique. Both approaches w.r.t. the VHE γ-ray regime are briefly introduced.

The IACT technique means that an air shower with its (integrated) light distribution is

[iv] For a source similar to the Crab Nebula as in Aharonian et al. (2006a), an experiment with an effective area of 10^5 m^2 would observe 2 γ rays per minute at 1 TeV, whereas at 10 TeV, the rate would fall to 2 events per hour.

reflected from the telescope mirrors onto a fast camera consisting of a fine grid of PMTs. Therefore, the entire shower is *imaged* onto the camera. On the basis of this shower image and the pointing information of the IACT, all relevant properties of the air shower can be determined. The first instrument to detect a γ-ray source (i.e. the Crab Nebula) was the Whipple 10 m-telescope (Weekes et al., 1989). This single-telescope instrument was succeeded by the second generation of IACTs, especially the HEGRA[v] telescope array (Daum et al., 1997) displaying the increased performance of an array of telescopes. The idea is to observe the shower with more than one telescope (stereoscopy), which provides additional information per telescope that can be used to improve the reconstruction of the event and the rejection of the background (described in the following sections).

Currently, the third generation of IACTs is exploring the GeV to TeV γ-ray sky for nearly a decade. IACTs like H.E.S.S. [vi] (phase 1 & 2, Hinton, 2004; Giebels, 2013), MAGIC[vii] (phase 1 & 2, Lorenz, 2004; Aleksić et al., 2012), and VERITAS[viii] (Weekes et al., 2002) have significantly contributed to the increase of the number of reported γ-ray sources since the detection of the Crab Nebula to 147.[ix] These IACTs have effective detection areas around $10^5\,\mathrm{m}^2$ with two to five telescopes on site thus providing an energy coverage from 25 GeV to almost 100 TeV. In combination with observations with the *Fermi*–LAT, the non-thermal universe is covered from MeV energies on up to high TeV energies.

A fourth generation of IACTs is *en route*. Here, a large multi-telescope array named CTA[x] (Doro & CTA Consortium, 2011) will be built covering layout-dependent a wider energy range. An energy range starting at low GeV energies and extending beyond 100 TeV with an overall better sensitivity of a factor of 10 is aimed for. The imaging technique will be discussed in detail in the following Section 3.3 using the example of the H.E.S.S. telescope array.

For the non-imaging air-Cherenkov telescopes (nIACTs), a different approach is pursued. The nIACT arrays consist of smaller detectors $\left(\mathcal{O}(1\,\mathrm{m}^2)\right)$ with a (mostly) wider field-of-view spread out over a large area. The air shower is not imaged onto a camera, but instead the light yield and time information are stored and used to sample and analyse the incoming shower front. However, as no image of the shower is recorded, the separation of γ-ray air shower from hadron ones becomes more difficult. Typical energy ranges begin at around 1 TeV as the fainter showers do not trigger enough of the individual and comparatively smaller detectors of the array to start the data acquisition. The advantage of these nIACTs is that they are cheaper than the IACTs, cover a large fraction of the sky and are therefore more suitable for sky surveys and the study of diffuse and (very) extended sources at multi-TeV energies (large effective detection area and FoV).

In general, nIACTs are mainly designed to study CRs at TeV to PeV energies (and higher), but not actually for γ rays. Among these experiments are Yakutsk (Dyakonov et al., 1973) and TUNKA (Budnev et al., 2010). Experiments like THEMISTOCLE

[v] HEGRA: High Energy Gamma Ray Astronomy, Canary Islands.
[vi] H.E.S.S.: High Energy Stereoscopic System, Namibia.
[vii] MAGIC: Major Atmospheric Gamma-Ray Imaging Cherenkov Telescope(s), Canary Islands.
[viii] VERITAS: Very Energetic Radiation Imaging Telescope Array System, Arizona.
[ix] As stated in the TeV catalogue *TeVCat* (*www.tevcat.uchicago.edu*), January 2014.
[x] CTA: Cherenkov Telescope Array, site tbd.

(Fontaine et al., 1990) and AIROBICC (Aharonian et al., 1991) are examples for non-IACTs designed to observe VHE γ-rays. With the AIROBICC experiment no γ-ray source could be detected, but the Crab Nebula was detected with THEMISTOCLE at TeV energies (Baillon et al., 1991).

Currently, a small prototype of the HiSCORE (Hundred$*i$ Square-km Cosmic ORigin Explorer) detector array has been built in Siberia and has already seen first light (Tluczykont et al., 2014). It aims for the energy range above 10 TeV and to close the gap in energy between the future CTA and the current ultra-high-energy (multi-PeV energies) CR experiments like the AUGER observatory (Zavrtanik, 2000).

3.3 HIGH ENERGY STEREOSCOPIC SYSTEM

FIGURE 3.10 The High Energy Stereoscopic System (H.E.S.S.) in its phase 2 with the five Cherenkov telescopes (CTs). The four smaller CTs are named CT1 to CT4 and constitute the phase 1. The inlay shows a satellite picture from *Google Earth* of the H.E.S.S. array with its giant telescope CT5 in the centre of the quadratic layout.

The High Energy Stereoscopic System (H.E.S.S.) is located in the Khomas Highlands in Namibia at 1 800 m above sea level. The acronym H.E.S.S. is in dedication to Victor Franz Hess who discovered the CRs in 1912 (Hess, 1912). The telescope system consists of four identical Cherenkov telescopes (CTs) placed on the corners of a square with a side length of 120 m (Fig. 3.10). The spacing of 120 m is a compromise between a large light-collection area and a high fraction of stereoscopic events at lowest energies. The spacing together with the altitude results in a nominal energy range of 100 GeV to almost 100 TeV. The integral-flux sensitivity is about 1 % of the flux of the Crab Nebula in 25 hrs for observations of a source with radius $\theta = 0.15°$ at low zenith angles (Aharonian et al., 2006a). The sensitivity decreases with increasing zenith angle and source size. Since H.E.S.S. is located in the southern hemisphere, it is perfectly suited to observe the Galactic Centre and the inner Galactic Plane.

The full telescope array with all four telescopes went into operation in December 2003. In the midst of 2012, a fifth, much larger telescope placed in the centre of the square went into operation. With this telescope, the performance of H.E.S.S. at lower energies has been improved and events with energies around 50 GeV can be observed (Stegmann, 2012).

In this work, only data from the four-telescope array were used. The description of the array setup and performance are meant to describe the four-telescope array only and the analyses done and described are based on this array.[i]

[i]For information on CT5, the interested reader is referred to Giebels (2013); Krayzel et al. (2013). A head-to-head comparison of CT5 with the smaller CTs can be found at *mpi-hd.mpg.de/hfm/HESS/pages/about/HESS_I_II*.

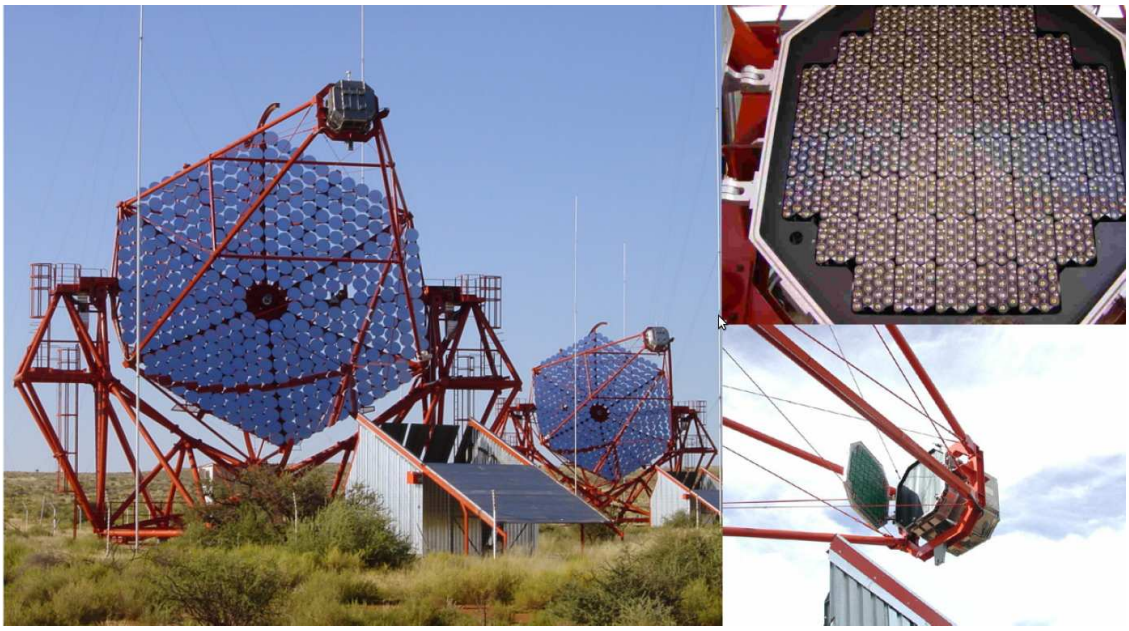

FIGURE 3.11 The H.E.S.S. telescopes and the Cherenkov camera. **LEFT:** Two of the four H.E.S.S.-phase 1 CTs. **RIGHT TOP:** View on Cherenkov camera and the 960 PMTs. **RIGHT BOTTOM:** Cherenkov camera mounted on the telescope structure with the lid open. Image adopted from Fernandes (2009).

3.3.1 CHERENKOV TELESCOPES

The H.E.S.S. telescope system in its initial configuration (phase 1) consisted of four identical Cherenkov telescopes (CTs). Each CT is comprised of three main parts: the mirror-support structure and the drive system, the mirrors and the camera.

MIRROR-SUPPORT STRUCTURE AND DRIVE SYSTEM The mirror-support structure has a diameter of 13 m and as a high rigidity of the structure in operation is desired, the support structure weighs nearly 60 tons. The CTs are mounted in an alt-az configuration and are fixed on steel rails, which provides an angular speed of 100° per min to point the telescope at any given position in the sky.[ii] However, in operation of the CT, bending effects caused by the weight of the structure and the mounted camera constitute a systematic error on the pointing accuracy. In Cornils et al. (2003); van Eldik et al. (2008), detailed studies were done to account for these bending effects and reduce the systematic pointing error (i.e. 20 arcsecs per axis).

REFLECTOR AND MIRRORS The reflector is built in the Davies–Cotton design (Davies & Cotton, 1957) and designed to hold a total of 382 spherical mirrors. These mirrors are aluminised and quartz-coated and reflect the incident light onto the camera, which is placed at the focal length of the telescope of 15 m. The optical reflectivity of each

[ii]For CT5, the peak positioning speed is 200° per min (in azimuth) and 100° per min (in elevation). The weight of the entire CT5 structure is 580 tons.

mirror is about 0.8 at blueish wavelengths at which the expected Cherenkov-light flashes are measured. These mirrors are round, 60 cm in diameter, add up to a mirror surface of 107 m^2 (the reflector) and are placed on a sphere of 15 m in radius.

The alignment of the mirrors is described in Cornils et al. (2003) and is done automatically for every mirror. Once aligned, the mirrors do not have to be re-aligned as they remain aligned over years. A re-alignment has to be done when mirrors are replaced or refurbished.

THE CAMERA The camera consists of 960 PMTs (see also Figure 3.11). A camera made of PMTs is favoured over a CCD camera (CCD: charged-coupled device) as only PMTs provide the fast read-out of an air-shower event lasting a few nanoseconds – for H.E.S.S., the read-out time is set to 16 ns.[iii] Each pixel of the Cherenkov camera is a PMT with a size of 0.16°. The total FoV of the camera is then about 5° × 5°. Such a large FoV is perfectly suited for surveys, the analysis of extended sources and, moreover, enables a simultaneous background estimation (discussed in Section 3.3.8).

Every PMT is equipped with a Winston cone (Winston, 1970) to suppress any stray light and to better focus the light onto the camera pixels. The 960 pixels are organised in 60 so-called *drawers*, and every drawer has its own high-voltage supply and read-out electronics. Therefore, the camera can still be used even if individual pixels or even complete drawers are subject to hardware failures or maintenance.

In addition, there are two small CCD cameras mounted on the CTs: the *sky*-CCD camera pointing towards the sky parallel to the optical axis of the CT and the *lid*-CCD camera pointing at the camera lid. The first one is used to observe the pointing and tracking accuracy (by comparison with reference stars in the sky), the second one for the mirror alignment and to determine the optical PSF (see Cornils et al., 2003).

3.3.2 DATA TAKING

Observations with the H.E.S.S. telescopes are conducted at astronomical darkness and in moon-less nights. These observations are divided into periods of $\sim$ 28 mins, which are called observation *runs*. In addition, different calibration runs are conducted and used to determine the properties of the telescopes to be considered and accounted for during the analysis and calibration steps. For these, it is referred to Aharonian et al. (2004).

During an observation campaign, a source is observed in *wobble mode*. Here, the centre of the telescope is not pointed directly at the source, but is generally offset by 0.5° . . . 0.7° in right ascension (RA) or declination (Dec). If a run is wobbled by RA+0.5°, the next wobble position would be the mirrored position RA − 0.5°, with the following runs *wobbled* at Dec ± 0.5°. In doing so, a homogeneous exposure of the FoV around the source is achieved.

Observations are conducted in this mode to reduce the systematic effects of the inhomogeneous camera response and to allow for a simultaneous background determination.

[iii] Larger time frames only increase the noise level in the camera and therefore reduce the sensitivity.

The camera response and the background-estimation method are discussed later on in Sections 3.3.7 and 3.3.8, respectively.

3.3.3 COINCIDENCE TRIGGER

Different trigger levels are set to avoid a too frequent data taking caused by hadronic air showers and the night-sky background (NSB). These trigger conditions apply to individual CTs and then system-widely to all four telescopes. The latter constitutes one of the advantages of two or more telescopes simultaneously in operation over a single-telescope system because the background can be reduced already on hardware level.

The 960 pixels of the CT camera are divided into 64 overlapping *sectors*. The first-level trigger requires three pixels within one sector to surpass the threshold of four photo-electrons (p.e.) each. If this condition is met, a time slot of 80 ns is open, in which a second CT has to report a first-level trigger. This condition is called the *coincidence* (or stereoscopic) trigger and successfully reduces the fraction of triggers caused by single muons that produce a bright signal in the individual camera (discussed in Section 3.3.6) and the NSB. If a positive coincidence trigger is communicated, every pixel of the triggered CTs is read out and written onto data-summary tapes (DSTs).

This coincidence trigger allows for a low trigger threshold. For example, a trigger threshold around 100 GeV at low zenith angles with a system trigger rate of 300 to 400 Hz was possible when the full four-telescope array went into operation around December 2003. More details can be found in Funk et al. (2005).

3.3.4 EVENT RECONSTRUCTION

The stored shower images do not only contain pixels with information of the triggered shower, but also of random NSB noise. Basically, two different approaches within the H.E.S.S. software framework exist to reconstruct the relevant shower parameters. On the one hand, one can model the entire shower image and then infer the relevant shower properties or on the other hand, one can try to remove these randomly triggered pixels and then derive the shower properties. Throughout this work, the latter approach is used and therefore presented in following. Details on the modelling of the entire shower image can be found in de Naurois & Rolland (2009); Becherini et al. (2011).

3.3.4.1 IMAGE PROCESSING AND IMAGE CLEANING

Before the shower properties can be derived, the telescope-wise images have to be preprocessed, i.e calibrated and the NSB noise has to be accounted for. The detailed calibration procedure can be found in Aharonian et al. (2004) and in the following, the relevant steps are briefly presented.

Before *cleaning* the image from the NSB noise that affects a lot of pixels over the whole FoV, the measured pixel intensities are converted into units of photo electrons and the *pedestals* are subtracted. A pedestal is the electronic noise that is measured in the dark. To clear the telescope-wise image from the random NSB noise, all pixels with values of

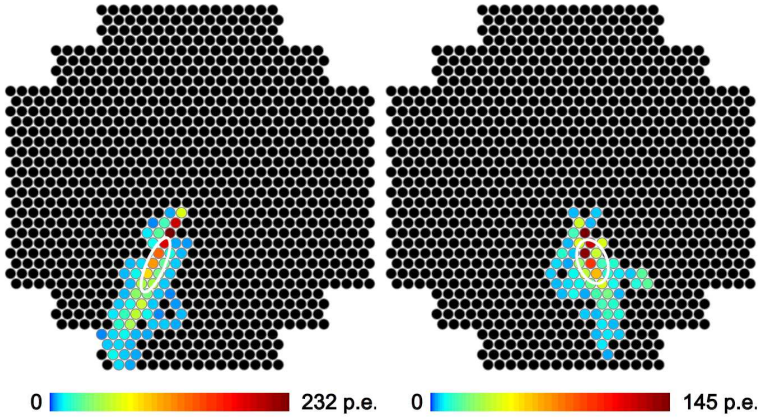

FIGURE 3.12 Cleaned camera image in units of photo electrons of a simulated γ-ray event (**LEFT**) and a hadron-induced shower (**RIGHT**). Both events were simulated at a similar energy of $\sim$ 2.5 TeV. The white ellipse represents the Hillas image of the respective shower image. Image adopted from Hampf (2012).

5 p.e. or less are removed if they do not have a neighbour with at least 10 p.e (i.e. the *5/10 image cleaning*).[iv] With this image-cleaning procedure, bright single pixels related to stars or fluctuations are removed and the resulting camera image is a contiguous sample of pixels representing the shower.

A further procedure to improve the performance of the event reconstruction is to introduce a minimum image size (image amplitude) because bright images are usually better reconstructed. As a drawback, this results in a loss in sensitivity for lower-energy events.

3.3.4.2 HILLAS ELLIPSE AND SCALED PARAMETERS

Gamma-ray showers appear more elliptically elongated in shape[v]. Hadronic showers are more subject to irregularities and in general broader (Sect. 3.2). In Figure 3.12, two cleaned images are shown: a VHE γ-ray shower image and a proton-induced one. Both showers were simulated for the same energy ($E \approx 2.5$ TeV). Compared to the γ-ray image, the image of the hadronic shower is less compact and exhibits a lower light yield (see also Section 3.2.4).

Hillas (1985) showed that air showers, regardless of their apparent arbitrariness, can be described by the first and second moments of the measured intensity distribution. Altogether five moments are derived: the *Hillas parameters*. The five moments are the centre of gravity (*cog*) of the image, the image amplitude (often referred to as *size*), and the second moments: the RMS value of the distribution along the minor axis (width), the RMS (root mean square) value along the major axis (length), and the inclination. These five parameters describe the shower images sufficiently well to distinguish γ ray and hadron showers and to proceed with the event analysis. Since γ-ray showers appear ellipse-like,

[iv] Alternatively, a 4/7 image cleaning is possible, which allows more pixels to remain in the camera image that could provide additional information on the shower, but leaves a more *noisy* image.

[v] The shape is more circle-like if the the event is observed at zenith and hits the telescope on-axis.

these images are often colloquially referred to as *Hillas ellipses* (Fig. 3.12).

A problem in this parametrisation of shower images is those ones that are close to the camera edge are mostly truncated. A significant fraction of their light yield can be beyond the camera and lead to a misdetermination of the Hillas parameters; the *cog* may be shifted or the orientation of the axes tilted w.r.t. the true shower properties. To circumvent this problem, a *nominal-distance cut* is introduced, which requires the *cog* to be within $1.5^\circ \ldots 2^\circ$ of the camera centre.

In a next step, the *scaled* Hillas parameters are calculated. For this, the width and the length are normalised w.r.t. the MC expectation for γ rays. For every telescope image and given the minor axis of the Hillas ellipse, i.e. the width w, the reduced scaled width w_{rsw} is determined through

$$w_{\mathrm{rsw}} = \frac{w - w_{\mathrm{MC}}}{\sigma_{\mathrm{MC}}}\,, \tag{3.17}$$

where the width w_{MC} and its uncertainty σ_{MC} are determined in MC simulations. For N telescopes with a reconstructed Hillas ellipse, the mean reduced scaled width (MRSW) is calculated by

$$\mathrm{MRSW} = \frac{1}{N} \sum_{j}^{N} w_{\mathrm{rsw},j}\,. \tag{3.18}$$

By design, the distribution of the MRSW is peaked around zero for VHE γ-ray events. Analogously, the mean reduced scaled length (MRSL) is calculated.

3.3.4.3 RECONSTRUCTION OF THE DIRECTION

On the basis of images, the direction of the shower can be reconstructed. For this, at least two[vi] shower images are superimposed onto one common camera-coordinate system (Fig. 3.13). The origin of the event is determined by the intersection point of the major axes of the participating shower ellipses. In general, the precision improves the more shower images are available to determine the intersection point. The difference between the reconstructed and true event direction from simulated data determines the PSF. The PSF depends on the analysis, and is energy and zenith-angle dependent. The reconstruction of the *impact parameter*, i.e. the distance between the impact point (the core position) of the event on the ground and the centre of the IACT, is done analogously, but with the reference frame being the ground level of the IACT. On average, the H.E.S.S. PSF is smaller than $\sim 0.1^\circ$ and the error on the impact parameter is less than 10 m (Aharonian et al., 2006a).

This introduced method is called *algorithm 1* in Hofmann et al. (1999), in which six other methods were proposed and tested. For example, *algorithm 3*, in which the additional information provided by the ratio of width and length is used to constrain and determine the impact distance (e.g. a larger ratio corresponds to a larger distance).[vii]

[vi] This is the requirement for stereoscopy. In principle, a shower can be reconstructed with only one shower image, but then with a worse overall goodness.

[vii] Within the software framework of the H.E.S.S. analysis package (HAP) used in this work for the event reconstruct both algorithms can be used.

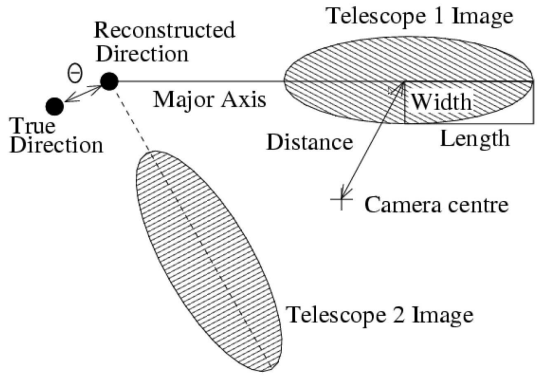

FIGURE 3.13 Stereoscopic reconstruction of the event direction by intersection of the major axes of two Hillas ellipses (in grey shade) in the camera reference frame. The intersection point of the major axes is the reconstructed direction, which is offset (or misreconstructed) w.r.t. the true direction by an angle θ. Image adopted from Aharonian et al. (2006a).

3.3.4.4 ENERGY RECONSTRUCTION

The true energy of an air shower is known from MC simulations for different observational parameters, e.g. the zenith angle, the azimuth angle, the impact parameter, and image size. The energy of a reconstructed shower is determined by comparing the impact parameter and the image size with those of the MC simulations and interpolated in cosine of the zenith angle. Thus, a good energy reconstruction requires a good reconstruction of the impact parameter.

In Figure 3.14, the correlation between the impact (core) distance and the angular distance between *cog* and the camera centre at simulated energies between 0.5 TeV and 50 TeV for a camera with a FoV of 5° in radius is depicted. Events with low energies are in general only observable at small angular offsets and small core distances because they are too faint to trigger the CTs at larger core distances. On the other hand, γ rays with energies beyond 10 TeV are still detectable at larger core distances and angular displacements from the camera centre.

3.3.5 GAMMA/HADRON SEPARATION

In general, γ-ray events coming from the source of interest are outnumbered by background events. Thus, it is required to reduce the background by a good discrimination method to distinguish between γ-ray events and the background.

3.3.5.1 HILLAS-MOMENTS-BASED GAMMA/HADRON SEPARATION

For this, the earlier-introduced MRSW parameter is used. This parameter is constructed in such a way that it peaks around zero for γ-ray events (Sect. 3.3.4.2). Since hadronic shower images are broader (Sect. 3.2.4), they result in a larger MRSW value. This is illustrated in Figure 3.15, where the relative distributions of the MRSW and the MRSL of

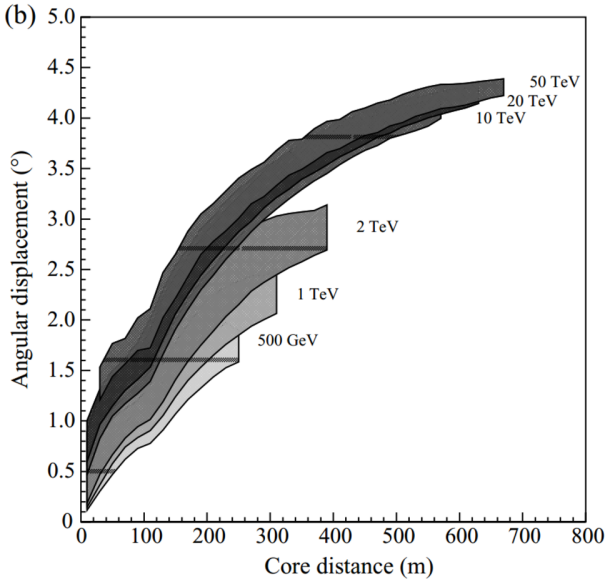

FIGURE 3.14 Correlation between core distance and angular distance (distance between *cog* and camera centre) simulated for a camera with a FoV of 5° radius for different γ-ray energies between 0.5 TeV and 50 TeV. They grey-shaded areas are the 68 % containment areas of the events w.r.t. the median of the distributions. Image adopted from Hinton (2009).

simulated γ-ray and proton events are shown and compared to data without a significant excess (*Off Data*). Especially, the MRSW parameter provides a strong discrimination power between γ rays and protons.

The so-called Hillas-based *standard cut* in H.E.S.S. data analysis to classify γ-ray events is $-2 < \mathrm{MRSW} < 0.9$ and $-2 < \mathrm{MRSL} < 2$ (Aharonian et al., 2006a). In addition, this *standard cut* includes a cut on the image size of 80 p.e. and a cut on the squared angle around the nominal source position of $\theta^2 = 0.0125\,\mathrm{deg}^2$ corresponding to $\theta \approx 0.11°$ and used in the case of point-like sources (angular extent of the source matches that of the PSF). Hence, the better the angular resolution (i.e. the PSF) the better on average the gamma/hadron separation, especially for point-like sources.

The event reconstruction and this gamma/hadron separation are part of the Hillas-moment-based analysis chain. This reconstruction and gamma/hadron separation are later on used in Chapter 4.

3.3.5.2 MULTI-VARIATE-BASED GAMMA/HADRON SEPARATION

There are more sophisticated methods to separate γ rays from hadrons; and within HAP framework the multi-variate algorithm TMVA results not only in an improved sensitivity, but also in higher event statistics (Ohm et al., 2009). This algorithm has been trained on the basis of MC data to *learn* how to identify a γ-ray shower (or a hadron). For this, all observables accessible from the shower image are used including higher moments of the intensity distribution in the camera. Once a sufficiently high efficiency for γ rays (or

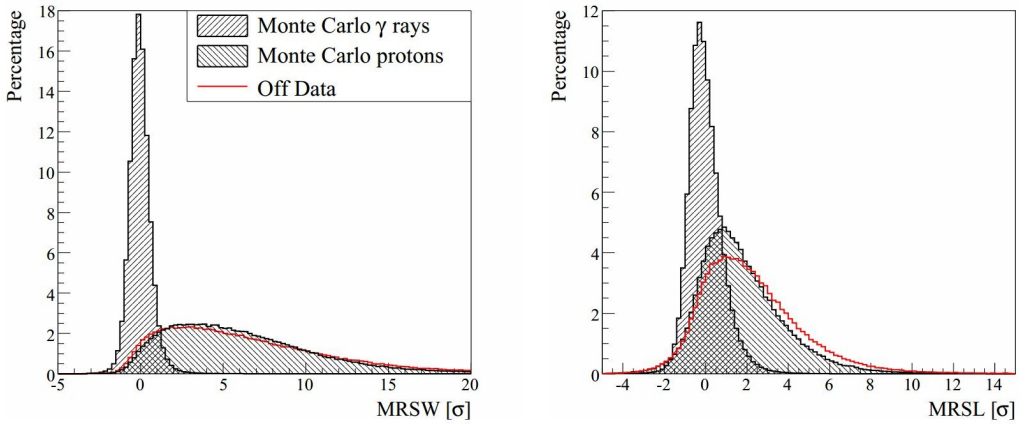

FIGURE 3.15 The relative distributions of the MRSW (**LEFT**) and MRSL (**RIGHT**) parameters of simulated events compared to observational data of a γ-ray source-free region (red line). Image adopted from Ohm (2010).

hadrons) is obtained for a set of shower parameters, the observed events in real data are flagged as γ-like, which states the probability of the event being a γ-ray shower.

In this work, also the ζ_{std} and the ζ_{hard} cuts of the multi-variate TMVA analysis for H.E.S.S. data are used (Ohm et al., 2009) to generate skymaps. This selection includes an image-size cut of 60 p.e., $\theta^2 = 0.0125\,\mathrm{deg}^2$ and a γ-ray cut efficiency of 0.84 for ζ_{std} or in the case of ζ_{hard}, an image-size cut of 160 p.e., $\theta^2 = 0.01\,\mathrm{deg}^2$ and a γ-ray cut efficiency of 0.83 are used.

The TMVA analysis exhibits on average a better sensitivity over the entire energy range of about 45 % compared to the MRSW approach (standard cuts). For a higher image size cut of 200 p.e. and a squared-angle cut of $\theta^2 = 0.01\,\mathrm{deg}^2$ (Hillas *hard* cuts), the performance of TMVA is about 20 % better (Ohm et al., 2009).

3.3.6 OPTICAL-EFFICIENCY CORRECTION

All elements of the telescope system are subject to degradation over time. This includes the mirrors, the camera, the Winston cones, and the involved electronics and results in a decline in the detection efficiency of the individual CTs and thus in a loss in sensitivity of the entire telescope array.

The measurable light yield in the camera is reduced leading to two effects: (1) events with energies around the initial trigger threshold do not trigger the CTs anymore and (2) not accounting for the loss in efficiency results in a wrong estimate of the reconstructed energy and therefore to a mismatch w.r.t. the MC simulations, which are produced for a specific efficiency at a specific reference time.

In Bolz (2004) it is shown that recorded muon rings can be used to determine the current throughput of all optical elements and therefore, also the current telescope efficiency (see Figure 3.16). Muon rings appear in the camera when the Cherenkov light of on-axis muon (at most 200 above the telescope) is reflected from the telescope mirrors onto the camera. Since the light yield of a relativistic muon is well known from MC simulations

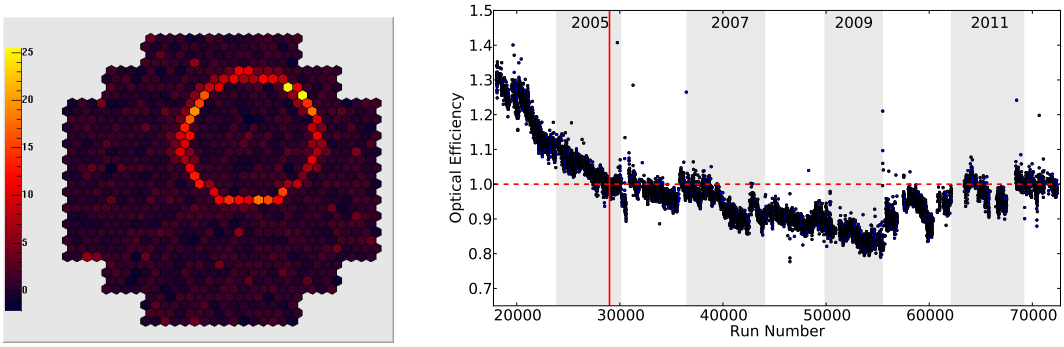

FIGURE 3.16 Muon ring and optical efficiency. **LEFT:** A fully-contained muon ring in units of photo electrons recorded within the H.E.S.S. camera used to determine the optical efficiency. Image adopted from *mpi-hd.mpg.de*. **RIGHT:** Optical efficiency per observation run (blue dots) for the four-telescope array starting at December 2003 and up to February 2012. Indicated are the relative efficiency of 1 (red-dashed line) and the reference period (solid red line; November 2005).

and the muon properties are reconstructable, the expected intensity can be compared to the measured one. Thus, an optical-efficiency correction (often called: muon correction) per observation run i is determined through

$$\mu_{\mathrm{corr},i} = \left(\frac{\eta_{\mathrm{eff},i}}{\eta_{\mathrm{eff},0}} \right)^{-1} , \tag{3.19}$$

where η_{eff} is the optical (or muon) efficiency normalised to a reference MC configuration $\eta_{\mathrm{eff},0}$. The optical efficiency is a relative efficiency w.r.t. the reference, but will be called optical efficiency for simplicity. Prior the reference time, the optical efficiency is therefore larger than 1. Since the light yield of an air shower image is proportional to the energy of the primary particle (Sect. 3.2), the energy of the reconstructed event can be corrected by scaling the reconstructed energy with the determined muon correction:

$$E_{\mathrm{corrected}} = \mu_{\mathrm{corr}} \, E_{\mathrm{reconstructed}} \, . \tag{3.20}$$

In Figure 3.16, the optical efficiency for the four-telescope system from December 2003 up to February 2012.[viii] November 2005 is the reference date for the MC data and therefore the optical efficiency is per design 1 around this time. From the course of the optical efficiency η_{eff} a saturation effect seems to set in after a initial steep decline (about 25 to 30 % from early 2004 to late 2005) within the first year and a half of full operation. However, at a nominal efficiency of 80 %, the mirrors of the CTs were replaced and refurbished within the year 2010 and 2012, which resulted in a recovery of the optical efficiency. Short-term variations indicate the different atmospheric conditions a few 100 m above the telescope site, e.g. smoke, dust or haze or changes on hardware level such as in the high-voltage supply of the PMTs.

[viii] Gaps within the curve indicate observations with less than four telescopes due to hardware issues or the mirror replacements. The efficiency for these periods with two or three is also available and does not differ from the one shown in Figure 3.16.

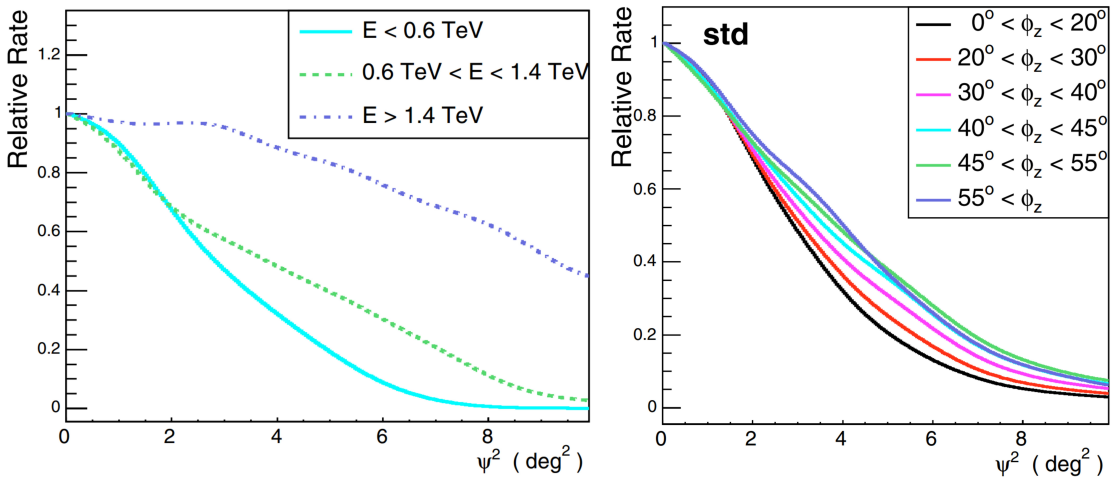

FIGURE 3.17 The camera acceptance for VHE γ rays vs. the angular distance from the camera centre (squared angle Ψ^2). **LEFT:** Relative rate (i.e. the same as the relative acceptance) for different energy ranges. **RIGHT:** The relative rate for γ rays from MC simulations of different zenith-angle bands and the Hillas standard cuts. Images adopted from Berge et al. (2007).

In Fernandes (2009); de los Reyes et al. (2013) it was shown that the optical efficiency can be used to derive an expected system trigger rate and thus to reject runs differing from the expected value as these potentially bias the spectral analysis.

3.3.7 CAMERA ACCEPTANCE

The response of the camera (the acceptance) to γ-ray events is not uniform over the entire camera FoV. The reason is that through the event selection criteria, especially the nominal-distance cut, a bias is introduced. Events reconstructed at larger camera offsets are more often discarded by the nominal-distance cut and therefore the rate of reconstructed events drops with distance from the camera centre.

This response can be considered the detection efficiency or the probability of detecting events over the camera FoV. It is usually calculated by summing up the events within the squared distance from the camera centre and in a good approximation, this acceptance is assumed to be radially symmetric w.r.t. the centre of the camera.

Within the inner $\sim$ 1° of the camera, the loss in efficiency relatively small, but increases with increasing distance from the centre. At around 2°, the efficiency has deteriorated to values below 0.5 (see Figure 3.17). Berge et al. (2007) estimated the relative uncertainty on the camera acceptance to be 3 % or less, and only for observations under high zenith angles ($\gtrsim$ 55°) larger deviations are observed.

In addition, the camera acceptance is strongly energy-dependent (see left-hand side of Figure 3.17). Lower-energy events are preferably reconstructed at lower offsets (see also Figure 3.14), whereas the acceptance for events with higher energies comparatively constant up to larger offsets of about 2°. Hence, a bias towards the energy w.r.t. the offset from the camera centre is introduced. Additionally, also a zenith-angle and azimuth-angle

dependence are observed, which are small compared to the energy dependence described above (Fig. 3.17, right).

As a consequence of the radial drop of the acceptance, a source is normally observed within the inner 1° of the camera, which usually means re-observations in case a of serendipitous discovery of a γ-ray source at larger offsets from the camera centre. In skymaps, the differences in the acceptance have to be accounted for.

3.3.8 BACKGROUND ESTIMATION

Despite the stereoscopic observations, the selection criteria, the gamma/hadron separation, and θ^2 cut around the assumed source position, the background still outnumbers the desired γ-ray photons from the source of interest by a factor of up to about 20. Thus, further analysis methods and techniques have to be applied to determine the number of excess counts from the source region (often called ON region).

Events are measured from the ON region and include both: *real* γ-ray events from the source and background events towards the same direction:

$$\begin{aligned} \text{Observed events} &= \gamma\text{-rays from the source + background events}\,, \\ \gamma\text{-rays from the source} &= \text{observed events} - \text{background events}\,. \end{aligned}$$

The background is dominantly composed of hadronic events, but also includes γ-ray events from the source that failed the gamma/hadron separation or diffuse γ-ray emission as well as electrons classified as γ-ray photons. The background is estimated with a control region (called OFF region) that is displaced w.r.t. the ON region.

EXCESS COUNTS The VHE γ-ray excess N_{excess} from the ON region is then

$$N_{\text{excess}} = N_{\text{ON}} - \alpha N_{\text{OFF}}\,, \tag{3.21}$$

where N_{ON} and N_{OFF} are the number of events in the ON and OFF regions, respectively. The factor α is the overall normalisation between both regions and accounts for the respective differences between ON and OFF, e.g. solid angle or exposure.

Given this, the purpose of any background-estimation method is to determine N_{OFF} with a preferably low statistical uncertainty. This is achieved by simply increasing N_{OFF} and a corresponding decrease of α.[ix] These spatially separated OFF regions have to be source-free (i.e. not showing a significant γ-ray signal) or N_{OFF} would be overestimated and thus N_{excess} underestimated.

STATISTICAL SIGNIFICANCE The statistical significance of N_{excess} is calculated in a likelihood-ratio approach (Eq. 17; Li & Ma, 1983). Here, the null hypothesis is that there is no excess coming from the source ($N_{\text{excess}} = 0$) and that the apparent excess is caused by the background.

[ix] The quantities N_{ON}, N_{OFF}, and α are calculated in energy intervals to determine the excess per energy in order to reconstruct an energy spectrum.

The significance S (in units of standard deviations from the null hypothesis) is defined as

$$S = \sqrt{2}\sqrt{N_{\mathrm{ON}}\log\left(\frac{\alpha'}{\alpha}\frac{N_{\mathrm{ON}}}{N_{\mathrm{ON}}+N_{\mathrm{OFF}}}\right)+N_{\mathrm{OFF}}\log\left(\alpha'\frac{N_{\mathrm{OFF}}}{N_{\mathrm{ON}}+N_{\mathrm{OFF}}}\right)}, \tag{3.22}$$

where $\alpha' = 1 + \alpha$.

In the following, the background-estimation methods used to determine N_{OFF} are described. This is required to calculate the VHE γ-ray excess and significance skymaps, but also energy spectra (see also Section 3.3.9).

3.3.8.1 *On/Off* OBSERVATIONS AND BACKGROUND METHOD

The *classical* idea of the *On*/*Off* background is the alternation of direct observations of the source (*On* observations) and an empty (i.e. source-free) FoV close-by (*Off* observation) to determine the background. Ideally, it is alternated between observations of the *On* and the *Off* FoV without a too large separation in time.

In this observation scheme, it is assumed that *On* and *Off* observations do not differ (for a given observation duration, the background rate should not deviate from *On* to *Off*) and that the camera acceptance is identical. Moreover, systematic effects are considered to affect both FoVs equally and thus it is assumed that the subtraction does not introduce further systematics. This method has been in use for single-telescope systems, like Whipple (Weekes et al., 1989) or MAGIC (Lorenz, 2004). For equal durations of *On* and *Off* observations, one achieves a background normalisation $\alpha \approx 1$.

***On/Off*-BACKGROUND METHOD WITH H.E.S.S.** Usually, *On*/*Off* observations are not conducted with the H.E.S.S. telescopes. However, it is still possible to use this background method. In this case, archival extra-Galactic data without a significant excess are used as *Off* observations taken at similar azimuth angle and altitude, but not separated in time more than half a year w.r.t. the actual *On* data.

This background method is only used to determine the quantities for a spectral reconstruction and its application means that other methods (introduced below) are not applicable. It is assumed that the FoVs behave identically w.r.t. the aforementioned properties and in determination of the background in energy intervals, it is assumed that the muon correction accounts for the time variance between the *On* and *Off* data sets.

LIMITATIONS Observations conducted in the *On*/*Off* mode usually mean spending the double amount (if $\alpha \approx 1$ is aimed for) of dark time (about 1000 hrs per year for H.E.S.S. observations) on one source region. This not preferred (precious dark time is lost which could be spent to observe other sources) and therefore generally avoided.

Besides the applied muon correction, a second assumption is that the FoVs are identical. However, this may not be always valid and therefore could be a cause of systematic errors (e.g. due to differences the event rate, different acceptances or a source in the *Off* FoV just below the detection threshold).

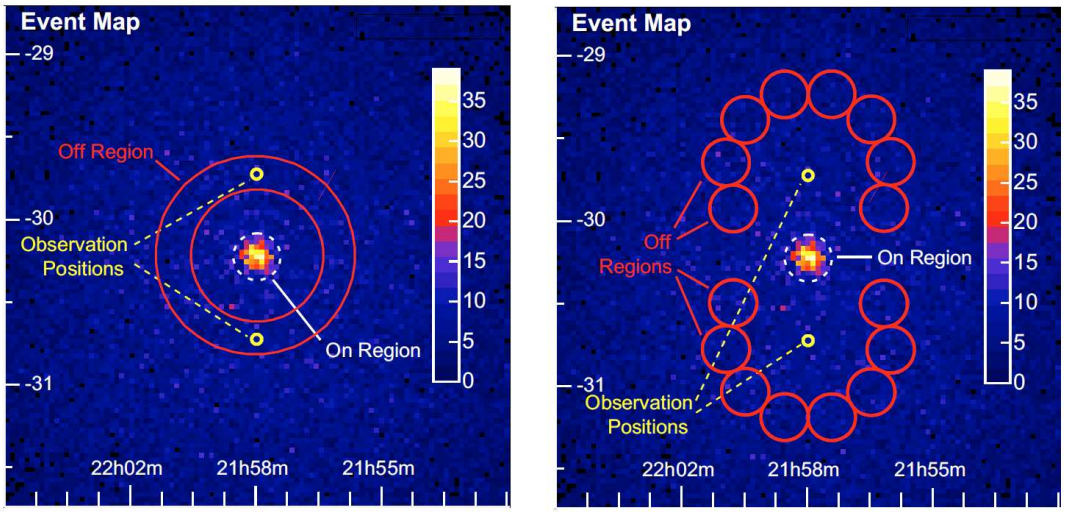

FIGURE 3.18 Schematic overlay of the ring-background method and the reflected-region background method on a γ-ray excess skymap. **LEFT:** The ring-background method is illustrated by the red-lined ring denoted as *Off region* around the ON region (On region). Additionally, the two observation positions are indicated. **RIGHT:** The reflected-region background w.r.t. the observation positions is depicted. The images are adopted from Berge et al. (2007).

3.3.8.2 WOBBLE OBSERVATIONS AND THE REFLECTED-REGION BACKGROUND METHOD

A different approach to determine the background without expense of additional dark time is possible with IACTs equipped with cameras providing a large FoV. *Wobble* observations mean that the centre of the FoV is not pointed directly at the source of interest, but is slightly offset (wobbled) in right ascension or declination, see also Section 3.3.2 and Figure 3.18.

In doing so, the observed source (ON region) is always located at the same radial distance w.r.t. the camera centre and allows to place background regions (OFF) at the very same radial offset by reflecting them from the source position w.r.t. the camera centre. As a result, ON and OFF share the same camera acceptance and no relative correction is needed. If the ON and OFF regions are equally-sized, the background normalisation is proportional to the inverse number of OFF regions: $\alpha = 1/n_{\mathrm{OFF}}$. In order to not overestimate the background, VHE γ-ray emission regions in the FoV have to be excluded if they overlap with any of the OFF regions.

With H.E.S.S., large wobble offsets ($> 0.7°$) are possible, but are subject to higher losses in the acceptance and thus only used for the observations of extended sources. Usually offsets between 0.5° and 0.7° are chosen. This background-estimation method is used to determine the background for energy spectra. Additional systematic errors are not introduced since no further corrections to the data are done. It is possible to use the reflected-region background method to produce skymaps, but this is usually not done. In the H.E.S.S. analysis, this is the standard to determine the background for energy spectra.

LIMITATIONS The only assumption made is that the camera acceptance is radially symmetric. As the OFF regions are *a priori* set with the choice of the wobble offset, the limitations are of mainly geometrical nature. The number of OFF regions and therefore the sensitivity of the reflected-region background method is limited by the presence of additional sources and VHE γ-ray emission in the FoV. If the centre of the FoV points directly into the source of interest, the ON and OFF regions overlap and the background cannot be determined. This occurs in the analysis of serendipitously discovered sources and for the standard observations pattern, also for sources with radii larger than 0.7°.

3.3.8.3 RING BACKGROUND

The ring-background method consists of a ring surrounding the ON region (see Figure 3.18). VHE γ-ray emission regions within the ring have to be excluded. Gradients across the FoV, as long as they are linear within the ring, are averaged out by design of this background. The thickness of the ring and the ring radii determine α. Despite the fact that the ON region will in general experience a different acceptance, these differences are normally averaged out. For extended sources from about 1° in size, the differences in the acceptance do not cancel out and a correction is done.

This technique is currently only used for source detection and morphological studies. Especially in clear FoVs and in the analysis of a point-like source or moderate-extended one ($\theta \lesssim 0.5^\circ$), this background method is chosen.

LIMITATIONS The ring-background method is limited by the angular size of the ON region. The larger the source, the larger the inner ring radius is chosen, which leads to $\alpha > 1$ for very extended sources. In these cases, the differences in the acceptance becomes larger. Systematic effects related to the acceptance correction increase as well.

3.3.8.4 TEMPLATE BACKGROUND

The template background model (Rowell, 2003) utilises a different approach to determine the background. Usually, events that do not meet the criteria in the gamma/hadron separation for γ-ray events are discarded. Here, they are used to model the background. The background selection is (a) with the MRSW parameter $2 < \text{MRSW} < 10$ and (b) with TMVA $\zeta > 0.9$. Since the ON and OFF regions are now defined in parameter space and not through a spatial selection, ON and OFF events are co-located (i.e. at same location in the sky).

Now, events passing the γ-ray cuts are named γ-like and events passing the hadron cuts are named hadron-like events.[x] Henceforth, the ON region is called signal region. The background normalisation α is determined from the data in the FoV excluding the signal region and further γ-ray emission regions.

On the left-hand side of Figure 3.19, the basic idea of this method is illustrated. The events from data are divided into a γ-like sample (bottom FoV) and a hadron-like sample (top FoV); γ-ray emission regions are therefore in both skymaps and are excluded in the

[x] However, γ-like events still include hadron events that pass the same cuts and *vice versa*.

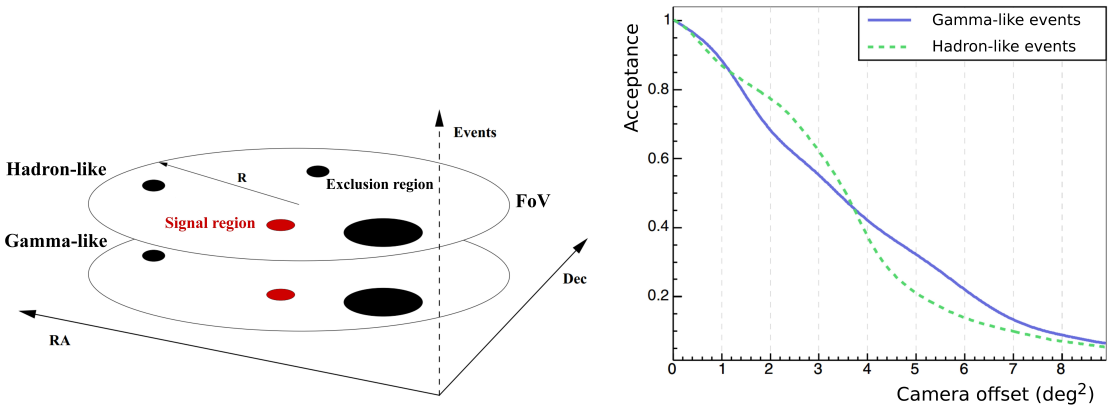

FIGURE 3.19 The template background model. **LEFT:** Schematic display of the concept of the template background model with the two samples of events (gamma-like and hadron-like) defined in parameter space, but otherwise sharing the same properties. Image adapted from Rowell (2003). **RIGHT:** Relative acceptance for the gamma-like and hadron-like regime as a function of the squared radial distance from the camera centre. Image adapted from Berge et al. (2007).

calculation of the background normalisation that also accounts for the difference of the events in the respective regime. In addition, the acceptance of the camera for the γ-like events and the hadron-like events differs (see right-hand side of Figure 3.19), but it also changes over the FoV with the zenith angle.

The correction is determined in a higher-order polynomial fit P to the gamma-like (g) and to the hadron-like (h) sample and is a function of the distance from the camera centre θ and the zenith angle z. After a normalisation to 1 at the origin of the camera offset the template-background correction at a given position θ is then

$$\alpha(\theta) = \frac{P_{\mathrm{g}}^{\mathrm{FoV}}(\theta, z)}{P_{\mathrm{h}}^{\mathrm{FoV}}(\theta, z)}\,, \tag{3.23}$$

Equation 3.21 is therefore modified:

$$N_{\mathrm{excess}}(\theta) = N_{\mathrm{g}}(\theta) - \alpha(\theta) N_{\mathrm{h}}(\theta)\,. \tag{3.24}$$

This background method is only in use to produce skymaps and has the advantage that it is not constrained by geometric aspects in the FoV. Therefore, it can also be used for every extended sources. Also, this method accounts for local effects in the FoV (e.g. stars or defective pixels in the camera) appear in both regimes at the same location and are virtually cancelled out as long as they effect both regimes equally.

LIMITATIONS Compared to the other background estimation methods, the template normalisation α is not calculated by simple geometrical means, but requires a good knowledge of both acceptances. Yet, correcting the data with this α that is calculated on the basis of two intrinsically difference camera acceptances introduces an additional source of a systematic error. Additionally, after excluding the signal region and other known

VHE γ-ray emission regions, there has to be sufficient data in the FoV to calculate $\alpha(\theta)$. If there are not enough data to calculate the γ-like and the hadron-like acceptance curves, then these acceptances have to be extrapolated or interpolated for the respective radial distance and an additional systematic error is introduced. Also, at the edge of the camera, the acceptance is biased due to truncated and misreconstructed events, especially in hadron-like regime. This leads to a ring-like (fake/systematic) excess at the border of the FoV not caused by the template-background as such but through the relative changes of camera acceptances of γ-like and hadron-like events.

3.3.8.5 BRIGHT STARS

Stars in the FoV are a problem for the CT camera as an overexposure of single pixels by bright stars can damage the camera. To avoid this, the respective pixels are switched off. It is observed that the event rate of γ rays drops towards the star position depending on the brightness of the star, but also on the analysis configuration and selection cuts (Berge et al., 2007). For example, in the Hillas-based analysis using an minimum image size of 80 p.e., stars brighter than 5 in magnitude (in Johnson's B band) lead to a local dip in the event rate of $\sim$ 10 % within $\sim$ 0.3°. The shower images of events with small core distances will fall onto parts of the camera with turned-off pixels and therefore have holes in their profile. These images are then likely discarded in the event reconstruction and lead to fewer reconstructed events in the direction of the star. This effect is negligible for higher cuts on the image size (Berge et al., 2007).

Berge et al. (2007) reported the effect of bright stars in combination with different background-determination methods. For the reflected-region background method and the ring-background method, a negative excess at the star position is observed. Both methods estimate the background through displaced OFF regions that exhibit higher event rates than the region affected by star.

For the template-background model, a positive excess towards the star is observed. This is most likely because the hadron images are to a higher fraction affected by a turned-off pixels. Since hadronic shower images are broader they will fall more likely onto the camera regions with turned-off pixels. These events are discarded by the image size cut as a significant amount of the light yield is missing to meet the required image-size threshold. As a result, a larger dip is observed in the event rate of the hadron-like events than in that of the γ-like events and both lead to a positive excess at the star position. The affect is stronger, the closer the turned-off pixels are located towards the camera centre.

As a consequence: if a bright star is located towards the direction of a (potential) VHE γ-ray source, the background is potentially either overestimated (with displaced background methods or underestimated (e.g. the template background model). This results in a potential systematic bias in the source detection and analysis. In the HAP framework, stars brighter than 5^{mag} are excluded with a circle of 0.2° radius from the computation of the acceptance.

3.3.8.6 Acceptance correction from extra-Galactic data

Most background-estimation methods require a good knowledge of the camera acceptance. As many sources in the Galactic Plane are extended and often embedded in regions with diffuse γ-ray emission, large parts of the FoV are excluded and cannot be used to determine the acceptance. Since also bright stars affect the acceptance, they are excluded as well. Therefore, the acceptance has to be estimated through interpolation or extrapolation. Especially, the extrapolation for larger source regions introduces a systematic error. Therefore, data of (extra-Galactic) source-free regions are used to determine a precalculated look-up of the camera acceptance to be used in the analysis of Galactic sources.

The look-ups of the camera acceptance are used in the H.E.S.S. analysis package (HAP) and are available for different analysis methods, sets of selection cuts, and for both γ-ray events and background (hadron) events. In total, 2615 H.E.S.S. observation runs pointing away from the Galactic Plane and mostly into regions without a VHE γ-ray source were selected to determine the camera acceptance; any significant VHE γ-ray emission region was generously excluded. The acceptances were calculated and stored in intervals of the zenith angle and the azimuth angle. The ranges are chosen such as to have an almost even exposure in all 14 zenith-angle bins from 0° to 65°. Thus, the data of a run with its mean zenith angle is corrected with the look-ups obtained by interpolation between the respective zenith-angle intervals.

For more information on the acceptance look-ups it is referred to Gast (2012); Peille (2012). Later on, in Chapter 7, these acceptance look-ups will be discussed in more detail.

3.3.9 Spectral reconstruction

In detail, the spectral reconstruction and its requirements are discussed in Chapter 4. For now, the basic principle is introduced.

Apart from the morphology of a source, its measured flux and spectral shape are important source properties. For this, at least the effective detection area A_{eff} for γ rays of the IACT for a set of selection and quality cuts at a given zenith angle and offset have to be known. It is a function of the reconstructed energy. The ON and OFF events are preferably determined with the reflected-region background method in energy intervals ΔE[xi]. Together with the livetime t, the differential energy spectrum per energy bin i is

$$\frac{d\Phi_i}{dE} = \frac{1}{t_i\,\Delta E_i}\left(\sum_{j=1}^{N_{\mathrm{ON},j}} \frac{1}{A_{\mathrm{eff},j}} - \alpha \sum_{k=1}^{N_{\mathrm{OFF},k}} \frac{1}{A_{\mathrm{eff},k}}\right). \tag{3.25}$$

The best-fit spectrum (e.g. a power law with $d\Phi/dE = \Phi_0\,E^{-\Gamma}$ with normalisation Φ_0 and power-law index Γ) is obtained through an iterative fit of Equation 3.25 (e.g., Aharonian et al., 2006a). However, as the effective area is a function of the reconstructed energy, it has to be weighted by the assumed spectral behaviour after every iteration step. For weak sources, a dependence on the bin width in energy ΔE is observed.

[xi] The bin width in energy is normally chosen to exhibit a minimum significance, usually $2\ldots5\,\sigma$, calculated according to Li & Ma (1983).

Chapter 4

Template Background Spectrum

In this chapter, the Template Background Spectrum (TBS) method is introduced. The TBS method has been developed to determine the background for the spectral reconstruction of extended sources, sources in complex FoVs, and especially when the reflected-region background (RrBg) method cannot be used. In the following, the acronym TBS is used when referring to this background-estimation method or to quantities related to it.

Challenges to current spectral background-estimation methods Most VHE γ-ray emitters away from the (inner) Galactic Plane or of extra-Galactic origin are point-like sources, i.e. their angular extent matches or does not significantly deviate in size from the PSF of the IACT. In these cases and if the observations were not conducted in *On* mode, the spectral reconstruction is done using the RrBg method. Usually, these extra-Galactic FoVs contain a single VHE γ-ray source and the background estimation is not subject to limitations as pointed out in Section 3.3.8.2.

However, most sources along the Galactic Plane are extended w.r.t. the PSF. A couple of them fill a large fraction of the FoV or are located in complex regions limiting the application of the RrBg method. Therefore, additional observations of γ-ray source-free regions under similar observation conditions are required to estimate the background for the reconstruction of energy spectra. This additional expense of the limited dark time (about 1000 hrs per year for H.E.S.S.) is not favoured.

If the observations were not done in the classical *On*/*Off* mode (Sect. 3.3.8.1), one may use *Off* observations from a data base if the temporal variation of the detector response is known and accounted for (e.g. through muon rings; Sect. 3.3.6). Because it is not always possible to find matching pairs *a posteriori*, data without a background estimate are lost. Besides, dedicated studies on systematics when using extra-Galactic data from a data base to spectrally reconstruct Galactic data have not been published so far.

Motivation for the template background model The template background (TBg) model is used to generate skymaps and defines the background in parameter space (Sect. 3.3.8.4). Unlike the RrBg method, *On* runs can be analysed since the background estimate is not displaced, but determined from the same source region. Thus, the TBg method has its strengths where the RrBg is limited. The challenge of this background-estimation method is the determination of the normalisation between the γ-ray and hadron events from the source region.

OUTLINE This chapter is split into two parts. The first part includes the general idea and concept of TBS to be used for the spectral reconstruction of IACT data. This part is in general independent from the choice of the IACT system. Therefore selection criteria and parameter values, which depend on the IACT and its data, are only stated if necessary for the understanding. A detailed discussion is given on the determination of the background normalisation for the TBS method and on the handling of statistical and systematic errors.

In the second part (starting at Section 4.5), H.E.S.S. data were used to study and test TBS in detail. Here, the complete set of introduced selection cuts and parameters is given as used in the analysis of the H.E.S.S. data. To validate this new method, the spectral results on selected VHE γ-ray sources obtained with TBS are compared to those of state-of-the-art background-estimation methods.

4.1 THE CONCEPT

With the use of the TBg model in TBS, there are three more or less direct implications and aspects in the analysis to be considered before a spectral reconstruction of a source is possible.

1. ENERGY DEPENDENCE For the reconstruction of energy spectra, source and background events and the background normalisation need to be determined for individual intervals in energy (e.g. Sect. 3.3.9). Since the background normalisation of the TBg model is the ratio of two acceptances (Eq. 3.23), which intrinsically vary with energy and zenith angle (see Figures 3.17 and 3.19 and discussion thereof), this ratio will not remain constant for the different energy intervals. Therefore, an energy dependence of the TBg normalisation is introduced:

$$\alpha(E, z, \theta) = \frac{N_{\mathrm{g}}^{\mathrm{FoV}}(E, z, \theta)}{N_{\mathrm{h}}^{\mathrm{FoV}}(E, z, \theta)} \,. \tag{4.1}$$

Here, $N_{\mathrm{g}}^{\mathrm{FoV}}$ and $N_{\mathrm{h}}^{\mathrm{FoV}}$ are the gamma-like and hadron-like events from the data in the FoV for the three-dimensional set of energy E, zenith angle z and distance from the camera centre θ. Note that the signal region and other known γ-ray sources in the FoV are excluded here.

2. CAMERA ACCEPTANCE In Section 3.3.7, it was described that the camera acceptance changes with energy and zenith angle for γ rays (Fig. 3.17) and furthermore, is different for hadrons (Fig. 3.19). In previous works, it was concluded that these differences do not allow for a spectral reconstruction based on the TBg model (e.g. Berge et al., 2007). It was argued that the acceptance corrections of the respective γ-ray and hadron events introduce systematic uncertainties. Moreover, the estimated background ought to consist of events with a similar distribution in energy as the events from the source.

However, as the template normalisation is the ratio of gamma-like and hadron-like events, any relative difference is intrinsically accounted for through Equation 4.1. Moreover, there is no need to correct the individual acceptances because a relative acceptance

correction and a relative exposure correction are already included.[i] As Equation 4.1 also accounts for the energy and the zenith-angle dependence of the background normalisation as long as the gamma-like and hadron-like share the same intervals in reconstructed energy and zenith angle.

3. LOW EVENT STATISTICS The third point is a direct consequence of the three-dimensional dependence of the template correction. Since the data are divided into intervals of energy, zenith angle, and camera offset, a run-by-run calculation of $\alpha(E, z, \theta)$ for all required parameter sets of (E, z, θ) may not always be possible due to insufficient event statistics. This occurs mainly in the analysis of very large sources ($\theta \gtrsim 1°$).[ii]

This matter is dealt with by omission of the standard run-by-run approach and by construction of a so-called *look-up table*. This means, at first data are accumulated run-by-run and sorted into intervals of (E, z, θ) before calculating $\alpha(E, z, \theta)$. The TBS correction $\alpha(E, z, \theta)$ is stored in a three-dimensional grid: the aforementioned look-up table (LuT). Because the hadron-like events from the signal region are identically binned in energy and zenith angle as the LuT is, they can be corrected by retrieving the appropriate $\alpha(E, z, \theta)$.

In the remainder of this chapter, α will always refer to the full dependency $\alpha(E, z, \theta)$, unless stated elsewise. In general, *data in the FoV* implies that the signal region and possible other γ-ray emission regions are excluded.

4.2 LOOK-UP TABLE

For every observation run, every reconstructed event from the data in the FoV that has passed a predefined and analysis-dependent set of selection cuts is classified as gamma-like or hadron-like in the gamma/hadron separation (Sect. 3.3.5). The *modus operandi* is analogously to the procedure for the standard TBg model and not restricted to a specific gamma/hadron-separation method or parameter. For this study, the MRSW-based selection cut was used.

After the classification, the event is filled into the bins of the LuT w.r.t. its reconstructed energy, reconstructed zenith angle and reconstructed offset from the camera centre. The binning is chosen, such that a sufficient amount of events is found in nearly every set of (E, z, θ) to adequately calculate α and its statistical error, and to sample its course in θ. The exact parameter ranges and bin widths of the LuT are dependent on the performance of the IACT, but also on the desired resolution of the spectrum.[i] The only information stored in the LuT is the number of gamma-like and hadron-like events, $N_{\mathrm{g}}^{\mathrm{FoV}}$ and $N_{\mathrm{h}}^{\mathrm{FoV}}$ from the data in FoV and the inferred template normalisation α with its statistical error $\sigma(\alpha)$ for every interval of (E, z, θ); see Figure 4.1.

[i] In general, the intrinsic systematic uncertainty of the acceptances is unlikely to be reduced by the division. However, it may reduce systematic uncertainties potentially introduced by the polynomial fit to both acceptances before calculating the TBg normalisation (see Equation 3.23).

[ii] Here, the RrBg method mostly completely fails to determine the background.

[i] This will be discussed on the basis of the H.E.S.S. data later on.

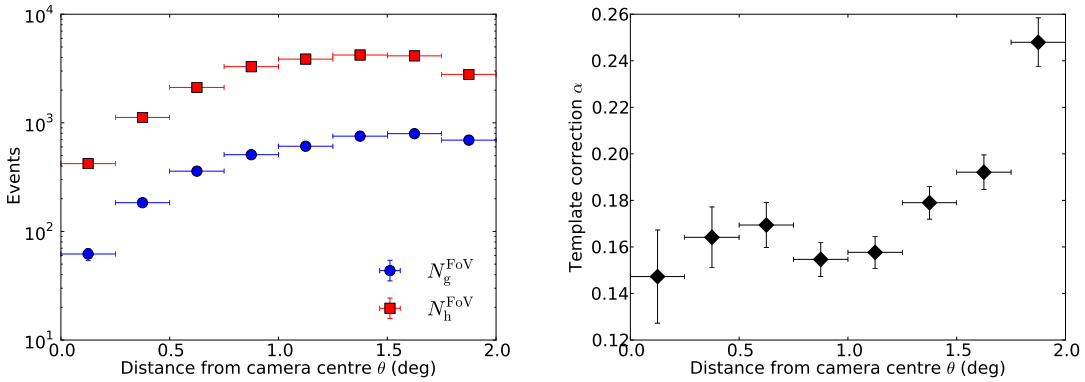

FIGURE 4.1 Example of the calculation of α. Here, H.E.S.S. data on Centaurus A (Aharonian et al., 2009c) were used in the energy interval of 1 TeV to 1.3 TeV and the zenith-angle range 20° to 30°. **LEFT:** Events classified either as gamma-like (N_g^{FoV}, blue circles) or hadron-like (N_h^{FoV}, red squares) are filled into histograms w.r.t. their reconstructed distance from the camera centre θ. **RIGHT:** The template correction α calculated through division of N_g^{FoV} and N_h^{FoV} (Eq. 4.1).

4.2.1 LOSS IN OPTICAL EFFICIENCY

The LuT requires a good knowledge of the parameters, especially the energy, which involves two aspects in the IACT data analysis: the loss in detection efficiency and the energy resolution at low energies. For most IACTs, this loss in optical efficiency is monitored by using the information of muon rings in the camera (muon correction; Sect. 3.3.6) and mostly accounted for in the event-wise energy reconstruction.

The loss in optical efficiency affects the energy reconstruction (accuracy of the energy estimate w.r.t. MC simulations) and the energy resolution (precision of the energy estimate) in the IACT-data analysis. Especially, the performance at lowest energies deteriorates, which, for example, can be seen in the so-called energy-resolution matrix or in the relative energy bias. Those will be presented on the basis of H.E.S.S. data later on in Section 4.5.1. For now, the general implications for the LuT are described.

Both aspects have in common that, if they are not accounted for, the LuT will be filled with gamma-like and hadron-like events with incorrectly reconstructed energies and therefore lead to an incorrect background normalisation, especially when the data set is comprised of observations separated by a year or more.

Since events in the same energy bin of the LuT will exhibit different energy biases as they are often taken in observations with varying properties (e.g. zenith angle or offset), events with a too large bias have to be excluded beforehand.[ii] In the standard analysis, any cut on the quality of the energy resolution or the energy bias can be applied at the end of the analysis chain when the spectrum is reconstructed.

For TBS, however, all selection and quality cuts have to be applied before filling events into the LuT to calculate α and also before accumulating the signal-region events.

[ii] Although the more sophisticated forward-folding approach (introduced later in Section 4.4) is used to determine the spectrum, the run-by-run energy-resolution matrices cannot account for this issue.

After all, events in the FoV and in the signal region have to experience the exact same selection criteria. *A posteriori* it is not possible to apply an energy-resolution dependent or energy-bias dependent cut on α, especially when the observation runs are spread over a wide range of zenith angles and wobble offsets. Therefore, an *a priori* zenith angle and wobble-offset dependent cut is introduced: the energy threshold.

The energy threshold is determined through the relative energy bias E_{bias} between simulated and reconstructed energies in MC simulations and usually between 10 % and 20 %, but deteriorates towards low energies. This cut assures that all events processed in the TBS analysis exhibit on average the same (or a better) energy resolution and at the same time that events with a poorly reconstructed energy towards the lower energy end are rejected. The energy threshold used for TBS and based on H.E.S.S. data will be presented in Section 4.5.1.3.

4.2.2 BRIGHT STARS

Bright stars lead to a local distortion of the acceptance at their radial distance $\theta_\star$ from the camera centre and affect the hadron-like events stronger than gamma-like events (Sect. 3.3.8.5). These distortions can only affect the TBS analysis of a source if they are located at the same radial distance from the camera centre as the signal region is. However, because sources are usually observed at different wobble offsets, any star will exhibit a varying offset $\theta_\star$ w.r.t. the camera centre and the source from run to run. Any effect is therefore negligible and is averaged out in the LuT creation.

In this study, bright stars with apparent magnitudes of 5^{mag} and brighter are excluded in the calculation of the acceptance to avoid any bias in this study.[iii]

4.2.3 TEMPLATE CORRECTION VS. ENERGY, ZENITH ANGLE, AND CAMERA OFFSET

The template correction varies with energy, zenith angle, and camera offset and results in an intrinsic uncertainty of the correction. This is important to the discussions in the following sections and is therefore discussed here.

In Figure 4.2, the template correction is shown for different intervals of the reconstructed parameters energy, zenith angle, and camera offset (calculated from H.E.S.S. data on Centaurus A; Aharonian et al., 2009c). On the left-hand side, the template correction is plotted against the zenith angle for different fixed energy and camera-offset intervals. On the right-hand side, the template correction is plotted against the energy for fixed zenith angle and camera-offset intervals. Since observations in the VHE γ-ray regime are background dominated, $\alpha < 1$; but because energy and zenith angle vary, α will change, too.

[iii] This is also done in order to be consistent with the standard H.E.S.S. data analysis presented and compared to later on.

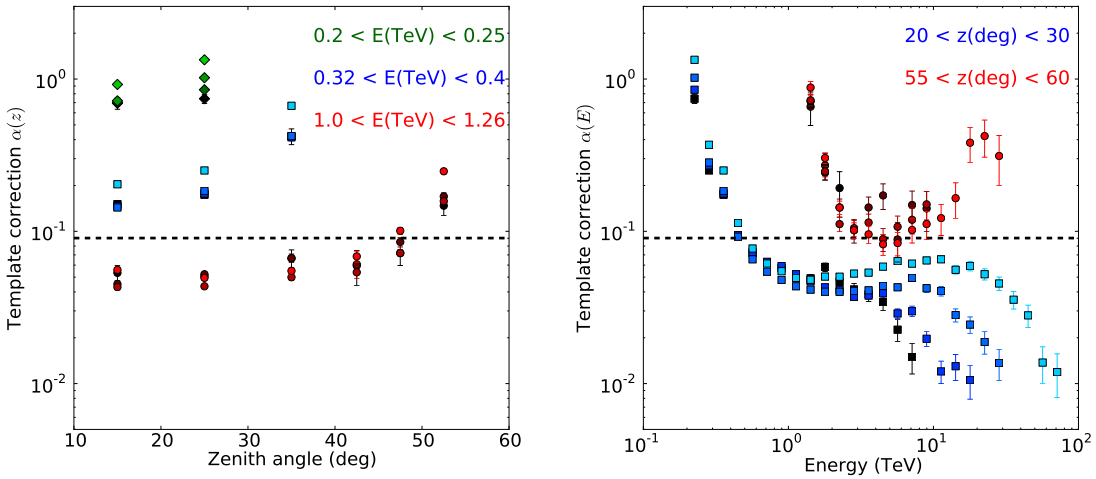

FIGURE 4.2 The template correction α calculated with H.E.S.S. data on Centaurus A (Aharonian et al., 2009c) through Equation 4.1 for different offsets $\theta = \{0.125°, 0.625°, 1.125°, 1.625°\}$ marked by the respective colour transition from dark to light. The black-dashed line indicates the overall template correction of the standard TBg for the entire data set. **LEFT:** Zenith-angle dependence of α calculated for three energy intervals 0.2 TeV to 0.25 TeV, 0.32 TeV to 0.4 TeV, and 1.0 TeV to 1.26 TeV depicted as green diamonds, blue squares, and red circles, respectively. **RIGHT:** Energy dependence of α calculated for the zenith-angle intervals 20° to 30° (blue squares) and 55° to 60° (red circles).

4.2.3.1 TEMPLATE CORRECTION VS. ENERGY

From the two plots in Figure 4.2, the general tendency of the template correction is directly readable: the template correction α decreases with increasing energy. At low energies, especially around the energy threshold, fewer events are found in the data (after the event reconstruction and event selection). Since shower images of hadrons are fainter than those of γ rays at the same energy (Sect. 3.2.4), they are affected stronger at the lowest energies. Therefore, $\alpha \approx 1$ at low energies. This is also to be seen in Figure A.1 where the histograms of the gamma-like and hadron-like events are shown that were used to calculate α in Figure 4.2.

As the energy increases, the relatively more hadrons lead to a decrease in α. Here, α appears to saturate at around 1 TeV thus indicating the best-achievable performance of the gamma/hadron separation for this analysis.

4.2.3.2 TEMPLATE CORRECTION VS. ZENITH ANGLE

The template correction α increases with increasing zenith angle. Although also depending on the energy range, the dependence of α is rather weak at low zenith-angle ranges (Fig. 4.2, left).

Usually, low zenith angles mean high event numbers in both event classes and there-

fore also a lower value of the template correction. As the zenith angle increases fewer events trigger the telescope and subsequently remain in the data, which are used to calculate α. Therefore, the relative difference between gamma-like and hadron-like event numbers leads to a rise in α (see also Figure A.2 for the respective histograms).

4.2.3.3 TEMPLATE CORRECTION VS. CAMERA OFFSET

In order to map the scatter of α in θ, four offset intervals are chosen, i.e. $0.0^\circ - 0.25^\circ$, $0.5^\circ - 0.75^\circ$, $1^\circ - 1.25^\circ$, and $1.5^\circ - 1.75^\circ$. The first interval represents the performance of α at the camera centre. The second interval, indicates performance of the background normalisation at the wobble offset of 0.5° to 0.7° for point sources. The other two correspond either to a larger wobble offset or would be used in the analysis of a larger source. For the different camera-offset intervals, a relative scatter of α of 20 % to 30 % per zenith angle is observed.

Because of the strong correlation between the reconstructed camera offset and the reconstructed energy (Fig. 3.14), the event statistics are not sufficient to calculate α towards smaller camera offsets. Here, the number of gamma-like events from data in FoV decreases, the higher the energy range is. This is clearly see in the right plot of Figure 4.2 for the template correction calculated for the zenith-angle range between 20° and 30° (blue markers), where a fanning out of the template correction at energies around 8 TeV is observable.

4.3 TBS CORRECTION

In general, the task is to estimate the background normalisation of the TBg and to calculate the number of excess events within an energy bin. For this, the three-dimensional dependence (E, z, θ) has to be reduced to one dimension (E) while accounting for the uncertainty on the excess counts in the course of this reduction.

After having computed the three-dimensional LuT from the data in the FoV, the tabulated $\alpha(E, z, \theta)$ values are then used to correct the individual hadron-like events from the signal region w.r.t. their reconstructed properties (E, z, θ). To increase the precision of this procedure, the template correction is determined through an interpolation along the three-dimensional grid rather than just a simple application of the tabulated binned α values.

4.3.1 INTERPOLATION

In Figure 4.3, H.E.S.S. data on Vela X (Abramowski et al., 2012b) were used to illustrate the template correction α calculated according to Equation 4.1 and plotted against the camera offset θ for a fixed energy interval ΔE and a fixed zenith-angle bin Δz. In the following, the linear interpolation is described, and the calculated set of $\alpha(\Delta E, \Delta z, \theta)$ will be called *nodes* of the interpolation.

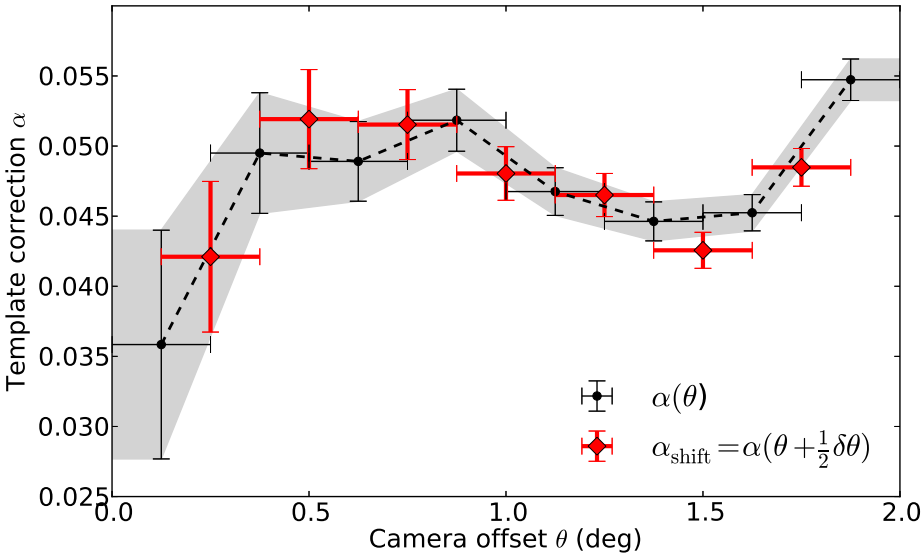

FIGURE 4.3 The template correction $\alpha(\theta)$ for TBS based on H.E.S.S. data on Vela X (Abramowski et al., 2012b) for the energy interval $\Delta E = (1, 1.3)$ TeV and the zenith-angle range $\Delta z = (20°,30°)$. The α nodes are calculated according to Equation 4.2 and shown as black circles together with the corresponding 1 σ envelope (grey-shaded area). The dashed black line illustrates the interpolation line along which a β_i value will be obtained. The parameter $\delta\theta$ is the bin width in θ. The shifted reference nodes, α_{shift}, are drawn as red diamond markers.

For a hadron-like event with its reconstructed energy E_i, reconstructed zenith angle z_i, and reconstructed camera offset θ_i, for which the statements $E_i \epsilon \Delta E$ and $z_i \epsilon \Delta z$ are true and a set of $\alpha(\Delta E, \Delta z, \theta)$ is available in the LuT, the interpolated template correction β_i is calculated through

$$\begin{aligned} \beta_i(\theta_i) &= \frac{\theta_{\text{high}} - \theta_i}{\theta_{\text{high}} - \theta_{\text{low}}}\alpha(\theta_{\text{low}}) + \frac{\theta_i - \theta_{\text{low}}}{\theta_{\text{high}} - \theta_{\text{low}}}\alpha(\theta_{\text{high}}) \\ &= c_{\text{low}}\alpha_{\text{low}} + c_{\text{high}}\alpha_{\text{high}}, \end{aligned} \tag{4.2}$$

with $c_{\text{low}} + c_{\text{high}} = 1$ and where θ_{low} and θ_{high} are next neighbours of θ_i and mark location of the respective nodes α_{low} and α_{high}. The respective errors are $\sigma(\alpha_{\text{low}})$ and $\sigma(\alpha_{\text{high}})$. It is assumed that the errors on θ_i are negligible. The interpolation along the nodes is depicted in Figure 4.3 as dashed line.

In principle, the error on the interpolation can be calculated through a simple error propagation. This leads to a smaller statistical error compared to the statistical errors on the nodes since the knowledge of the interpolated quantity becomes more precise based on the two reference points. However, from an analysis point of view, the assumption of linear dependence between a pair of nodes may not adequately represent the *real* template correction. In addition, the nodes are subject to statistical fluctuations and the resulting line of interpolation could be tilted. The error propagation cannot account for these cases

and underestimates the *real* uncertainty on β_i. Hence, although the statistical errors on α can be low, the interpolation might be incorrect. Following example should explain the issue in simple words (see Figures 4.1 and 4.3):

Statistics tells us that on average (i.e. considering all intervals $\delta\theta$ for $(\Delta E, \Delta z)$) the calculated α values represent the *real* template correction sufficiently well, but statistical outliers may still be present. Since sources are normally observed at specific and fixed wobble offsets that correspond to matching values of camera offset, a source is therefore mostly corrected by one or two intervals of the camera offset per $(\Delta E, \Delta z)$. If one of them contains a statistically significant outlier, the calculated template correction is incorrect for *all* events falling in this bin. This leads to an overprediction or underprediction of the background and possibly to residuals in the final spectrum. The statistical error would not account for this *miscorrection*.

For TBS, the uncertainty of the interpolation is therefore estimated by the $1\,\sigma$ envelope ϵ around the nodes (grey-shaded area in Figure 4.3):

$$\epsilon(\theta_i) = c_{\text{low}}\sigma(\alpha_{\text{low}}) + c_{\text{high}}\sigma(\alpha_{\text{high}})\,. \tag{4.3}$$

As the *a priori* binning might not be optimal, a reference set of template correction is calculated. This reference, $\alpha_{\text{shift}}(\Delta E, \Delta z, \theta + \frac{1}{2}\delta\theta)$, is calculated with the same requirements as α, but the camera-offset intervals are shifted by half a width (red diamond markers in Figure 4.3). Assuming that the normal set of α represents the real template correction sufficiently well then, in most cases, the shifted set α_{shift} should be within the $1\,\sigma$ area. Hence, α_{shift} is used to identify potential *more-than-*1σ *outliers* and is used as uncertainty estimate if it lies outside the $1\,\sigma$ envelope. For data sets with low event statistics within $(\Delta E, \Delta z, \theta)$, these outliers will be most likely of statistical nature, whereas these outliers in data sets with high event numbers (here, statistical errors are negligible) may be a systematic effect (of the binning in the analysis or of the camera acceptance of the IACT). Whenever α_{shift} does not lie within ϵ, the distance $\nu = \left|0.5(\alpha_{\text{low}} + \alpha_{\text{high}}) - \alpha_{\text{shift}}\right|$ is used as the error estimate:

$$\sigma(\beta_i) = \max(\epsilon, \nu)\,. \tag{4.4}$$

In most cases, α_{shift} lies indeed within ϵ and showing that the linear interpolation between the nodes is a good approximation. However, at $\theta = 1.5°$ (see Figure 4.3) the interpolation differs w.r.t. the shifted set and for this, the error estimate is determined through Equation 4.4 to be $\sigma(\beta_i) = \nu$.

4.3.2 EXTRAPOLATION

In data sets, in which relatively few events in the FoV are available, a complete set of α cannot be calculated for all $(\Delta E, \Delta z)$ intervals and therefore β_i cannot be always estimated through Equation 4.2. The reason may be a large signal region, many known TeV sources in the FoV to be excluded, simply less exposure, or the correlation between energy and camera offset. In any case, grid points in the LuT remain empty and the template correction is determined based on the closest known entry. The uncertainties on the real shape of the template correction discussed in Section 4.3.1 now have a stronger impact. In TBS,

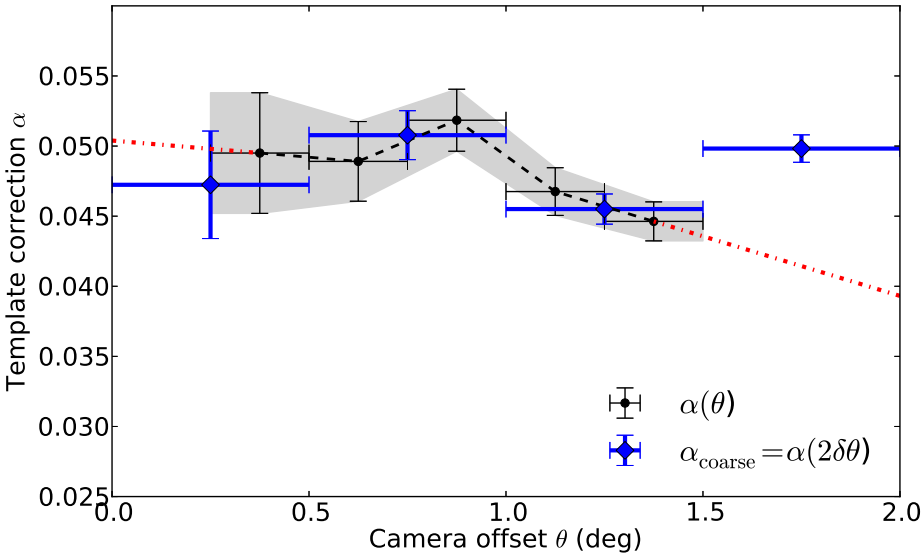

FIGURE 4.4 Example of an extrapolation for TBS based on the same data as in Figure 4.3, but with some data points hidden to highlight the extrapolation task. The additional nodes α_{coarse} (blue diamonds) are used to extrapolate the template correction to lower or higher offsets.

mainly three cases occur, in which the template correction has to be determined through extrapolation.

CASE 1 If an event with offset θ_i does not lie between two nodes, but within the original bin for which a regular $\alpha(\Delta E, \Delta z, \theta)$ could be calculated, its value and error, α_{next} and $\sigma(\alpha_{\mathrm{next}})$, respectively, are taken as estimate:

$$\beta_i(\theta_i) = \alpha_{\mathrm{next}} \pm \sigma(\alpha_{\mathrm{next}})\,. \tag{4.5}$$

CASE 2 If θ_i lies outside α_{next}, a different approach is used. For this, coarser-binned sets of α are calculated with each exhibiting a bin width doubled w.r.t. the initial binning $\delta\theta$. The coarser values, $\alpha_{\mathrm{coarse}}(\Delta E, \Delta z, 2\delta\theta)$, are used as an indicator for the shape of α.

In Figure 4.4, the same $\alpha(\theta)$ is plotted as in Figure 4.3, but with some of the α nodes discarded in order to show the general problem of extrapolation task in TBS. An extrapolation based on the next-closest regular computed α node would lead to a wrong estimate of the correction (compare the red dashed-dotted line with the blue diamond markers): at lower offsets, one tends to overpredict the template correction, whereas the shape at larger offsets suggests a lower value, thus gravely underpredicting the correction. Not accounting for this, could lead to an overprediction of the excess events (when underpredicting β) or an underprediction of the excess events (when overpredicting β). The quantities α_{next} and α_{coarse} are used to estimate the template correction:

$$\beta_i(\theta_i) = \frac{1}{2}(\alpha_{\mathrm{next}} + \alpha_{\mathrm{coarse}})\,. \tag{4.6}$$

As they are mostly not statistically independent, error propagation of Equation 4.6 is not possible. Therefore, the relative error of α_{next} is taken as estimate:

$$\sigma(\beta_i) = \beta_i \frac{\sigma(\alpha_{\text{next}})}{\alpha_{\text{next}}} \,. \tag{4.7}$$

If the bin width of the coarser reference sets are larger than a factor 2 (i.e. 4 or 8), the error estimate is set to account for this larger uncertainty:

$$\sigma(\beta_i) = \beta_i \max\left(\frac{\sigma(\alpha)}{\alpha}\right) , \tag{4.8}$$

where the maximum relative error of the regularly-computed α in the $(\Delta E, \Delta z)$ bin is used.

Case 3 If less than two regularly computed nodes remain within $(\Delta E, \Delta z)$, the extrapolation is not carried out. If an *effective* template correction for this energy bin can be calculated (introduced in the following section), that correction value and its error are used as the estimate. In the unlikely event of that not being possible, the entire energy bin is discarded from the further analysis and not used later on in the spectral reconstruction (see discussion in Section 4.4).

4.3.3 Effective TBS Correction

After the computation of the event-wise correction factors β_i through interpolation and extrapolation, the task is to combine those $(\Delta E, \Delta z, \theta)$-dependent quantities into a solely energy-dependent expression to be used in the spectral reconstruction. For this, an effective correction factor within each energy bin is calculated, which is used later on to estimate uncertainty on the excess counts and also to constitute a quantity to be comparable with the background normalisation of other background-estimation methods.[i]

For m hadron-like events from the signal region within a zenith-angle interval Δz_j of altogether n zenith-angle intervals for fixed energy bin ΔE, every event with its template-correction value $\beta_{i,j}$ (determined via Equations 4.2, 4.5, or 4.6), the effective correction per energy bin ΔE is:

$$\beta_{\text{eff}}(\Delta E) = \frac{\text{corrected hadrons}}{\text{hadrons}} = \frac{\sum_j^n \sum_i^m \beta_{i,j}(\Delta E, \Delta z_j, \theta_i)}{N_{\text{h}}^{\text{s}}(\Delta E)} \,, \tag{4.9}$$

where $N_{\text{h}}^{\text{s}}(\Delta E)$ is the total number of hadron-like events within ΔE. The individual β_i are statistically not independent. Therefore, an error propagation of Equation 4.9 is not permitted and an alternative method is introduced.

In Figure 4.5, H.E.S.S. data on Vela X are used to create a histogram of the calculated estimated template-correction values β (top panel). The energy range is 1 to 1.3 TeV and consists of data from three zenith-angle intervals: $\Delta z_{j=1} = 20° - 30°, \Delta z_{j=2} = 30° -$

[i] In TBS, the best-fit spectrum is also determined using a χ^2 minimisation, which requires an error estimate (see Section 4.4).

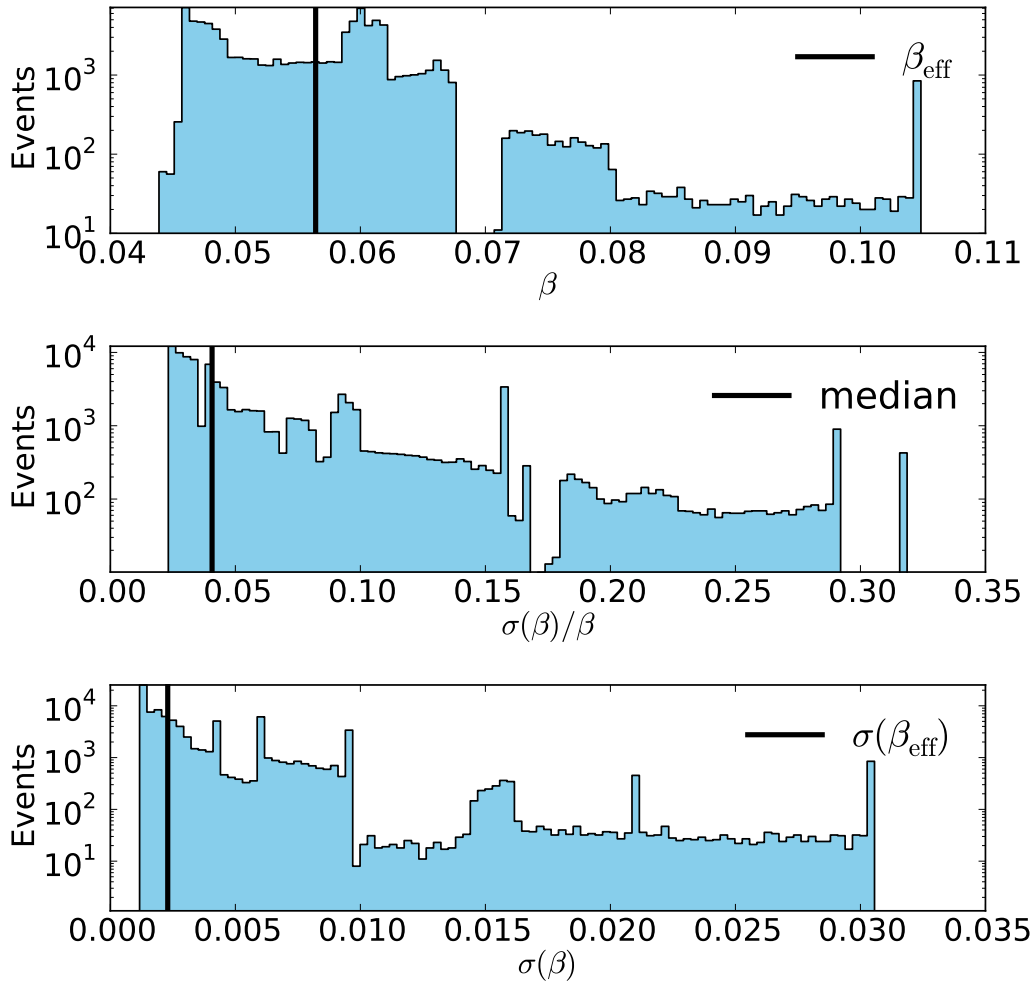

FIGURE 4.5 Sample of β from H.E.S.S. data on Vela X (Abramowski et al., 2012b) for $\Delta E = 1-1.3$ TeV including data from the zenith-angle ranges $(20°, 30°)$, $(30°, 40°)$, and $(40°, 45°)$. **TOP:** Sample of corrected hadrons β after interpolation and extrapolation. The respective value β_{eff} is marked by the black line. **MIDDLE:** Sample of relative error. Marked by the black line is the median relative error used to calculate $\sigma(\beta_{\mathrm{eff}})$. **BOTTOM:** Sample of the absolute errors. Marked is the value of $\sigma(\beta_{\mathrm{eff}})$, which is estimated through the median relative error (black line in the middle plot).

$40°$, and $\Delta z_{j=3} = 40° - 45°$. The respective β_i values are found to be overlapping and stretched out over the entire parameter range. For the two lower zenith-angle bins, the template correction is $0.05 < \beta_i(\Delta z_{j=1,2}) \lesssim 0.07$. This is expected since the zenith-angle dependence of the template correction is rather weak for small zenith angles (Sect. 4.2.3). For the third interval, $0.04 < \beta_i(\Delta z_{j=3}) < 0.11$ is found, which means the values calculated for this zenith-angle interval cover the entire range in β.

For different energy ranges and zenith-angle bands, the distributions will differ in shape and clustering and it is therefore not obvious, what the *best* means is to quantify the error. Therefore, as a robust approach, the median of the distribution of the relative errors, $\sigma(\beta_i)/\beta_i$, is taken to determine the error on β_{eff}:

$$\sigma(\beta_{\text{eff}}) = \beta_{\text{eff}} \,\text{median}\left(\frac{\sigma(\beta_i)}{\beta_i}\right). \tag{4.10}$$

In the middle panel of Figure 4.5, the histogram of the relative errors is shown with its derived median value. These errors span a range from $\sim 2\,\%$ to $32\,\%$, for which the median is found to be at $4\,\%$. For comparison, the absolute errors of the respective template corrections are given in the bottom panel together with the calculated $\sigma(\beta_{\text{eff}})$. Here, they span a dynamical range of 30 (0.001 to 0.031).

Similar to other background normalisation, one can derive an energy-averaged and parameter-integrated overall correction for TBS. Essentially, this means the sum over all q energy bins is added to Equation 4.9:

$$\alpha_{\text{TBS}} = \frac{\sum_k^q \sum_j^n \sum_i^m \beta_{ijk}(\Delta E_k, \Delta z_j, \theta_i)}{\sum_k^q N_{\text{h}}^{\text{s}}(\Delta E_k)}. \tag{4.11}$$

This α_{TBS} can be used to compare with the background-normalisation factors of other background-estimation methods.

4.3.4 EXCESS EVENTS

After correction of the data and determination of β_{eff}, the excess events are calculated through

$$N_{\text{excess}}(\Delta E) = N_{\text{g}}^{\text{s}}(\Delta E) - \sum_j^n \sum_i^m \beta_{i,j}(\Delta E, \Delta z_j, \theta_i), \tag{4.12}$$

and with Equation 4.9:

$$N_{\text{excess}}(\Delta E) = N_{\text{g}}^{\text{s}}(\Delta E) - \beta_{\text{eff}} N_{\text{h}}^{\text{s}}(\Delta E). \tag{4.13}$$

The corresponding error on the excess counts is then:

$$\sigma(N_{\text{excess}}) = \sqrt{N_{\text{g}}^{\text{s}} + \beta_{\text{eff}}^2 N_{\text{h}}^{\text{s}} + \left(\sigma(\beta_{\text{eff}}) N_{\text{h}}^{\text{s}}\right)^2}. \tag{4.14}$$

For most background-estimation methods, the third term of Equation 4.14 (i.e. the error on the background normalisation) is negligible and generally not considered. For TBS, $\left(\sigma(\beta_{\text{eff}}) N_{\text{h}}^{\text{s}}\right)^2$ includes not only the statistical errors on the calculation, but also the systematic uncertainties of the interpolation and the extrapolation (discussed above), and both may of them may not always be negligible. The importance and impact of this additional term will be discussed on the basis of the results on analysed H.E.S.S. data.

4.4 SPECTRAL RECONSTRUCTION

The spectral parameters of the VHE γ-ray source are determined by comparing an expected distribution of excess counts (based on the instrument response of the IACT) with the derived TBS excess. This procedure is called *forward folding* and requires a good knowledge of the effective area (the collection area in which an air-shower event can be detected) and the energy resolution (probability of a simulated event of energy E to be reconstructed at energy E') of the IACT. Besides, for TBS, an analysis energy threshold has to be determined (see Section 4.2). This set is called instrument response (IR).

The two spectral shapes implemented are a simple power law (Eq. 4.15) and a power law with an exponential cutoff (Eq. 4.16).

$$\frac{d\Phi}{dE}(\Phi_0, \Gamma) = \Phi_0(1\,\mathrm{TeV}) \left(\frac{E}{1\,\mathrm{TeV}}\right)^{-\Gamma} \tag{4.15}$$

$$\frac{d\Phi}{dE}(\Phi_0, \Gamma, \lambda) = \Phi_0(1\,\mathrm{TeV}) \left(\frac{E}{1\,\mathrm{TeV}}\right)^{-\Gamma} \exp\left(-\lambda\, E\right), \tag{4.16}$$

where Φ_0 is the flux normalisation at 1 TeV in units of $\mathrm{TeV}^{-1}\,\mathrm{m}^{-2}\,\mathrm{s}^{-1}$, Γ the (dimensionless) power-law index, and λ the inverse cutoff in units of TeV^{-1}. Based on these spectral shapes predicted number of excess events is calculated.

4.4.1 FORWARD FOLDING

The run-wise predicted events n_{pred} for an energy bin ΔE are calculated for an assumed spectral behaviour, e.g. a simple power law $d\Phi/dE = \Phi_0\, E^{-\Gamma}$, where $\Psi = \Psi(\Phi_0, \Gamma)$ are the spectral parameters that need to be determined. Following the approach in Arnaud (1996), the predicted excess events per observation and fixed energy bin ΔE is defined by

$$n_{\mathrm{pred}}(E', \Psi) = T\, \Sigma(E \mapsto E', z_{\mathrm{obs}}, \omega_{\mathrm{obs}})\, A_{\mathrm{eff}}(E, z_{\mathrm{obs}}, \omega_{\mathrm{obs}}) \int dE \frac{dN}{dE}(E, \Psi), \tag{4.17}$$

where A_{eff} and Σ are the effective area and the energy resolution, respectively and that are determined for the wobble offset ω_{obs} and the zenith angle z_{obs} of the observation. For l observation runs, the total expected number of events is calculated through $N_{\mathrm{pred}} = \sum_i^l n_{\mathrm{pred},i}(E' > E_{\mathrm{thres},i})$, where $E_{\mathrm{thres},i}$ is the aforementioned energy threshold per observation. This energy threshold is applied to the observation data and therefore must be applied here as well.

Now, it is possible to determine the set of Ψ that leads to the best match of the predicted and observed excess counts.

4.4.2 CHI-SQUARE MINIMISATION

The χ^2 minimisation implemented in the TBS framework is similar to the approach in Arnaud (1996). To determine the best set of spectral parameters Ψ describing the observed excess-event distribution of the source (N_{excess}), the Ψ is searched that minimises

the following expression for all q energy bins ΔE:

$$\chi^2(\Psi) = \sum_{i=1}^{q} \frac{\left(N_{\mathrm{excess},i}(\Delta E_i) - N_{\mathrm{pred},i}(\Delta E_i, \Psi)\right)^2}{\sigma_i \left(N_{\mathrm{excess},i}(\Delta E_i)\right)^2}\,, \tag{4.18}$$

where $N_{\mathrm{excess},i}$ and its error $\sigma_i\left(N_{\mathrm{excess},i}\right)$ are calculated through Equations 4.13 and 4.14, respectively.

The advantage of this method is that it accounts for the individual uncertainties, and therefore the assumptions on the uncertainty of the TBS correction are included in the fit procedure. In addition, this method naturally provides a goodness-of-fit. In general, one aims to obtain $\chi^2/n_{\mathrm{dof}} \approx 1$ (a detailed discussion is found in Andrae et al., 2010), where n_{dof} is the number of degrees of freedom; it is the difference between the number of data points and the model parameters of Ψ (in Eq. 4.18: $n_{\mathrm{dof}} = q - 2$, for a power law).

Gaussian statistics are required in the calculation and error propagation of α and β_{eff}, but also in Equation 4.14 for the gamma-like and hadron-like events. Therefore, the best-fit spectrum is obtained by only considering energy bins of Gaussian statistics from the signal region and in the calculation of the template correction.

4.4.3 Maximum likelihood

Following Piron et al. (2001), the likelihood function depends on the spectrum and the expected background events $\tilde{N}_{\mathrm{h}}$ and is the product of the Poissonian probability distributions of gamma-like events N_{g} and the hadron-like events N_{g} from the signal region:

$$\mathcal{L}(\Psi, \tilde{N}_{\mathrm{h},i}) = \prod_{i=1} \mathcal{P}(N_{\mathrm{g},i})\mathcal{P}(N_{\mathrm{h},i})\,, \tag{4.19}$$

where the predicted hadron-like events are determined by maximisation of $\mathcal{L}$. As a result, the best-fit spectral shape Ψ is determined by maximising

$$\log \mathcal{L}(\Psi) = \sum_{i=1}^{q} \left(\tilde{N}_{\mathrm{g},i} \log(N_{\mathrm{pred},i} + \beta_{\mathrm{eff},i}\tilde{N}_{\mathrm{h},i}) + N_{\mathrm{h},i} \log(\tilde{N}_{\mathrm{h},i}) - a_i\tilde{N}_{\mathrm{h},i} - N_{\mathrm{pred},i}\right)\,, \tag{4.20}$$

where $a_i = \beta_{\mathrm{eff},i} + 1$ and $\tilde{N}_{\mathrm{g},i}$ is the number of predicted gamma-like events from the signal region:

$$\tilde{N}_{\mathrm{g},i} = N_{\mathrm{pred},i} + \beta_{\mathrm{eff},i}\tilde{N}_{\mathrm{h},i}\,. \tag{4.21}$$

As above, the total number of predicted excess events $N_{\mathrm{pred},i}$ is the sum of the predicted excess events per run (Eq. 4.17). The number of predicted hadron-like events $\tilde{N}_{\mathrm{h},i}$ is calculated through:

$$\tilde{N}_{\mathrm{h},i} = (2a_i\beta_{\mathrm{eff},i})^{-1} \left(b_i + \sqrt{b_i^2 + 4a_i\beta_{\mathrm{eff},i}N_{\mathrm{h},i}N_{\mathrm{pred},i}}\right)\,, \tag{4.22}$$

where

$$b_i = \beta_{\mathrm{eff},i}\left(N_{\mathrm{g},i} + N_{\mathrm{h},i}\right) - a_iN_{\mathrm{pred},i}\,. \tag{4.23}$$

In the TBS framework, the likelihood method is the standard approach to reconstruct the spectral properties of a source. It does not need Gaussian statistics and the specifically calculated errors, therefore the spectral reach can extended to higher energies. However, both methods can be used to estimate the systematic error of the TBS method.

EXTRAPOLATION (CASE 3)

In Section 4.3.2, it was discussed that it is sometimes not possible to determine the effective template correction for an energy bin. In this case, the excess counts (Eq. 4.13) cannot be determined and the respective energy bin ΔE is omitted in Equations 4.17,4.18, 4.20. However, the omission of a single bin does not constitute a problem in the forward folding because this method is rather insensitive to the actual choice of bins and their content. One may expect a bias in the spectral-shape determination if too many bins are discarded or if energy bins are missing around a spectral feature (e.g. spectral break or cutoff in energy).

4.4.4 BUTTERFLY PLOTS

The aim of the forward-folding method is the determination of the spectral parameters and not actually flux points.[i] Therefore, flux points can be obtained by scaling the residuals of the fit ($N_{\mathrm{excess}} - N_{\mathrm{pred}}$) to the expected flux. Since the binning in energy is rather fine, these flux points are usually not significant for most sources. It is possible to rebin the spectrum and re-calculate the excess and the flux points for this coarser binning. However, this is not done nor aimed for in present study of TBS.

Therefore, the $1\,\sigma$ uncertainty of the spectrum is depicted for every differential energy spectrum obtained with TBS (this area is often called *butterfly* or *bow-tie*). This uncertainty is determined through the full error propagation of the parameters of the spectral shape (Eqs. 4.15 and 4.16) and accounting for their correlation. For legibility reasons, $d\Phi/dE = \Phi'$ is chosen. The $1\,\sigma$ error around the best-fit of the spectrum is then

$$\sigma\left(\Phi'\right) = \sqrt{\sum_{i=1}^{m}\left(\frac{\partial\Phi'}{\partial\Psi_i}\sigma\left(\Psi_i\right)\right)^2 + 2\sum_{i=1}^{m-1}\left(\frac{\partial\Phi'}{\partial\Psi_i}\frac{\partial\Phi'}{\partial\Psi_{i+1}}\right)\mathrm{cov}\left(\Psi_i, \Psi_{i+1}\right)}\,, \tag{4.24}$$

where $\sigma\left(\Psi_i\right)$ is uncertainty of the parameter Ψ_i and $\mathrm{cov}\left(\Psi_i, \Psi_{i+1}\right)$ the covariance between the parameters Ψ_i and Ψ_{i+1}.

[i] This is aimed at in the backward-folding approach (Sect. 3.3.9).

4.5 APPLICATION TO H.E.S.S. DATA

In the preceding sections, the concept of the TBS method was explained. It was discussed how the background normalisation changes with energy, zenith angle, and camera offset and what assumptions are made to determine to calculate the excess counts and the respective uncertainties. Although H.E.S.S. data were used, the assumptions made and the implications drawn apply to the analysis of IACT data in general.

In this section, TBS is tested and cross-checked with the H.E.S.S. analysis package (HAP, version `12-03_pl02`). As H.E.S.S. data (DST version `12-03`) were used to develop TBS, the parameter values and ranges stated from here on apply only to H.E.S.S. data. However, a simple adjustment of ranges and parameter settings should suffice for the analysis of other IACT data (given the available MC data as well). Moreover, any gamma/hadron separation (in parameter space) can be used in TBS to distinguish γ rays and the hadron-like background.

In the following, the generation of the IR to be used in TBS is presented before the results on H.E.S.S. data and the implications for TBS are discussed later on. In Appendix A.2, the framework of TBS that was developed and programmed in this thesis is presented along with the tools of the analysis chain and a short description.

4.5.1 INSTRUMENT RESPONSE

The response of the telescope array to an air-shower event has to be well understood in order to draw conclusions on the nature of the analysed source. With the detector response, it is possible to determine energy spectra and fluxes. It is required in the reconstruction of the spectrum, but also earlier in the analysis when the energy threshold cut is applied.

For TBS, existing H.E.S.S. MC data were reprocessed to produce a complete new set of IR data for the forward folding, and therefore a few more words are spent on MC data and the IR.

MONTE CARLO DATA For TBS, H.E.S.S. MC data were used to calculate the IR data for γ rays. The H.E.S.S. nomenclature for these MC data is `phase1b_desert`. They were produced for the four-telescope array for the reference time November 2005 when the optical efficiency of the telescopes was determined to be around $\sim 70\,\%$. The applied muon correction is used to scale the efficiency to these MC data. The MC data are produced by simulating events of certain parameters like energy, zenith angle and offset from the camera centre, but also for the telescope configuration and atmospheric conditions resembling the atmosphere over Namibia.

The H.E.S.S. MC data were simulated for a seed differential-energy spectrum with a power-law index of 2 from an energy of 10 GeV onwards, for wobble offsets up to 3°, and for zenith angles up to 70°. The bin width in zenith angle accounts for the increasing solid angle and the larger path to be traversed through the atmosphere and is therefore roughly equally-spaced in $\cos z$. These simulations were done for an azimuth angle of 0° (north) and 180° (south) to account for the orientation of the Earth's magnetic field

affecting the expected CR flux. These simulated events are then compared with those detected and reconstructed by running the reconstruction algorithms in use to analyse real data. In doing so, it is possible to determine the characteristics of the telescope array and how the detector responds to an air-shower event as a function of energy, zenith angle, offset, telescope multiplicity, and azimuth angle. Based on these MC data provided by the H.E.S.S. collaboration, selection criteria are determined to define a γ-ray event.

GAMMA-RAY EVENTS The so-called *standard cuts* as defined in Aharonian et al. (2006a) were applied meaning that the individual images had to contain at least 80 p.e. after the 5/10 image cleaning (see Section 3.3.4.1). Gamma-like events are those that pass the cut on the Hillas parameters MRSW and MRSL. The allowed parameter ranges are $-2 < \mathrm{MRSW} < 0.9$ and $-2 < \mathrm{MRSL} < 2$. Additionally, the maximum-allowed impact parameter was set to 1000 m.

According to this γ-ray selection, the H.E.S.S. MC data were reprocessed to calculate IR for TBS. Two sets of IR data were generated for different source radii θ_{src}:

- for a point source with $\theta_{\mathrm{src}} \approx 0.11^\circ$ and
- a *full enclosure* data set without a θ_{src} cut for extended sources.

The IR data were produced for an energy range from 100 GeV to 100 TeV in 60 intervals on a logarithmic energy scale. The zenith-angle range is 0° to 55° and the wobble offsets range from 0° to 2.5°. All IRs were produced for the standard cuts, for both mentioned azimuth angles and only for the full four-telescope array. This set of the IR is chosen as it assures a high-quality data of the H.E.S.S. IACT (good energy resolution and a low energy threshold).

HADRON EVENTS MC simulations of hadrons were not used in this work and are conceptionally not needed. The idea of this method foresees that the TBg normalisation accounts for the relative difference between γ-ray and hadron events (see Sect. 4.1).

Hadron-like events are defined by $5 < \mathrm{MRSW} < 20$, without a cut on the MRSL parameter, but otherwise with the same selection cuts for the gamma-like events. This range is set to have a rather clean hadron sample without any contamination from γ rays and sufficient statistics. However, as the hadron-like events from the signal region and in the FoV are identically binned and processed, differences or inaccuracies due to the chosen MRSW range are on average cancelled out.

With the selection for γ rays, the IR data are calculated for the available parameter ranges. These IR data are presented in the following.

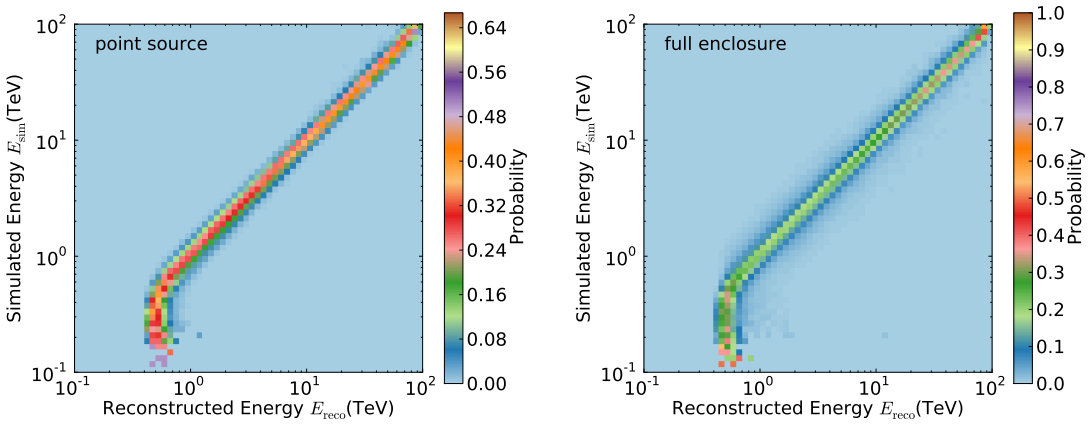

FIGURE 4.6 The energy-resolution matrices with simulated energy vs. the reconstructed energy for a simulated wobble offset of 0.5° and a zenith angle of 45° for the northern hemisphere. **LEFT:** The energy-resolution matrix for a point source. **RIGHT:** The energy-resolution matrix for the case of a extended source (full enclosure).

4.5.1.1 ENERGY RESOLUTION

The energy resolution is not perfect, the energies of reconstructed events are mostly scattered around the simulated value. To estimate this spread, the simulated and reconstructed energies are directly compared.

For the forward folding, the energy resolution is produced as a normalised 60 × 60 matrix. In this matrix $\Sigma(E_{\mathrm{sim}} \mapsto E_{\mathrm{reco}})$, the probability is contained that an event with a simulated energy E_{sim} is reconstructed at an energy E_{reco}. In Figure 4.6, it is shown that the H.E.S.S. energy reconstruction is sufficiently precise (the diagonal through the matrix has a relatively small width). However, at low energies the energy reconstruction fails to estimate the correct energy. The reason is that these images are too faint for a precise reconstruction and therefore, all events at these low energies fall more or less into the same reconstructed-energy bin. Hence, the sensitivity towards lowest energies deteriorates and the energy at which this occurs is zenith angle and offset dependent. The spread around the simulated energies becomes larger for the full-enclosure data because events with a poorer energy estimate and otherwise discarded with the cut on angular distance are now included in this data set.

MUON CORRECTION The optical efficiency of the IACT deteriorates with time and causes a shift of the diagonal in the energy-resolution matrix. Therefore, a correction to the matrix has to be done. The muon correction of the energy-resolution matrix Σ is simply a shift of the matrix entries along the diagonal, which means:

$$\Sigma'(E_{\mathrm{sim}} \mapsto E_{\mathrm{reco}}) = \Sigma(\mu_{\mathrm{corr}} E_{\mathrm{sim}} \mapsto \mu_{\mathrm{corr}} E_{\mathrm{reco}})\,. \tag{4.25}$$

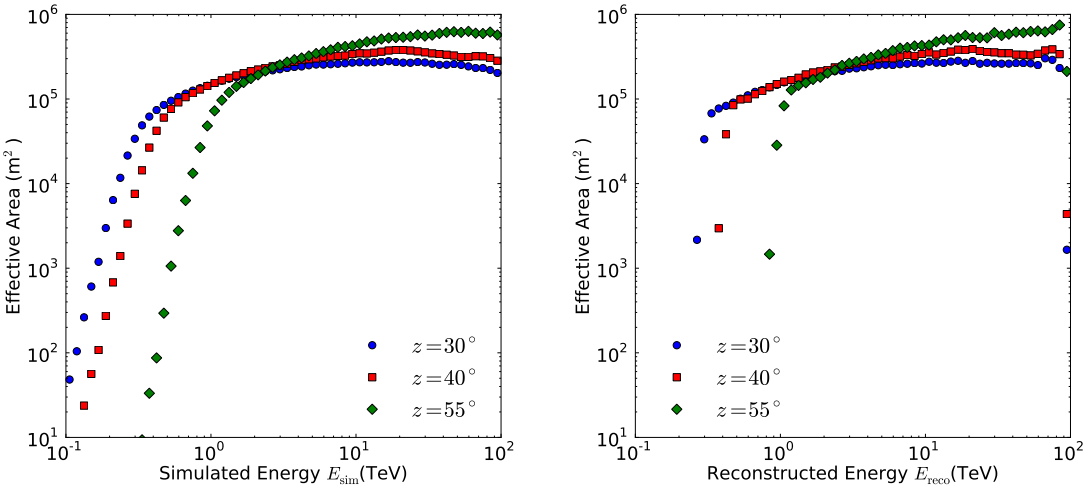

FIGURE 4.7 Effective area calculated for a simulated wobble offset of 0.5° for three different simulated zenith angles (southern hemisphere). **LEFT:** The effective areas are shown as function of the simulated energy. **RIGHT:** The effective areas are shown as function of the reconstructed energy.

4.5.1.2 EFFECTIVE AREA

The effective area A_{eff} of an IACT is the detection area, in which an event can be detected. This area is much larger than the detector itself as the events are not directly detected, but only their induced light pool. The effective area for γ-ray events is defined as:

$$A_{\text{eff}}(E, z, \omega, a) = \frac{N_{\text{reco}}(E, z, \omega, a, \Upsilon)}{N_{\text{sim}}(E, z, \omega, a)} \pi R_{\text{max}}^2 \,, \tag{4.26}$$

where E, z, ω, a indicate the energy, the zenith angle, the wobble offset, and the azimuth-angle dependence of the A_{eff} and R_{max} is the maximum impact distance, for which the MC events N_{sim} were simulated. The number of events that were reconstructed and survived the γ-ray event selection (Υ) is N_{reco}. For a given set of simulation parameters (z, ω, a), the effective area is a function of energy. On average, the effective area is about 10^5 m^2.

In Figure 4.7, the effective area for three different zenith angles is depicted as function of the simulated energy and the reconstructed energy. The latter is determined by folding the respective energy resolution with the simulated effective area.

MUON CORRECTION In a first-order approximation, the loss in efficiency is corrected by scaling the energy axis of the effective area with the appropriate muon correction μ_{corr} of the observation:

$$A'_{\text{eff}}(E') = A_{\text{eff}}(\mu_{\text{corr}} E) \tag{4.27}$$

where $A'_{\text{eff}}(E')$ is the muon-corrected effective area.

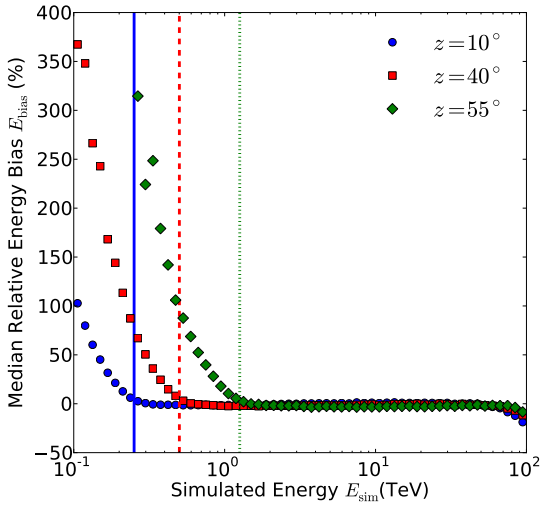

FIGURE 4.8 The median relative energy bias for a point source on the southern hemisphere with a simulated wobble offset of 0.5° and three different zenith angles with the respective energy threshold: 10° (blue circles and solid line), 40° (red squares and dashed line) and 55° (green diamonds and short-dashed line).

4.5.1.3 ENERGY THRESHOLD

In general, the classical forward-folding method does not need an energy threshold cut (assuming a good knowledge of the IACT properties with time and energy). However, for TBS, events with an insufficiently well estimated energy have to be rejected beforehand (see Section 4.1). The energy threshold is determined through the relative energy bias per energy bin:

$$E_{\mathrm{bias}}(z_{\mathrm{sim}}, \omega_{\mathrm{sim}}) = \left| \frac{E_{\mathrm{reco}} - E_{\mathrm{sim}}}{E_{\mathrm{sim}}} \right| (z_{\mathrm{sim}}, \omega_{\mathrm{sim}})\,\mathrm{TeV}\,. \tag{4.28}$$

The energy threshold E_{thres} is the succeeding energy bin of the one, for which the absolute value of median relative bias is smaller than 10 % is found.

In Figure 4.8, the dependence of the relative energy bias and the energy threshold are shown for three different zenith angles. It is clearly visible, that the threshold increases with increasing zenith angle.

Alternative definitions were also tested to define the energy threshold and summarised in Appendix A.4.

MUON CORRECTION The muon correction of the energy threshold is analogously to the treatment of the reconstructed energy in general:

$$E'_{\mathrm{thres}} = \mu_{\mathrm{corr}} E_{\mathrm{thres}}\,. \tag{4.29}$$

The effective areas, the energy thresholds, and the energy-resolution matrices are calculated for fixed zenith angles and wobble offsets. In the analysis of observation data, these IR data have to be calculated for the zenith angle and the wobble offset of the respective run. This is done by a bilinear interpolation and described in Appendix A.3.

4.5.2 ANALYSIS OF H.E.S.S. DATA

In this section, TBS is used on published H.E.S.S. data in order to assess and validate the performance of this new method. At first sources are analysed, for which the RrBg method can be used: the Crab Nebula, Centaurus A, HESS J1745–290 and HESS J1507–622. The findings of TBS are compared to the H.E.S.S. publications and to a re-analysis with HAP because most of the data sets used here vary from the ones used in the original publications.[i] Finally, also spectra of H.E.S.S. sources are reconstructed with TBS, which cannot be analysed with the RrBg: Vela X and Vela Junior.

These sources are located in different FoVs, share different properties, and provide different challenges to the analysis, which will be used to estimate the performance of TBS.

LOOK-UP TABLE The general concept and the generation of the LuT has already been introduced and discussed in Section 4.2. Therefore, the parameter ranges are briefly mentioned in the following.

As for the MC data, the binning in the logarithmic energy scale is either 2, 4, 5, 10 or 20 bins per decade and the 10 bins per decade are the standard value in TBS. This binning is a compromise between allowing for sufficient statistics in the respective bins (split into subintervals of zenith angle and camera offset) and a sufficiently high number of degrees of freedom in the spectral reconstruction.

The binning in the zenith-angle range is chosen to match that of the H.E.S.S. MC data, which means the range is span by the simulated set of zenith angles of $\{0°, 10°, 20°, 30°, 40°, 45°, 50°, 55°, 60°, 63°\}$. Although MC data and observations runs up to a mean zenith angle of 55° are used, these runs still contain events with higher reconstructed zenith angles and therefore the range of the LuT in zenith angle has to extend towards higher values.

The maximum allowed event offset is 2° and the bin width in θ is set to 0.25°. This value is a factor 2 to 3 higher than the energy-averaged PSF for γ rays, but is chosen to be wider to account for the much larger hadronic PSF.

RUN SELECTION Data on the sources were selected using the standard data-quality selection (Aharonian et al., 2006a). This selection discards observations that failed certain criteria w.r.t. the observation (e.g. the pointing accuracy), the hardware (e.g. broken pixels in the camera), the weather (e.g. clouds in the FoV), or basic analysis results (e.g. a too low system trigger rate). Additionally, the runs had to meet the properties of the IR data generated for TBS, which means that only four-telescope runs were considered with a mean run zenith angle $z_{\mathrm{obs}} < 55°$ and a wobble offset $\omega_{\mathrm{obs}} < 2.5°$. H.E.S.S. observation runs are normally $\sim$ 28 mins long, but sometimes aborted earlier to due clouds in the sky or hardware problems. Therefore, the minimum requirement was set to 10 mins.

In the analysis, each run has to contain data from the signal region and also from the FoV (excluding the signal region and other possible sources). With this requirement, *un-*

[i] The results using HAP are to be regarded as preliminary, do not supersede the original published values and are only stated for testing purpose.

TABLE 4.1 Observation properties of re-analysed H.E.S.S. data sets. Stated are the coordinates in right ascension and declination, the radius of the source θ_{src}, the median run zenith angle z_m, the median run wobble offset z_m, and the livetime t.

Source	RA (J2000) deg	Dec (J2000) deg	θ_{src} deg	z_m deg	ω_m deg	t hrs
[a]Crab Nebula	83.633	22.014	0.11	47	0.5	9.7
[b]Centaurus A	201.365	-43.019	0.11	22	0.7	82.4
[c]HESS J1745–290	266.416	-29.008	0.11	18	0.7	90.4
[d]HESS J1507–622	226.720	-62.350	0.22	39	0.7	6.1
[e]Vela X	128.750	-45.600	0.8	25	0.9	54.6
[f]Vela Junior	133.000	-46.367	1.0	34	1.1	12.1

[a]Aharonian et al. (2006a); [b]Aharonian et al. (2009c); [c]Aharonian et al. (2009b); [d]Acero et al. (2011); [e]Abramowski et al. (2012b); [f]Aharonian et al. (2005b).

intended On and *Off* runs are avoided. The signal region has to be fully contained within 2° of the camera centre because a truncated source could lead to a biased analysis, especially for very extended sources. However, for very large sources (e.g. Vela Junior with a radius of 1°), this criterion is loosened a bit. In addition, this cut avoid possible problems with the camera acceptance towards the edge of the FoV. Additionally, for the sources the Crab Nebula, Centaurus A, HESS J1745–290, and HESS J1507–622 runs were chosen which could be analysed with the RrBg in order to directly compare the spectral results TBS.

The selected source and the properties of these data sets are summarised in Table 4.1. The results of the analyses of these sources with the TBg implemented in the TBS framework are given in Table 4.2. The processed data statistics for the spectral forward folding are tabulated in Table 4.3.

EXCLUSION REGIONS For the Galactic sources, other VHE γ-ray sources and potential diffuse emission regions were excluded on the basis of the more sensitive TMVA analysis. Here, γ-ray emission regions are excluded at a $5\,\sigma$ threshold combined with an additional extension of 0.3° (STANDARD-ζ cut, Carrigan et al., 2012).

For extra-Galactic sources and sources far off the inner Galactic Plane, the internal H.E.S.S. source catalogue including so-called *hot spots* (i.e. potential sources) and not-published sources. For these mostly faint point-like sources, the exclusion region is set to 0.2°.

Strong sources ($\geq$ 10 % of the flux of the Crab Nebula in the same energy band) that are not covered by the TMVA exclusion regions are excluding with a radius $\theta_{\mathrm{ex}} = \theta_{\mathrm{src}} + 0.2°$.

Stars in the FoV brighter than 5 magnitudes are excluded with a radius of 0.2° to avoid any effects and biases when creating the LuT.[ii]

[ii]This bright-star list used in TBS was initially generated by Chaves (2009).

TABLE 4.2 Properties of re-analysed H.E.S.S. data sets with the standard TBg model after application of the run-wise energy threshold. The excess-to-background-ratio (EB) is $N_{\mathrm{excess}}/(\alpha_{\mathrm{std}}\, N_{\mathrm{h}}^{\mathrm{s}})$. The significance S is calculated through Equation 3.22.

Source	$N_{\mathrm{g}}^{\mathrm{s}}$	$N_{\mathrm{h}}^{\mathrm{s}}$	α_{std}	N_{excess}	E/B	S σ
Crab Nebula	3770	3629	0.0883	3450	10.77	96.4
Centaurus A	3115	30931	0.0903	323	0.12	5.7
HESS J1745–290	7245	38272	0.0934	3670	1.03	50.8
HESS J1507–622	824	7694	0.0852	169	0.26	6.1
Vela X	114944	1081572	0.0975	9439	0.09	27.3
Vela Junior	37033	353199	0.0922	4482	0.14	23.2

TABLE 4.3 Results of the analysis with TBS. Stated are the event statistics for the energy range for which the background normalisation α_{TBS} could be calculated.

Source	E_{min} TeV	E_{max} TeV	$N_{\mathrm{g}}^{\mathrm{s}}$	$N_{\mathrm{h}}^{\mathrm{s}}$	α_{TBS}	N_{excess}
Crab Nebula	0.63	39.8	3582	3427	0.103	3228
Centaurus A	0.32	39.8	3079	30046	0.094	265
HESS J1745–290	0.25	39.8	7229	37993	0.096	3579
HESS J1507–622	0.63	25.1	775	6983	0.086	172
Vela X	0.79	63.1	112039	1038193	0.105	3474
Vela Junior	0.30	20.0	36044	339308	0.093	4624

CROSS-CHECK ANALYSIS WITH HAP As the analysis in this work differs from the original one done in the respective H.E.S.S. publications (e.g. different data sets, updated calibration and reconstruction, different exclusion regions), the results obtained with TBS were cross checked using the latest HAP framework and the RrBg method to reconstruct spectra – if possible. The same cut in MRSW was used to define gamma-like events in the gamma/hadron separation. Besides the same runlist, the same exclusion regions were used.

The best-fit spectra reconstructed within the HAP framework are determined in a fine-binned maximum log-likelihood approach similar to Piron et al. (2001). Altogether, 108 bins of identical width in energy (in logarithmic scale) are used and range from 10 GeV to above 300 TeV. Because data points obtained in the forward folding are in general not significant, the relative errors on the data points obtained with TBS and HAP are compared to probe the additional uncertainty introduced by TBS. However, in case of non-Gaussian statistics within a bin, no data point is shown.

Because the fit parameters of a spectral shape are correlated, contours of $1\,\sigma$ and $2\,\sigma$ are calculated for the best-fit results of TBS and compared with the results of the cross check and the published H.E.S.S. spectrum. These plots are in Appendix A.5.

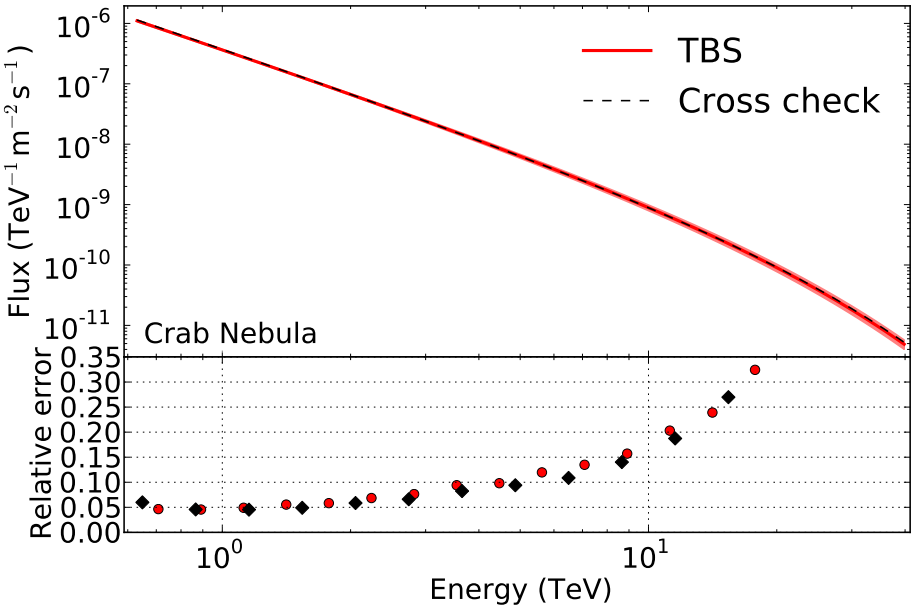

FIGURE 4.9 Results of the forward folding for the Crab Nebula with TBS (red line and circles) and the cross check with the RrBg (black diamonds and dashed line). The red area indicates the 1 σ uncertainty. Missing data points for the relative error indicate non-Gaussian event statistics and therefore these points and the corresponding cross-check values are not calculated.

4.5.2.1 THE CRAB NEBULA

The Crab Nebula (Aharonian et al., 2006a) is one of the best-studied objects in the sky. In TeV γ rays, this PWN is the strongest stable point-like source known so far. This source is chosen because of its high ratio of excess-to-background (EB, i.e. $N_{\mathrm{excess}}/(\alpha_{\mathrm{std}}\, N_{\mathrm{h}}^{\mathrm{s}})$ of about 11, therefore it is a good candidate to test TBS concerning the concept, the analysis chain, and the forward folding; thus the analysis of this source is to be considered a proof-of-concept study. The observations used here span an observation zenith-angle range from 45° to 54°, whereas the wobble offset is constantly at 0.5°. In total, 9.7 hrs are used here (i.e. one hour of fewer data compared to the data set III in Aharonian et al. (2006a)).

The Crab Nebula was best fit with a power law with exponential cut-off in Aharonian et al. (2006a) and therefore, this model assumption was tested. A very good agreement is found for the spectral results for the Crab Nebula obtained with TBS and the cross check with the RrBg method. The errors on the spectral shape and the flux points calculated with TBS and the RrBg method are of the same size (see Table 4.4), Figure 4.9, and Appendix A.4). For TBS, the template correction was mainly determined through interpolation. The analysis using the χ^2-minimisation method in TBS, results in an energy range that ends at 20 TeV due to insufficient Gaussian statistics from the signal region. However, the spectral results are compatible with those of the likelihood approach in TBS.

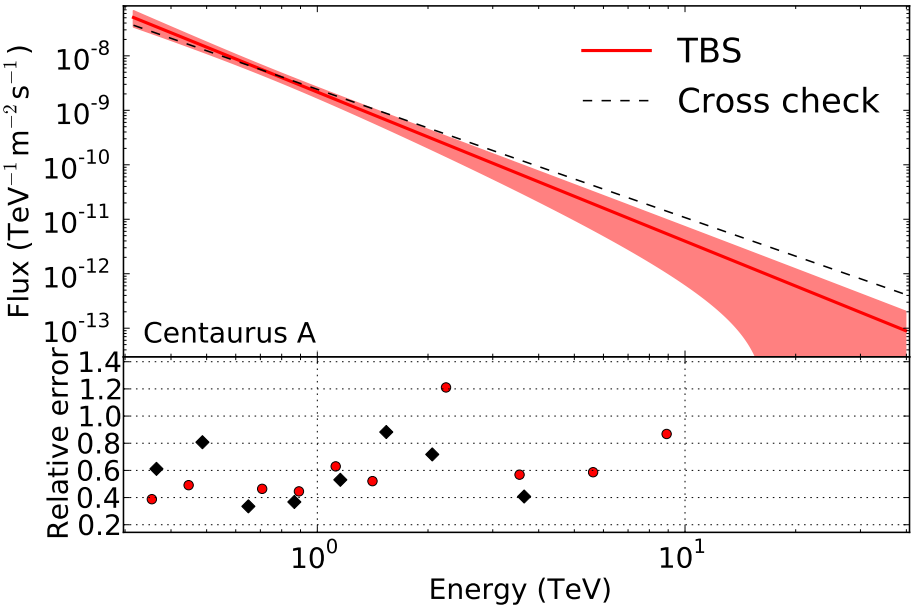

FIGURE 4.10 Results of the forward folding for Centaurus A with TBS (red line and circles) and the cross check with the RrBg (black diamonds and dashed line). The red area indicates the $1\,\sigma$ uncertainty. Missing data points for the relative error indicate non-Gaussian event statistics and therefore these points and the corresponding cross-check values are not calculated. Two TBS and cross-check data points lie outside the zoomed-in range.

4.5.2.2 CENTAURUS A

Centaurus A is a faint extra-Galactic point source with an integrated flux of less than 1 % of the that of the Crab Nebula in the same energy range (Aharonian et al., 2009c) and located in a clear FoV. The data set used in this work, exhibits a comparatively large observation zenith-angle range of 19° to 54°. The wobble positions lie between 0.4° and 0.5°. Compared to the data in Aharonian et al. (2009c), 30 hrs of exposure are missing.

The spectrum of Centaurus A as reported in Aharonian et al. (2009c) is reproduced. Despite the shorter exposure, the uncertainties on the fit results from the TBS and the cross-check analysis are smaller and both spectra extend to higher energies than in Aharonian et al. (2009c). In both cases, this is a direct consequence of the used forward folding and the resulting higher number of degrees of freedom. The overall agreement is good, but the cross-check analysis results in a slightly (but insignificantly) harder power-law index than determined with TBS or found in Aharonian et al. (2009c). The comparison of the best-fit results is found in Table 4.4 and in Figure 4.10. In Figure 4.10, the derived power-law spectra are plotted. For this faint source, most flux points are insignificant and exhibit large errors. The χ^2 evaluation is also sensitive up to $\sim$ 10 TeV at the applied energy binning.

Table 4.4

Analysis	E_{min} TeV	E_{max} TeV	$\Phi_0(1\,\mathrm{TeV})$ $\mathrm{TeV}^{-1}\mathrm{m}^{-2}\mathrm{s}^{-1}$	Γ	λ TeV^{-1}	$F(>E_{\mathrm{min}})$ % Crab	χ^2/n_{dof}
Crab Nebula							
TBS (log $\mathcal{L}$)	0.63	40	$(3.89 \pm 0.10)\,10^{-7}$	2.36 ± 0.05	0.07 ± 0.01	104.8 ± 2.1	–/15
TBS (χ^2)	0.63	20	$(3.82 \pm 0.11)\,10^{-7}$	2.40 ± 0.06	0.05 ± 0.01	104.7 ± 2.1	7.2/12
RrBg (HAP, cross check)	0.63	40	$(3.96 \pm 0.10)\,10^{-7}$	2.38 ± 0.05	0.05 ± 0.01	106.9	–/43
RrBg (HAP, cross check)	0.63	20	$(3.92 \pm 0.11)\,10^{-7}$	2.41 ± 0.06	0.05 ± 0.02	106.9	–/34
RrBg (Aharonian et al., 2006a)	0.45	65	$(3.84 \pm 0.09)\,10^{-7}$	2.41 ± 0.04	0.07 ± 0.01	102.4	12.6/9
Centaurus A							
TBS (log $\mathcal{L}$)	0.32	40	$(2.16 \pm 0.47)\,10^{-9}$	2.74 ± 0.31		0.7 ± 0.2	–/18
TBS (χ^2)	0.32	10	$(2.10 \pm 0.51)\,10^{-9}$	2.74 ± 0.37		0.7 ± 0.2	11.8/12
RrBg (HAP, cross check)	0.32	40	$(2.43 \pm 0.45)\,10^{-9}$	2.35 ± 0.18		0.7	–/50
RrBg (HAP, cross check)	0.32	10	$(2.43 \pm 0.44)\,10^{-9}$	2.47 ± 0.25		0.7	–/35
RrBg (Aharonian et al., 2009c)	0.25	6	$(2.45 \pm 0.52)\,10^{-9}$	2.73 ± 0.45		0.8	12.6/9

Summary of the results on the Crab Nebula and Centaurus A for the different analyses with TBS (maximum log $\mathcal{L}$, χ^2 minimisation), the respective cross-check analyses with HAP, and the published H.E.S.S. spectra. The energy ranges (E_{min},E_{max}) were chosen to match that of the TBS analysis and the cross check. The results on the flux normalisation at 1 TeV (Φ_0), the power law (Γ), the inverse cut-off (λ), the integral flux above E_{min} (in percentage of the Crab Nebula flux above the same energy) are given together with the degrees of freedom and the χ^2 value. Spectra without a χ^2 value were obtained with a maximum log-likelihood approach (Piron et al., 2001); see also Section 4.4.

4.5.2.3 GALACTIC-CENTRE SOURCE HESS J1745–290

HESS J1745–290 is a bright point-like source in the Galactic Centre and regularly observed with H.E.S.S. (Aharonian et al., 2009b). As the H.E.S.S. telescopes are located on the southern hemisphere such that the inner Galactic Plane and the Centre can be observed at very low zenith angles close to the zenith, mean run zenith angles range from 4° up to 54°. It is located in a complex region with many nearby sources, embedded in a large diffuse γ-ray emission region. For the analysis in TBS, this meant that large parts of the FoV are excluded and therefore could not be used to calculate the LuT of α. Due to the diffuse-emission region, this source has been observed in a larger wobble-offset range from 0.7° to 2°.

Runs with $z_{\text{obs}} > 55°$ are not considered due to the range of the MC data used in TBS, but were used in Aharonian et al. (2009b). To make up for this loss of data, $\sim$ 30 hrs of non-HESS J1745–290-dedicated observations runs from the vicinity were included.

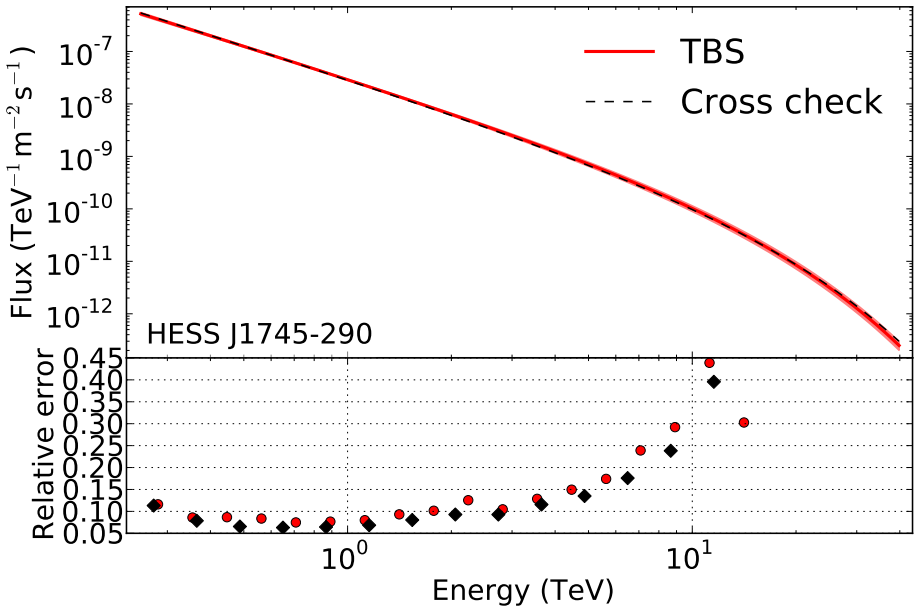

FIGURE 4.11 Results of the forward folding for HESS J1745–290 with TBS (red line and circles) and the cross check with the RrBg (black diamonds and dashed line). The red area indicates the 1 σ uncertainty. Missing data points for the relative error indicate non-Gaussian event statistics and therefore these points and the corresponding cross-check values are not calculated.

In Figure 4.11, the spectra (a power law with exponential cut-off) obtained with TBS and the RrBg method are depicted. The best-fit results of TBS and the cross-check analysis are nearly identical. Moreover, the uncertainty on the spectral parameters are of the same size (see Table 4.5.2.4 and Figure 4.11). However, compared to the published results in Aharonian et al. (2009b), a 20 % higher flux normalisation is found for the results of TBS and the cross-check analysis (see also Figure A.6).

A discussion on the differences of the published spectrum and the two spectra of TBS and the cross check is appended.

DISCUSSION OF OBSERVED DIFFERENCES To test for a selection effect and any variation in the data, subsets of the data were analysed separately with TBS and the RrBg method.

1. The data set was split into two subsets of equal exposure and re-analysed.

2. Only data of HESS J1745–290 -dedicated observations were analysed.

None of these analyses differed significantly from the results presented in Figure 4.11 and Table 4.5.2.4. Hence, the spectra of these subsets analysed with TBS and the cross check are still compatible and therefore still result in a significantly higher flux normalisation than in Aharonian et al. (2009b).

A possible explanation could be the exclusion regions used in this work, which are much larger than in Aharonian et al. (2009b). However, as neither the background normalisation α, the number of OFF regions nor the relevant numbers on $N_{\mathrm{ON}}, N_{\mathrm{OFF}}$ nor the placement of exclusion regions are quoted, it is not possible reproduce the published-analysis configuration in this work. However, it is stated that the OFF regions were not placed within the diffuse-emission regions and that this diffuse emission at a 13 % level was not subtracted The results of analysis with TBS and with HAP, both without excluding the diffuse emission, remained incompatible with Aharonian et al. (2009b). A perhaps more convincing reason could be the improvements in event reconstruction (including the muon correction) and in the analysis chains over the last nearly 10 yrs for H.E.S.S. and also updated MC simulations, especially for the time when the HESS J1745–290 data were taken.

Given the very good agreement between TBS and the cross-check analysis, the difference w.r.t. the published H.E.S.S. results is unlikely to be caused by the analysis chains of TBS and the RrBg in HAP as both chains are totally independent and only rely on the same event reconstruction and the same initial MC data (from which different IR files are generated for TBS and in HAP). Any systematic effect could therefore be related to the event and energy reconstruction.

From an analysis point of view, the deep exposure means that statistical errors are negligible (see also discussion on this in Aharonian et al., 2009b) and the observed differences are due to some (unknown) systematic effect(s) in the analysis with TBS and RrBg method in HAP. However, for this work, the agreement between HAP and TBS is very good.

4.5.2.4 HESS J1507–622

The γ-ray source HESS J1507–622 (Acero et al., 2011) is located at a Galactic latitude of $b \approx -3.5°$ and therefore off the Galactic Plane. With a source radius of 0.22°, HESS J1507–622 is the smallest of the extended sources analysed in this work. The data set used here is comprised of just 6 hrs of observations, which is about 30 % less exposure than used in Acero et al. (2011). The mean run zenith angles are within a narrow band of 38° to 40° and the wobble offsets are all between 0.6° and 0.8°.

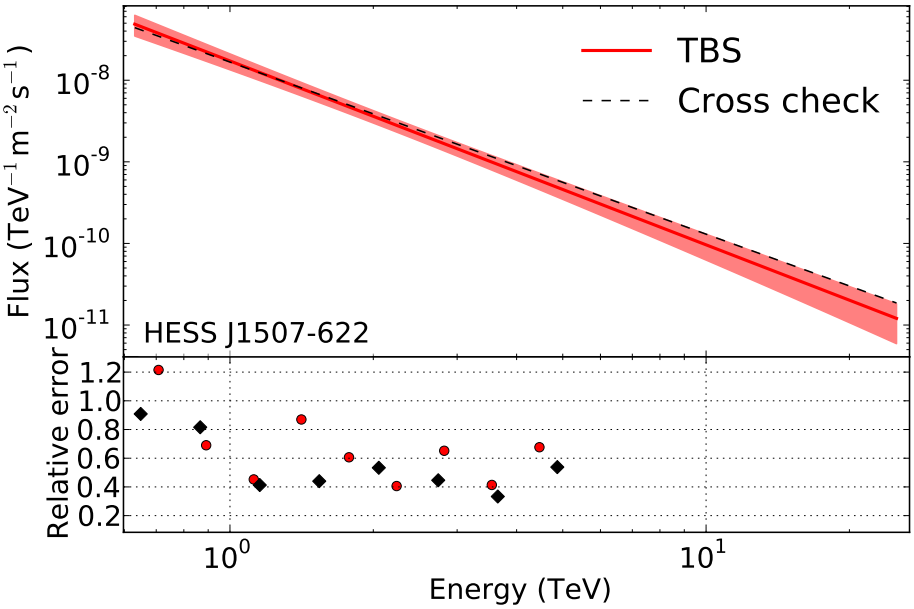

FIGURE 4.12 Results of the forward folding for HESS J1507–622 with TBS (red line and circles) and the cross check with the RrBg (black diamonds and dashed line). The red area indicates the $1\,\sigma$ uncertainty. Missing data points for the relative error indicate non-Gaussian event statistics and therefore these points and the corresponding cross-check values are not calculated. One TBS and some cross-check data points lie outside the zoomed-in range.

In Figure 4.12, the derived differential energy spectrum of a simple power law is shown. Both analysis methods (TBS and RrBg method) are in good agreement, also w.r.t. the reported spectrum in Acero et al. (2011). These results are summarised in Table 4.5.2.4. The correlation plot of the best-fit spectral parameters is shown in Figure A.7. Since only 6 hrs of data were used, there are fewer gamma-like events in the energy bins above 6 TeV and so that the spectrum in TBS using the χ^2 minimisation does not extend to higher energies for the chosen binning in energy.

Table 4.5

Analysis	E_{min} TeV	E_{max} TeV	$\Phi_0(1\,\mathrm{TeV})$ $\mathrm{TeV}^{-1}\mathrm{m}^{-2}\mathrm{s}^{-1}$	Γ	λ TeV^{-1}	$F(>E_{\mathrm{min}})$ % Crab	χ^2/n_{dof}
HESS J1745–290							
TBS (log $\mathcal{L}$)	0.25	40	$(3.22 \pm 0.13)\,10^{-8}$	2.04 ± 0.05	0.11 ± 0.02	6.6 ± 0.2	–/19
TBS (χ^2)	0.25	16	$(3.09 \pm 0.16)\,10^{-8}$	2.08 ± 0.06	0.08 ± 0.03	6.7 ± 0.2	15.9/15
RrBg (HAP, cross check)	0.25	40	$(3.12 \pm 0.12)\,10^{-8}$	2.08 ± 0.05	0.10 ± 0.02	6.7	–/52
RrBg (HAP, cross check)	0.25	16	$(3.09 \pm 0.14)\,10^{-8}$	2.13 ± 0.06	0.08 ± 0.03	6.9	–/41
RrBg (Aharonian et al., 2009b)	0.16	70	$(2.55 \pm 0.06)\,10^{-8}$	2.10 ± 0.04	0.07 ± 0.01	5.0	23/26
HESS J1507–622							
TBS (log $\mathcal{L}$)	0.63	25	$(1.72 \pm 0.38)\,10^{-8}$	2.25 ± 0.19		5.4 ± 1.0	–/14
TBS (χ^2)	0.63	6	$(1.63 \pm 0.45)\,10^{-8}$	2.09 ± 0.30		5.4 ± 1.1	4.5/8
RrBg (HAP, cross check)	0.63	25	$(1.67 \pm 0.37)\,10^{-8}$	2.11 ± 0.16		5.5	–/39
RrBg (HAP, cross check)	0.63	6	$(1.59 \pm 0.39)\,10^{-8}$	1.92 ± 0.25		5.8	–/23
RrBg (Acero et al., 2011)	0.5	65	$(1.80 \pm 0.40)\,10^{-8}$	2.24 ± 0.16		4.7	–/6

Summary of the results on HESS J1745–290 and HESS J1507–622 for the different analyses with TBS (maximum log $\mathcal{L}$, χ^2 minimisation), the respective cross-check analyses with HAP, and the published H.E.S.S. spectra. The energy ranges (E_{min},E_{max}) were chosen to match that of the TBS analysis and the cross check. The results on the flux normalisation at 1 TeV (Φ_0), the power law (Γ), the inverse cut-off (λ), the integral flux above E_{min} (in percentage of the Crab Nebula flux above the same energy) are given together with the degrees of freedom and the χ^2 value. Spectra without a χ^2 value were obtained with a maximum log-likelihood approach (Piron et al., 2001); see also Section 4.4.

4.5.2.5 VELA X

The PWN Vela X (Abramowski et al., 2012b) is a very large VHE γ-ray source. This source is described by an radius of 0.8° which encompasses the so-called *Vela X cocoon*. Owing its large size, the spectrum cannot be reconstructed using the RrBg method and the results in Abramowski et al. (2012b) were produced using the *On*/*Off* background. Therefore, this work does not include a cross-check analysis with the RrBg. This source is very bright and its spectrum is best-described by a power law with exponential cutoff (Abramowski et al., 2012b).

This data set includes some additional runs that could not be used in Abramowski et al. (2012b), apparently lacking matching *Off* runs. The observation run zenith angles cover a range from 22° to 41°. The wobble-offset range begins at 0.1° and extends up to 1.4°.

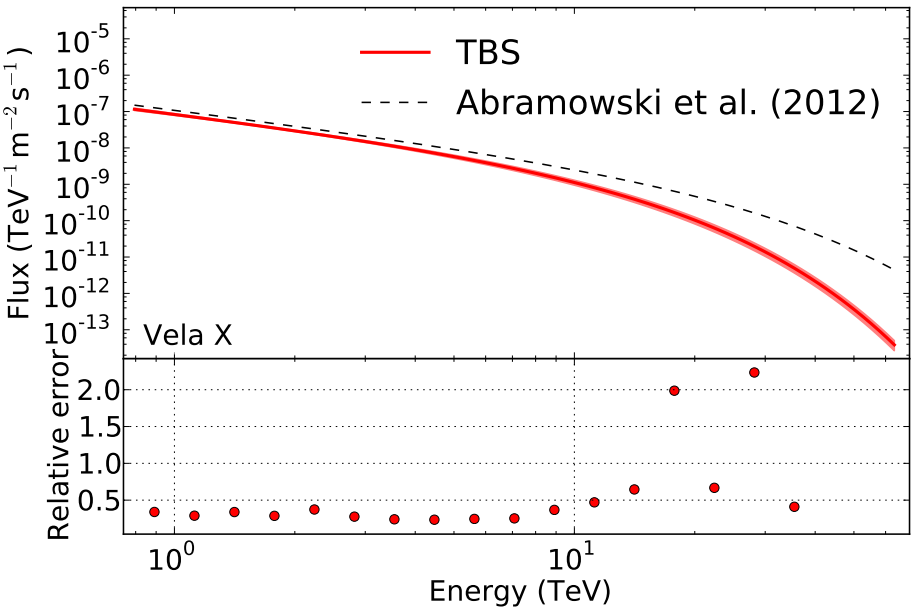

FIGURE 4.13 Results of the forward folding for Vela X with TBS (red line and circles) and the results with *On*/*Off* analysis (black dashed line; Abramowski et al., 2012b). The red area indicates the 1 σ uncertainty. Missing data points for the relative error indicate non-Gaussian event statistics and therefore these points and the corresponding cross-check values are not calculated. It has been zoomed into the bottom panel for a better legibility, but truncating the data point at the highest energy bin with a very large relative error. Data points from Abramowski et al. (2012b) could not be obtained.

As a sufficient amount of events in the signal region and from the FoV (excluding the signal region and other γ-ray emission regions) are provided, the spectrum extends up to 60 TeV, which is roughly the maximum-energy bin with a significant flux point reached in Abramowski et al. (2012b). Only the energy bin at $\sim$ 44 TeV (i.e. the energy bin between 39 and 52 TeV) was excluded from the fit procedure as no template correction

could be calculated and about 800 hadron-like events from the signal region remained without correction for the majority of the respective zenith angle and camera offset bins at this energy.

The spectrum reconstructed with TBS and depicted in Figure 4.13 is compatible within $\sim 3\,\sigma$ with the reported spectrum in Abramowski et al. (2012b). The best-fit normalisation and the exponential cutoff in energy are found to be lower than reported; the TBS-determined values are about 20 % (w.r.t. Φ_0) and 7 TeV (w.r.t. Γ) lower. The reconstructed power-law index were consistent (see Table 4.5.2.6 and Figure A.8). This result is also obtained with the χ^2 minimisation.

DISCUSSION OF OBSERVED DIFFERENCES The statistical errors are negligible because this large source region and the large exposure result in a sufficiently large amount of events from the signal region in every energy bin; for example, the relative errors on the gamma-like samples are below 1 % at lower energies and increase up to 10 % at around 60 TeV.[iii] Therefore, the analysis of this source is generally dominated by systematic effects.

The systematic uncertainty of the *On*/*Off*-background method is estimated to be 8 % on the integral flux and 0.08 on the power-law index (reported in Abramowski et al., 2012b). The spectrum derived with the χ^2 method takes the uncertainties estimated for the excess events into account and leads to higher errors on the best-fit parameters of the spectral shape. Assuming that the interpolation and the extrapolation of the template correction provide a sufficiently accurate estimate of the *true* background normalisation and that their uncertainties are not underestimated (Sect. 4.3.1, 4.3.2, and 4.3), the systematic uncertainties can be estimated by comparing the uncertainties on the best-fit parameters obtained through the maximum likelihood and the χ^2 method. Thus, for the analysis of Vela X, the relative systematic uncertainty on the integral flux is around 7 %, the error on the power-law index would be around 0.2, and the systematic error on the normalisation is about 11 %. These systematic uncertainties is arise to a large faction from the extrapolation of the template correction to lower camera offsets at the high-energy end of the spectrum.

In addition, the analysis configurations are not the same because a stricter cut on the image size of 200 p.e. was used in Abramowski et al. (2012b), but is not implemented in TBS, yet. A higher cut on the image size provides a better event reconstruction and background determination, which may affect the reconstruction of the spectral shape. It is also possible that the TBS correction overestimates the true background or, *vice versa* that the archival extra-Galactic data from the H.E.S.S. data base in combination with the *On*/*Off*-background method led to an underestimate of the true background.

[iii] The relative errors on the hadron samples are even lower.

4.5.2.6 VELA JUNIOR

The shell-type SNR Vela Junior is just about 3° away from Vela X. Vela Junior is one of the largest sources detected in the TeV sky, its source radius of 1° means that the RrBg method cannot be used to reconstruct the spectrum. Therefore, the *On*/*Off*-background method was used in Aharonian et al. (2005b) and therefore a new analysis is not done in this work. The power-law spectrum derived in Aharonian et al. (2005b) is used as reference for TBS. The here data set analysed contained about 8 hrs of fewer data than in the H.E.S.S. publication. The mean run zenith angles range from $z_{\mathrm{obs}} = 25° \ldots 43°$ and the wobble-distance range is 0.5° to 1.1°.

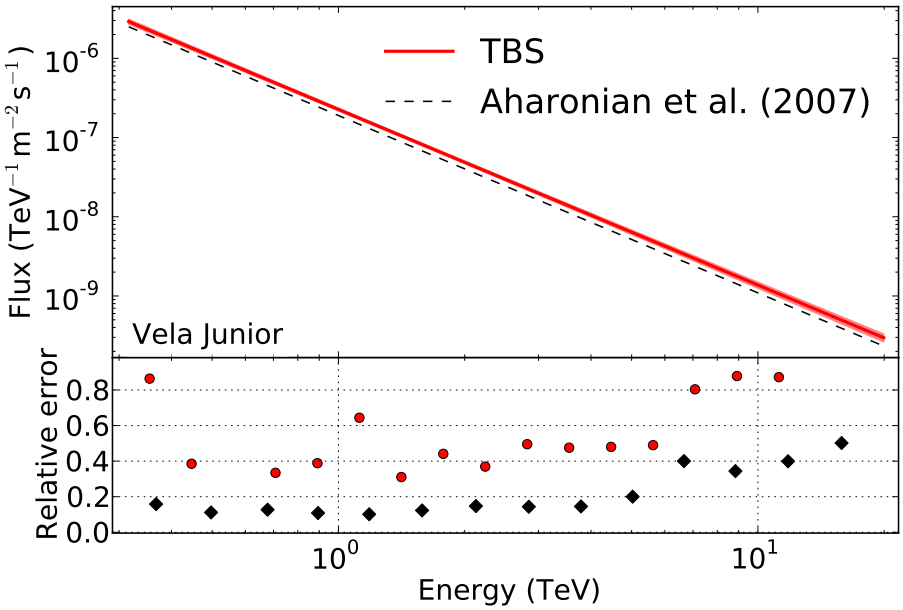

FIGURE 4.14 Results of the forward folding for Vela Junior with TBS (red line and circles) and the results with *On*/*Off* analysis (black dashed line; Aharonian et al., 2005b). The red area indicates the $1\,\sigma$ uncertainty. Missing data points for the relative error indicate non-Gaussian event statistics and therefore these points and the corresponding cross-check values are not calculated. It has been zoomed into the bottom panel for a better legibility, but truncating the three data points with large relative errors.

The possible TBS energy range would extend to about 25 TeV, but was matched to that of the H.E.S.S. publication. Overall a good agreement is found (Fig. 4.14 and A.9). The results are summarised in Table 4.5.2.6. Similar as for Vela X, systematic effects on the background estimate and analysis (TBS vs. *On*/*Off*-background method) are dominant as the statistical uncertainties do not play a role for this large source. With the same assumptions, the results of the χ^2 evaluation can be used to estimate the systematic uncertainty introduced by the interpolation and extrapolation. For the integral flux, a relative error of 11,% is found and for the power-law index the absolute systematic error is around 0.1.

Table 4.6

Analysis	E_{min} TeV	E_{max} TeV	$\Phi_0(1\,\mathrm{TeV})$ $\mathrm{TeV}^{-1}\mathrm{m}^{-2}\mathrm{s}^{-1}$	Γ	λ TeV^{-1}	$F(> E_{\mathrm{min}})$ % Crab	χ^2/n_{dof}
Vela X							
TBS (log $\mathcal{L}$)	0.8	63	$(9.65 \pm 0.50)\,10^{-8}$	1.29 ± 0.08	0.15 ± 0.02	39.3 ± 1.2	–/15
TBS (χ^2)	0.8	63	$(9.52 \pm 1.59)\,10^{-8}$	1.32 ± 0.29	0.14 ± 0.06	38.8 ± 3.9	4.5/15
On/Off (Abramowski et al., 2012b)	0.8	60	$(11.6 \pm 0.6)\,10^{-8}$	1.36 ± 0.06	0.07 ± 0.01	54.7	–/–
Vela Junior							
TBS (log $\mathcal{L}$)	0.3	20	$(2.27 \pm 0.09)\,10^{-7}$	2.22 ± 0.04		60.0 ± 2.7	–/16
TBS (χ^2)	0.3	20	$(2.23 \pm 0.30)\,10^{-7}$	2.27 ± 0.13		60.2 ± 9.4	11.2/16
On/Off (Aharonian et al., 2005b)	0.3	20	$(1.90 \pm 0.08)\,10^{-7}$	2.24 ± 0.04		50.2	–/–

Summary of the results on Vela X and Vela Junior for the different analyses with TBS (maximum log $\mathcal{L}$, χ^2 minimisation) and H.E.S.S. publications. The energy ranges (E_{min},E_{max}) were chosen to match that of the reported spectrum. The results on the flux normalisation at 1 TeV (Φ_0), the power law (Γ), the inverse cut-off (λ), the integral flux above E_{min} (in percentage of the Crab Nebula flux above the same energy) are given together with the degrees of freedom and the χ^2 value. Spectra without a χ^2 value were obtained with a maximum log-likelihood approach (Piron et al., 2001); see also Section 4.4.

4.6 DISCUSSION

In this section, the results presented in Section 4.5.2 are discussed in the light of general implications on TBS. The main difference to other background-estimation methods is that the template correction is not set by geometrical aspects, but defined in parameter space and has to be calculated through observed events w.r.t. energy, zenith-angle, and camera offset. This leads to an non-negligible error on the template correction and might hamper the performance of TBS. It is not possible to state an absolute systematic error produced by the TBS method because potential systematic errors are considered in the analysis chain at different stages. Comparing the spectral results on the sources presented above, the uncertainty on the individual spectral parameters is compatible with that of the RrBg method and also with the *On*/*Off*-background method. Results using the χ^2 minimisation indicate a dominant contribution of the TBS method to the overall uncertainty.

4.6.1 CONTRIBUTION OF TBS TO THE TOTAL UNCERTAINTY

From Equation 4.14 it is obvious (given an accurate determination of the correction itself), that as long as the statistical errors on the gamma-like $N_{\mathrm{g}}^{\mathrm{s}}$ and hadron-like $N_{\mathrm{h}}^{\mathrm{s}}$ events are larger than the estimated uncertainties on the effective template correction β_{eff}, TBS is not limited by the correction and the assumptions made in Section 4.3. To investigate the contribution of the TBS-introduced term, Equation 4.14 is re-written as:

$$\begin{aligned} \sigma(N_{\mathrm{excess}})^2 &= N_{\mathrm{g}}^{\mathrm{s}} + \beta_{\mathrm{eff}}^2 N_{\mathrm{h}}^{\mathrm{s}} + \left(\sigma(\beta_{\mathrm{eff}}) N_{\mathrm{h}}^{\mathrm{s}}\right)^2 \\ 1 &= \frac{N_{\mathrm{g}}^{\mathrm{s}}}{\sigma(N_{\mathrm{excess}})^2} + \frac{\beta_{\mathrm{eff}}^2 N_{\mathrm{h}}^{\mathrm{s}}}{\sigma(N_{\mathrm{excess}})^2} + \frac{\left(\sigma(\beta_{\mathrm{eff}}) N_{\mathrm{h}}^{\mathrm{s}}\right)^2}{\sigma(N_{\mathrm{excess}})^2} \,. \end{aligned} \tag{4.30}$$

For simplicity and legibility reasons, the above equation representing the normalised error contribution (ec) to the overall error on the excess is written as:

$$1 = \mathrm{ec}\,(\mathrm{g}) + \mathrm{ec}\,(\mathrm{h}) + \mathrm{ec}\,(\beta_{\mathrm{eff}}) \,. \tag{4.31}$$

The third term in Equation 4.31, namely $\mathrm{ec}(\beta_{\mathrm{eff}})$, is the non-negligible contribution to the overall error in TBS, which will be discussed on the basis of the analysis results of the previous introduced H.E.S.S. sources.

In Figure 4.15 and 4.16, the individual error contributions per energy bin used in the fit procedure are calculated according to Equation 4.31 and plotted. For this, only bins with Gaussian statistics are used. As expected, the error contribution of the hadron-like term is always negligible. For the Crab Nebula, Centaurus A, and HESS J1745–290 the statistical error on the gamma-like regime is dominant because of the relatively few gamma-like events. For HESS J1745–290 and HESS J1507–622, the contribution of the TBS method to the overall error is around 10 % to 30 % level, mainly because of a larger fraction of events for which the correction has to be extrapolated towards lower camera offsets.

The errors on the large sources Vela X and Vela Junior are dominated by $\mathrm{ec}(\beta_{\mathrm{eff}})$ with a contribution of 80 to 95 % to the overall error (see Figure 4.16). For these two sources,

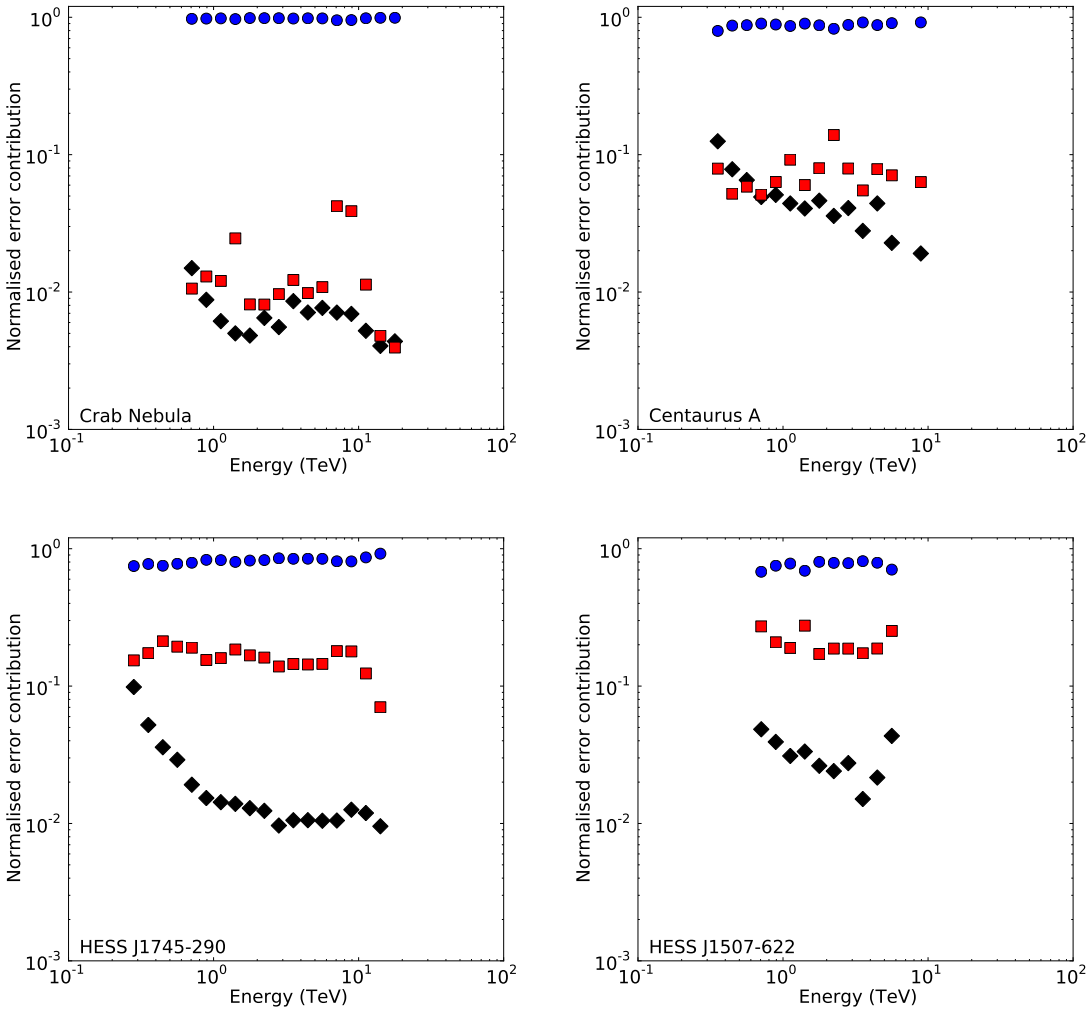

FIGURE 4.15 The normalised error contribution as defined in Equation 4.31 for the data sets of the Crab Nebula (**TOP LEFT**), Centaurus A (**TOP RIGHT**), HESS J1745–290 (**BOTTOM LEFT**), and HESS J1507–622 (**BOTTOM RIGHT**). For each source, the error contribution w.r.t. to the gamma-like events (ec(g),blue circles), the hadron-like events (ec(h), black diamonds), and the template correction (ec(β_{eff}), red squares) are depicted.

statistical errors for events from the signal region are negligible. Conversely, the large source sizes leave fewer data in the FoV to calculate the template correction for every bin in (E, z, θ). Therefore, the errors on the TBS method dominantly arise from the extrapolation. This uncertainty is reflected in the larger errors on the spectral parameters derived with the χ^2 minimisation and the larger relative errors on the individual data points. For the point sources and the moderately extended source HESS J1507–622, these errors are compatible with state-of-the-art background-estimation methods. In the case of Vela X and Vela Junior, the relative error on data points is about a factor of higher and around 40 %.

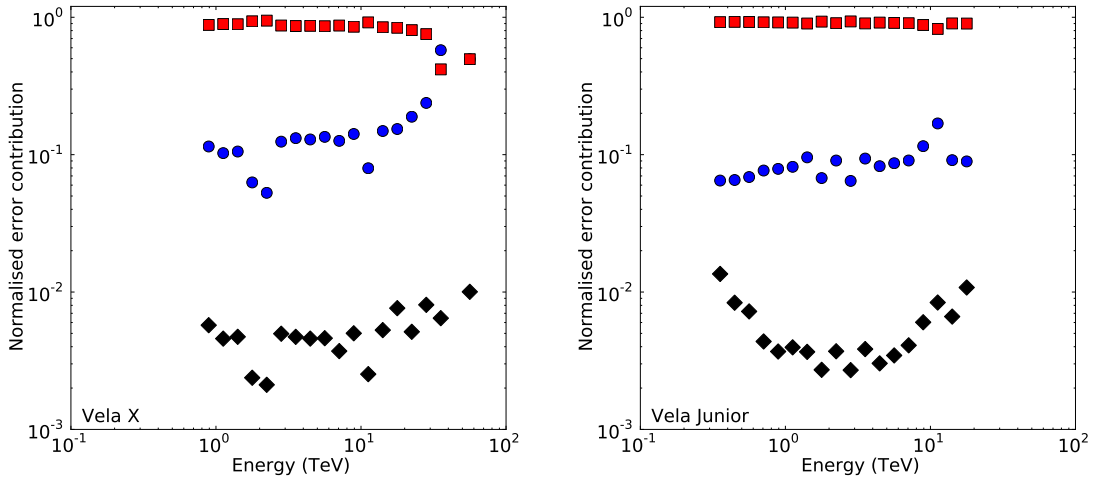

FIGURE 4.16 The normalised error contribution as defined in Equation 4.31 for the data sets of Vela X (**LEFT**) and Vela Junior (**RIGHT**). For each source, the error contribution w.r.t. to the gamma-like events (ec(g),blue circles), the hadron-like events (ec(h), black diamonds), and the template correction (ec(β_{eff}), red squares) are depicted.

Although these larger errors are large, it has to be noted that all errors on the data points determined in TBS always include systematic errors. The results of the likelihood analysis with TBS that agree well with the results of the RrBg method and with the *On*/*Off*-background method (at least in the case of Vela Junior) motivate that the background normalisation is sufficiently well determined. The small reduced χ^2 values ($\chi^2/n_{\text{dof}} < 1$) in the analysis of the very extended sources could indicate the errors on the interpolation and extrapolation were possibly too conservatively set.

4.6.2 CHOICE OF PARAMETERS

Some of the parameters in the analysis chain are not optimised but reasonably set. One advantage of TBS is that signal-region data and the data in the FoV are handled identically and therefore inaccuracies or assumptions in the analysis chain or the correction are on average accounted for (also because the template correction is a relative correction). In the following, a short discussion on the parameters and their settings is given.

ENERGY, ZENITH ANGLE, AND CAMERA OFFSET The *a priori* choice of the bin widths in energy, zenith angle, and camera offset is not optimised, but to a certain extent already determined beforehand. From the five available binning options in energy (2,4,5,10, and 20 bins per decade in logarithmic energy scale), 10 appeared to be a good comprise between a high number of degrees of freedom and a sufficiently well sampling of the energy-dependent template correction. The zenith-angle intervals are adopted from the MC simulations. The bin width in camera offset of $\delta\theta = 0.25°$ is chosen that it under-

samples the γ-ray PSF and accounts for the larger hadron PSF. Moreover, it has to be a multiple of 1 and 2 as coarser binnings are used in the extrapolation of α and the total width in θ is 2°.

In general, a too-fine binning in either parameter can lead to empty grid points in the LuT of α and therefore to a more frequent need to extrapolate the requested template correction. Finally, the uncertainties on the excess will become larger.

HADRON-LIKE REGIME AND THE MRSW The MRSW range of $5 < \text{MRSW} < 20$ is chosen to define the hadron-like regime such that this sample does not contain gamma-like events. Also, it is assured that a sufficient amount of the data is accumulated to calculate the LuT of α. A different, more gamma-like MRSW selection of $0.9 < \text{MRSW} < 5$ was tested. This resulted in a much smaller amount of data to determine α leading to larger uncertainties in the TBS correction (higher fraction of extrapolation required). The spectral results did not differ significantly from the results presented above.

4.7 SUMMARY & CONCLUSIONS

In this work, we proposed and tested a new method to estimate the background for VHE γ-ray spectra. Template Background Spectrum (TBS) enables spectral reconstruction in crowded FoVs and for extended sources where other standard methods fail (mainly) due to geometrical limitations. Moreover, no *Off* data have to be used.

The basic idea is the accumulation of data binned in energy, zenith angle and camera offset to create template-correction look-ups from the FoV data (excluding the source region and other γ-ray emission regions), which are then used to correct the identically-binned data from the source of interest. Moreover, the template correction accounts for any relative difference in the gamma-like and hadron-like regimes.

TBS was tested on published H.E.S.S. data in various FoVs and for different types of sources (strong to faint, point-like to extended, located in rather empty or in rather crowded FoVs). On average, good agreement was found between the spectra reported by the H.E.S.S. collaboration and in this work. Although H.E.S.S. data were used, the method can be used for any IACT data.

Now, besides the *On*/*Off*-background method and the RrBg method, TBS is the third general method to reconstruct energy spectra, but the first one to not need *Off* data to reconstruct extended sources. Compared to the two former ones, new and different issues have to be tackled, which led to higher statistical and systematic errors on the background normalisation.

For very large sources, systematic effects of the TBS correction dominate, but in general, the results are compatible with those obtained with the *On*/*Off*-background method. As systematic uncertainties are already incorporated in the error estimate of the TBS correction, it is not possible to disentangle this contribution from the statistical uncertainty and to determine a *purely* systematic error on the best-fit parameters. The differences between the likelihood method and the χ^2 evaluation may serve as an estimate on the systematic effects of the TBS method in its current implementation. The errors on the spec-

tral results of the likelihood method in TBS are comparable with those of state-of-the-art background-estimation methods. Moreover, this indicates that the background normalisation is sufficiently well determined. Spectral points include systematic errors and can be a factor of 2 higher than found for *On*/*Off*-background method for very extended sources; otherwise the uncertainty is comparable with that of the RrBg method for point sources and moderately extended regions.

4.8 OUTLOOK

The ansatz of an energy and zenith-angle-dependent treatment of the template normalisation offers new possibilities. For example, it enhances the power of the normal TBg method in producing skymaps in which every event would then be corrected according to its (E,z,θ) dependence, and therefore contribute to morphological studies of (extended) sources.

Unlike RrBg where On and OFF have to be of the same shape (normally circles), TBS does not require a symmetric signal regions, which makes it possible to define arbitrarily-formed (i.e. better suited) regions for spectral analyses and will lead to a better E/B ratio.

Using the latest advances in background rejection/determination (e.g. decision-tree-based algorithms), the performance of TBS could be further enhanced. Opposed to the used MRSW selection, these methods provide comparatively more events statistics for the analysis as events are not discarded from the sample (through a selection cut), but assigned a gamma-likeness and hadron-likeness to be used in the further analysis. In general, any selection cut or algorithm which improves the separation of gamma-like and hadron-like events compared to the Hillas approach will possibly lead to an improvement of TBS.

The major uncertainty of TBS is the extrapolation, especially for very large sources because fewer data remain to estimate the TBS correction. Although camera-acceptance look-ups are in use to generate skymaps, thus avoiding extrapolation issues in complex FoVs or for large sources, it has to be investigated if LuTs generated from extra-Galactic observations and split into in E, z, θ can be applied to any FoV and source or if the systematic uncertainties in the background, of the TBg method or of TBS dominate. Most probably, one would (at least) introduce a time dependence t as a new parameter of TBS to calculate $\alpha(E, z, \theta, t)$ or a dependence based on the optical efficiency.

As mentioned in this chapter, the parameter ranges chosen were found to give consistent results w.r.t. published spectra. Given the results presented here, the zenith-angle range should be increased in order generate these IR data (effective area, energy threshold, and energy-resolution matrix) and to be to analyse high zenith-angle data, e.g. of HESS J1745–290 (see Section 4.5.2.3). It is left to be seen if the use of 2 and 3-telescope data (discarded here) does lead to an improvement (as more data would be available) when included into the TBS analysis chain or if the template correction behaves differently for such data and has thus to be treated separately from the 4-telescope data. However, it is also possible to introduce an adaptive binning in energy, where the respective bin widths increase with energy in order to accumulate more statistics at the highest energies.

In detailed follow-up studies on TBS aiming at increasing the performance, restricting the events to 4-telescope events will lead to a better energy reconstruction and resolution. As more events are rejected, one would have to combine such an approach with a coarser binning.

In principle, the same approach can be used for the RingBg method, which would reduce the systematic error because only gamma-like events are used requiring only one acceptance correction. However, for large sources and in crowded regions its application is stronger limited than the TBg model. This concept of an energy-dependent treatment of a non-spatial parameter to estimate the background contribution to energy spectra could in principle also be applied to other air-shower experiments than IACTs.

Chapter 5

Discovery of Extended VHE Gamma-Ray Emission from the Vicinity of the Young Massive Stellar Cluster Westerlund 1

This refereed and published H.E.S.S. collaboration paper was written together with Stefan Ohm who did the H.E.S.S. data analysis and the morphology studies. In the following, my contribution is explained.

Own contribution In terms of contributed paper sections, these were the stellar-cluster part of the *Introduction*, the entire sections of *Discussion* and *Summary and conclusions*.

Thus, the focus was the search for a plausible counterpart to the TeV source. For this, it was searched in archival databases for objects in the FoV that could possibly be related to HESS J1646–458. Also, available MWL data from radio (HI and CO) and X-ray (*Chandra* satellite) observations were investigated. Acceleration scenarios linked to magnetars, binary systems, PWNe, and SCs were investigated and elaborated; emphasis was on models linked to SCs (e.g.models as in Leitherer et al., 2010; Oskinova, 2005; Silich et al., 2005; Weaver et al., 1977) and pulsars (Mattana et al., 2009). For all objects, the relevant properties were gathered (e.g. age, distance, mass, kinetic energy, or luminosities) and discussed in context of the H.E.S.S. observations and the MWL data.

A&A 537, A114 (2012)
DOI: 10.1051/0004-6361/201117928

Astronomy & Astrophysics

Discovery of extended VHE γ-ray emission from the vicinity of the young massive stellar cluster Westerlund 1

H.E.S.S. Collaboration: A. Abramowski[1], F. Acero[2], F. Aharonian[3,4,5], A. G. Akhperjanian[6,5], G. Anton[7], A. Balzer[7], A. Barnacka[8,9], U. Barres de Almeida[10,⋆], Y. Becherini[11,12], J. Becker[13], B. Behera[14], K. Bernlöhr[3,15], E. Birsin[15], J. Biteau[12], A. Bochow[3], C. Boisson[16], J. Bolmont[17], P. Bordas[18], J. Brucker[7], F. Brun[12], P. Brun[9], T. Bulik[19], I. Büsching[20,13], S. Carrigan[3], S. Casanova[13], M. Cerruti[16], P. M. Chadwick[10], A. Charbonnier[17], R. C. G. Chaves[3], A. Cheesebrough[10], L.-M. Chounet[12], A. C. Clapson[3], G. Coignet[21], G. Cologna[14], J. Conrad[22], M. Dalton[15], M. K. Daniel[10], I. D. Davids[23], B. Degrange[12], C. Deil[3], H. J. Dickinson[22], A. Djannati-Ataï[11], W. Domainko[3], L. O'C. Drury[4], F. Dubois[21], G. Dubus[24], K. Dutson[25], J. Dyks[8], M. Dyrda[26], K. Egberts[27], P. Eger[7], P. Espigat[11], L. Fallon[4], C. Farnier[2], S. Fegan[12], F. Feinstein[2], M. V. Fernandes[1], A. Fiasson[21], G. Fontaine[12], A. Förster[3], M. Füßling[15], Y. A. Gallant[2], H. Gast[3], L. Gérard[11], D. Gerbig[13], B. Giebels[12], J. F. Glicenstein[9], B. Glück[7], P. Goret[9], D. Göring[7], S. Häffner[7], J. D. Hague[3], D. Hampf[1], M. Hauser[14], S. Heinz[7], G. Heinzelmann[1], G. Henri[24], G. Hermann[3], J. A. Hinton[25], A. Hoffmann[18], W. Hofmann[3], P. Hofverberg[3], M. Holler[7], D. Horns[1], A. Jacholkowska[17], O. C. de Jager[20], C. Jahn[7], M. Jamrozy[28], I. Jung[7], M. A. Kastendieck[1], K. Katarzyński[29], U. Katz[7], S. Kaufmann[14], D. Keogh[10], D. Khangulyan[3], B. Khélifi[12], D. Klochkov[18], W. Kluźniak[8], T. Kneiske[1], Nu. Komin[21], K. Kosack[9], R. Kossakowski[21], H. Laffon[12], G. Lamanna[21], D. Lennarz[3], T. Lohse[15], A. Lopatin[7], C.-C. Lu[3], V. Marandon[11], A. Marcowith[2], J. Masbou[21], D. Maurin[17], N. Maxted[30], M. Mayer[7], T. J. L. McComb[10], M. C. Medina[9], J. Méhault[2], R. Moderski[8], E. Moulin[9], C. L. Naumann[17], M. Naumann-Godo[9], M. de Naurois[12], D. Nedbal[31], D. Nekrassov[3], N. Nguyen[1], B. Nicholas[30], J. Niemiec[26], S. J. Nolan[10], S. Ohm[32,25,3], E. de Oña Wilhelmi[3], B. Opitz[1], M. Ostrowski[28], I. Oya[15], M. Panter[3], M. Paz Arribas[15], G. Pedaletti[14], G. Pelletier[24], P.-O. Petrucci[24], S. Pita[11], G. Pühlhofer[18], M. Punch[11], A. Quirrenbach[14], M. Raue[1], S. M. Rayner[10], A. Reimer[27], O. Reimer[27], M. Renaud[2], R. de los Reyes[3], F. Rieger[3,33], J. Ripken[22], L. Rob[31], S. Rosier-Lees[21], G. Rowell[30], B. Rudak[8], C. B. Rulten[10], J. Ruppel[13], V. Sahakian[6,5], D. Sanchez[3], A. Santangelo[18], R. Schlickeiser[13], F. M. Schöck[7], A. Schulz[7], U. Schwanke[15], S. Schwarzburg[18], S. Schwemmer[14], F. Sheidaei[11,20], M. Sikora[8], J. L. Skilton[3], H. Sol[16], G. Spengler[15], Ł. Stawarz[28], R. Steenkamp[23], C. Stegmann[7], F. Stinzing[7], K. Stycz[7], I. Sushch[15,⋆⋆], A. Szostek[28], J.-P. Tavernet[17], R. Terrier[11], M. Tluczykont[1], K. Valerius[7], C. van Eldik[3], G. Vasileiadis[2], C. Venter[20], J. P. Vialle[21], A. Viana[9], P. Vincent[17], H. J. Völk[3], F. Volpe[3], S. Vorobiov[2], M. Vorster[20], S. J. Wagner[14], M. Ward[10], R. White[25], A. Wierzcholska[28], M. Zacharias[13], A. Zajczyk[8,2], A. A. Zdziarski[8], A. Zech[16], and H.-S. Zechlin[1]

(Affiliations can be found after the references)

Received 22 August 2011 / Accepted 12 October 2011

ABSTRACT

Aims. Results obtained in very-high-energy (VHE; $E \geq 100$ GeV) γ-ray observations performed with the H.E.S.S. telescope array are used to investigate particle acceleration processes in the vicinity of the young massive stellar cluster Westerlund 1 (Wd 1).

Methods. Imaging of Cherenkov light from γ-ray induced particle cascades in the Earth's atmosphere is used to search for VHE γ rays from the region around Wd 1. Possible catalogued counterparts are searched for and discussed in terms of morphology and energetics of the H.E.S.S. source.

Results. The detection of the degree-scale extended VHE γ-ray source HESS J1646–458 is reported based on 45 h of H.E.S.S. observations performed between 2004 and 2008. The VHE γ-ray source is centred on the nominal position of Wd 1 and detected with a total statistical significance of $\sim 20\sigma$. The emission region clearly extends beyond the H.E.S.S. point-spread function (PSF). The differential energy spectrum follows a power law in energy with an index of $\Gamma = 2.19 \pm 0.08_{\rm stat} \pm 0.20_{\rm sys}$ and a flux normalisation at 1 TeV of $\Phi_0 = (9.0 \pm 1.4_{\rm stat} \pm 1.8_{\rm sys}) \times 10^{-12}$ TeV^{-1} cm^{-2} s^{-1}. The integral flux above 0.2 TeV amounts to $(5.2 \pm 0.9) \times 10^{-11}$ cm^{-2} s^{-1}.

Conclusions. Four objects coincident with HESS J1646–458 are discussed in the search of a counterpart, namely the magnetar CXOU J164710.2–455216, the X-ray binary 4U 1642–45, the pulsar PSR J1648–4611 and the massive stellar cluster Wd 1. In a single-source scenario, Wd 1 is favoured as site of VHE particle acceleration. Here, a hadronic parent population would be accelerated within the stellar cluster. Beside this, there is evidence for a multi-source origin, where a scenario involving PSR J1648–4611 could be viable to explain parts of the VHE γ-ray emission of HESS J1646–458.

Key words. open clusters and associations: general – gamma rays: stars – astroparticle physics

⋆ Supported by CAPES Foundation, Ministry of Education of Brazil.
⋆⋆ Supported by Erasmus Mundus, External Cooperation Window.

1. Introduction

The long-standing question on the origin and acceleration mechanisms of hadronic and leptonic Galactic cosmic rays (GCRs) is still not settled, despite considerable progress. The detection of very-high-energy (VHE) γ-ray emission from shell-type supernova remnants (SNRs), e.g. Cassiopeia A, RX J1713–3946, RX J0852.0–4622, RCW 86, SN 1006 (summarised in Hinton & Hofmann 2009), and recently HESS J1731–347 (H.E.S.S. Collaboration et al. 2011) and Tycho's SNR (Acciari et al. 2011) supports the widely accepted idea of SNRs being acceleration sites of GCRs. It has been noted for many years that the Galactic SNR population provides sufficient energy input to sustain the CR flux measured at Earth. The underlying theory assumes that electrons and protons are injected into SNR shock fronts where they are accelerated via the diffusive shock acceleration process up to energies of $\sim 10^{15}$ eV (Krymskii 1977; Axford et al. 1977; Bell 1978; Blandford & Ostriker 1978). The ability of SNRs to accelerate electrons up to the so-called knee in the differential energy spectrum of the GCRs and our common belief that this holds for protons, too, constitute the paradigm that SNRs are the long-thought sources of GCRs. In interactions with the ambient medium, i.e. matter and electromagnetic fields, these GCRs then produce VHE γ rays which can be detected by current imaging atmospheric Cherenkov telescope (IACT) systems, e.g. H.E.S.S., MAGIC, VERITAS or CANGAROO-III. Additionally, evolving SNRs could explain the chemical composition up to the knee region. Furthermore, core-collapse supernovae could explain observed overabundances of some isotopes, e.g. ^{22}Ne (Higdon & Lingenfelter 2003). However, recent studies applied to RX J1713–3946 highlight potential problems for a dominant hadronic interpretation for this object (Ellison et al. 2010) and motivate the search for other acceleration sites and processes.

SNR shells are not the only sites in the Galaxy where GCRs can be produced via diffusive shock acceleration. One alternative scenario is particle acceleration in strong shocks in colliding wind binaries (CWBs). Massive stars are to a large extent bound in binary systems (e.g. Zinnecker 2003; Gies 2008), generally exhibit high mass-loss rates ($10^{-5}\,M_\odot\,\mathrm{yr}^{-1}$–$10^{-3}\,M_\odot\,\mathrm{yr}^{-1}$) and drive strong supersonic winds with velocities of the order of a few $10^3\,\mathrm{km\,s}^{-1}$. When these winds collide in a stellar binary system they form a wind-wind interaction zone where charged particles can be accelerated to high energies (e.g. Eichler & Usov 1993). Electrons can then up-scatter stellar photons present in the wind collision zones via the inverse Compton (IC) process to GeV energies (Mücke & Pohl 2002; Manolakou et al. 2007). On the other hand, relativistic nucleons can inelastically scatter with particles in the dense wind and produce π^0s which subsequently decay into VHE γ rays (Benaglia & Romero 2003; Bednarek 2005; Domingo-Santamaría & Torres 2006; Reimer et al. 2006). Apart from acceleration in binaries, GCRs can be accelerated in the winds of single massive stars (e.g. Montmerle 1979).

Another scenario involves collective stellar winds: It is commonly accepted that the bulk (if not all) of the core-collapse SN progenitor stars and CWBs evolve from collapsing gas condensations in giant molecular clouds (e.g. Zinnecker & Yorke 2007) and mostly remain close to their birthplaces in groups of loosely bound associations or dense stellar clusters. When the winds of multiple massive stars in such systems collide they form a collective cluster wind which drives a giant bubble ($O(100\,\mathrm{pc})$), also referred to as *superbubble* (SB), filled with a hot ($T \approx 10^6$ K) and tenuous ($n < 1\,\mathrm{cm}^{-3}$) plasma (e.g. Weaver et al. 1977; Silich et al. 2005). At the wind interaction zones, e.g. at the termination shock of the stellar cluster wind, turbulences in form of magneto-hydrodynamic (MHD) fluctuations and weak reflected shocks can build up. Unlike SNR shock fronts and CWBs where GCRs are accelerated through the 1st order Fermi acceleration, turbulences in SB interiors can accelerate particles to very high energies also via the 2nd order Fermi mechanism (e.g. Bykov 2001). Moreover, after a few million years, supernova explosions of massive stars ($M > 8\,M_\odot$) in the thin and hot SB environment eventually lead to efficient particle acceleration at the boundary of the SB or at MHD turbulences and further amplify existing MHD turbulences (e.g. Ferrand & Marcowith 2010, and references therein). The interaction of these GCRs with the ambient medium including molecular clouds or electromagnetic fields leads to the production of VHE γ rays which can then be studied on Earth. Therefore, stellar clusters are promising targets to study acceleration and propagation processes of GCRs.

One of the most prominent objects among stellar clusters in the Galaxy is Westerlund 1 (Wd 1). After its discovery in 1961 (Westerlund 1961) subsequent observations have established Wd 1 as the most massive stellar cluster in our Galaxy placing a lower limit on its mass of $10^5\,M_\odot$ (Clark et al. 2010). An unprecedented accumulation of evolved massive stars is found without indication of the presence of an early-type main-sequence star. Amongst the most massive stars, 24 Wolf-Rayet stars (binary fraction ≥62%) have been detected and a number of ∼150 OB super- and hypergiants (binary fraction ∼30%) is expected (Crowther et al. 2006; Dougherty et al. 2010, and references therein).

The analysis of *Chandra* data revealed an arc minute-scale extended diffuse X-ray emission (Muno et al. 2006b) which is only seen for a few young stellar associations in the Galaxy, for example RCW 38 (Wolk et al. 2002) and possibly the Arches cluster (Law & Yusef-Zadeh 2004) as well as in the Large Magellanic Cloud in 30 Doradus C (Bamba et al. 2004) and DEM L192 (Cooper et al. 2004). The total X-ray luminosity of the observed diffuse emission within 5′ of Wd 1 is dominated by its non-thermal component and amounts to $L_\mathrm{X} \approx 3 \times 10^{34}\,\mathrm{erg\,s}^{-1}$ which represents just a fraction of 10^{-5} of the total mechanical power in this system (Muno et al. 2006b). However, models as in Oskinova (2005) predict a thermal X-ray luminosity of $\sim 10^{37}\,\mathrm{erg\,s}^{-1}$ for stellar clusters comparable to Wd 1, which was clearly not observed by *Chandra* for Wd 1. As for previous observations, there remains the open question into which channel most of the unobserved energy is dissipated.

The detection of VHE γ-ray emission from HESS J1646–458 was initially reported in Ohm et al. (2010a) and Ohm et al. (2010b). This paper focuses on a detailed spectral and morphological study of the emission region and investigates a possible multi-source origin. An in-depth search for plausible counterparts is conducted and possible acceleration-mechanism scenarios are elaborated.

2. H.E.S.S. observations and data analysis

Given the large ∼5° field of view (FoV) combined with the good off-axis sensitivity, observations with H.E.S.S. are perfectly suited to cover the vicinity of Wd 1 and allow for the detailed morphological study of extended sources such as HESS J1646–458. Thereby any large-scale non-thermal VHE γ-ray emission around Wd 1 can be probed.

2.1. The H.E.S.S. experiment

The High Energy Stereoscopic System (H.E.S.S.) is an array of four imaging atmospheric Cherenkov telescopes located in the Khomas Highland of Namibia, 1800 m above sea level. The telescopes are identical in construction and each one is comprised of a 107 m^2 optical reflector composed of segmented spherical mirrors. These focus the incident light into a fine-grained camera built of 960 photomultiplier tubes. By means of the *imaging atmospheric Cherenkov technique* (see e.g. Hillas 1985) Cherenkov light, emitted by the highly-relativistic charged particles in extensive air showers, was imaged by the mirrors onto the Cherenkov camera. A single shower was recorded by multiple telescopes under different viewing angles. This allowed for the stereoscopic reconstruction of the primaries' direction and energy with an average energy resolution of 15% and an event-by-event angular resolution better than 0.1° (Gaussian standard deviation, Aharonian et al. 2006a).

2.2. The data set

The region around Wd 1 was observed during the H.E.S.S. Galactic Plane Survey (GPS) in 2004 and 2007 (Aharonian et al. 2006c; Chaves et al. 2008). Additionally, follow-up observations pointing in the direction of Wd 1 have been performed from May to August 2008. Data taken under unstable weather conditions or with malfunctioning hardware were excluded in the standard data quality selection procedure (Aharonian et al. 2006a). Also, pointed observations on Wd 1 at very large zenith angles of more than 55° were excluded due to systematic effects in the description of the camera acceptance at such low altitudes for an extended source like HESS J1646–458. After quality selection and dead time correction the total observation time of 45.1 h was reduced to a live time of 33.8 h. Observations have been carried out at zenith angles from 21° to 45° with a mean value of 26° and an average pointing offset from the Wd 1 position of 1.1°.

2.3. Analysis technique

The data set presented here was processed using the H.E.S.S. Standard Analysis for shower reconstruction (Aharonian et al. 2006a) and the Boosted Decision Trees (BDT) method to suppress the hadronic background component (Ohm et al. 2009)[1]. By parametrising the centre of gravity and second moments of the recorded extensive air shower image (Hillas 1985) in multiple telescopes the shower geometry of the incident primary particle was reconstructed stereoscopically. The directional information together with the measured image intensity was used to reconstruct the energy of the event. Since observations have been conducted over four years, the optical reflectivity of the H.E.S.S. mirrors varied and the gains of the photomultipliers changed. This effect has been taken into account in the spectral reconstruction by calibrating the energy of each event with single muon rings (Aharonian et al. 2006a). The decision tree-based machine learning algorithm BDT returns a continuous variable called ζ which was used to select γ-ray-like events. Cutting on this parameter results in an improvement in terms of sensitivity compared to the H.E.S.S. Standard Analysis of ∼20% and ∼10% for spectral and morphological analysis, respectively (Ohm et al. 2009).

[1] The software which was used to analyse the VHE γ-ray data presented in this work is the *H.E.S.S. analysis package (HAP)* in version 10-06-pl07.

Similar to the H.E.S.S. Standard Analysis, two sets of γ-ray selection cuts have been defined in Ohm et al. (2009). For the production of sky images the $\zeta_{\rm hard}$-*cuts* are used. They require a minimum intensity of 160 photo electrons (p.e.) in each camera image yielding a superior angular resolution of less than 0.1° even at large offsets of 2.5° from the telescope pointing position. Additionally, 30% more background events are rejected resulting in a 10% higher sensitivity compared to the H.E.S.S. Standard Analysis. For the spectral analysis a low energy threshold is desirable for a broad energy coverage and achieved by applying the $\zeta_{\rm std}$-*cuts* with a 60 p.e. cut on the image intensity. For the data set under study, this infers an energy threshold of 450 GeV for spectral analysis and 700 GeV for morphological analysis.

For two-dimensional sky image generation and morphology studies, the *template* background model (Rowell 2003; Berge et al. 2007) is applied. For this method the CR background is estimated in parameter space rather than in angular space. In this analysis, the BDT output parameter ζ has been used to define signal and background regions. The normalisation α between signal and background is calculated as the fraction of all events in the FoV falling into the signal regime, excluding source regions, divided by the number of all events in the FoV in the background regime, again excluding all source regions. The system acceptance to measure γ-ray like and CR-like events drops off radially with the distance to the telescope pointing position. Since this acceptance is different for both types of events, a correction is applied to α. Sky images obtained with the *template* background model agree with sky images generated with the *ring* background method. The *ring* background method estimates the signal-like hadronic CR contribution at each trial position on the sky by integrating events in an annulus centred on that position, excluding potential source regions.

Figure 1 shows the VHE γ-ray count map of the region around Wd 1 and reveals very extended γ-ray emission. The complex morphology apparent in the sky image and a potential multi-source origin of the emission is investigated and discussed in detail in Sect. 3. Since it is not possible to estimate the background from the same FoV due to the fact that observations have been carried out within regions of VHE γ-ray emission, the *On-Off* background estimation method is utilised to extract spectral information for the whole emission region, indicated as a white circle in Fig. 1. Here, the CR background is subtracted from the source region (*On data*) using extragalactic observations taken without any VHE γ-ray signal in the FoV (*Off data*). To ensure similar observational conditions for *On* and *Off data*, only *On-Off* pairs of observations are considered that were taken at similar zenith angles and within four months of each other, resulting in a total live time of 20 h for the *On data* set used for spectral analysis. The absolute normalisation α between *On* and *Off data* is calculated using the fraction of total events in both observations (again, excluding potential source regions). The *reflected* background method (Berge et al. 2007) is used to derive spectral information for smaller regions and the full data set as discussed in Sects. 3.2 and 3.3.

All studies presented in this work were cross-checked by a second analysis chain which is based on the H.E.S.S. standard event reconstruction scheme (Aharonian et al. 2006a) using the Hillas second moment method (Hillas 1985) and an independent calibration of pixel amplitudes and identification of problematic or dead pixels in the IACT cameras. Additionally, the *Model Analysis* (de Naurois & Rolland 2009) for the selection of γ-ray-like events has been utilised to cross-check the spectral results. All analyses give compatible results.

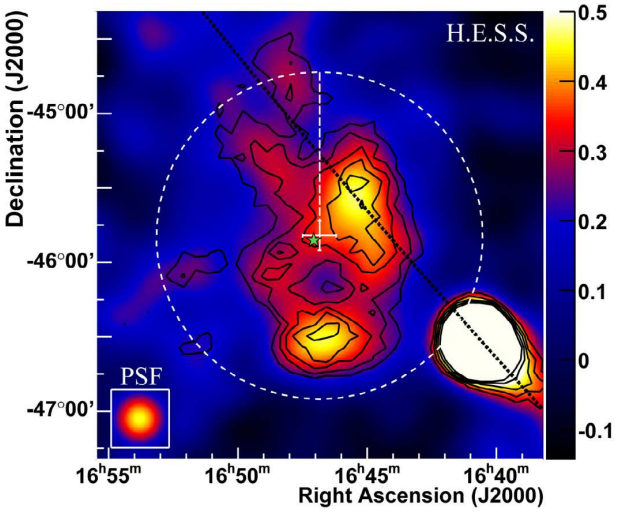

Fig. 1. H.E.S.S. excess map of the region around Wd 1 corrected for the camera acceptance, in units of equivalent on-axis VHE γ-ray events per arcmin^2 and obtained with the *template* background method. The image is smoothed with a 2D Gaussian kernel with a variance of 0.12° to reduce the effect of statistical fluctuations. Significance contours between 4σ and 8σ are overlaid in black, obtained by integrating events within a radius of 0.22 degrees at each given position. The green star marks the position of Wd 1, the white cross the best fit position of the VHE γ-ray emission and the black dashed line the Galactic plane. The inlay in the lower left corner represents the size of a point-like source as it would have been seen by H.E.S.S. for this analysis and the same smoothing, normalised to the maximum of HESS J1646–458. The dotted white circle has a radius of 1.1° and denotes the region which was used for the spectral reconstruction of the VHE γ-ray emission. Note that the bright region in the lower right corner is the source HESS J1640–465 detected during the GPS (Aharonian et al. 2006c).

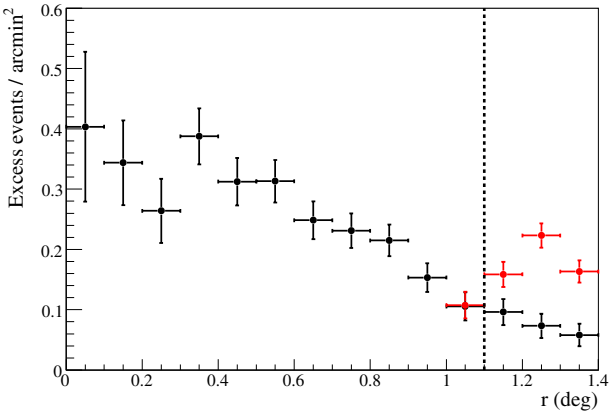

Fig. 2. H.E.S.S. radial profile relative to the best-fit position of the VHE γ-ray emission. The dotted vertical line denotes the 95% containment radius used to obtain the spectrum shown in Figure 4. Note that the region covering the bright source HESS J1640–465 (see Figure 1) has been excluded for the radial profile shown in black by omitting a circle segment with $220° \leq \phi \leq 260°$ for radii of $1.0° \leq r \leq 1.4°$. The red graph displays the radial profile without excluding HESS J1640–465.

3. VHE results

3.1. Position

Figure 1 shows a background-subtracted, camera acceptance-corrected image of the VHE γ-ray counts per arcmin^2 of the 3°× 3° FoV centred on the best fit position of the γ-ray excess as obtained with the *template* background method. The acceptance correction has been performed using γ-ray like background events that pass the γ-ray selection cuts. The map is smoothed with a Gaussian kernel with a variance of 0.12° to reduce the effect of statistical fluctuations and to highlight significant morphological features. Significance contours from 4σ to 8σ are overlaid after integrating events within a radius of 0.22° at each trial source position. This integration radius is matched to the rms of the Gaussian to resample significant features in the sky image and is chosen a priori to match the integration radius typically used in the GPS analysis for the search of slightly extended sources (Aharonian et al. 2006c). Given the extended and complex morphology of the VHE γ-ray emission the position obtained from a two-dimensional Gaussian fit convolved with the H.E.S.S. PSF to the raw excess count map obtained for $\zeta_{\rm hard}$-*cuts* is used to derive an estimate on the centre of gravity of the emission. The two-dimensional Gaussian fit gives a best fit position of RA $16^{\rm h}46^{\rm m}50^{\rm s}\pm27^{\rm s}$ and Dec $-45°49'12''\pm7'$ (J2000). Within statistical errors the centre of gravity of the VHE γ-ray emission is consistent with the nominal Wd 1 cluster position of RA $16^{\rm h}47^{\rm m}00.40^{\rm s}$ and Dec $-45°51'04.9''$ (J2000). Based on the radial profile shown in Fig. 2 the 95% containment radius of the VHE γ-ray emission relative to the best fit position is determined to be 1.1°. This radius is used to extract the energy spectrum presented in Sect. 3.3. Note that although the sky image gives the impression that the region used for spectral reconstruction is contaminated by γ rays from HESS J1640–465, this is mostly an artifact of the smoothing procedure. The real contribution is less than 10% in a ring between 1.0 and 1.1 degree from the best fit position and only 0.8% in the whole spectral extraction region. Within the integration region of 1.1° a total of 2771 ± 139 γ-ray excess events at a significance level of 20.9σ pre-trials (20.1σ post-trials) are found.

3.2. Morphology

In order to investigate the multi-source hypothesis two emission regions *A* and *B* (shown in Fig. 3 (left)) are considered. The radii of 0.35° and 0.25° of region *A* and *B*, respectively, are chosen according to the widths of the two substructures. A one-dimensional slice in the uncorrelated excess image along the major axis between the two regions has been produced. The fit of two separate sources with Gaussian shape results in a χ^2 of 2.0 for 4 degrees of freedom with a probability of 74%. The probability that the emission is explained by a single Gaussian profile or a constant value is found to be rather low at 0.2% and 0.1%, respectively. An *F*-test also supports the multi-source hypothesis, given that the probabilities that the constant or single Gaussian emission models are preferred over the double Gaussian fit are <0.02 and <0.01, respectively.

Figure 3 (left) also suggests a contribution from diffuse VHE γ-ray emission along the Galactic plane which extends 1° to 2° from region *A* north-eastwards. This impression is supported by the one-dimensional slice shown in Fig. 3 (bottom right), where the significance of the emission in all bins with distance $0.5° \leq d \leq 1.8°$ from the centre of region *A* is between 2σ and 4σ. This diffuse emission could be due to unresolved VHE γ-ray sources or a Galactic diffuse emission component, caused by the interaction of GCRs with molecular

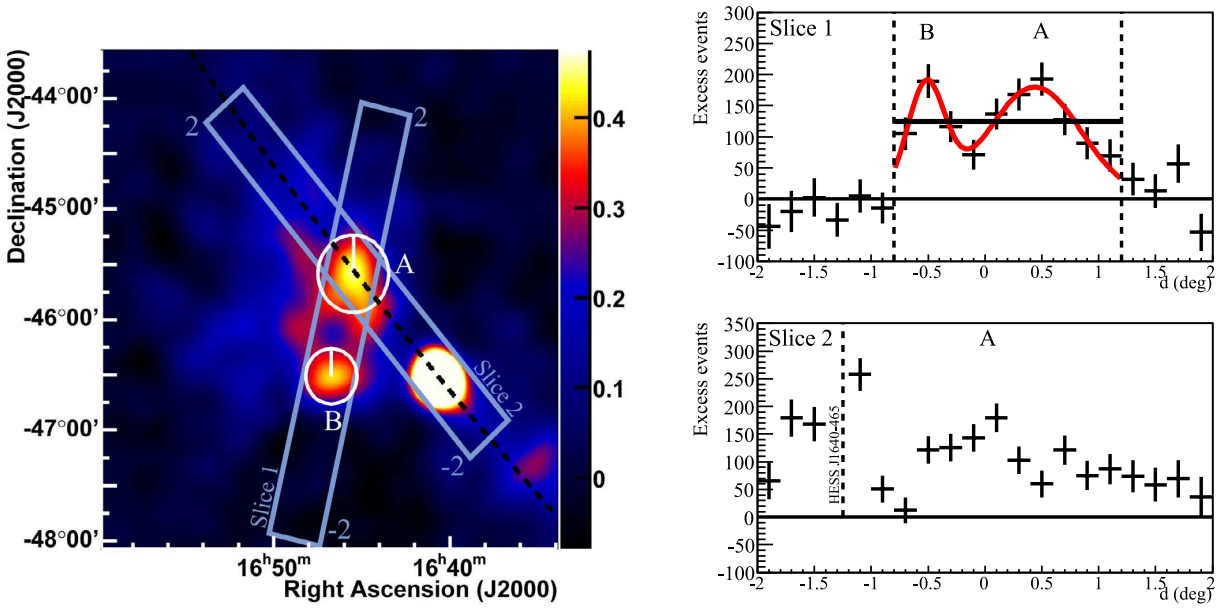

Fig. 3. *Left*: H.E.S.S. excess map as shown in Fig. 1 but for an enlarged region of 4.5° × 4.5°. The blue-grey boxes denote the regions used to generate the one-dimensional slices shown on the right. The white circles denote regions *A* and *B* which were used for spectral reconstruction (Table 2). The weak γ-ray emission seen in the lower right corner next to HESS J1640–465 is HESS J1634–472, also detected during the GPS (Aharonian et al. 2006c). *Right, top*: distribution of VHE γ-ray excess events in the blue-grey box, oriented along the two emission regions associated to HESS J1646–458 and starting at low Declination angles. The results of a fit of a constant and of two sources with Gaussian shape are indicated as black and red line, respectively. *Right, bottom*: same as top, but oriented along the Galactic plane, starting at low Right Ascension angles, close to the bright source HESS J1640–465 at $d = -1.25°$. The slice has been truncated at 350 excess events in order to emphasize the VHE γ-ray emission from HESS J1646–458.

material located along the Galactic plane. As will be shown later in Fig. 6, there is indeed molecular material located in this region which could act as target for the interaction with CRs (as described in e.g. Casanova et al. 2009) and could account for part of the observed emission. The statistics of region *A* and *B* compared to the entire source region as obtained with the *template* background method are given in Table 1.

The studies presented here show some evidence for a multi-source morphology and a separation into multiple VHE γ-ray sources. Moreover, spectral variations across the whole emission region, e.g. as observed for HESS J1825–137 (Aharonian et al. 2006d) or in the case of the H.E.S.S. sources in the Westerlund 2 field (Abramowski et al. 2011), could be apparent, which would further support the multi-source hypothesis. In this case, an energy-dependent morphology can be expected. To test this hypothesis, the complete data set has been divided into a low-energy band, containing events with reconstructed energies $E < 1.0$ TeV and a high-energy band, containing events with reconstructed energies $E > 1.0$ TeV. The unsmoothed excess maps in coarse bins of 0.3° width are used to test the underlying distribution. A χ^2 test is performed using the number of excess events in each bin and reveals a value of 95.4 for 76 degrees of freedom (four bins covering HESS J1640–465 have been excluded in the calculation). Prior to the test a χ^2 probability p_0 of 0.05 is defined to accept/reject the null hypothesis. The *p*-value of the test is 6.5% $> p_0$, such that the null hypothesis that both excess maps follow the same underlying distribution cannot be rejected. Although no energy-dependent morphology can be detected from this test, a multi-source origin is preferred given the low probabilities for the single source fits.

3.3. Spectrum

The spectrum obtained for the whole emission region using the *On-Off* background estimation method is shown in Fig. 4. In the fit range between 0.45 TeV and 75 TeV, the spectrum is well described by a power law: $\mathrm{d}N/\mathrm{d}E = \Phi_0 \times (E/1\ \mathrm{TeV})^{-\Gamma}$ with a photon index $\Gamma = 2.19 \pm 0.08_{\mathrm{stat}} \pm 0.20_{\mathrm{sys}}$, and a differential flux normalisation at 1 TeV of $\Phi_0 = (9.0 \pm 1.4_{\mathrm{stat}} \pm 1.8_{\mathrm{sys}}) \times 10^{-12}\,\mathrm{TeV}^{-1}\,\mathrm{cm}^{-2}\,\mathrm{s}^{-1}$. This translates into an integral flux above 0.2 TeV of $F(>0.2\ \mathrm{TeV}) = (5.2 \pm 0.9) \times 10^{-11}\,\mathrm{cm}^{-2}\,\mathrm{s}^{-1}$. The χ^2 for the power law fit is 9.9 for 7 degrees of freedom, yielding a χ^2 probability of 19%.

Additionally, the differential energy spectra for region *A* and *B* are determined using the *reflected* background estimation method with results found to be consistent with the *On-Off* background technique. The integral flux above 0.2 TeV as well as the spectral results obtained from a power-law fit are summarised in Table 2 and compared to the results for the spectral analysis of the whole 1.1° region. The differential energy spectra for these two regions are shown in Fig. 4 as well. Within statistical errors, no change in photon index between the three studied regions is apparent, further supporting the lack of energy-dependent morphology across the source based on the current data.

4. Discussion

In this section, the spectral and morphological results are used to elaborate possible acceleration scenarios related to HESS J1646–458. Although the morphological analysis prefers a two-source approach (at the ~2.5σ level), the similarity of the

Table 1. VHE γ-ray statistics for the regions shown in Figs. 1 and 3.

Region	RA (J2000) deg	Dec (J2000) deg	θ deg	*On* events	*Off* events	α	Excess events	Significance σ
Full	251.856	−45.909	1.1	19 032	1 107 471	0.014682	2771	20.1
A	251.370	−45.585	0.35	2313	120 104	0.014998	511	10.0
B	251.682	−46.513	0.25	1149	58 995	0.014876	271	6.5

Table 2. Spectral properties of the different TeV extraction regions.

Region	Φ_0(1 TeV) 10^{-12} TeV^{-1} cm^{-2} s^{-1}	Γ	F(>0.2 TeV) 10^{-11} cm^{-2} s^{-1}	% total
Full	9.0 ± 1.4	2.19 ± 0.08	5.2 ± 0.9	100
A	2.1 ± 0.3	2.11 ± 0.12	1.1 ± 0.2	21 ± 4
B	1.4 ± 0.2	2.29 ± 0.17	0.8 ± 0.2	15 ± 4

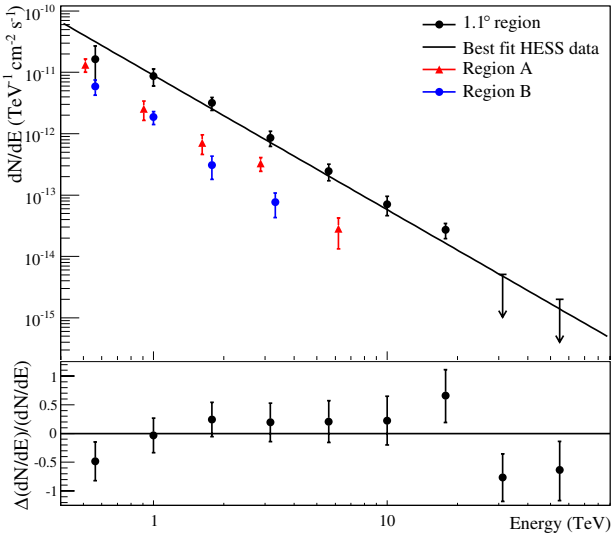

Fig. 4. *Top*: differential VHE γ-ray energy spectrum of HESS J1646–458. The data are fit by a power law $dN/dE = \Phi_0 \times (E/1\ \mathrm{TeV})^{-\Gamma}$. Arrows indicate the 95% upper limits for spectral bins which are compatible with a zero flux within 1σ. Also shown are spectra as obtained for region *A* and *B*. *Bottom*: residuals of the power-law fit for the 1.1° γ-ray emission region.

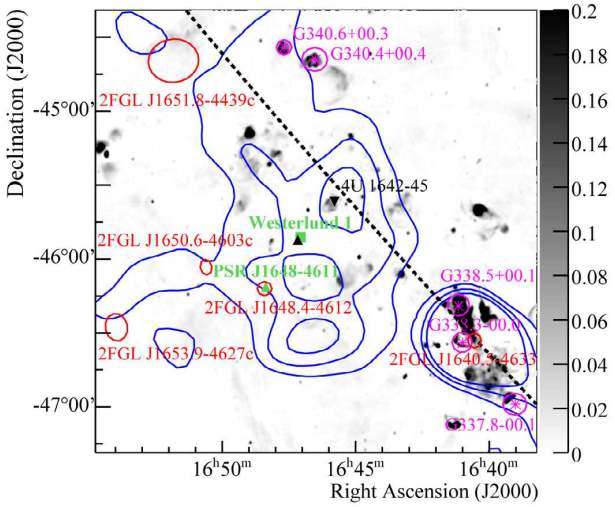

Fig. 5. H.E.S.S. smoothed VHE γ-ray excess contours in blue overlaid on the Molonglo 843 MHz map (grey scale, in Jy/beam; Green et al. 1999). Also shown are SNRs (purple, Green 2009), the pulsar PSR J1648–4611 (Manchester et al. 2005), the LMXB 4U 1642–45 (Forman et al. 1978), *Fermi*-LAT sources (Abdo et al. 2011), the magnetar CXOU J164710.2–455216 (Muno et al. 2006a) as a black upright triangle and the stellar cluster Wd 1.

spectra from region *A* and *B* does not allow to substantiate the preference for a two-source scenario further. Owing to this ambiguity, we pursue both possibilities through all portrayed counterpart scenarios.

Due to the large size of HESS J1646–458 (~2°), a few objects that could be regarded as potential VHE γ-ray emitter are found in the region of interest. Besides the massive stellar cluster Westerlund 1, a high spin-down power pulsar PSR J1648–4611 (Manchester et al. 2005) which has recently been discovered to be a high-energy γ-ray pulsar with a possible unpulsed γ-ray component is found (Kerr 2009; Abdo et al. 2010, 2011). Furthermore, the low-mass X-ray binary (LMXB) 4U 1642–45 (Forman et al. 1978), the magnetar candidate CXOU J164710.2–455216 (Muno et al. 2006a) and three unidentified *Fermi*–LAT sources, 2FGL J1650.6–4603c, 2FGL J1651.8–4439c and 2FGL J1653.9–4627c (Abdo et al. 2011) are located within HESS J1646–458 (Fig. 5).

In the following, the discussion will focus only on the astrophysically associated objects with known distance and energetics.

4.1. 4U 1642–45

The X-ray bright LMXB 4U 1642–45 with an accreting neutron star lies within the strong emission region *A* (Fig. 5) and is located at a distance of 8.5 to 11.8 kpc (van Paradijs & White 1995; Grimm et al. 2002; Gilfanov et al. 2003). It exhibits an average X-ray luminosity of $L_X \approx 10^{38}$ erg s^{-1} and Grimm et al. (2002) reported of periods of super-Eddington luminosity from *ASM* observations.

So far, only high-mass X-ray binary systems have been associated with point-like and variable VHE γ-ray sources (e.g. LS 5039, Aharonian et al. 2005, 2006e). At 8.5 to 11.8 kpc, HESS J1646–458 would be 320 to 450 pc in size and region

Table 3. Properties and inferred γ-ray luminosities of the pulsars and the VHE γ-ray emission regions.

Object / Region	τ 10^5 yrs	d kpc	P_0 s	$\dot{P}$ 10^{-13} s s^{-1}	$\dot{E}$ 10^{34} erg s^{-1}	$L_\gamma{}^{(1)}$ 10^{34} erg s^{-1}
CXOU J164710.2–455216[a]	1.8	5	10.6	9.2	3×10^{-3}	26
PSR J1648–4611[b]	1.1	5.7	0.2	0.2	21	34
HESS J1646–458	–	4.3	–	–	–	19
Region *A*	–	4.3	–	–	–	4.6
Region *B*	–	4.3	–	–	–	2.9

Notes. [(1)] Obtained by scaling the observed VHE γ-ray flux between 0.1 and 100 TeV to the nominal or adopted distance of the respective object.
References. [(a)] Muno et al. (2006a); Israel et al. (2007). [(b)] Manchester et al. (2005).

A 100 to 144 pc, for angular diameters of 2.2° and 0.7° respectively. These inferred source sizes are well beyond the H.E.S.S. PSF in this analysis (26 to 35 pc in diameter). A check for variability at the position of 4U 1642–45 did not reveal any indication of such as has been observed, e.g. in the case of LS 5039 and HESS J0632+057 (Aharonian et al. 2006e, 2007).

In summary, an association of 4U 1642–45 and the entire VHE γ-ray emission region is unlikely. The extent of the subregion *A* also disfavours a scenario with 4U 1642–45 and a subregion as well. An association with region *A* would be solely based on spatial coincidence but would then present a new class of VHE γ-ray sources.

4.2. CXOU J164710.2–455216

This anomalous X-ray pulsar is considered a magnetar and has been associated with Wd 1 given its apparent proximity to the cluster and the low probability of a random association (Muno et al. 2006a). Shortly after its X-ray discovery, an outburst in X-rays was reported from *Swift* observations (Campana & Israel 2006). Additionally, *XMM-Newton* observations were conducted prior to and after the outburst (Muno et al. 2007; Israel et al. 2007).

The observed X-ray luminosity is $L_X \approx 3 \times 10^{33}$ erg s^{-1} which increased during the outburst by a factor of $\sim$ 100. The rotation period is 10.6 s with a derivative of $\dot{P} = 9.2 \times 10^{-13}$ s s^{-1} which infers an X-ray spin-down power of $\dot{E} = 3 \times 10^{31}$ erg s^{-1} and a characteristic age of $\tau = 1.8 \times 10^5$ yrs. The surface magnetic-field strength is $\sim 1 \times 10^{14}$ G. The relevant properties of CXOU J164710.2–455216 are listed in Table 3.

Since the X-ray luminosity exceeds the rotational spin-down power, this suggests that the observed X-ray emission is not due to spin-down processes, but some other form. For magnetars, the intense magnetic field can yield considerable power in magnetic dissipative processes. Following Zhang (2003), such power can be of the order $L_{\rm mag} \approx 10^{35}$ erg s^{-1}, which, for CXOU J164710.2–455216, would dominate over the rotational spin-down power. If acceleration of particles to TeV energies occurs due to magnetic energy release one could expect a rather compact TeV-emission region similar to spin-down powered TeV pulsar wind nebulae (PWNe) like the Crab nebula (Aharonian et al. 2006a).

However, it is still under investigation if magnetars can exhibit PWNe in general. For most pulsars, the respective PWNe would be too faint to be detected in X-rays (Gaensler & Slane 2006). In the VHE γ-ray regime, young ($O(10^3$ yrs)) and high spin-down power ($O(10^{34}$ erg s^{-1})) magnetars seem to be promising objects (Halpern & Gotthelf 2010).

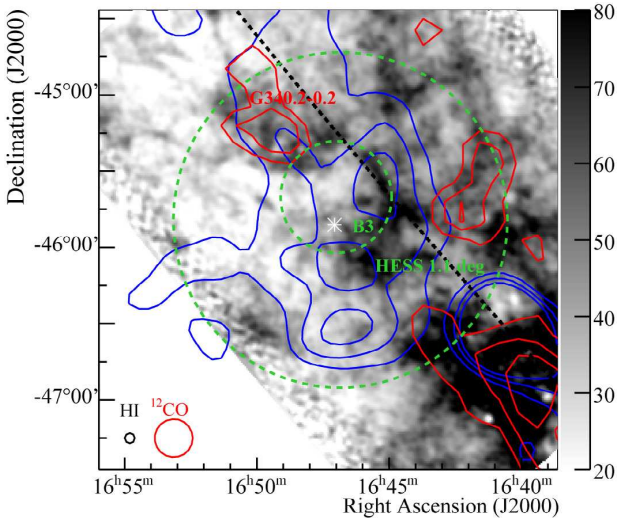

Fig. 6. HI 21 cm line emission map at a radial velocity of about -55 km s^{-1} (McClure-Griffiths et al. 2005) between 20 and 80 K. Bright regions are HI-depleted whereas dark regions are HI-dense. Overlaid are the CO contours (red) at 12.5, 22.5 and 32.5 K (Dame et al. 2001) along with the smoothed HESS J1646–458 contours in blue. The estimated position of the HI void *B3* is marked by the small green dashed circle (Kothes & Dougherty 2007). The large green dashed circle indicates the region used for the spectral reconstruction in the TeV regime and to compute the ambient matter density. The position of Wd 1 is marked by a white star in the centre. The circles in the lower left corner indicate the beam sizes of the respective radio observations.

However, the rotational spin-down power of CXOU J164710.2–455216 is too low to account for both the entire observed VHE γ-ray emission and either subregion. Therefore, any acceleration of particles would have to involve a magnetic energy release with a power output of $L_{\rm mag} \geq 10^{35}$ erg s^{-1}. The observed emission could then be explained by an energy conversion process that operates with efficiency up to 100% but the size of HESS J1646–458 ($\sim$160 pc at the distance of the magnetar) stands in contradiction to the expected compact region. Either of the two subregions could be energetically explained with efficiencies in the order of 0.5 but again as one would expect the resulting PWN to be compact and close to the magnetar itself, these scenarios are disfavoured as well.

All in all, VHE γ rays from CXOU J164710.2–455216 is not a favoured scenario to account for HESS J1646–458 or parts from it as its relevant properties and current (V)HE γ-ray observations do not support such an approach.

4.3. PSR J1648–4611

Among known VHE γ-ray sources, PWNe are the most abundant source type: Roughly one third of these sources are associated with PWN systems (e.g. Hinton & Hofmann 2009). The pulsar is found to be located in the centre of the nebula (e.g. the Crab nebula, Aharonian et al. 2006a) or offset from it (e.g. the Vela X nebula, Aharonian et al. 2006b). Most of the VHE γ-ray-emitting PWNe are spatially extended and offset from the pulsar position and efficient in terms of converting available spin-down power into γ-ray emission. In general, PWNe firmly associated with known pulsars convert 10% at most of their spin-down power into γ-ray luminosity (Gallant 2007).

The high spin-down power pulsar PSR J1648–4611 with $\dot{E} = 2.1 \times 10^{35}\,\mathrm{erg\,s^{-1}}$ (Manchester et al. 2005) is located within the emission region HESS J1646–458 and associated with the *Fermi*-LAT source 2FGL J1648.4–4612 (Abdo et al. 2011). Pulsed γ-ray emission with the rotation period of PSR J1648−4611 as well as signatures for a constant (possible PWN) contribution have been reported. Therefore, this object has to be considered a γ-ray pulsar at low GeV energies. Inspection of archival *Chandra* data with 10 ks exposure (obsid: 11836) shows no indication for the presence of an X-ray counterpart to PSR J1648–4611. Following the relation between spin-down power and X-ray luminosity of PWNe (Mattana et al. 2009), the expected X-ray luminosity $L_X \approx 5 \times 10^{30}\,\mathrm{erg\,s^{-1}}$ of the associated PWN would not be detectable with current X-ray instruments and is hence consistent with the non-detection with *Chandra*.

The first attempt to explain HESS J1646–458 is a single-source scenario which is motivated by the presence of the HE pulsar PSR J1648–4611. The inferred γ-ray luminosity (0.1−100 TeV) at the distance of PSR J1648–4611 would require a conversion efficiency $\epsilon_{\mathrm{eff}} \approx 1$. Additionally, the size of the VHE γ-ray-emitting region would extend over roughly 200 pc which is a factor 3−10 larger than known extended VHE γ-ray-emitting PWN systems. Given the size, cooling losses would lead to considerable softening of the VHE γ-ray spectrum and a downward shift of the maximum energy with increasing distance from the pulsar – similar to the spectral softening of HESS J1825–137 (Aharonian et al. 2006d). The VHE γ-ray photon index reconstructed at the position of PSR J1648−4611 is $\Gamma = 2.37 \pm 0.43$ using the *reflected*-background regions method and assuming a point-like source origin. This is compatible within statistical errors with the emission of the entire region. However, the available statistics do not permit firm conclusions about potential spectral changes across HESS J1646–458 to be drawn. In summary, the unprecedented high efficiency needed and the size of the VHE γ-ray emission region disfavour HESS J1646–458 as a very extended PWN.

In a two-source approach as motivated in Sect. 3.2, a displacement of PSR J1648–4611 from either subregion is apparent. The pulsar is displaced by ∼50−70 pc from region *A* and *B*. These offsets are large compared to those of known VHE γ-ray PWNe but could in principle be explained by relative proper motion of the pulsar assuming a transversal velocity of $O(500\,\mathrm{km\,s^{-1}})$ which is at the upper end of the range of known transversal motions of pulsars (Manchester et al. 2005). In this scenario, one of the two subregions could in principle be powered by the pulsar with $\epsilon_{\mathrm{eff}} \approx 0.1 \ldots 0.2$. In this case, the morphology would reflect the ambient conditions, e.g. one of the subregions could be the result of the expansion of the PWN into a low-density medium or could be due to an asymmetric reverse shock of the SNR.

Recently, Luna et al. (2010) proposed that a region of low density in CO seems to partially match structures in preliminary VHE γ-ray data (Ohm et al. 2010b) and for which a SN event with PSR J1648–4611 as precursor could be responsible. However, the kinematic age of the cavity is about 55 times larger than the characteristic age of PSR J1648–4611 and the inferred subsonic expansion velocity is insufficient to accelerate particles up to the VHE γ-ray regime. Moreover, other SNR candidates at the position of this cavity are not to be found in archival data and the morphology of HESS J1646–458 does not strongly motivate a shell-like structure centred at about $16^{\mathrm{h}}47^{\mathrm{m}}23.3^{\mathrm{s}}$, $-45°42'5.2''$ with an inner radius of ∼0.5° (Luna et al. 2010). Although it cannot be ruled out that this cavity could be blown as a consequence of a SN it seems unplausible that the whole ∼25 pc-thick shell would expand uniformly at 6−8 km s^{-1} and thereby giving rise to particle acceleration up to TeV energies.

Similarly as concluded for the magnetar, HESS J1646–458 seems unlikely to be explained as a very extended PWN powered by PSR J1648–4611. Either one of the subregions could be explained by an offset PWN. The inferred offsets would be comparatively large but the required efficiency would be amongst known TeV PWNe.

4.4. Westerlund 1

The motivation for H.E.S.S. observations of the Wd 1 region has been outlined earlier (see Sect. 1) and the analysis of HESS J1646–458 revealed that Wd 1 is located close to the centroid of the VHE γ-ray emission. Hence this massive cluster is an interesting object to consider. As some of its properties are still subject of on-going investigation certain assumptions are made: *(1)* Due to the high visual extinction of $A_v \approx 12^{\mathrm{mag}}$, distance estimates based on photometry and spectroscopy vary strongly between 1.1 kpc and 5.5 kpc (Westerlund 1987; Piatti et al. 1998; Clark et al. 2005; Brandner et al. 2008). Kothes & Dougherty (2007) derived a distance of 3.9 kpc based on the HI line emission which Luna et al. (2010) extrapolated to 4.3 kpc using the IAU distance recommendation to the Galactic Centre of 8.5 kpc. In this work, we adopt the 4.3 kpc albeit using a more recent Galactocentric distance estimate of 8.33 kpc (Gillessen et al. 2009). *(2)* Different model-dependent approaches to estimate the age suffer from the apparent lack of main-sequence stars. Recently, Negueruela et al. (2010) estimated the age to be ≳5 Myr and an age of 5 Myr is adopted here. *(3)* A cluster mass of $10^5\ M_\odot$ is assumed.

Estimates based on the stellar population of Wd 1 imply that 80 to 150 stars with initial masses exceeding 50 $M_\odot$ have already undergone a SN explosion (Muno et al. 2006b). However, neither radio nor X-ray observations have revealed any SNR candidate. In order to estimate the total kinetic energy dissipated by the system through SNe and stellar winds the *Starburst99* cluster evolution model (Leitherer et al. 1999; Vázquez & Leitherer 2005; Leitherer et al. 2010) has been used. The default parameters with the standard Kroupa initial mass function (with the exponents 1.3 and 2.3, (Kroupa 2002)) and the *evolutionary*-model option, have been chosen. The total energy dissipated at the nominal age of Wd 1 including stellar winds and SNe amounts to $E_{\mathrm{kin}} = 3.0 \times 10^{53}$ erg.

For an adiabatically expanding wind (Weaver et al. 1977; Silich et al. 2005), a structured and expanding (∼30 km s^{-1}) hot bubble with an outer shock radius of ∼250 pc is expected to form around Wd 1 even if only a moderate number of 50 OB stars are considered. However, a dedicated search for such a super bubble-like structure in HI and CO data at the radial velocity of

Wd 1 did not reveal any signatures of such a feature (McClure-Griffiths et al. 2005; Kothes & Dougherty 2007). The latter authors find indications for a much smaller (55 pc) and slowly expanding ($3\,\mathrm{km\,s^{-1}}$) feature (*B3* in Kothes & Dougherty 2007), see Fig. 6. However, in this first approximation, radiative cooling is not considered although this cooling process might affect the evolution of stellar cluster winds (e.g. discussed in Wünsch et al. 2008).

Kothes & Dougherty (2007) interpret the formation of the HII region complex G340.2−0.2 (depicted in Fig. 6) as triggered by the stellar wind activity of Wd 1. Indeed, if Wd 1 is located at a distance of 4.3 kpc some correlation between VHE γ rays and the location of this HII region is expected.

An average gas density for atomic hydrogen n_{HI} and molecular gas $n_{\mathrm{H_2}}$ can be derived using available HI and CO data in the velocity range of Wd 1 (-50 to $-60\,\mathrm{km\,s^{-1}}$) for the entire 1.1° region of interest. For this, all pixel values in this velocity range and within 1.1° from the cluster position are considered as well as the SGPS beam size (130 arcsecs) and the oversampling factor (11.97). With the HI intensity-mass conversion factor of $1.823 \times 10^{18}\,\mathrm{cm^{-2}/(K\,km\,s^{-1})}$ (Yamamoto et al. 2003), the result[2] is $n_{\mathrm{HI}} = 0.24\,\mathrm{cm^{-3}}$. In the CO data (Dame et al. 2001), a low-density region around the cluster seems to be apparent as well (Fig. 6). This feature is larger than *B3*. With a beam size of 450 arcsecs and a oversampling factor of 1, the application of the conversion factor of CO to H_2 of $1.5 \times 10^{20}\,\mathrm{cm^{-2}/(K\,km\,s^{-1})}$ (Strong et al. 2004) leads to an average density of H_2 molecules in units of atomic hydrogen of $n_{\mathrm{H_2}} = 12.16\,\mathrm{cm^{-3}}$. Note that the X factor used for the CO data incorporates caveats pointed out in Strong et al. (2004). The required energy in CRs to power the γ-ray emission can now be estimated:

$$E_{\mathrm{CR}} = 2.1 \times 10^{50} \left(\frac{L_{>1\,\mathrm{GeV}}}{5.8 \times 10^{35}\,\mathrm{erg\,s^{-1}}} \right) \left(\frac{n_{\mathrm{HI}} + n_{\mathrm{H_2}}}{12.4\,\mathrm{cm^{-3}}} \right)^{-1} \mathrm{erg},$$

where $L_{>1\,\mathrm{GeV}}$ is the high-energy luminosity computed with the spectral results presented earlier between 1 GeV and 1 PeV.

When interpreted in a single-source scenario, the required efficiency for transferring kinetic energy in shocks or turbulences into energetic particles through acceleration is therefore at the level of ∼0.1%. For a similar argument as for the PWN interpretation, a leptonic origin of the VHE γ-ray emission is difficult to reconcile with the large extent of HESS J1646–458 which translates into a size of 160 pc at the distance of the cluster. Given the large photon density in the environment of Wd 1, a fast convective transport of the electrons would be required to prevent them from cooling. Hence a dominant hadronic origin is favoured in this approach.

A possible two-source scenario would also consist of a dominant hadronic CR component as the stellar photon field would lead to a rapid cooling of VHE electrons. In this case, bright VHE γ-ray structures would trace dense features in HI and CO. In particular, region *A* lies at the edge of *B3* and is coincident with dense structures in HI (see Fig. 6) which would naturally provide sufficient target material. Region *B*, however, remains comparatively dark as HI and CO data do not suggest a higher abundance of target material.

In summary, Wd 1 and its massive stars favour a hadronic mechanism for the entire emission region. Here, the size and the inferred energetics of HESS J1646–458 could be plausibly explained. In case of the two subregions, or multiple source regions in general, more observational data in all wavelength bands and detailed modelling are required.

[2] The density n is proportional to $\sum b^2 p_i R^{-1} f_s^{-2}$ where p_i are the pixel values of the HI or CO map, R the radius of the region of interest, b the beam size of the respective experiment and f_s is the oversampling factor in the respective HI or CO maps used.

5. Summary and conclusions

In summary, HESS J1646–458 is a new VHE γ-ray source found towards the unique massive stellar cluster Westerlund 1 and a number of other potential counterparts. The large size of HESS J1646–458 however, over 2 degrees in diameter making it one of the largest TeV sources so far detected by H.E.S.S., presents a challenge in identifying a clear counterpart (or a number of counterparts) to explain the VHE γ-ray emission.

The detection of degree-scale VHE γ-ray emission, namely HESS J1646–458, towards the stellar cluster Westerlund 1 with a total significance of 20σ from H.E.S.S. observations performed in the years 2004, 2007 and 2008 (33.8 hrs live time) is reported. The energy spectrum between 0.45 TeV and 75 TeV of the entire region is best fit by a simple power law with an index $\Gamma = 2.19 \pm 0.08_{\mathrm{stat}} \pm 0.2_{\mathrm{sys}}$ and a normalisation at 1 TeV $\Phi_0 = (9.0 \pm 1.4_{\mathrm{stat}} \pm 1.8_{\mathrm{sys}}) \times 10^{-12}\,\mathrm{TeV^{-1}cm^{-2}s^{-1}}$ with $\chi^2/\mathrm{ndf} = 9.9/7$. The integrated flux above 0.2 TeV amounts to $(3.49 \pm 0.52) \times 10^{-11}\,\mathrm{cm^{-2}\,s^{-1}}$. The VHE γ-ray luminosity between 0.1 and 100 TeV is $1.9 \times 10^{35}\,(d/4.3\,\mathrm{kpc})^2\,\mathrm{erg\,s^{-1}}$.

The centroid of HESS J1646–458 is consistent with the nominal position of Wd 1. The observed VHE γ-ray emission region has a diameter of about 2° which translates into a spatial extent of 160 pc at the distance of Wd 1 or 200 pc at the distance of PSR J1648–4611. In either case, the size of HESS J1646–458 would be the largest among currently known VHE γ-ray sources, if the emission is of a single-source origin. This is supported by the lack of spectral changes across HESS J1646–458 within statistical errors. Although there is some evidence for a multi-source morphology, the limited statistics hamper a detailed investigation into the presence of multiple sources.

In a scenario where one astrophysical object is responsible for HESS J1646–458, Wd 1 could naturally account for the required injection power provided that about 0.1% ($n/12.4\,\mathrm{cm^{-3}}$) of the kinetic energy released by stellar winds and supernova explosions are converted into particle acceleration. In this case, the stellar wind and SNe activity of Wd 1 would strongly affect the surroundings but also reflect the ambient conditions.

In a split of HESS J1646–458 into two distinct subregions, however, a superposition of two or more sources adding up to the observed VHE γ-ray emission region could be possible. In this case, one of the subregions could also be explained by a PWN with comparatively large offset from PSR J1648–4611. Despite the spatial coincidence, the LMXB 4U 1642–45 and the magnetar CXOU 164710.2–455216 are not likely to account for HESS J1646–458 or parts of it.

Further multiwavelength observations (in particular those covering the VHE γ-ray source in full), and deeper VHE γ-ray coverage will no doubt be valuable in shedding light on the nature of this source.

Acknowledgements. The support of the Namibian authorities and of the University of Namibia in facilitating the construction and operation of H.E.S.S. is gratefully acknowledged, as is the support by the German Ministry for Education and Research (BMBF), the Max Planck Society, the French Ministry for Research, the CNRS-IN2P3 and the Astroparticle Interdisciplinary Programme of the CNRS, the UK Particle Physics and Astronomy Research Council (PPARC), the IPNP of the Charles University, the South African Department of Science and Technology and National Research Foundation, and by the University of Namibia. We appreciate the excellent work of the technical support staff in Berlin, Durham, Hamburg, Heidelberg, Palaiseau, Paris,

Saclay, and in Namibia in the construction and operation of the equipment. This research has made use of NASA's Astrophysics Data System. This research has made use of the SIMBAD database, operated at CDS, Strasbourg, France. SO acknowledges the support of the Humboldt foundation by a Feodor-Lynen research fellowship.

References

Abdo, A. A., Ackermann, M., Ajello, M., et al. 2010, Fermi/Large Area Telescope 1 year catalog, http://fermi.gsfc.nasa.gov/ssc/data/access/lat/1yr_catalog/1FGL_catalog_v2.pdf
Abdo, A. A., Ackermann, M., Ajello, M., et al. 2011, Fermi/Large Area Telescope 2 year catalog, http://fermi.gsfc.nasa.gov/ssc/data/access/lat/2yr_catalog/
Abramowski, A., Acero, F., Aharonian, F., et al. 2011, A&A, 525, A46
Acciari, V. A., Aliu, E., Arlen, T., et al. 2011, ApJ, 730, L20
Aharonian, F., Akhperjanian, A. G., Aye, K., et al. 2005, Science, 309, 746
Aharonian, F., Akhperjanian, A. G., Bazer-Bachi, A. R., et al. 2006b, A&A, 448, L43
Aharonian, F., Akhperjanian, A. G., Bazer-Bachi, A. R., et al. 2006a, A&A, 457, 899
Aharonian, F., Akhperjanian, A. G., Bazer-Bachi, A. R., et al. 2006c, ApJ, 636, 777
Aharonian, F., Akhperjanian, A. G., Bazer-Bachi, A. R., et al. 2006d, A&A, 460, 365
Aharonian, F., Akhperjanian, A. G., Bazer-Bachi, A. R., et al. 2006e, A&A, 460, 743
Aharonian, F. A., Akhperjanian, A. G., Bazer-Bachi, A. R., et al. 2007, A&A, 469, L1
Axford, W. I., Leer, E., & Skadron, G. 1977, in International Cosmic Ray Conference, 11, International Cosmic Ray Conference, 132
Bamba, A., Ueno, M., Nakajima, H., & Koyama, K. 2004, ApJ, 602, 257
Bednarek, W. 2005, MNRAS, 363, L46
Bell, A. R. 1978, MNRAS, 182, 443
Benaglia, P., & Romero, G. E. 2003, A&A, 399, 1121
Berge, D., Funk, S., & Hinton, J. 2007, A&A, 466, 1219
Blandford, R. D., & Ostriker, J. P. 1978, ApJ, 221, L29
Brandner, W., Clark, J. S., Stolte, A., et al. 2008, A&A, 478, 137
Bykov, A. M. 2001, Space Sci. Rev., 99, 317
Campana, S., & Israel, G. L. 2006, The Astronomer's Telegram, 893, 1
Casanova, S., Aharonian, F. A., Gabici, S., et al. 2009, in AIP Conf. Ser.
Chaves, R. C. G., de Oña Wilhemi, E., & Hoppe, S. 2008, in AIP Conf. Ser. 1085, ed. F. A. Aharonian, W. Hofmann, & amp, F. Rieger, 219
Clark, J. S., Negueruela, I., Crowther, P. A., & Goodwin, S. P. 2005, A&A, 434, 949
Clark, J. S., Negueruela, I., Ritchie, B., Crowther, P., & Dougherty, S. 2010, The Messenger, 142, 31
Cooper, R. L., Guerrero, M. A., Chu, Y., Chen, C., & Dunne, B. C. 2004, ApJ, 605, 751
Crowther, P. A., Hadfield, L. J., Clark, J. S., Negueruela, I., & Vacca, W. D. 2006, MNRAS, 372, 1407
Dame, T. M., Hartmann, D., & Thaddeus, P. 2001, ApJ, 547, 792
de Naurois, M., & Rolland, L. 2009, Astropart. Phys., 32, 231
Domingo-Santamaría, E., & Torres, D. F. 2006, A&A, 448, 613
Dougherty, S. M., Clark, J. S., Negueruela, I., Johnson, T., & Chapman, J. M. 2010, A&A, 511, A58
Eichler, D., & Usov, V. 1993, ApJ, 402, 271
Ellison, D. C., Patnaude, D. J., Slane, P., & Raymond, J. 2010, ApJ, 712, 287
Ferrand, G., & Marcowith, A. 2010, A&A, 510, A101
Forman, W., Jones, C., Cominsky, L., et al. 1978, ApJS, 38, 357
Gaensler, B. M., & Slane, P. O. 2006, ARA&A, 44, 17
Gallant, Y. A. 2007, Ap&SS, 309, 197
Gies, D. R. 2008, in Massive Star Formation: Observations Confront Theory, ed. H. Beuther, H. Linz, & T. Henning, ASP Conf. Ser., 387, 93
Gilfanov, M., Revnivtsev, M., & Molkov, S. 2003, A&A, 410, 217
Gillessen, S., Eisenhauer, F., Trippe, S., et al. 2009, ApJ, 692, 1075
Green, D. A. 2009, Bull. Astron. Soc. India, 37, 45
Green, A. J., Cram, L. E., Large, M. I., & Ye, T. 1999, ApJS, 122, 207
Grimm, H., Gilfanov, M., & Sunyaev, R. 2002, A&A, 391, 923
Halpern, J. P., & Gotthelf, E. V. 2010, ApJ, 725, 1384
H.E.S.S. Collaboration, Abramowski, A., Acero, F., et al. 2011, 531, A81
Higdon, J. C., & Lingenfelter, R. E. 2003, ApJ, 590, 822
Hillas, A. M. 1985, in International Cosmic Ray Conference, ed. F. C. Jones, 3, 445
Hinton, J. A., & Hofmann, W. 2009, ARA&A, 47, 523
Israel, G. L., Campana, S., Dall'Osso, S., et al. 2007, ApJ, 664, 448
Kerr, M. 2009
Kothes, R., & Dougherty, S. M. 2007, A&A, 468, 993
Kroupa, P. 2002, Science, 295, 82
Krymskii, G. F. 1977, Akademiia Nauk SSSR Doklady, 234, 1306
Law, C., & Yusef-Zadeh, F. 2004, ApJ, 611, 858
Leitherer, C., Schaerer, D., Goldader, J. D., et al. 1999, ApJS, 123, 3
Leitherer, C., Ortiz Otálvaro, P. A., Bresolin, F., et al. 2010, ApJS, 189, 309
Luna, A., Mayya, Y. D., Carrasco, L., & Bronfman, L. 2010, ApJ, 713, L45
Manchester, R. N., Hobbs, G. B., Teoh, A., & Hobbs, M. 2005, AJ, 129, 1993
Manolakou, K., Horns, D., & Kirk, J. G. 2007, A&A, 474, 689
Mattana, F., Falanga, M., Götz, D., et al. 2009, ApJ, 694, 12
McClure-Griffiths, N. M., Dickey, J. M., Gaensler, B. M., et al. 2005, ApJS, 158, 178
Montmerle, T. 1979, ApJ, 231, 95
Mücke, A., & Pohl, M. 2002, in Interacting Winds from Massive Stars, ed. A. F. J. Moffat & N. St-Louis, ASP Conf. Ser., 260, 355
Muno, M. P., Clark, J. S., Crowther, P. A., et al. 2006a, ApJ, 636, L41
Muno, M. P., Law, C., Clark, J. S., et al. 2006b, ApJ, 650, 203
Muno, M. P., Gaensler, B. M., Clark, J. S., et al. 2007, MNRAS, 378, L44
Negueruela, I., Clark, J. S., & Ritchie, B. W. 2010, A&A, 516, A78
Ohm, S., van Eldik, C., & Egberts, K. 2009, Astropart. Phys., 31, 383
Ohm, S., Fernandes, M. V., de Ona Wilhelmi, E., et al. 2010a, in 25th Texas Symposium on Relativistic Astrophysics
Ohm, S., Horns, D., Reimer, O., et al. 2010b, in ASP Conf. Ser. 422, ed. J. Martí, P. L. Luque-Escamilla, & J. A. Combi, 265
Oskinova, L. M. 2005, MNRAS, 361, 679
Piatti, A. E., Bica, E., & Claria, J. J. 1998, A&AS, 127, 423
Reimer, A., Pohl, M., & Reimer, O. 2006, ApJ, 644, 1118
Rowell, G. P. 2003, A&A, 410, 389
Silich, S., Tenorio-Tagle, G., & Añorve-Zeferino, G. A. 2005, ApJ, 635, 1116
Strong, A. W., Moskalenko, I. V., Reimer, O., Digel, S., & Diehl, R. 2004, A&A, 422, L47
van Paradijs, J., & White, N. 1995, ApJ, 447, L33
Vázquez, G. A., & Leitherer, C. 2005, ApJ, 621, 695
Weaver, R., McCray, R., Castor, J., Shapiro, P., & Moore, R. 1977, ApJ, 218, 377
Westerlund, B. 1961, AJ, 66, 57
Westerlund, B. E. 1987, A&AS, 70, 311
Wolk, S. J., Bourke, T. L., Smith, R. K., Spitzbart, B., & Alves, J. 2002, ApJ, 580, L161
Wünsch, R., Tenorio-Tagle, G., Palouš, J., & Silich, S. 2008, ApJ, 683, 683
Yamamoto, H., Onishi, T., Mizuno, A., & Fukui, Y. 2003, ApJ, 592, 217
Zhang, B. 2003, in Proceedings of the International Workshop on Strong Magnetic Fields and Neutron Stars, 83
Zinnecker, H. 2003, in A Massive Star Odyssey: From Main Sequence to Supernova, ed. K. van der Hucht, A. Herrero, & C. Esteban, IAU Symp., 212, 80
Zinnecker, H., & Yorke, H. W. 2007, ARA&A, 45, 481

[1] Universität Hamburg, Institut für Experimentalphysik, Luruper Chaussee 149, 22761 Hamburg, Germany
e-mail: milton.virgilio.fernandes@physik.uni-hamburg.de
[2] Laboratoire Univers et Particules de Montpellier, Université Montpellier 2, CNRS/IN2P3, CC 72, Place Eugène Bataillon, 34095 Montpellier Cedex 5, France
[3] Max-Planck-Institut für Kernphysik, PO Box 103980, 69029 Heidelberg, Germany
[4] Dublin Institute for Advanced Studies, 31 Fitzwilliam Place, Dublin 2, Ireland
[5] National Academy of Sciences of the Republic of Armenia, Yerevan
[6] Yerevan Physics Institute, 2 Alikhanian Brothers St., 375036 Yerevan, Armenia
[7] Universität Erlangen-Nürnberg, Physikalisches Institut, Erwin-Rommel-Str. 1, 91058 Erlangen, Germany
[8] Nicolaus Copernicus Astronomical Center, ul. Bartycka 18, 00-716 Warsaw, Poland
[9] CEA Saclay, DSM/IRFU, 91191 Gif-Sur-Yvette Cedex, France
[10] University of Durham, Department of Physics, South Road, Durham DH1 3LE, UK
[11] Astroparticule et Cosmologie (APC), CNRS, Université Paris 7 Denis Diderot, 10 rue Alice Domon et Léonie Duquet, 75205 Paris Cedex 13, France (UMR 7164: CNRS, Université Paris VII, CEA, Observatoire de Paris)

[12] Laboratoire Leprince-Ringuet, École Polytechnique, CNRS/IN2P3, 91128 Palaiseau, France
[13] Institut für Theoretische Physik, Lehrstuhl IV: Weltraum und Astrophysik, Ruhr-Universität Bochum, D 44780 Bochum, Germany
[14] Landessternwarte, Universität Heidelberg, Königstuhl, 69117 Heidelberg, Germany
[15] Institut für Physik, Humboldt-Universität zu Berlin, Newtonstr. 15, 12489 Berlin, Germany
[16] LUTH, Observatoire de Paris, CNRS, Université Paris Diderot, 5 place Jules Janssen, 92190 Meudon, France
[17] LPNHE, Université Pierre et Marie Curie Paris 6, Université Denis Diderot Paris 7, CNRS/IN2P3, 4 place Jussieu, 75252 Paris Cedex 5, France
[18] Institut für Astronomie und Astrophysik, Universität Tübingen, Sand 1, 72076 Tübingen, Germany
[19] Astronomical Observatory, The University of Warsaw, Al. Ujazdowskie 4, 00-478 Warsaw, Poland
[20] Unit for Space Physics, North-West University, Potchefstroom 2520, South Africa
[21] Laboratoire d'Annecy-le-Vieux de Physique des Particules, Université de Savoie, CNRS/IN2P3, 74941 Annecy-le-Vieux, France
[22] Oskar Klein Centre, Department of Physics, Stockholm University, Albanova University Center, 10691 Stockholm, Sweden
[23] University of Namibia, Department of Physics, Private Bag 13301, Windhoek, Namibia
[24] Laboratoire d'Astrophysique de Grenoble, INSU/CNRS, Université Joseph Fourier, BP 53, 38041 Grenoble Cedex 9, France
[25] Department of Physics and Astronomy, The University of Leicester, University Road, Leicester, LE1 7RH, UK
e-mail: physoh@leeds.ac.uk
[26] Instytut Fizyki Jądrowej PAN, ul. Radzikowskiego 152, 31-342 Kraków, Poland
[27] Institut für Astro- und Teilchenphysik, Leopold-Franzens-Universität Innsbruck, 6020 Innsbruck, Austria
[28] Obserwatorium Astronomiczne, Uniwersytet Jagielloński, ul. Orla 171, 30-244 Kraków, Poland
[29] Toruń Centre for Astronomy, Nicolaus Copernicus University, ul. Gagarina 11, 87-100 Toruń, Poland
[30] School of Chemistry & Physics, University of Adelaide, Adelaide 5005, Australia
[31] Charles University, Faculty of Mathematics and Physics, Institute of Particle and Nuclear Physics, V Holešovičkách 2, 180 00 Prague 8, Czech Republic
[32] School of Physics & Astronomy, University of Leeds, Leeds LS2 9JT, UK
[33] European Associated Laboratory for Gamma-Ray Astronomy, jointly supported by CNRS and MPG

Chapter 6

The Unidentified very-high-energy Gamma-Ray Source HESS J1614–518

The work on this source began as a collaborative effort with Gavin Rowell on a H.E.S.S. collaboration paper. In the course of my work on this source I was handed over the corresponding authorship. From there on, I updated and re-wrote major parts of the draft that is currently in the H.E.S.S.-internal reviewing stage. All analyses (of H.E.S.S. and Fermi–LAT data), the investigation of archival data, the study of literature, and the discussions and the interpretation of all results presented in the following were done on my own and from scratch. Completely new are the statistical approach in the morphological study, the complete Fermi–LAT section, and the PWN discussion. Moreover, the discussions on the X-ray data from Suzaku, on Pismis 22, the pulsars were studied and elaborated in more detail.

The VHE γ-ray source HESS J1614–518 was discovered during the first scan[i] of the inner Galactic Plane with the H.E.S.S. telescope system in 2004 (Aharonian et al., 2005a). The position was determined to be (242.658°,−51.686°) in right ascension and declination (J2000) with a source radius of 0.2°. Through subsequent observations consisting of additional scan runs of the Galactic Plane and dedicated observations on this source, HESS J1614–518 was established as an extended bright TeV γ-ray source with an integral flux above 0.2 TeV of 25 % of that of the Crab Nebula in the same energy range (Aharonian et al., 2006b). Yet, this source remained without a counterpart in other wavelengths making HESS J1614–518 one of the brightest unidentified sources in the TeV γ-ray sky.

Follow-up studies showed that HESS J1614–518 is best-described by a two-peak structure (Rowell et al., 2008) and suggested the old stellar cluster Pismis 22 as a possible counterpart (Ohm et al., 2010). Motivated by Suzaku XIS observations, further counterpart scenarios were put forward involving an anomalous X-ray pulsar or an SNR origin (Matsumoto et al., 2008; Sakai et al., 2011).

In this work, additional unpublished H.E.S.S. data on HESS J1614–518 were used to search for morphological or spectral features providing insight into the nature of this source (Sect. 6.1). An extensive study of archival multi-wavelength (MWL) data was conducted in search of possible counterpart(s) of HESS J1614–518 (Sects. 6.2 and 6.3).

[i] *Scan* means non-dedicated observations conducted in order to map the Galactic Plane.

TABLE 6.1 Available high-quality H.E.S.S. data on HESS J1614–518 divided into periods of years. Stated are the mean run zenith angle and the mean wobble offset.

Year	Live time hrs	mean($z_{\rm obs}$) deg	mean($\omega_{\rm obs}$) deg	Reference
2004	16.3	33.4	1.3	Aharonian et al. (2005a)
2005	4.0	37.6	2.2	Aharonian et al. (2006b)
2007	2.7	30.3	0.8	this work
2008	1.7	29.2	2.2	this work
2009	6.1	30.1	2.0	this work
2011	2.2	29.0	1.3	this work
Total	32.9	32.5	1.4	

6.1 H.E.S.S. OBSERVATIONS AND DATA ANALYSIS

The region around HESS J1614–518 was observed in the first and second Galactic-Plane Scan with H.E.S.S. in the years 2004 and 2005 (Aharonian et al., 2005a, 2006b). In 2007, an X-ray outburst of the low-mass X-ray binary (LMXB) 4U 1608–52 prompted further observations of the vicinity of HESS J1614–518. Otherwise, the region around HESS J1614–518 has benefited in the following years from the H.E.S.S. objective to achieve a deep exposure within the inner Galactic Plane.

After rejecting runs affected by hardware problems and bad weather in the standard H.E.S.S.-data quality selection (Aharonian et al., 2006a), about 33 hours of high-quality data were accumulated between the years 2004 and 2011 up to an offset from $\sim 3^\circ$ w.r.t. the nominal source location. Moreover, 85 % of the data were taken with all four telescopes in operation. The mean run zenith angle of the observations is 32.5° and the mean of the run pointing-offset is 1.4°. The year-wise run properties are summarised in Table 6.1. As a result, about 13 more hours of data were used compared to Aharonian et al. (2006b), i.e. a third of more data.

In this work, the data were analysed using the H.E.S.S. analysis package (version `12-03pl02`). The calibration version of the data is `12-03`. As outlined in Section 3.3.4.4, the data are corrected for their different optical efficiency using the information of muon rings recorded by the telescope cameras.

For the morphological studies presented in the following, a good gamma/hadron separation and a good angular resolution are desirable, therefore the TMVA $\zeta_{\rm hard}$ cuts were used to separate γ rays and hadrons (Sect. 3.3.5). The background has been determined using the TBg model (Sect. 3.3.8.4). Many observations point *a posteriori* directly into the TeV γ-ray emission region, which makes it difficult to determine the camera acceptance from the individual run data. Therefore, the extra-Galactic look-ups of the camera acceptances were used (Sect. 3.3.8.6).

The background contribution to the energy spectra was determined using the Template Background Spectrum (TBS) introduced in Chapter 4. Here, a lower energy threshold is

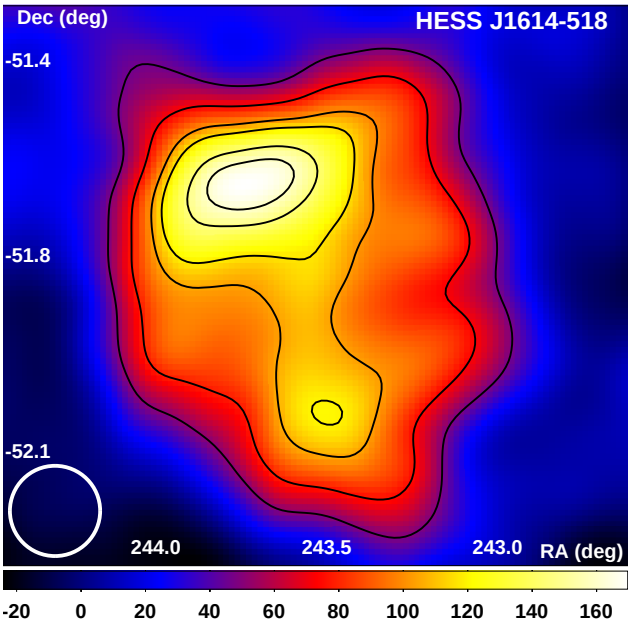

FIGURE 6.1 Smoothed exposure-corrected VHE γ-ray excess counts map in J2000 coordinates. Events are integrated within a radius of 0.1° at every bin centre. The black contours represent VHE γ-ray excess significance levels of $4, 6, 8, 9, 11, 12\,\sigma$. The white circle represents the H.E.S.S. PSF for this analysis and is 0.08°. The image was smoothed with a Gaussian of $\sigma = 0.08°$ to reduce statistical noise.

aimed for and thus, the standard Hillas cuts were applied. These results are to be found later in Section 6.1.2.

As a result of the TMVA ζ_{hard} analysis, HESS J1614–518 is detected with a significance of $26.4\,\sigma$ with 4018 γ-like events, 168781 hadron-like events and with a background normalisation of 0.0151 resulting in 1463 excess events. The source region is significantly larger than in previous analyses and now best-described by a circle of 0.51° in radius at (243.534°, −51.864°), which implies a shift of 0.07° w.r.t. the location in Aharonian et al. (2005a).

6.1.1 MORPHOLOGY

In Figure 6.1, the VHE γ-ray excess skymap is shown. The skymap has been produced using an integration radius of 0.1° at every bin centre and smoothed with a standard Gaussian with $\sigma = 0.08°$ (representing the PSF of this analysis) to reduce statistical noise in the skymap. Overlaid are the significance contours from $4\,\sigma$ to $8\,\sigma$ (in steps of $2\,\sigma$) and $9\,\sigma$, $11\,\sigma$, and $12\,\sigma$ (Eq. 3.22).

The source HESS J1614–518 is elongated along the declination axis. In the north of HESS J1614–518, a strong and extended emission region with a peak significance of $12.7\,\sigma$ is visible and extends towards the south of the source where a pronounced subregion is found as well with a peak significance of $9.1\,\sigma$.

In the following, a study is conducted to test for possible multi-source origins prompted

by the apparent two-peak structure seen in Figure 6.1 and by the results in Rowell et al. (2008) where a two-peak structure was favoured. Additionally, a search for an energy-dependent evolution in morphology was done.

6.1.1.1 MULTI-SOURCE HYPOTHESIS

HESS J1614–518 includes two pronounced subregions, one towards the north and the other one towards the south. To quantify this visual impression, a similar excess skymap was produced, but consisting of uncorrelated bins of 0.1° width. In this skymap, a rectangular slice with a dimension of $\sim 1.6° \times 0.6°$ was placed along the source encompassing most of the VHE γ-ray emission of HESS J1614–518 and both subregions of interest (see Figure 6.2, left). The events within this slice were projected against the major axis in 16 bins and resulted in a 1-dimensional projection (i.e. a histogram) of the initial 2-dimensional skymap. Analogously produced skymaps of the γ-like and the hadron-like events and of the background-normalisation were used to propagate the statistical errors on the excess. For convenience and to reduce the number of parameters to model later on, the excess-events distribution are normalised to the total amount of excess events within 0.4° (to avoid a contribution from HESS J1616–508 (Aharonian et al., 2005a) and the diffuse emission connecting both sources) and 1.4° (tail of zero-excess bins; Fig. 6.2, right).

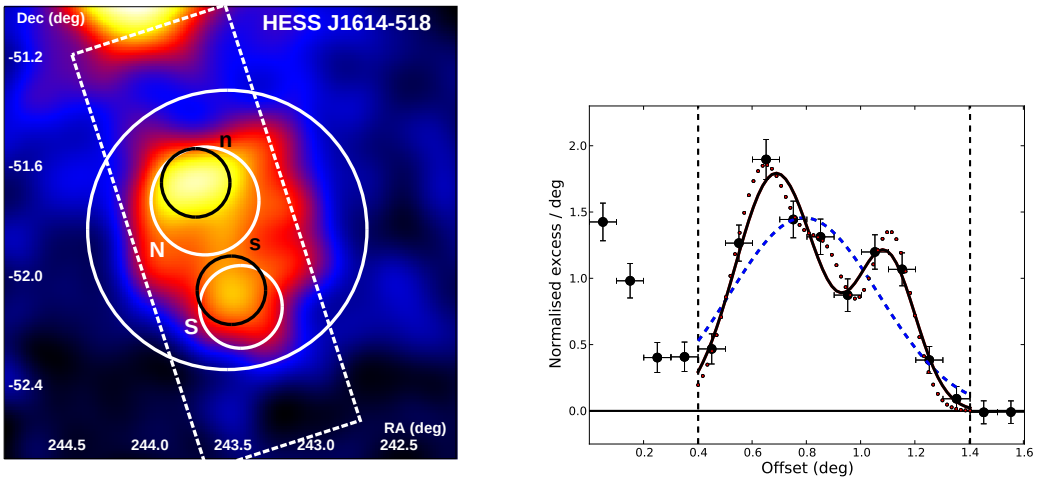

FIGURE 6.2 The slice along HESS J1614–518 and the subregions. **LEFT:** The same smoothed excess skymap as in Figure 6.1 but for a larger FoV. In this $1.6° \times 1.6°$ VHE γ-ray excess skymap, the slice and the northern and southern subregions (discussed later) are depicted. The subregions are used for the spectral analysis later on. The bright truncated source towards the north is HESS J1616–508 (Aharonian et al., 2005a). **RIGHT:** The distribution of excess events along the slice. The black solid line depicts the fit of two extended sources, the blue-dashed line represents the model of a single Gaussian and the red-dotted line is the representation of a three-source fit (1 point source and two extended sources). HESS J1616-508 and the diffuse emission connecting HESS J1616-508 and HESS J1614–518 are excluded from the fit.

Different source hypotheses were tested on the normalised events distribution along the slice, ranging from a single point-source origin up to three sources as superpositions of individual normalised Gaussian distributions adding up to the observed TeV source HESS J1614–518.

The normalised Gaussian distribution, which represents a single source is

$$g(x, \vec{p}) = g(x, \sigma, \mu) = \frac{1}{\sqrt{2\pi\sigma^2}} \exp\left(-\frac{(x-\mu)^2}{2\sigma^2}\right), \tag{6.1}$$

where σ is the standard deviation and μ the expected value of the Gaussian. The model parameters to be estimated are $\vec{p}$. The superposition of m Gaussian distributions is then

$$g_m(x, \vec{p}) \quad = \quad \sum_{i=1}^{m} N_i \, g_i(x, \sigma_i, \mu_i) \,. \tag{6.2}$$

The factor N_i is the additional normalisation of the individual Gaussian distribution, for which the condition $\sum_i N_i = 1$ has to be met.

Motivated by the results of Rowell et al. (2008) a test for different source hypotheses was done starting with a single-source scenario and then increasing the number of model parameters to test for a three-source contribution to HESS J1614–518, thus $m = 3$. The following two substitutions have been used:

$$N_2 \quad = \quad 1 - N_1 - N_3 \,, \tag{6.3}$$

where the number of the model parameters is reduced by one as the N_i are not independent from one another, and:

$$\mu_2 \quad = \quad \mu_1 + \Delta\mu \,, \tag{6.4}$$

for which the distance between the peaks is fit rather than the peak position of the second Gaussian itself.

The PSF of this analysis is described by a symmetric two-dimensional Gaussian with $\sigma = 0.08°$. Therefore, 68 % containment radius $\sigma_{68\,\%}$ of the projection onto one axis is $0.08° / \sqrt{2}$ and constitutes the lower boundary for the fit of a single source.[i] Hence, the standard deviation of the Gaussian in Equations 6.1 and 6.2 consists of the 68 % containment radius (representing the point source) and an additional component accounting for any extended feature:

$$\sigma^2 = \sigma^2_{68\,\%} + \sigma^2_{\text{ext}} \,. \tag{6.5}$$

On the basis of the above introduced equations, nine model assumptions were tested on the data of the slice, starting with the fit of single point source up to a fit of three extended sources. The various source assumptions are summarised in Table 6.2.

Each model was fit to the data using the least-squares method

$$\chi^2 = \sum_{i=1}^{M=10} \frac{\left(n_{\text{pred}} - n_{\text{obs}}\right)^2}{\sigma(n_{\text{obs}})^2} \,, \tag{6.6}$$

[i] The PSF is $\sigma^2_{\text{PSF}} = \sigma^2_x + \sigma^2_y$. Projected onto one axis and because of the symmetry of the H.E.S.S. PSF ($\sigma_x = \sigma_y$) one gets $\sigma^2_{68\,\%} = \sigma^2_x = \sigma^2_{\text{PSF}}/2$.

TABLE 6.2 Summary of the different source models to be tested on the data along the slice over HESS J1614–518. Altogether, a superposition of three Gaussian models is used to describe the data on the right-hand side of Figure 6.2. A point-like source (pnt-src) model means the width is set to the size of the 68 % containment radius along one projected axis. The model of an extended source (ext-src) means that Equation 6.5 is used for the σ of the respective Gaussian. Indicated are the model parameters fixed and left to vary in the fit of the slice data.

#	Model	Model parameters $\vec{p}$	
		fixed	free
i.	1 pnt-src	$\sigma = \sigma_{68\,\%}$	μ
ii.	1 ext-src	—	μ,σ
ii.	2 pnt-srcs	$\sigma_{1,2} = \sigma_{68\,\%}$	μ_1, $\Delta\mu$, N_1
iv.	1 pnt-src + 1 ext-src	$\sigma_2 = \sigma_{68\,\%}$	μ_1, $\Delta\mu$, N_1, σ_1
v.	2 ext-src	—	μ_1, $\Delta\mu$, N_1, $\sigma_{1,2}$,
vi.	3 pnt-srcs	$\sigma_{1,2,3} = \sigma_{68\,\%}$	$\mu_{1,3}$, $\Delta\mu$, $N_{1,3}$
vii.	2 pnt-srcs + 1 ext-src	$\sigma_{1,3} = \sigma_{68\,\%}$	$\mu_{1,3}$, $\Delta\mu$, $N_{1,3}$, σ_2
viii.	1 pnt-src + 2 ext-srcs	$\sigma_3 = \sigma_{68\,\%}$	$\mu_{1,3}$, $\Delta\mu$, $N_{1,3}$, $\sigma_{1,2}$
ix.	3 ext-srcs	—	$\mu_{1,3}$, $\Delta\mu$, $N_{1,3}$, $\sigma_{1,2,3}$

where n_{pred} is the number of predicted counts per bin and n_{obs} the observed counts per bin with the respective error $\sigma(n_{\mathrm{obs}})$. Altogether there are $M = 10$ bins in the fit range of the slice (see Figure 6.2).

On the basis of the χ^2 value and the degrees of freedom, the probability p that the fit describes the data can be inferred. Therefore, the p value is used to reject inappropriate model representations of the slice. However, to estimate the improvement of a fit w.r.t. the previous one, the F–test proposed in Bevington (1969) is used:

$$F = \frac{(\chi_1^2 - \chi_2^2)/(n_{\mathrm{dof},1} - n_{\mathrm{dof},2})}{\chi_2^2/n_{\mathrm{dof},2}}\,, \tag{6.7}$$

where χ_1^2 is the χ^2 value of the simple model with $n_{\mathrm{dof},1}$ degrees of freedom that is tested against the next-complex[ii] model with the respective quantities χ_2^2 and $n_{\mathrm{dof},2}$. This test relies on that the two independent χ^2 values with their respective degrees of freedom underlie an $F(n_{\mathrm{dof},1} = 1, n_{\mathrm{dof},2})$ distribution. In this case, Equation 6.7 is reduced to

$$F = \frac{\Delta\chi^2}{\chi_2^2/n_{\mathrm{dof},2}}\,, \tag{6.8}$$

where $\Delta\chi^2 = \chi_1^2 - \chi_2^2$.

Although not considered in Bevington (1969) as general requirement of the test, it is assumed that the models of one and two Gaussians are nested within the model of three Gaussians. On the basis of Equation 6.8, following requirements for this test can

[ii] Complex refers to one additional model parameter.

TABLE 6.3 Summary of morphological analysis results for the different source hypotheses (see Table 6.2 for the model descriptions). The χ^2 value of the fit, the degrees of freedom n_{dof}, and the inferred probability p_{χ^2} are stated. The improvement of the fit w.r.t. the previous one is determined with the F–test (Bevington, 1969), for which the probability that the next-complex model fits the data better is given (p_F).

Model	χ^2	n_{dof}	p_{χ^2}	F	p_F
i.	1274.81	9	0	—	—
ii.	52.30	8	1.4×10^{-8}	187.0	1.000
iii.	163.80	7	0	−4.76	0
iv.	20.85	6	0.002	41.1	0.999
v.	6.65	5	0.25	10.7	0.978
[a]vi.	11.68	5	0.04	*not defined*	
[b]vi.	11.68	5	0.04	3.9	0.896
vii.	2.94	4	0.57	11.9	0.974
viii.	2.03	3	0.57	1.3	0.669
ix.	1.64	2	0.44	0.5	0.441

[a] Model vi vs. v.
[b] Model vi vs. iv.

be inferred: the next-complex model has to result in an improvement, i.e. $\chi^2_2 \overset{!}{<} \chi^2_1$ or $\Delta\chi^2 \overset{!}{>} 0$. Of course, this F–test implies $n_{\mathrm{dof},2} - 1 = n_{\mathrm{dof},1}$. Given the F value, its cumulative distribution function is used to determine the probability that the next-complex model results in an improvement.

The results of the different model assumptions and the comparison with the next-complex one are summarised in Table 6.3. By design, the F–test only tests for relative model improvements, but does not take the goodness-of-fit of the input models into account. Therefore, the best-fit model is chosen as a combination of the χ^2 results and the F statistic. Based on the χ^2 evaluation, the single-source models (i. and ii.) as well as the model of two point sources (iii.) are significantly rejected. The model of one extended and one point source (iv.) is disfavoured by its low p value of 0.002 ($\sim 3\,\sigma$).

The best fit is the model consisting of two extended sources (v.). The next-complex models result either in a worsening (three point sources) or are not significantly better (e.g. two point sources and one extended source). The parameters of the best-fit models for a single source (ii.) , a two-source origin (v.) and a three-source hypothesis (vii.) are tabulated in Table 6.4 and illustrated in Figure 6.2. As a result of this study, a two-source origin is preferred for HESS J1614–518 as a single-source nature is rejected and the three-source models do not lead to a significant improvement w.r.t. the chosen two-source model.

TABLE 6.4 Best-fit results for the models of one (ii.), two (v.), and three sources (vii.). Stated are the results of the fit parameters and the derived quantities (see also Tables 6.2 and 6.3).

	Model		
Parameter	ii.	v.	vii.
N_1	1.00	0.32 ± 0.06	0.27 ± 0.02
μ_1	0.79 ± 0.02	1.09 ± 0.02	1.11 ± 0.01
σ_1	0.33 ± 0.01	0.15 ± 0.02	0.06
$\Delta\mu$		-0.40 ± 0.01	-0.46 ± 0.02
N_2		0.68 ± 0.06	0.53 ± 0.06
μ_2		0.69 ± 0.03	0.65 ± 0.02
σ_2		0.20 ± 0.02	0.16 ± 0.02
N_3			0.20 ± 0.06
μ_3			1.12 ± 0.01
σ_3			0.06
p value	1.4×10^{-8}	0.25	0.57

6.1.1.2 ENERGY DEPENDENCE

An energy-dependent change of HESS J1614–518 could be viable when searching for possible counterparts. For this, the data set was divided into two subsets: a low-energy set containing events with reconstructed energies below 1 TeV and a high-energy one with events above 1 TeV. In Figure 6.3, both skymaps are shown. They are produced analogously to the energy-integrated one in Figure 6.1. Apparently, the structure of HESS J1614–518 changes from the low-energy sample to the high-energy one. At energies below 1 TeV, the source appears to be more compact with a strong northern emission region and a rather weak substructure towards the south. Both these subregions are located at the same place w.r.t. Figure 6.1. However, at higher energies, the source becomes circle-like in structure. It exhibits a large diffusive component with pronounced and more compact emission region in the north.

To quantify the observation of an apparent morphology change with energy, a χ^2 test was used to test the hypothesis if both skymaps follow the same underlying distribution. As chosen in the slice discussion, the low and high-energy skymaps used for the test consisted of coarser uncorrelated bins of 0.1° width and were $1^\circ \times 1^\circ$ in size. The χ^2 function is defined as

$$\chi^2 = \sum_i \frac{(n_{<,i} - N \cdot n_{>,i})^2}{\sigma^2(n_{<,i}) + N^2\sigma^2(n_{>,i})}\,, \tag{6.9}$$

where $n_{<,i}$ and $n_{>,i}$ are the excess events from the low ($E < 1\,\mathrm{TeV}$) and high-energy ($E > 1\,\mathrm{TeV}$) sample, respectively, with the corresponding statistical errors $\sigma(n_{<,i})$ and $\sigma(n_{>,i})$. The overall normalisation $N = \sum n_{<,i} / \sum n_{>,i}$ accounts for the difference in the total number of events.

The χ^2 test resulted in $\chi^2 = 139.1$ with 99 degrees of freedom. Hence, both skymaps

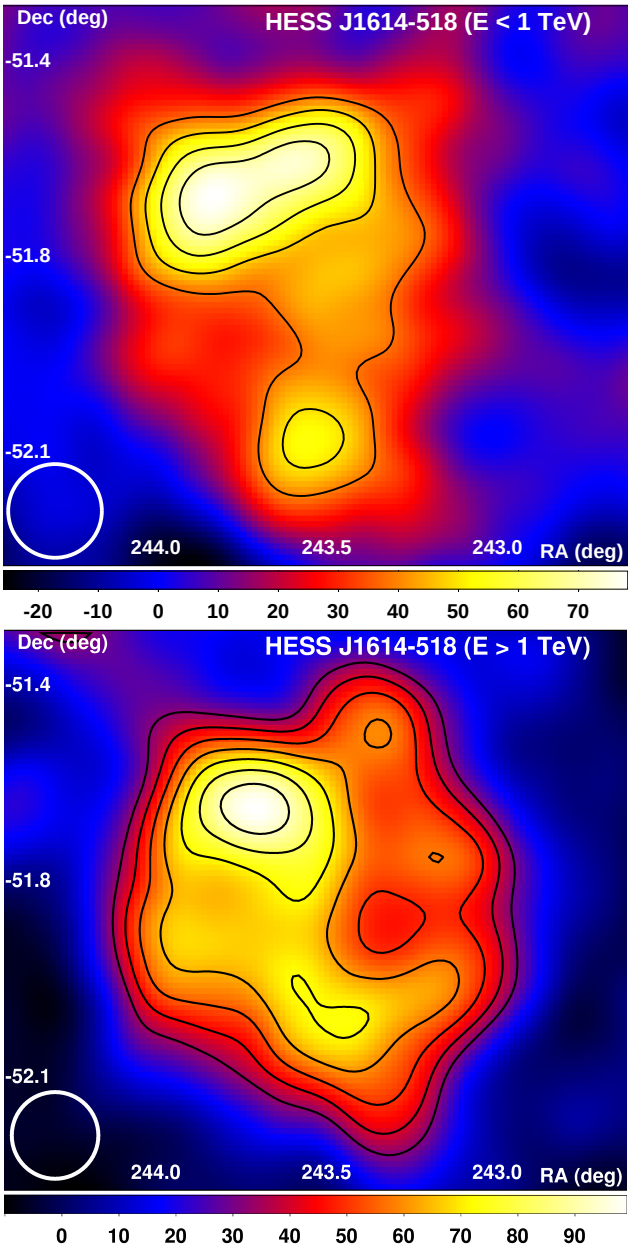

FIGURE 6.3 Smoothed exposure-corrected VHE γ-ray excess counts map in J2000 coordinates. Events are integrated over a radius of 0.1° and the images are smoothed with a Gaussian of $\sigma = 0.08°$, which represents the PSF (depicted as white circle) of both analyses. **TOP:** Counts map of events with energies $E < 1$ TeV. The significance-contour levels are from 4 to 7 σ in steps of 1 σ. **BOTTOM:** Counts map of events with energies $E > 1$ TeV. The significance-contour levels are 4 to 10 σ in steps of 1 σ.

are compatible within 2.6 σ. This is not a significant deviation from the null hypothesis that both maps follow the same underlying distribution, but may be considered a hint for an energy-dependent change in morphology.

SUMMARY The presented morphological studies favour an apparent multi-source origin of HESS J1614–518. Any scenario invoking a single-source contribution is rejected. A fit of a constant-emission scenario with a value 0.85 ± 0.04 is rejected as well ($\chi^2 = 197.2$, $n_{\mathrm{dof}} = 9$, $p = 0$). However, based on the data at hand, a three-source structure is not significantly better than a double-source origin. Based on the energy-dependent study, there appears to be a hint for a change in morphology from lower to higher energies.

6.1.2 SPECTRAL STUDIES

A circular region of 0.51° radius was used to encompass the VHE γ-ray emission from HESS J1614–518. This radius is chosen on the basis of the $4\,\sigma$ contours of HESS J1614–518 in order to spatially separate the source from HESS J1616–508 located north-east (indicated in Figure 6.2).

Motivated by the results above, where a two-source structure was preferred, regions in the north and south of HESS J1614–518 were defined. Based on the fit to the slice (model v.), two extended sources were placed and named HESS J1614–518N and HESS J1614–518S. Furthermore, two point-source regions were placed at the respective significance peaks of HESS J1614–518 (HESS J1614–518n and HESS J1614–518s). Finally, it is aimed for to compare the changes in the spectral behaviour of the subregions w.r.t. one another and to the entire HESS J1614–518 source. This could provide additional information on the source, perhaps similar to the findings in Aharonian et al. (2006d) where a spectral softening[iii] with increasing distance from the TeV-emission peak of HESS J1825–137 (a PWN) was observed. The position and the radii of the regions to be analysed are tabulated in Table 6.5.

A three-source origin cannot be investigated in a spectral analysis. The regions overlap and any spectral information would thus be biased.

TABLE 6.5 HESS J1614–518 and its subregions for the spectral reconstruction. The locations were determined from the morphology studies. Stated are the coordinates and the source radii θ_{src}.

Region	RA (J2000) deg	Dec (J2000) deg	θ_{src} deg
HESS J1614−518	243.534	−51.864	0.51
HESS J1614−518N	243.666	−51.758	0.20
HESS J1614−518n	243.720	−51.692	0.11
HESS J1614−518S	243.453	−52.145	0.15
HESS J1614−518s	243.510	−52.084	0.11

For the spectral analysis with TBS, the data sets of every individual region (entire region, N/n and S/s) had to suffice two conditions. Firstly, the respective ON (signal) region has to be fully contained within the run. This is to assure that no bias in the spectral

[iii] *Soft* refers to an increasing value of the spectral index.

TABLE 6.6 Results of the TBS analyses of the H.E.S.S. data on HESS J1614–518 and its subregions. The $E_{\mathrm{min,max}}$ determine the energy range, for which the TBS-background normalisation could be calculated. This is therefore the energy range of the reconstructed spectrum. The $N^{\mathrm{s}}_{\mathrm{g,h}}$ are the numbers of the gamma-like and hadron-like events from the source region, α_{TBS} is the average TBS correction (Eq. 4.11), N_{excess} are the excess events obtained at a significance S (Eq. 3.22).

Source	E_{min}	E_{max}	$N^{\mathrm{s}}_{\mathrm{g}}$	$N^{\mathrm{s}}_{\mathrm{h}}$	α_{TBS}	N_{excess}	S σ
HESS J1614–518	0.3	31.6	9206	85851	0.087	1698	18.1
HESS J1614–518N	0.3	25.1	2346	19564	0.085	674	14.8
HESS J1614–518n	0.3	15.9	792	6159	0.086	263	10.1
HESS J1614–518S	0.3	31.6	1219	10728	0.084	320	9.7
HESS J1614–518s	0.3	15.9	712	6086	0.084	203	8.1

analysis through a partly covered ON region is introduced. This is also of importance as difference in the individual spectra are looked for. Secondly, a maximum wobble offset $\omega_{\mathrm{max}} = 2^\circ$ is introduced, which is a requirement of the TBS method.[iv] Hence, for the analysis of the individual regions, the required condition for every run with wobble offset ω_{obs} is:

$$\omega_{\mathrm{obs}} \leq 2^\circ - \theta_{\mathrm{src}} \,. \tag{6.10}$$

In addition, only four-telescope observations are considered. Therefore, the amount of data is reduced to 10.7 hrs on HESS J1614–518 and 16.3 and 16.8 hrs on the northern and southern subregions, respectively. The results of the analysis with TBS are to be found in Table 6.6.

As in Rowell et al. (2008), the simple power law was found to describe the data best. The entire source is described by a power law with index $\Gamma = 2.40 \pm 0.05$ and a normalisation at 1 TeV of $\Phi_0 = (8.47 \pm 0.44) \times 10^{-8}\,\mathrm{m^{-2}s^{-1}\,TeV^{-1}}$. The integral flux above 0.3 TeV is 24.1 % of that of the Crab Nebula above the same energy threshold.

The entire source was also fit with a power law with an exponential cutoff. The respective best-fit results were $\Phi_0 = (13.5 \pm 1.6) \times 10^{-8}\,\mathrm{m^{-2}s^{-1}\,TeV^{-1}}$ with a hard power-law index of $\Gamma = 1.71 \pm 0.15$ and an early cutoff at 3.1 TeV ($\lambda = 0.322 \pm 0.085$). The obtained flux points and the residuals of these two fit are depicted in Figure B.1. The improvement of the fit of power law with an exponential cutoff appears to be significant because the TS value is 36.5 (Eq. 3.11). On the other hand, the last four spectral points are compatible with zero and approach non-Gaussian statistics. Therefore, in a conservative approach, the significance of the improvement is determined through the F–test comparing the power-law fit ($\chi^2/n_{\mathrm{dof}} = 13.24/15$) with the fit of an additional exponential cutoff ($\chi^2/n_{\mathrm{dof}} = 6.35/14$). With Equation 6.8, a value of $F = 15.2$ is found, which quantifies the improvement of the fit to be $2.9\,\sigma$.

[iv] As mentioned earlier, the TBg model is sensitive to the description of events towards the camera edge (see also Section 3.3.8.4).

TABLE 6.7 Spectral parameters for HESS J1614−518 and its subregions. The best-fit parameters of the power law are determined with TBS with n_{dof} degrees of freedom. F is the integral flux above the energy threshold E_{min} (see Table 6.6) in units of the flux of the Crab Nebula above the same energy threshold.

Region	$\Phi_0(1\,\mathrm{TeV})$ $10^{-8}\,\mathrm{TeV}^{-1}\mathrm{m}^{-2}\mathrm{s}^{-1}$	Γ	n_{dof}	$F(>E_{\mathrm{min}})$ % Crab
HESS J1614–518	8.47±0.44	2.40±0.05	18	24.1±1.4
HESS J1614–518N	2.34±0.16	2.43±0.08	17	6.8±0.5
HESS J1614–518n	1.34±0.13	2.23±0.11	15	3.6±0.4
HESS J1614–518S	1.25±0.13	2.31±0.11	17	3.4±0.4
HESS J1614–518s	1.11±0.14	2.26±0.13	15	3.0±0.4

The larger subregions North (N) and South (S) are both described best by a simple power law ($\Gamma_{\mathrm{N}} = 2.43 \pm 0.08$ and $\Gamma_{\mathrm{S}} = 2.31 \pm 0.11$) and the fit of an additional exponential cutoff did not lead to an improvement. Both spectral indices match that of the entire region within $1\,\sigma$. The fit of the point-like subregions on the respective significance peaks led to not significantly harder spectra ($\Gamma_{\mathrm{n}} = 2.23 \pm 0.11$; $\Gamma_{\mathrm{s}} = 2.26 \pm 0.13$). All fit results are tabulated in Table 6.7 and depicted in Figure 6.4.

SUMMARY Comparing the spectral results summarised in Table 6.7, there is no spectral change across HESS J1614-518 but merely an indication that the spectrum gets harder towards the peaks of the subregions. However, there is an indication of at least $2.9\,\sigma$ that a power law with an exponential cutoff is favoured over a simple power law.

The spectral results of the χ^2 minimisation were compatible with those presented here and are used to estimate the systematic error introduced by TBS (w.r.t. interpolation and extrapolation; see also discussion in Section 4.6). For the full region, the systematic errors of the TBS method on the integral flux (in units of the Crab Nebula flux) and the power-law index are $F_{\mathrm{sys}} = 1.5\,\%$ and $\Gamma_{\mathrm{sys}} = 0.02$. For the extended subregions north (N) and south (S): $F^{\mathrm{N}}_{\mathrm{sys}} = 0.1\,\%$ and $\Gamma^{\mathrm{N}}_{\mathrm{sys}} = 0.01$ and $F^{\mathrm{S}}_{\mathrm{sys}} < 0.1\,\%$ and $\Gamma^{\mathrm{S}}_{\mathrm{sys}} = 0.03$, respectively.

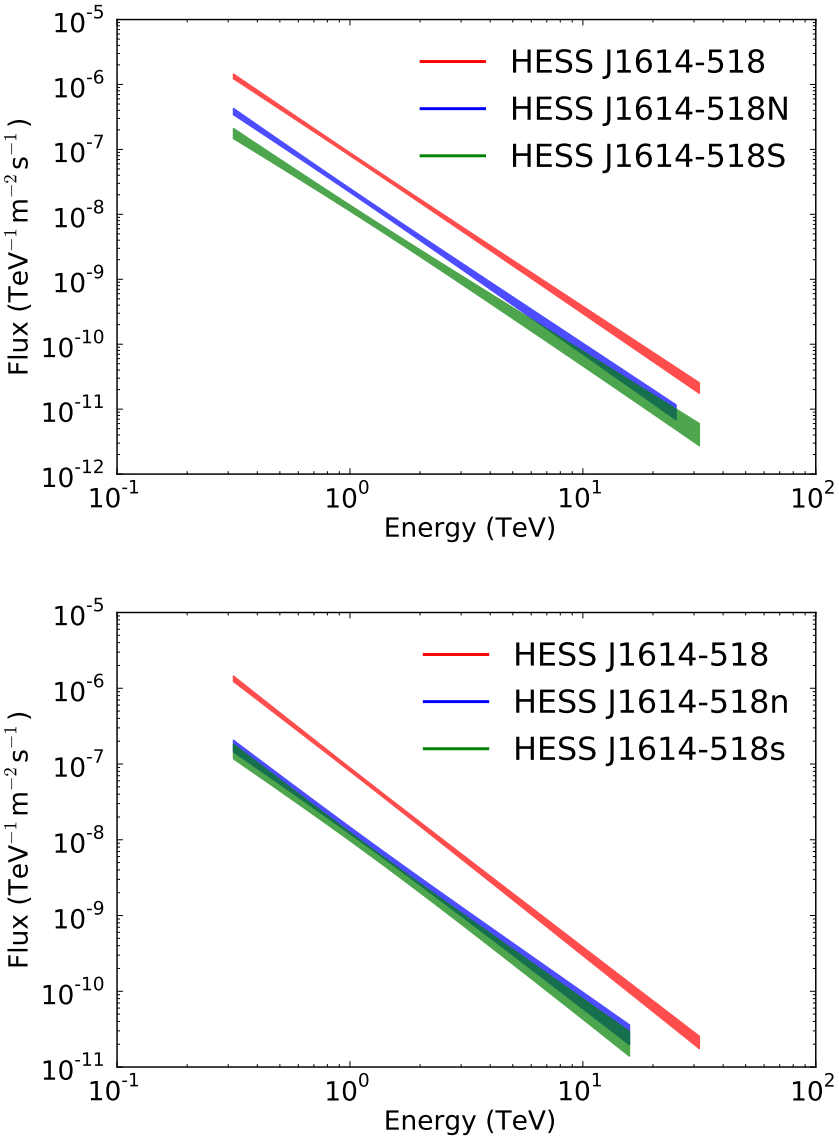

FIGURE 6.4 Differential energy spectra of HESS J1614–518 and the analysed subregions depicted with the 1 σ butterflies. **TOP:** The simple power-law spectra of the entire source region and the two subregions defined in the morphology fits. **BOTTOM:** The simple power-law spectra of the entire source and the two point-like subregions defined through the peaks in significance.

6.2 MULTI-WAVELENGTH DATA

In this section, available MWL data on HESS J1614−518 are reviewed. These archival data range from radio up to GeV energies.

In Figure 6.5, reported keV and GeV sources from Suzaku, *Swift*/XRT, *Fermi*–LAT observations are depicted and discussed in the following sections.

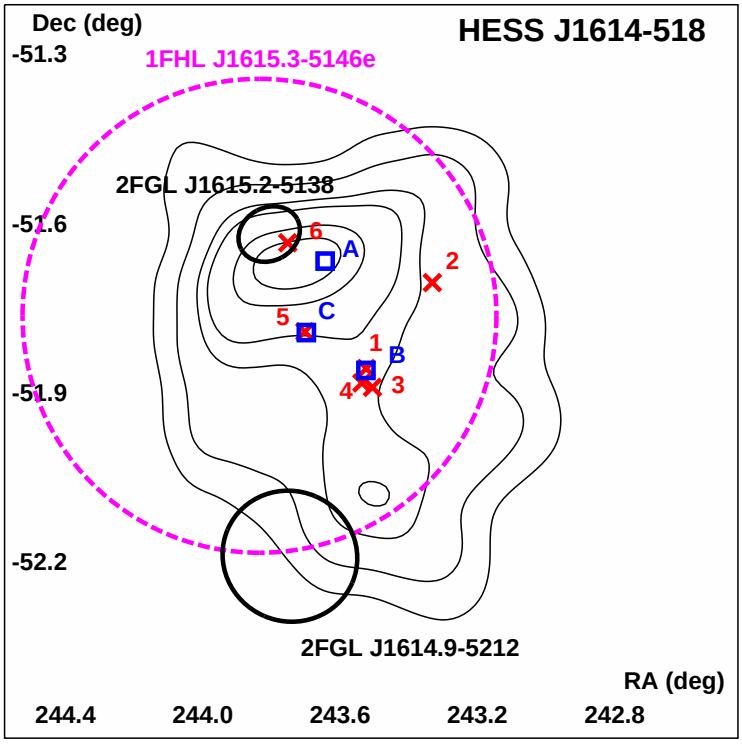

FIGURE 6.5 Skymap depicting HESS J1614–518 (thin black contours), the two 2FGL sources (thick-black solid ellipses) from Nolan et al. (2012) and the extended source 1FHL J1615.3–5146e (large magenta-dashed circle) from Paneque et al. (2013). The ellipses of the 2FGL sources indicate the positional uncertainty, whereas the circle of the 1FHL source is the actual size of the uniform-disk model used in the analysis of 1FHL J1615.3–5146e. In addition, the three reported Suzaku sources in Matsumoto et al. (2008), namely A, B, C, are indicated as blue squares. The six *Swift*/XRT sources are marked as red crosses (Landi et al., 2006, 2007).

6.2.1 *Fermi*–LAT DATA

In the second *Fermi*–LAT catalogue (2FGL; Nolan et al., 2012) two sources within HESS J1614–518 were reported: 2FGL J1615.2−5138 and 2FGL J1614.9–5212. Both sources remained unidentified, but 2FGL J1615.2–5138 was associated with HESS J1614–518. The source 2FGL J1615.2–5138 is located close to the north subregion HESS J1614–518N, whereas 2FGL J1614.9–5212 is in the immediate vicinity of HESS J1614–518S (see Figure 6.5).

In the first high-energy catalogue of *Fermi*–LAT (1FHL), Paneque et al. (2013) reported an extended high-energy source 1FHL J1615.3–5146e detected between 10 GeV to 500 GeV. This source was associated with HESS J1614–518. Its morphology was described as a uniform disk and a with a diameter of $\sim 0.8°$, a large part of HESS J1614–518 is covered. All three above mentioned GeV sources are depicted in Figure 6.5 and their spectral properties are to be found in Table 6.8.

TABLE 6.8 Spectral parameters of the three reported *Fermi*–LAT sources in the vicinity of HESS J1614–518.

GeV source	E_{min} GeV	E_{max} GeV	Γ	F 10^{-11} erg cm^{-2} s^{-1}
[a]2FGL J1615.2–5138	0.1	100	2.29±0.10	9.14±1.04
[a]2FGL J1614.9–5212	0.1	100	1.98±0.18	2.53±0.64
[b]1FHL J1615.3–5146e	10	500	1.88±0.13	9.22±1.66

[a] Nolan et al. (2012).
[b] Paneque et al. (2013).

The presence of 1FHL J1615.3–5146e motivated further analyses of the *Fermi*–LAT data down to 100 MeV as the presence of a low-energy cutoff (colloquially called π^0 bump) could be indicative for a hadronic scenario in which the observed VHE γ-ray emission could be dominantly due to a π^0 decay (also Section 2.1.3). Also, the absence of such a feature could point at a scenario with electrons likely being the parent-particle population.

6.2.1.1 EXTENDED-SOURCE ANALYSIS OF 1FHL J1615.3–5146E

The following *Fermi*–LAT analysis has been done with the Fermi Science Tools of version `v9r31p1` and the instruments response function `P7SourceV6`. The analysis was done using *Enrico*[i], which is an open-source tool that chains the different steps of the standard *Fermi*–LAT analysis[ii] together. The initial source-model file was produced using the public tool `make2FGLxml.py`.[iii] For all tools, the default or recommended standard values and choices were used.

[i] http://enrico.readthedocs.org/en/latest/index.html
[ii] http://fermi.gsfc.nasa.gov/ssc/data/analysis/scitools/
[iii] http://fermi.gsfc.nasa.gov/ssc/data/analysis/user/

The *binned* likelihood analysis was used in the energy range between 100 MeV to 300 GeV. The data set comprised of all available data since mission start of the *Fermi* satellite adding up to more than 5 years of data (MET[iv]: 239557417 s to 400840224 s). Front and back-converted events were selected (Sect. 3.1.2). The ROI with a radius of 15° (and 20° for the energy range between 100 MeV to 300 MeV) contained all reported 2FGL sources (Nolan et al., 2012) and four extended 1FHL sources (Paneque et al., 2013) within ~ 10° of HESS J1614–518. For three of the four 1FHL sources, namely 1FHL J1615.3–5146e (i.e. the source of interest), 1FHL J1616.2–5054e, and 1FHL J1633.0–4746e, no public `FITS` templates for the analysis were available (this was only the case for MSH 15–52). Therefore, these templates (uniform disks) were produced following the detailed *Fermi*–LAT analysis instruction for extended sources.[v]

GLOBAL FIT BETWEEN 100 MEV AND 300 GEV As the sources and their spectral properties in Nolan et al. (2012) are based on roughly 2 yrs of data and because the 1FHL sources do not include spectral information of energies below 10 GeV, all sources in the ROI were analysed to determine updated spectral parameters. The respective 2FGL sources were excluded if found within one of the 1FHL sources. In the case of 1FHL J1615.3–5146e, this meant exclusion of the two aforementioned 2FGL sources within HESS J1614–518.

The spectral parameters of all sources within 4° of 1FHL J1615.3–5146e were left free to be varied in the analysis. For sources up to 8°, only the flux normalisations were left free. Beyond 8°, all spectral parameters of the sources in the ROI were fixed to their reported value. The normalisation of the Galactic diffuse model was left free to vary and that of the isotropic diffuse model was fixed to its catalogued value. As 1FHL J1615.3–5146e was best-described by a simple power law, this spectral shape is assumed for the entire energy range.

As a result for 1FHL J1615.3–5146e, the flux normalisation at 396 GeV is $(7.11 \pm 0.54) \times 10^{-7}\,\mathrm{GeV}^{-1}\,\mathrm{m}^{-2}\,\mathrm{s}^{-1}$ with a slightly larger index of $\Gamma = 2.01 \pm 0.01$ compared to $\Gamma = 1.88 \pm 0.13$ in Paneque et al. (2013), see also Table 6.8.

FIT OF INDIVIDUAL ENERGY BINS BETWEEN 100 MEV AND 300 GEV The energy range of 100 MeV to 300 GeV was divided into six subranges, for which the binned-analysis was done using the resulting source model file of the global fit. The integral flux of 1FHL J1615.3–5146e was fit and the power-law index fixed. The same was done for the two extended sources 1FHL J1616.2–5054e and 1FHL J1633.0–4746e. Four variable sources within 6° from 1FHL J1615.3–5146e mentioned in Nolan et al. (2012) were fit leaving the normalisation free. The four sources are 2FGL J1620.6–5111c, 2FGL J1603.8–4904, 2FGL J1610.1–4808, and 2FGL J1650.1–5044. Otherwise, the parameters of all other sources in the ROI were fixed to their values of the global fit.

For the lowest energy bin, i.e. 100 - 300 MeV, the analysis appeared not to be stable. Although the likelihood analysis converged, the flux estimates varied within 10 decades in logarithmic energy scale for 1FHL J1615.3–5146e. Apparently, the Galactic diffuse

[iv] MET = mission-elapsed time in seconds

[v] http://fermi.gsfc.nasa.gov/ssc/data/analysis/scitools/extended/extended.html

TABLE 6.9 Results of the binned-likelihood analysis of 1FHL J1615.3–5146e. The N_{pred} and TS are the number of predicted events from the source and test-statistic value, respectively, which are determined in the analysis (Sect. 3.1.3).

E_{min} GeV	E_{max} GeV	N_{pred}	TS	F $\mathrm{m^{-2}\,s^{-1}}$	Gal. diffuse model Fit option
0.1	0.3	0	0	$< 1.59 \times 10^{-4}$	fixed
0.1	0.3	29508.3	2712	$(5.16 \pm 0.23) \times 10^{-3}$	free
0.3	1	3169	109.6	$(2.96 \pm 0.37) \times 10^{-4}$	fixed
1	3	1245	154.0	$(8.46 \pm 0.76) \times 10^{-5}$	fixed
3	10	350	98.0	$(2.16 \pm 0.25) \times 10^{-5}$	fixed
10	30	91	50.1	$(5.40 \pm 0.94) \times 10^{-6}$	fixed
30	100	49	58.9	$(2.94 \pm 0.56) \times 10^{-6}$	fixed
100	300	10	14.7	$(6.13 \pm 2.47) \times 10^{-7}$	fixed

model had a dominant impact on the overall fit: when its normalisation was kept fixed to its value of the global fit (as done for all other energy bins), the estimated flux of 1FHL J1615.3–5146e decreased significantly below the detection threshold and thus a $2\,\sigma$ flux upper limit had to be calculated.[vi] However, when the normalisation of the diffuse model was left free to vary, the source was significantly detected and exhibited a flux level comparable to the other two extended sources.

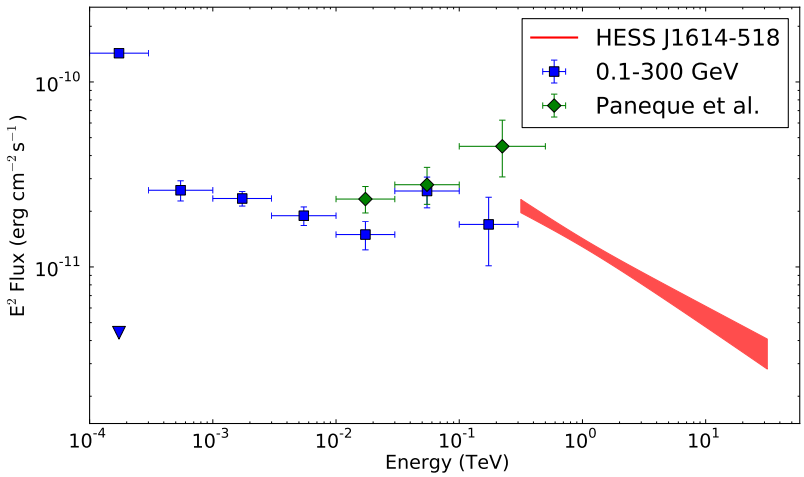

FIGURE 6.6 Spectral results of the *Fermi*–LAT analysis together with the results on HESS J1614–518. The spectrum of 1FHL J1615.3–5146e derived in this work (blue-square markers; the blue triangle depicts the flux upper limit at a 95 % confidence level) and from Paneque et al. (2013) (green-diamond markers) are depicted. The red area $1\,\sigma$ butterfly of the H.E.S.S. spectrum.

In Table 6.9, the results of the likelihood analysis are tabulated. A comparison with

[vi] This was done following the recommendation on *fermi.gsfc.nasa.gov/ssc/data/analysis/scitools/python_usage_notes.html*.

the results of Paneque et al. (2013) is given in Figure 6.6 where also the spectrum of HESS J1614–518 is depicted. The GeV spectra nicely connect to the TeV spectrum. However, there is no indication for a low-energy cutoff and therefore also no support for a pure hadronic scenario for HESS J1614–518 as in the case for the SNRs IC 443 and W 44 (Ackermann et al., 2013b). Apart from the systematics in the first bin of 1FHL J1615.3–5146e the overall GeV spectrum does not provide a hint for a downturn towards MeV energies like observed for the two mentioned SNRs (see also Figure 2.1).

6.2.2 X-RAY DATA

The detection of HESS J1614–518 with H.E.S.S. triggered follow-up observations with various X-ray satellites. Among these are *Swift*/XRT (Burrows et al., 2004), *Suzaku*-XIS (Koyama et al., 2007), and *XMM–Newton* (Jansen et al., 2001). In the following, these data and the results are briefly presented. The reported source detections are depicted in Figure 6.5.

6.2.2.1 *Swift*/XRT

There were six *Swift*/XRT sources (*Swift* sources 1 to 6) within HESS J1614–518 detected in a combined data set of 6.7 ks exposure (1.7 ks and 5 ks, respectively; Landi et al., 2006, 2007). Four of them (*Swift* sources 1-3 and 5) are likely to be stars, with at least one of them being a possible member star of Pismis 22, namely *Swift* source 1. *Swift* source 2 appears to be highly reddened. The *Swift* sources 5 and 6 are in the vicinity of HESS J1614–518N.

The reported fluxes between 2 and 10 keV of the first two brightest sources are $F_1 = 5.4 \times 10^{-13}\,\mathrm{erg\,cm^{-2}\,s^{-1}}$ and $F_2 = 6.6 \times 10^{-13}\,\mathrm{erg\,cm^{-2}\,s^{-1}}$.

6.2.2.2 *Suzaku*–XIS

The *Suzaku*-XIS observations towards the northern side of HESS J1614−518 revealed two extended sources (src A and src B), and one point-like (src C) source (Matsumoto et al., 2008).

The src A is located within the northern TeV subregion and was associated with HESS J1614−518N. The spectrum was described by a power-law index of 1.73 with a flux between 2 to 10 keV of $F_{src\,A} = 5.3 \times 10^{-13}\,\mathrm{erg\,cm^{-2}\,s^{-1}}$. The best-fit column density $n_{\mathrm{H,src\,A}} = 1.2 \times 10^{22}\,\mathrm{cm^{-2}}$ suggested a distance of $\sim$ 10 kpc for src A. If src A and HESS J1614–518 are physically related then the observed TeV-to-X-ray flux ratio of 34 is among the largest observed for extended VHE sources (Matsumoto et al., 2008).

The src B is located towards Pismis 22, but at a distance of 10 kpc favoured by the best-fit column density. This source is consistent with *Swift* source 1, but the observed flux was estimated to be a factor of three lower: $F_{src\,B} = (1.4 \pm 0.5) \times 10^{-13}\,\mathrm{erg\,cm^{-2}\,s^{-1}}$ and perhaps suggesting a time variability. However, in the XMM–*Newton* data no hint for such a variability was found (Matsumoto et al., 2008).

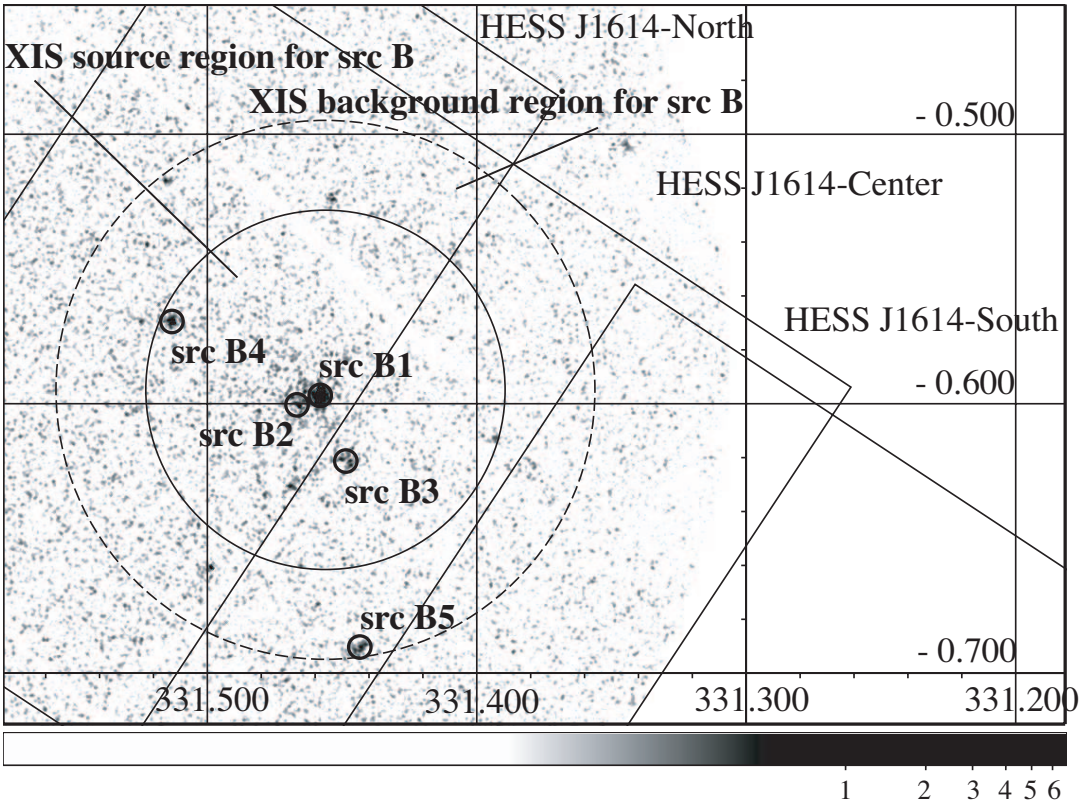

FIGURE 6.7 XMM–*Newton* count image (MOS 1 and 2) centred on src B close to Pismis 22 between 0.4 and 10 keV. The coordinates are stated in Galactic longitude and latitude. Indicated is the Suzaku src B (black solid circle) and the ring used to determine the background of src B (dashed circle). The five sources B1 to B5 are detected with XMM–*Newton*. Image adopted from Sakai et al. (2011).

The src C is identified to be a B9 V star (V: a dwarf) and is located half-way between src A and B. Besides for src C, no plausible counterpart was found to explain the X-ray sources A or B in the light of the TeV emission (Matsumoto et al., 2008).

Follow-up observations of the centre and the south of HESS J1614–518 were conducted. Towards HESS J1614–518S no X-ray emission was detected (Sakai et al., 2011). With archival XMM–*Newton* data, the extended src B was identified to consist of four point sources plus one additional point source in the background region of the previous analysis in Matsumoto et al. (2008).

The brightest of these sources, src B1 is found in the centre of the former src B (see Figure 6.7) and does not exhibit any time variability. The best-fit spectrum is a soft power law ($\Gamma = 5.2 \pm 0.6$), which is not significantly better than a simple black body model. The black-body solution resulted in a column density matching that of src A implying a distance of 10 kpc. Both models (soft spectra) motivate the presence of an *anomalous* X-ray pulsar[vii] as Sakai et al. (2011) argued. Sakai et al. (2011) discussed the probability

[vii] Anomalous X-ray pulsars are a subclass of magnetars with a very soft spectrum. See Mereghetti (2008) for a detailed review.

of HESS J1614–518 being the result of the proton accelerator based on the high TeV-to-X-ray flux ratio observed at HESS J1614–518N and src A, respectively and because an inverse-Compton scenario with electrons scattering of the cosmic microwave background would require a low B field of less than $1\,\mu$G (i.e. below the canonical value of $3\ldots5\,\mu$G within the Galactic plane). In this case, src A could be the SNR and src B1 the central compact object, i.e. associated (anomalous) X-ray pulsar.

6.2.2.3 *XMM–Newton*

About 40 ks of unpublished data that overlap with the north (19 ks, OBSID = 0406650101) and the south part (17 ks, OBSID = 0555660101) of the TeV source HESS J1614–518 are available. The results of the analysis of these data are subject to ongoing work and will be presented in forthcoming works (Abramowski et al., 2014, in prep.; Gewering-Peine, 2014, in prep.) and therefore cannot be discussed here. However, since none of the pulsars (see Section 6.3.5) have been detected, a limit on the flux can be derived. For 20 ks of exposure, the nominal sensitivity is $\sim 2\times10^{-14}$ erg cm^{-2} s^{-1} between 2 – 10 keV (estimated on the basis of Watson et al., 2001).

6.2.3 RADIO DATA

In general, any VHE accelerator is likely to leave its imprint(s) on the ambient medium. Therefore, archival radio data were searched for any spatial correlation with the TeV morphology of HESS J1614–518.

6.2.3.1 843 MHz CONTINUUM

In Figure 6.8 (left), the 843 MHz radio emission observed with the Molonglo Observatory Synthesis Telescope (MOST) from the Molonglo Galactic Plane Survey (Green et al., 1999) is shown. No obvious radio features spatially coincident with HESS J1614–518 were found. Moreover, there are no hints for a SNR in the immediate vicinity of HESS J1614–518. Towards the western edge of HESS J1614–518 HII regions are located. These are most likely of thermal origin (Russeil et al., 2005), but HII regions can also be formed by stellar-wind activity of SFRs as Kothes & Dougherty (2007) argued similarly for the existence of such regions close to Wd1. These regions are located at different distances based on the adopted radial velocity, e.g. G331.110-0.506 at 4.2 kpc (Russeil et al., 2005), but G331.1-0.4 with a velocity of −55 km/s could either be located at ∼ 3.6 kpc (near solution) or ∼ 11.1 kpc (far solution, see Appendix B).

6.2.3.2 NEUTRAL HYDROGEN (21 CM)

The inspection of archival HI data from the South Galactic Plane Survey (SGPS, McClure-Griffiths et al., 2005) revealed a void at the velocity range of −15 km/s to −22 km/s. This range translates into a distance of $1.2\ldots1.8$ kpc (near solution) or $13.4\ldots13.6$ kpc (far solution). It is interesting to point out that the near solution encompasses the distance

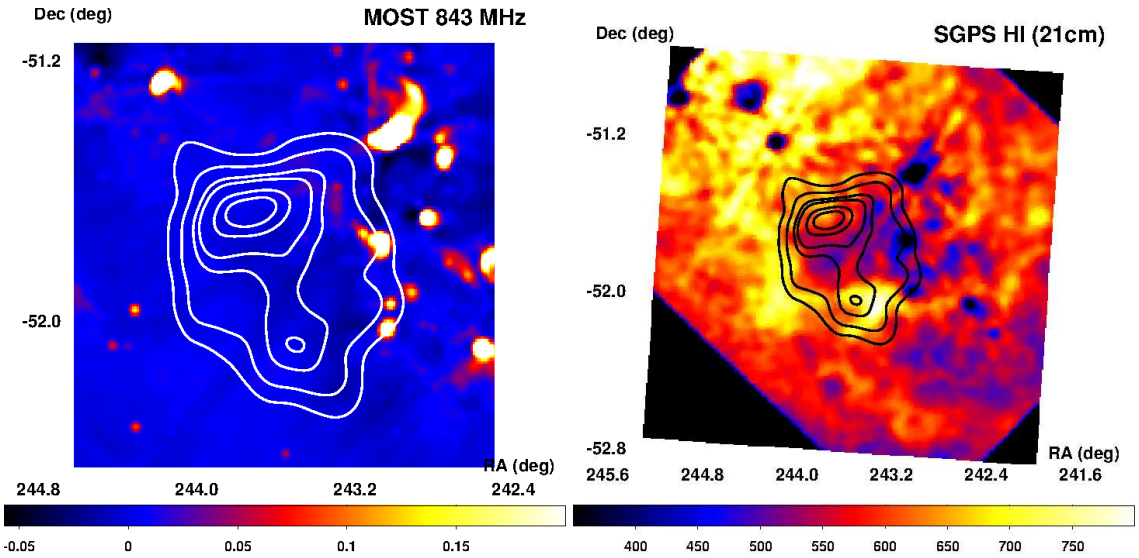

FIGURE 6.8 Radio images of the vicinity of HESS J1614–518. **LEFT:** MOST 843 MHz radio continuum image (Jy/beam) towards HESS J1614−518 (white significance contours, identical to those in Figure 6.1). **RIGHT:** HI 21 cm line emission map integrated between -22 and -15 km s^{-1} in units of K. Overlaid are the VHE significance contours of HESS J1614–518 (black contours). The velocity integration was performed by Rowell (priv. comm., 2013).

of the stellar cluster Pismis 22 (discussed in Section 6.3.1). The diameter of the void is $\sim 0.4°$, which translates into a physical size of 8.4 pc at 1.2 kpc or $\sim$ 94 pc at 13.4 kpc.

Otherwise, other (convincing) correlations between the VHE γ-ray morphology than found in the MOST 843 MHz and in HI data were not found. The inspection was done using the SkyView[viii] to access radio, IR, optical, UV, and X-ray wavelengths.

[viii] skyview.gsfc.nasa.gov

6.3 COUNTERPART SCENARIOS

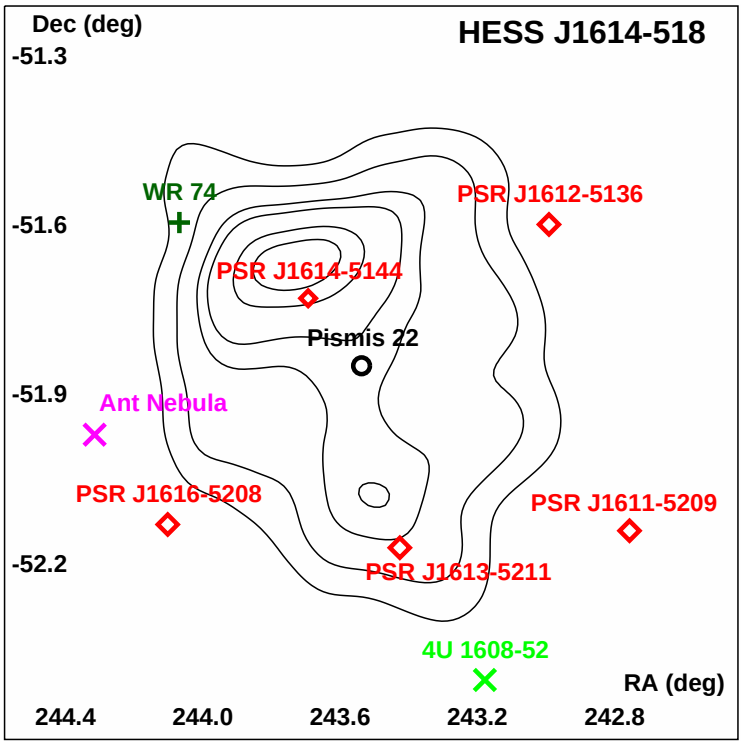

FIGURE 6.9 Image depicting the close-by astrophysical objects (possible counterparts) in the FoV of HESS J1614–518 (black contours). Among these objects are five radio pulsars (PSR J1611–5209, PSR J1612–5136, PSR J1613–5211, PSR J1614–5144, and PSR J1616–5208 marked as red diamonds) reported in Manchester et al. (2005), the stellar cluster Pismis 22 (Piatti et al., 2000) as black circle, the LMXB 4U 1608–52 as a light-green 'X' (Giacconi et al., 1974), the Ant Nebula as a magenta 'X' (Menzel, 1922), and the Wolf-Rayet star WR 74 as a dark-green cross (van der Hucht, 2001).

Several astrophysical objects are found within HESS J1614–518 and in its immediate vicinity. Among these are five pulsars, an old stellar cluster, a low-mass X-ray binary (LMXB) and two objects linked to late stages of the stellar evolution: a planetary nebula and a WR star (indicated in Figure 6.9). Based on the results presented earlier (Sects. 6.1 and 6.2), these objects are discussed in the light of them being possible counterparts to HESS J1614–518.

6.3.1 THE STELLAR CLUSTER PISMIS 22

The stellar cluster Pismis 22 was suggested as a counterpart candidate due to its location close to centre of HESS J1614–518 and because already a fraction of the usual kinetic energy deposited by stellar winds and SNe would be sufficient to explain the H.E.S.S. observations (Rowell et al., 2008; Ohm et al., 2010). In general, counterpart scenarios w.r.t. stellar clusters involve combinations of stellar winds (from single to collective wind activities) and occurred SNe (the remnant as well as the compact object). This was discussed in Section 2.2.2.

Although different methods to estimate the age of this cluster vary within a wide range of 5 . . . 65 Myrs, the most likely value is 40 ± 15 Myrs (Piatti et al., 2000). Its distance is 1.0 ± 0.4 kpc. Most of stars in the vicinity of Pismis 22 which are likely to be member stars lack a spectral-type determination leading to an unconstrained cluster mass. However, based on its age, Pismis 22 is unlikely to harbour any OB associations[i].

6.3.1.1 ISM

The void ($\sim 0.4^\circ$ in diameter) found in the SGPS HI data is located at the distance of Pismis 22 (see Section 6.2.3), this could indicate that acceleration processes linked to the cluster are responsible for void and perhaps also for the VHE γ-ray emission.

The mass of the HI shell within HESS J1614–518 is estimated to be $6.4 \times 10^3\,\mathrm{M}_\odot$ with hydrogen atom density $n \approx 90\,\mathrm{cm}^{-3}$ at 1 kpc. Here, a HI intensity-to-mass conversion factor of $1.8{\times}10^{18}\ \mathrm{cm}^{-2}\left(\mathrm{K\,km\,s}^{-1}\right)^{-1}$ (Dickey & Lockman, 1990) was used. In general, the void is found to be comparatively small with a diameter of 7 pc at a distance of 1 kpc after 40 Myrs, possibly hinting at a low initial cluster mass – as Wd1 (5 Myrs old, $\sim 10^5\,M_\odot$) exhibits a void of 55 pc in size (Kothes & Dougherty, 2007).

Based on this, the energy stored in the CRs E_{CR} can be calculated. For this, the cooling time for relativistic protons in matter

$$\tau_{\mathrm{pp}} \approx 1.7 \times 10^{15} \left(\frac{n}{1\,\mathrm{cm}^{-3}}\right)^{-1}\ \mathrm{s} \tag{6.11}$$

from Aharonian (2004) is used and results with the derived spectral parameters for the entire HESS J1614–518 region (Table 6.6) in

$$E_{\mathrm{CR}} \approx 1.2 \times 10^{47} \left(\frac{L_{>0.3\,\mathrm{TeV}}}{6.5 \times 10^{33}\,\mathrm{erg\,s}^{-1}}\right)\left(\frac{n}{90\,\mathrm{cm}^{-3}}\right)^{-1}\ \mathrm{erg}\,, \tag{6.12}$$

where $L_{>0.3\,\mathrm{TeV}}$ is the TeV luminosity above the observed energy threshold of 0.3 TeV scaled to the distance of Pismis 22.

6.3.1.2 KINETIC ENERGY AND STELLAR WINDS

Without the exact knowledge of the stellar content of Pismis 22, the kinetic energy deposited in this system is difficult to assess. Therefore, the `Starburst 99` cluster-evolution

[i] OB refers to high-mass stars of spectral type O and B.

model (Leitherer et al., 2010, and references therein) was used to estimate the expected kinetic-energy output by Pismis 22. The model results scale with the initial cluster $M_{\rm SC}$, which was the only parameter varied in this work; all other values are set to the defaults (see Appendix B.3).

As a result of the model, the current (i.e. $t = 40$ Myrs) luminosity powered by stellar winds and SNe is

$$L_{\rm kin}(t) \approx 5.2 \times 10^{36} \left(\frac{M_{\rm SC}}{10^3\,{\rm M}_\odot} \right) {\rm erg\,s^{-1}}\,. \tag{6.13}$$

The total kinetic energy estimated over a cluster life-time span $\Delta t = 40$ Myrs is

$$E_{\rm kin}(\Delta t) \approx 1.3 \times 10^{52} \left(\frac{M_{\rm SC}}{10^3\,{\rm M}_\odot} \right) {\rm erg}\,. \tag{6.14}$$

A fraction of the kinetic energy would be sufficient to explain HESS J1614–518 in terms of its energy requirement and also the current cluster luminosity would be sufficient to link HESS J1614–518 with Pismis 22. However, such a system with its output in kinetic energy would certainly leave its imprint in the cluster surroundings and the ISM. For example, the most massive known stellar cluster, Wd1, is surrounded by three voids in HI (Kothes & Dougherty, 2007). The largest void, with a diameter of ~ 55 pc, was suggested to be the effect of the combined cluster wind. The smaller ones are believed to be due to the onset of different late-type stages of the high-mass stars.

Models as in Silich et al. (2005) predict a cluster-wind driven void which is much larger (in the order of 100 pc) than the observed HI void (Sect. 2.2.2). However, this model may not be applicable to Pismis 22 because the stellar winds of this SC (the source power of collective cluster wind) should have ceased already. In addition, models as in Oskinova (2005) predict any stellar wind-driven activity to cease at around 40 Myrs of cluster age depending on the initial cluster mass. Hence, if the initial cluster mass of Pismis 22 would be significantly lower than $\sim 10^{5...6}\,M_\odot$, any collective cluster-wind activity has ceased much before 40 Myrs. Moreover, Oskinova (2005) predicted that (massive) stellar clusters at an age around 40 Myrs should still exhibit an X-ray-bright diffuse emission; mainly through SNe. A diffuse emission potentially visible in the Suzaku or XMM–*Newton* data were not reported in Sakai et al. (2011).

6.3.1.3 SNR SCENARIO

At an cluster age of ~ 40 Myrs, most OB stars would have evolved beyond to the supernova stage, perhaps suggesting an SNR origin for HESS J1614−518. Although a specific distance to the SNR is not preferred a priori, it is expected that the progenitor star is likely to a member of Pismis 22. At a distance of 1 kpc, the observed TeV-emission region with radius of 0.51° translates into 9 pc in radius. Using a Sedov-Taylor solution to approximate the SNR age based on the size and the ambient density of $90\,{\rm cm^{-3}}$ (Chevalier, 1982), the age of the SNR is 4.1×10^4 yrs, which places the SNR beyond the Sedov-Taylor phase and in the so-called *snow-plow* phase. At this stage, one would expect the SNR to be bright in other wavelengths as well but the inspection of archival MWL data does not reveal any convincing correlation with the TeV emission. Especially, the lack of matching X-ray data did not support this scenario.

6.3.2 THE WOLF-RAYET STAR WR 74

The star WR 74 (van der Hucht, 2001) is a Wolf-Rayet star of spectral type WN7, which sets the initial mass to more than $20\,M_\odot$. It is located at a distance of 4.4 kpc and north-east of the strong northern emission region HESS J1614–518N. For a typical WN7 star, the kinetic-wind energy can be estimated to be around $10^{37}\,\mathrm{erg\,s^{-1}}$ (Crowther, 2007). Hence, a fraction of a few percent would be needed to explain the entire TeV emission.

However for a scenario, in which WR 74 is the powering source of the TeV emission one would expect the emission to be centred around the WR star. And: in a scenario where HESS J1614–518(N) is the result of the interaction between the WR wind and the ambient matter, the ambient conditions at the distance of the WR 74 should reflect this. No convincing match in archival data were found between WR 74 and HESS J1614–518 or its subregions.

In summary, a counterpart scenario involving WR 74 is unlikely based on the TeV morphology and the molecular-gas distribution.

6.3.3 THE LOW-MASS X-RAY BINARY 4U 1608–52

The *atoll*-type[ii] LMXB 4U 1608–52 (Giacconi et al., 1974) is located about 0.2° south-west of HESS J1614–518S and at a distance of 3.6 kpc. 4U 1608–52 consists of a $1.4\,M_\odot$ neutron star with a stellar companion of spectral type late F to early G (Wachter et al., 2002).

In the years 2004 and 2007, several X-ray outbursts of this LMXB were reported (Remillard et al., 2005; Palmer et al., 2007). The former one being named a *superburst* with a flux rise between 0.2 and 12 keV up to 1.5 times of that of the Crab Nebula in the same energy band. The latter outburst triggered a few H.E.S.S. observations without a detection. 4U 1608–52 has been detected with INTEGRAL (Bird et al., 2004; Tarana et al., 2007), but not with the *Fermi*–LAT and at its location no hint for a TeV emission is seen.

The Eddington luminosity for this LMXB is $L_{\mathrm{Edd}} \approx 2 \times 10^{38}\,(M/1.4\,M_\odot)\,\mathrm{erg\,s^{-1}}$. According to Gierliński & Done (2002), 10 % of L_{Edd} constitutes the available energy budget for an atoll-type LMXB. For 4U 1608–52, this would be more than sufficient to explain HESS J1614–518, in terms of its energy requirements.

Unlike high-mass X-ray binaries, LMXBs are not known to be TeV accelerators. Moreover, any emission from this object would be expected to arise at the location of 4U 1608–52 itself. Although this LMXB could provide sufficient energy to account for HESS J1614–518, the extent and morphology (located outside HESS J1614–518) disfavours any scenario involving 4U 1608–52.

[ii] Atoll refers to a less luminous subclass of LMXBs showing distinct features in the luminosity evolution (e.g. Church et al., 2014, and references therein).

6.3.4 THE ANT NEBULA

The Ant Nebula (PN Mz 3; Menzel, 1922) is a planetary nebula located beyond the eastern boundary of HESS J1614–518. It is a system losing mass in form of dense winds and exhibiting bipolar outflows in north-south direction visible at various wavelengths from radio frequencies to optical wavelengths and X-ray energies (e.g. Santander-García et al., 2004, and references therein). This bipolar outflow together with its MWL appearance, which resembles an ant motivated its nomenclature.

Because the interior of the nebula is obscured by its own envelope, its nature is not clear: it may be caused by a single medium-mass star and its dense winds or may be also the result of a binary system with a white dwarf as companion (Schmeja & Kimeswenger, 2001; Zhang & Liu, 2006, and references therein). Subsequently, besides its mass, distance and velocities of the outflows are uncertain. The upper limit on its distance is 2.6 kpc (Smith, 2003). The nebula appears to expand at a velocity of $\sim 50\,\mathrm{km\,s^{-1}}$ (Lopez & Meaburn, 1983). This is consistent with other known planetary nebulae, although velocities up to $300\,\mathrm{km\,s^{-1}}$ seem possible (Frew & Parker, 2010). The lobes may expand at larger velocities (e,g, Santander-García et al., 2004).

However, any VHE γ-ray emission, either through acceleration in the expanding nebula or in the lobes, is expected to be centred around this object. The location of the Ant Nebula afield from HESS J1614–518 and the complex morphology of HESS J1614–518 disfavour such a scenario.

6.3.5 PULSARS AND PULSAR-WIND NEBULAE

Pulsars and pulsar-wind nebulae constitute the largest source class of identified Galactic counterparts in the VHE γ-ray regime. Hence, the presence of such an object could always be indicative for a PWN scenario.

As to be seen in Figure 6.9, five pulsars are in the FoV of HESS J1614–518 with two of them being within the TeV emission region. However, none of them have been detected in the HE regime with the *Fermi*–LAT nor with XMM–*Newton* in the X–ray band. In Table 6.10, a summary of the pulsar properties is given.

As none of these relatively old pulsars have been detected in X-rays, the expected X-ray luminosity L_X between 2 and 10 keV was estimated based on the empirical correlations of TeV PWNe and the associated pulsar in Mattana et al. (2009). The X-ray luminosity can be estimated through the pulsar spin-down power $\dot{E}$:

$$\log_{10}\left(\frac{L_\mathrm{X}}{\mathrm{erg\,s^{-1}}}\right) = 33.8 + 1.87\,\log_{10}\left(\frac{\dot{E}}{10^{37}\,\mathrm{erg\,s^{-1}}}\right). \tag{6.15}$$

Alternatively, L_X can be calculated using the characteristic age of the pulsar τ_c:

$$\log_{10}\left(\frac{L_\mathrm{X}}{\mathrm{erg\,s^{-1}}}\right) = 33.7 - 2.49\,\log_{10}\left(\frac{\tau_c}{10^{4}\,\mathrm{yrs}}\right). \tag{6.16}$$

A mean value for the expected X-ray luminosity $\bar{L}_\mathrm{X,exp}$ was calculated from Equations 6.15 and 6.16. Given the expected X-ray luminosity one can calculate a predicted TeV

TABLE 6.10 Properties of the pulsars in the FoV of HESS J1614−518 from Manchester et al. (2005). The table columns are the pulsar name in J2000, the distance estimate from dispersion measurements d, the barycentric period P_0 and its first time derivative $\dot{P}$, and the inferred quantities: the characteristic age τ_c, the spin-down power $\dot{E}$, and the surface magnetic flux density $B_{\rm surf}$.

Pulsar	d	P_0	$\dot{P}$	τ_c	$\dot{E}$	$B_{\rm surf}$
	kpc	s	10^{-15} s s^{-1}	Myrs	10^{34} erg s^{-1}	10^{12} G
J1611-5209	3.3	0.18	5.2	0.56	3.40	1.0
J1612-5136	18.2	0.48	3.8	2.0	0.13	1.4
J1613-5211	6.1	0.46	19.2	0.38	0.79	3
J1614-5144	9.6	1.53	7.4	3.3	10^{-3}	3.4
J1616-5208	7.4	1.03	28.9	0.56	0.11	5.5

TABLE 6.11 Mean expected X-ray (2 - 10 keV) and γ-ray (1 - 30 TeV) luminosities for the five pulsars calculated through Equations 6.15, 6.16, 6.17, and 6.18, respectively. Additionally, the observed luminosity for HESS J1614–518 (Full) and the extended northern (North) and southern (South) regions are computed at the pulsar's distance using the spectral shape determined in Section 6.1.2.

Pulsar	$\bar{L}_{\rm X,exp}$	$\bar{L}_{\gamma,\rm exp}$	$L^{\rm Full}_{\gamma,\rm obs}$	$L^{\rm North}_{\gamma,\rm obs}$	$L^{\rm South}_{\gamma,\rm obs}$
	10^{29} erg s^{-1}	10^{34} erg s^{-1}	10^{34} erg s^{-1}	10^{34} erg s^{-1}	10^{34} erg s^{-1}
J1611...	1.88	1.72	3.34	0.89	0.56
J1612...	0.05	1.59	99.6	26.5	16.6
J1613...	3.03	1.80	11.4	3.02	1.90
J1614...	0.01	1.57	27.5	7.32	4.60
J1616...	2.20	1.76	16.4	4.36	2.74

luminosity between 1 and 30 TeV (Mattana et al., 2009), either through the pulsars spin-down power:

$$\log_{10}\left(\frac{L_\gamma}{L_{\rm X}}\right) = 0.57 - 1.88\ \log_{10}\left(\frac{\dot{E}}{10^{37}\ {\rm erg\ s^{-1}}}\right), \tag{6.17}$$

or as a function of the characteristic age of the pulsar:

$$\log_{10}\left(\frac{L_\gamma}{L_{\rm X}}\right) = 0.89 + 2.14\ \log_{10}\left(\frac{\tau_c}{10^4\ {\rm yrs}}\right). \tag{6.18}$$

With the Equations 6.17 and 6.18 a mean expected γ-ray luminosity $\bar{L}_{\gamma,\rm exp}$ is determined. In Table 6.11, the X-ray and the γ-ray luminosities are summarised for all pulsars.

In general, the X-ray non-detections are consistent with the findings in Mattana et al. (2009) as the expected X-ray luminosities of the pulsars are $\sim 10^{29}$ erg s^{-1} or lower and hence, below the detection threshold of current X-ray experiments like XMM–*Newton*. The expected TeV luminosity at the pulsar distances are below the observed results for HESS J1614–518 or either of its subregions. Moreover, the spin-down power of four

of the five pulsars studied here are too low to energetically explain HESS J1614–518 or parts of it (compare $\dot{E}$ in Table 6.10 with the results in Table 6.11). The link between PSR J1614-5144 and HESS J1614−518N, and PSR J1613-5211 and HESS J1614−518S motivated by spatial conincidence is not supported by the inferred energetics as both pulsars are too weak to power the TeV emission.

PSR J1611–5209 The only pulsar, for which a sufficiently large $\dot{E}$ is observed, is PSR J1611–5209. Here, HESS J1614–518 would require an unlikely high conversion efficiency of $\dot{E}$ to L_γ of unity. However, the expected γ-ray luminosity from HESS J1614–518 is a factor of 2 lower than the luminosity scaled to the pulsar distance. On the other hand, either subregion would require a conversion efficiency of $0.2 \ldots 0.3$, but since PSR J1611–5209 is $\sim 1^\circ \ldots 1.5^\circ$ away from HESS J1614–518N or HESS J1614–518S, such a scenario appears unlikely. Also, the complex morphology of HESS J1614–518 cannot be explained by this pulsar offset from the TeV emission,

RELIC PWN SCENARIO In de Jager et al. (2009), PWN scenarios were discussed in the light of X-ray non-detections and named *relic* PWNe. Here, the old age of the pulsar resulted in a decline of the magnetic field strength and inevitably to a decline of the X-ray flux through synchrotron radiation, whereas the PWN could still remain bright in the VHE γ-ray regime. The initial pulsar spin-down power is found to be in the range of $10^{38} \ldots 10^{40}$ erg s^{-1} (Mattana et al., 2009, Eq. 8;); hence, an older population of electrons could explain (parts of) HESS J1614–518.

It is interesting to point out that PSR J1614-5144 lies at the same distance as Suzaku Src A (best fit for $\sim$ 10 kpc) thus indicating a possible connection between the pulsar, keV energies and HESS J1614–518N. Matsumoto et al. (2008) determined the distance of Suzaku Src A to be around 10 kpc, which matches that of PSR J1614-5144.

PREVIOUSLY *dark* H.E.S.S. SOURCES IDENTIFIED AS PWNE Any association of one of these pulsars with HESS J1614–518 would place them among the oldest and lowest spin-down powered TeV PWNe (de Oña Wilhelmi, 2011). Supporting a PWN scenario, Kargaltsev et al. (2013) showed in a population study that most TeV γ-ray PWNe (candidates) remain undetected in X-rays and at GeV energies (e.g. with *Fermi*–LAT) for spin-down powers below 10^{35} erg s^{-1}. In this respect, it cannot be ruled out that HESS J1614–518 or parts of this source are powered by a PWN, which is yet undetected in X-rays and at radio wavelengths.

This was the case for the previously unidentified TeV source HESS J1303–631, for which the pulsar PSR J1301–6305 was found to be the counterpart (Abramowski et al., 2012a). The faint and slightly extended X-ray PWN with a flux between 2 and 10 keV of $\sim 10^{-13}$ erg cm^{-2} s^{-1} was small (2 arcmin in size) compared to the H.E.S.S. source with a diameter of $\sim 0.4^\circ$. But that pulsar exhibits a larger spin-down power ($\sim 10^{36}$ erg s^{-1}) and is younger (11 kyrs) than any of the reported pulsars in the FoV of HESS J1614–518.

The TeV to X-ray ratio with $F_{1-30\,TeV}/F_{2-10\,\mathrm{keV}} = 156$ is the largest ratio observed so far (Abramowski et al., 2012a). In the case of HESS J1614–518, the X-ray non-detections of the pulsars with XMM–*Newton* set a limit of the flux to 2×10^{-14} erg cm^{-2} s^{-1} (Sect.

6.2.2.3). The HESS J1614–518 flux between 1 and 30 TeV is 2.5×10^{-11} erg cm^{-2} s^{-1}. Hence, the observed ratio $F_{1-30\,TeV}/F_{2-10\,\mathrm{keV}} = 1259$ would be highest observed ratio so far for a putative PWN scenario. Even if the TeV flux is compared to the Suzaku sources Src A and Src B, the ratios of 48 and 180, respectively, would still be among the highest observed ratios.

Also, the neighbouring source HESS J1616–508 was long considered to be a dark particle accelerator with a large TeV-to-X-ray flux ratio of more than 55 (Matsumoto et al., 2007). However, Acero et al. (2013) identified this source to be an ancient PWN given the presence of energetic pulsar, the hard HE to VHE spectrum, and the smooth connection of the observed fluxes from TeV to low GeV energies based on H.E.S.S. and *Fermi*–LAT data, respectively.

A PWN and therefore a leptonic scenario might be supported by the absence of a low-energy cutoff in the combined MeV-to-TeV spectrum. Moreover, the possible preference towards a TeV spectrum best-described by power-law with an exponential cutoff could further support such a scenario since firmly associated TeV PWNe show a clear cutoff in TeV spectra due to the efficient cooling of the accelerated leptons.[iii] In contrast, the HESS J1614–518 appears to be difficult to be explained by a PWN since two pronounced subregions are observed and no indication for a spectral softening is found.

6.3.6 UNDETECTED SNR

As discussed in the case of Pismis 22, a SNR scenario could explain HESS J1614–518. If so, than the void seen in the HI map could be its manifestation in the ISM leaving two possible distances at which this SN event could have taken place, namely ~ 1 kpc or ~ 13 kpc. In this scenario, one of the unidentified XMM–*Newton* point sources towards Pismis 22 could be the central compact object of the SN. However, the lack of a correlation between TeV and X-ray features (or with other MWL data in general) as observed for SN 1006 (Acero et al., 2010), could indicate a very young SNR in the free-expansion phase where radiation losses in other wavelengths remain negligible.

6.4 SUMMARY AND CONCLUSIONS

In this work, additional data on HESS J1614–518 were analysed. The TeV γ-ray source HESS J1614–518 is detected at a statistical significance of $26.4\,\sigma$ after 33 hrs of data. The source radius has increased from 0.2° to 0.51° and has therefore more than doubled since its original discovery reported by Aharonian et al. (2005a). Two pronounced sub-regions are visible at plain sight of the VHE γ-ray excess skymap and supported through the morphological studies conducted in this work. Also, there appears to be a hint for an energy-dependent change in morphology at a $2.6\,\sigma$ level. The entire source region is best fit with a simple power law with a normalisation at 1 TeV of $\Phi_0 = (8.47 \pm 0.44) \times 10^{-8}$ TeV^{-1} m^{-2} s^{-1} and an index of $\Gamma = 2.40 \pm 0.05$. A power law with an exponential

[iii] The only reported exception appears to be HESS J1908+063 (Aharonian et al., 2009a; de Oña Wilhelmi, 2011).

cutoff is favoured with least $2.9\,\sigma$. The spectral analyses of the subregions do not support a spectral change across HESS J1614–518. The integrated flux of HESS J1614–518 amounts to 24.1 % of flux of the Crab Nebula above the same energy threshold.

In this work, available *Fermi*–LAT data were analysed. The GeV and TeV spectra align smoothly. The analysis did not support a hadronic origin as no low-energy cutoff was found. However, the analysis obviously suffered from systematics at low MeV energies and therefore needs to be taken cautiously.

Additionally, data in the radio and the X-ray regime were investigated, but did not provide for convincing hint to explain HESS J1614–518. Different astrophysical objects were discussed in the light of being possible counterparts.

As one of the possible counterparts, Pismis 22 and a collective cluster-wind scenario could naturally provide the energy required to power HESS J1614–518. However, the available radio data do not support this source origin as the observed HI void appears to be too small and either hints at a low initial-cluster mass or the absence of such a scenario as counterpart for HESS J1614–518. It is difficult to assign a PWN origin to HESS J1614–518. The five pulsars in the FoV are too old, too weak and without a detected X-ray counterpart. The undetection in X-rays is predicted by Mattana et al. (2009); Kargaltsev et al. (2013) for such old and low-spin-down powered pulsars and therefore, a relic-PWN scenario cannot be excluded, but is challenged by the TeV morphology. An association with one of these pulsars (or with a yet undetected pulsar) would make HESS J1614–518 the PWN with the highest observed TeV-to-X-ray flux ratio (48 . . . 1259). A SNR origin was already discussed in Sakai et al. (2011). Indeed, a possible central compact object (Suzaku Src B or the XMM–*Newton* sources B1 to B4) in the centre of HESS J1614–518 could support this scenario. However, the lack of any convincing correlation between HESS J1614–518 and the ambient medium at various MWLs and also the lack of matching X-ray emission makes it difficult to reconcile a SNR origin.

Thus, the nature of HESS J1614–518 remains unrevealed and mysterious. This source is still one of the *darkest* sources in the TeV γ-ray sky.

6.5 OUTLOOK

More data in the VHE regime would be useful to manifest the apparent energy-dependent change in morphology and to verify the hint for a spectral change across the source (i.e. north to south). As only 33 hrs of data on this source were available and less than half of these for spectral studies, at least the double amount of data through dedicated observations would be needed.

The available X-ray data do not entirely cover HESS J1614–518 region, but only the pronounced subregions. A complete and preferably deep X-ray coverage on this source would be helpful to understand acceleration and emission processes in and around this source. The *Fermi*–LAT analysis of 1FHL J1615.3–5146e suffered from systematics. Since its location does not perfectly matching that of HESS J1614–518, it may be worthwhile to abandon 1FHL J1615.3–5146e and use the TeV emission region as template for a new *Fermi*–LAT analysis instead.

Chapter 7

Search for very-high-energy Gamma-Rays from the Gould Belt

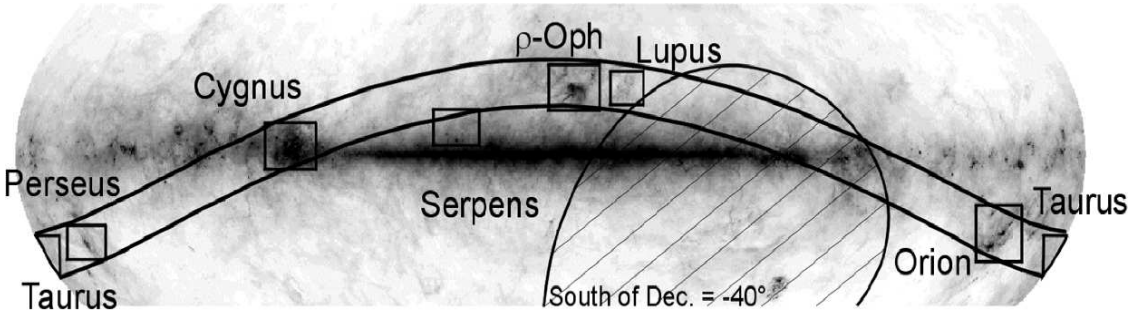

Figure 7.1 The Gould Belt depicted on the 100 μm emission map observed with Infrared Astronomical Satellite (Neugebauer et al., 1984). Marked are the most-famous cloud members and regions. Image adopted from *jach.hawaii.edu/JCMT/surveys/gb*.

[i] The Gould Belt was discovered by Herschel (1847) and studied by Gould (e.g. in Gould & Galle, 1874). It is a dense structure traced by molecular clouds, cloud complexes and SFRs (Fig. 7.1). About two thirds of all known high-mass stars within 600 pc are found to be members of the GB. Even if only early spectral types between O and B2.5 are considered, the fraction is still 50 %. The GB is inclined w.r.t. the Galactic Plane by $17.2^\circ \pm 0.3^\circ$ and its elliptical shape is described by its major axis of 354 ± 5 pc and minor axis of 232 ± 5 pc with a height of ~ 60 pc. There are indications that the elliptical shape extends about 100 pc inwards and therefore, the GB might be rather considered a disk (Guillout et al., 1998). The Sun is located about 100 pc off from centre of the GB (Fig. 7.2).

The formation of the GB is still a subject to ongoing investigation, and different explanations have been put forward to explain this tilted belt. Among these is, for example, a scenario of a giant molecular cloud of 400-500 pc in diameter and a mass of $10^6 - 10^7\ M_\odot$ falling into the spiral arm. Or a series of SNe and stellar-wind activities or a γ-ray burst, or combinations thereof. The GB is best-modelled by either a cylindrical three-dimensional shock wave or a local superbubble. Depending on the model, the predicted age of the

[i] A nice overview on the GB is given in Grenier (2004, and references therein), which is used here for the introductory words.

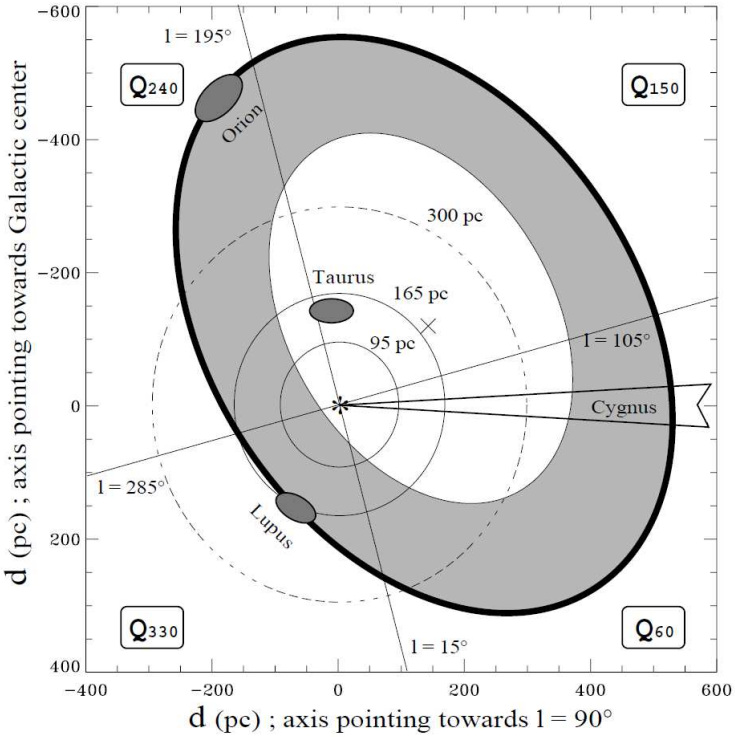

FIGURE 7.2 Schematic display of the Gould Belt (grey-shaded area) and some of its cloud complexes w.r.t. the location of the Sun (cross marker). Image adopted from (Guillout et al., 1998).

GB varies between 15 Myrs (superbubble) and 26 Myrs (shock wave), which is younger than the age based on stellar observations (30 to 80 Myrs). A detailed summary of these models is given in Grenier (2004, and references therein).

Among the unidentified EGRET sources (Hartman et al., 1999, see also the introduction in Chapter 3), nearly 40 of these were thought to be from within the GB. As discussed in Chapter 2, high-mass stars and SFRs can provide a sufficient reservoir of kinetic energy and were therefore considered as possible sources. However, the lack of counterparts at radio and X-ray wavelengths made an association difficult and therefore left these sources *dark*. None of these sources correlated with the overabundant high-mass O stars. Grenier (2004) argued that these sources might only be efficient γ-ray emitters, perhaps linked to neutron stars, and ruled out objects such as binaries (as they would shine bright in X-rays) and SNRs (as they would appear extended given the proximity).

The GB clouds are clearly visible as dense and large structures over the entire sky (Fig. 7.1). In Figure 7.3, the GB clouds that were targeted with the H.E.S.S. telescope are illustrated. The clouds are CO(1-0)-emission bright structures, which are significantly larger than the H.E.S.S. FoV.

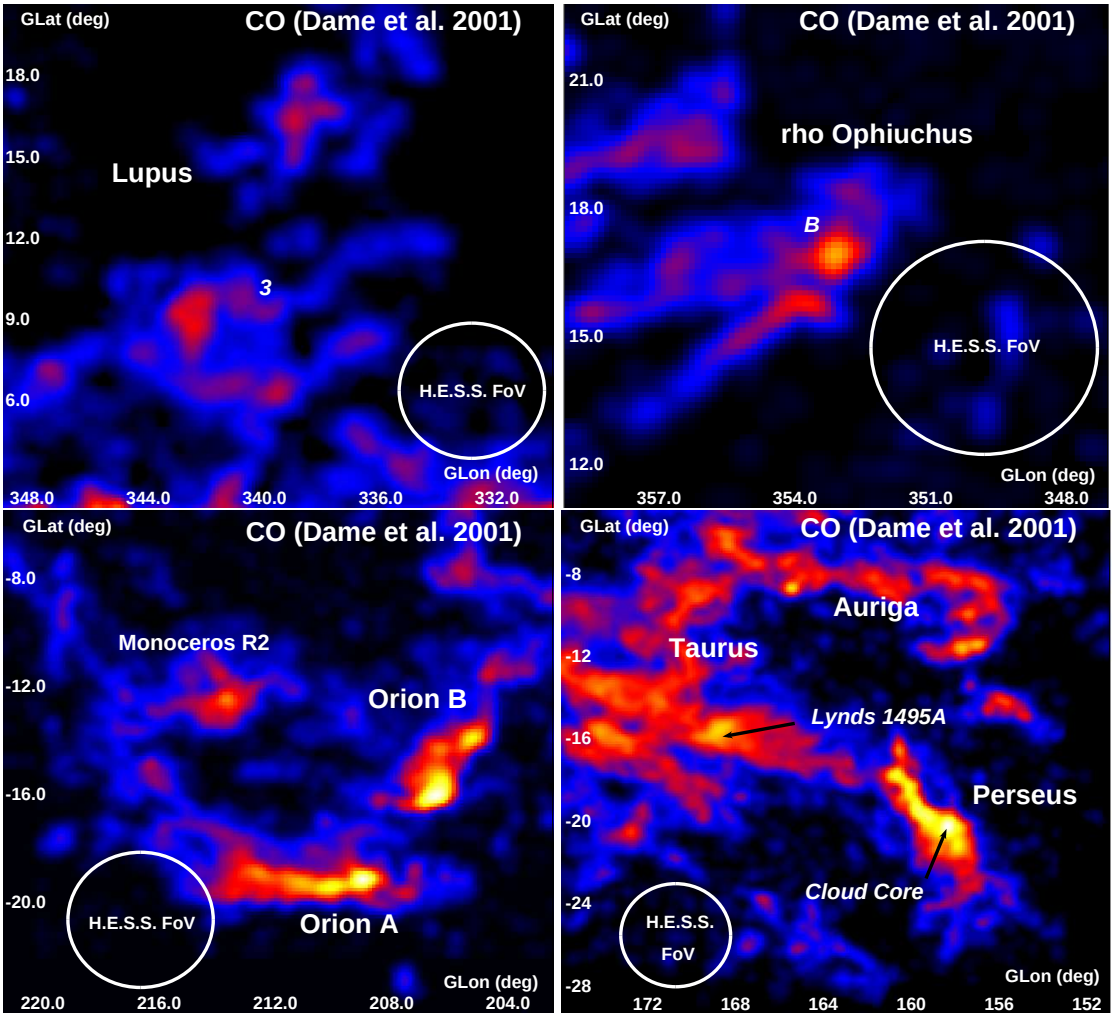

FIGURE 7.3 The CO(1-0) radio map (in units of K) integrated over the entire velocity range from Dame et al. (2001) of the studied GB regions in the Galactic coordinate system. For a better visibility of the clouds, the colour scale is truncated between 0 and 90 K (transition from black to blue at 1 K, from blue to red at 20 K, and from red to yellow at 50 K). Because the size of the clouds vary, the H.E.S.S. FoV with a diameter of $\sim 5^\circ$ is indicated by a white circle. **LEFT TOP:** The Lupus-cloud complex consisting of nine subclouds. The position of cloud 3 (the H.E.S.S. target) is marked. **RIGHT TOP:** The ρ–Ophiuchus cloud with the subcloud *B*. **LEFT BOTTOM:** The Orion-cloud complex consisting of Orion A and Orion B. Additionally, the cloud Monoceros R2 is marked. **RIGHT BOTTOM:** The Taurus/Auriga complex and the Perseus cloud region. The subclouds of interest, namely Lynds 1495A and the core of the Perseus cloud, are indicated as well.

7.1 *Fermi*–LAT OBSERVATIONS

The molecular clouds and cloud complexes associated with the GB appear bright in HE γ rays, mainly through interactions of the cloud matter with relativistic protons giving rise to γ rays through π^0 decay. The HE γ-ray emission above 100 MeV traces the clouds very well. Only in the case of Lupus, the cloud is not clearly visible and most likely outshone by the diffuse emission around the Galactic Centre and from the Galactic Plane (see Appendix C.1 for the HE skymaps and a brief overview of *Fermi*–LAT sources in the FoV).

A spectral analysis of these clouds is not possible in the standard *Fermi*–LAT analysis framework: these clouds and the γ-ray emission towards them are included in the Galactic diffuse-emission model and therefore considered a background in the analysis of *Fermi*–LAT data. Yang et al. (2013) generated an individual Galactic diffuse-emission model excluding GB-associated clouds and cloud complexes. With this updated model, ten GB-associated regions were analysed using a minimum energy of 300 MeV up to $\sim$ 30 GeV. All sources were detected as large extended emission regions with sizes in the order of $10 \ldots 100\,\mathrm{deg}^2$ and at a significance level of $30 \ldots 100\,\sigma$. As a result, all spectra were well fit with simple power laws of $\Gamma \approx 2.85$. This result is compatible with the earlier results of Neronov et al. (2012). Moreover, Neronov et al. (2012) argued that the similarity of the individual spectra and the observed fluxes indicate that these clouds are *passive*. They serve as target material for proton-proton collisions and do not contain a CR accelerator (visible in the HE regime).

The integral fluxes in the HE regime of the GB clouds that were also observed with H.E.S.S. are presented in Table 7.1. Since the reported spectra of the GB sources indicate a spectral break at low GeV energies that is not further specified in Yang et al. (2013), the calculated integral fluxes are to be considered a conservative estimate that will slightly overestimate the GeV flux.

TABLE 7.1 The integral fluxes between 0.3 GeV and 300 GeV ($F_{0.3-300\,\mathrm{GeV}}$) of the GB clouds observed with *Fermi*–LAT and also targeted with H.E.S.S. The spectral results are based on Yang et al. (2013); a power law with $\Gamma = 2.85$ is assumed for all clouds. The angular size and the flux normalisation at 3 GeV are stated.

Cloud	Angular size deg^2	$\Phi_0(3\,\mathrm{GeV})$ $10^{-5}\,\mathrm{GeV}^{-1}\,\mathrm{m}^{-2}\,\mathrm{s}^{-1}$	$F_{0.3-300\,\mathrm{GeV}}$ $10^{-4}\,\mathrm{m}^{-2}\,\mathrm{s}^{-1}$
[1]Lupus	—	—	—
Taurus	101	9.8 ± 1.0	1.64
Orion A	28	6.9 ± 0.7	1.15
Perseus	27	3.7 ± 0.3	0.62
ρ–Oph	68	9.5 ± 0.8	1.59

[1] The Lupus-cloud complex at high energies (see also Figure C.1) and results on this cloud were not reported in Yang et al. (2013).

7.2 H.E.S.S. OBSERVATIONS AND DATA ANALYSIS

Among the GB-associated clouds and cloud complexes, following clouds were observed with the H.E.S.S. telescope: Lupus (the wolf), Ophiuchus (the serpent bearer), Orion (the hunter), Perseus (Greek mythological hero) and the Taurus region (the bull). In general, these cloud complexes are larger than the H.E.S.S. FoV thus making it impossible to encompass the entire cloud in the camera (Fig. 7.3). Therefore, the densest and most compact regions of the clouds were targeted: the Lupus 3 cloud, ρ-Oph B cloud, Orion A, the core of Perseus, and Lynds 1495A (see Table 7.2).

TABLE 7.2 GB cloud complexes observed with H.E.S.S.. The target coordinates, the assumed cloud radius, the mass estimate, and the distance are taken from Aharonian et al. (2005c).

Cloud	RA (J2000) deg	Dec (J2000) deg	θ_{cloud} deg	M_{cloud} $10^3\,M_\odot$	d kpc
Lupus 3	242.25	-39.117	0.3	0.3	0.15
Lynds 1495A	64.65	28.417	2.0	1	0.14
Orion A	84.074	-5.884	0.5	20	0.5
Perseus Core	52.437	31.225	0.4	4	0.35
ρ–Oph B	246.796	-24.475	0.4	1.4	0.17

Based on the *Fermi*–LAT results by Yang et al. (2013) and assuming that the GeV spectra connect smoothly (unbroken) with the flux in the TeV regime, the extrapolated fluxes in Table 7.3 for the observed GB sources are well below (i.e. a factor $\sim 10^{-4}$) the nominal H.E.S.S. sensitivity (see Section 3.3). In this case and in the absence of TeV-particle accelerators within the cloud, no TeV γ-ray emission is expected.

On the other hand, the inspection of the skymaps of *Fermi*–LAT data above 10 GeV seem to provide a weak hint that VHE γ-ray emission may be observable towards the dense parts of Orion A and ρ–Oph B. This hint is based on the apparent spatial correlation between the highly smoothed counts map above 10 GeV and cloud structure (see Figures C.3 and C.5 in Appendix C.1 and discussion therein). In this work, the available H.E.S.S. data on the GB summarised in Table 7.4 were analysed with HAP (version `13-03pl01`).

TABLE 7.3 Extrapolated TeV fluxes for the GB sources based the spectral results in the MeV-to-GeV range presented in Yang et al. (2013). The factor $\Omega_{\mathrm{HESS}}/\Omega_{\mathrm{Fermi}}$ accounts for the different angular sizes of the source regions in the *Fermi*–LAT analysis (Table 7.1) and the assumed source radii of the H.E.S.S. targets (Table 7.2). The energy threshold is calculated for the H.E.S.S. observations at the wobble offsets and the zenith angles listed in Table 7.4. The integral flux above this threshold is calculated by extrapolation of the GeV spectrum and correcting for the smaller assumed H.E.S.S. -source size.

Cloud	$\Omega_{\mathrm{HESS}}/\Omega_{\mathrm{Fermi}}$	E_{min} TeV	$F(>E_{\mathrm{min}})$ $10^{-12}\,\mathrm{m}^{-2}\,\mathrm{s}^{-1}$
Lupus 3	—	0.25	—
Lynds 1495A	0.12	1.00	6.19
Orion A	0.03	0.25	12.8
Perseus Core	0.02	1.26	0.23
ρ–Oph B	0.01	0.25	4.63

TABLE 7.4 H.E.S.S. data on the GB cloud complexes analysed in this work.

Cloud	Period	mean(z_{obs}) deg	mean(ω_{obs}) deg	Live time hrs
Lupus 3	2006, 2012	20.7	0.6	3.1
Lynds 1495A	2007	53.5	0.9	9.7
Orion A	2006, 2007	24.2	0.8	12.0
Perseus Core	2009	54.7	0.7	4.2
ρ–Oph B	2006	26.9	0.9	11.5

7.3 SEARCH FOR VHE GAMMA-RAY EMISSION

Motivated by the soft GeV spectra of $\Gamma_{\text{Fermi}} = 2.85$, the TMVA-based ζ_{std} cuts with an image-size cut of 60 p.e. were used for the gamma/hadron separation. This resulted in a lower energy threshold compared to the ζ_{hard} cuts and in a better gamma/hadron separation compared to the Hillas-based analysis for the skymap generation (Sect. 3.3.5).

The background for the skymaps was determined using the TBg model (Sect. 3.3.8.4) as the presence of faint and extended diffuse γ-ray emission is anticipated, which could possibly be cancelled out by the RingBg method more easily. In addition, the TBg skymaps only include events with a maximum offset of 2° to reduce the camera-edge effect. The RingBg method was applied to cross check the results and for this, events were considered within 2.5° of the camera centre. The inner ring radius was 0.5° and had a thickness of 0.2°.

The skymaps are produced by integrating events within a radius of 0.22°.[i] For every bin in the skymaps, the significance is calculated according to Equation 3.22. To reduce the noise introduced by statistical fluctuations, each skymap is smoothed with a Gaussian function with a σ of the size of the PSF.

Bright stars in the FoV may a distortion of the local acceptance and lead to systematic effects at the respective position (Sect. 3.3.8.5). In the case of the TBg model, usually a slight overcorrection is observed resulting in a positive significance. The RingBg method leads to an underestimate of the excess at the stellar position. Therefore, stars listed in the Hipparcos Star Catalogue (Perryman et al., 1997) that are brighter in apparent magnitude than 5 in the Johnson V band are depicted in all skymaps. In the analysis, the star position is excluded with a radius of 0.2° when determining the camera acceptances.

Besides the skymaps, one-dimensional histograms of significance values in the respective skymaps are produced. Unless the background estimates suffer from systematics (e.g. in the acceptance correction) or from potential and yet unknown γ-ray sources in the FoV, the significance distribution is a standard Gaussian distribution with $\sigma = 1$ and $\mu = 0$. The colour bars of the skymaps are truncated to range consistently between $-4\,\sigma$ and $+4\,\sigma$.

[i] This larger integration radius is appropriate for faint and extended sources and also used when scanning FoVs for possible γ-ray sources (Aharonian et al., 2005a).

7.3.1 LUPUS 3

In Figure 7.4, the VHE γ-ray significance skymaps are shown for the analysis with the TBg model (left) and the RingBg method (right). The CO(1-0) contours (6 to 18 K in steps of 3 K) of the Lupus 3 subcloud are depicted as black-dashed lines (Dame et al., 2001). There is one reported *Fermi*–LAT source in the FoV, namely 2FGL J1610.6–4002, which is associated with a flat-spectrum radio quasar (FSRQ[ii]) by Nolan et al. (2012), but not detected in this analysis. In Perryman et al. (1997), three bright stars are found: HIP 78655 (1, 4.90^{mag}), HIP 78384 (2, 3.42^{mag}), and HIP 78918 (3, 4.22^{mag}).

In the left skymap, a possible extended region (a contiguous structure of $2\,\sigma$ to $\sim 3\,\sigma$ regions) towards the cloud structure is apparent, which is not visible in the skymap produced with the RingBg method (right). Within this region, no known VHE γ-ray accelerator is found. The significance distributions do not support a possible hint for γ-ray emission.

As this region is located towards the cloud, an enlarged source region with a radius $\theta = 1^\circ$ was defined at the coordinates (242.643°, −37.966°) and re-analysed with the TBg model and the RingBg method (inner ring radius of 1.1°). The TBg analysis resulted in a background normalisation $\alpha_{\mathrm{TBg}} = 0.028$ and 159 excess events at a statistical significance of $3\,\sigma$. In the RingBg analysis, 48 excess events were derived at a $0.5\,\sigma$ level with a background normalisation $\alpha_{\mathrm{RingBg}} = 2.59$. Therefore, no further evidence for extended VHE γ-ray emission is found towards this region in the dedicated analyses.

[ii] FSRQs are a subclass of active galactic nuclei with a flat spectrum at radio wavelengths.

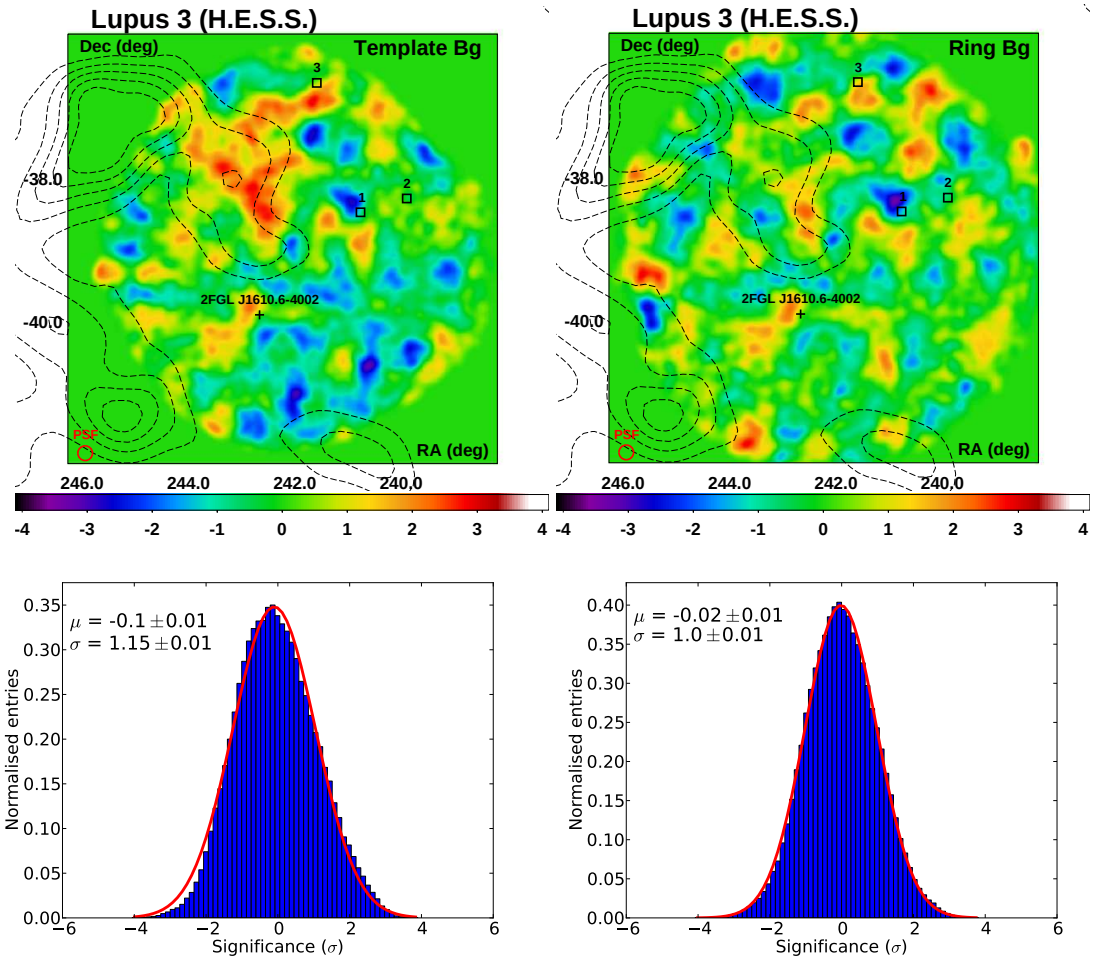

FIGURE 7.4 The 6° × 6° VHE γ-ray significance images of the Lupus 3 cloud. Depicted are the CO contours (Dame et al., 2001) from 6 to 18 K in steps of 3 K (dashed line), the GeV source 2FGL J1610.6–4002 (Nolan et al., 2012) and three bright stars (1 to 3, see text for more information) from Perryman et al. (1997). The red circle represents the 68 %-containment PSF of this analysis (~ 0.1°). The skymaps are calculated by integration of events within a radius of 0.22° and smoothed with a Gaussian σ of the size of the PSF. Below each skymap is the respective significance distribution with μ and σ of a standard normalised-Gaussian distribution. **LEFT:** VHE γ-ray significance skymap obtained with the TBg model. **RIGHT:** VHE γ-ray significance skymap obtained with the RingBg method.

7.3.2 LYNDS 1495A

Figure 7.5 shows the FoV around the Taurus subcloud Lynds 1495A. The CO(1-0) contours of the Taurus cloud are depicted as dashed lines from 10 to 25 K in steps of 5 K (Dame et al., 2001). There is one bright star, namely HIP 20250 (4.97^{mag}) reported in Perryman et al. (1997). No GeV source from Nolan et al. (2012) is reported in this FoV.

In both VHE γ-ray significance skymaps no evidence for γ-ray emission towards Lynds 1495A is found. However, at the northern and southern boundaries of the skymap, regions high positive significances are visible in the analysis with the TBg model. This leads to the distortion of the respective significance distribution. This is most likely an artifact of the analysis related to the camera-edge effect of the acceptance in combination with the TBg model and the high-zenith-angle observations (see also Sections 3.3.7 and 3.3.8.4).

The analysis with the RingBg method resulted in a clear FoV and a normalised significance distribution around 0. Thus, no convincing evidence for VHE γ-ray emission towards Lynds 1495A is found.

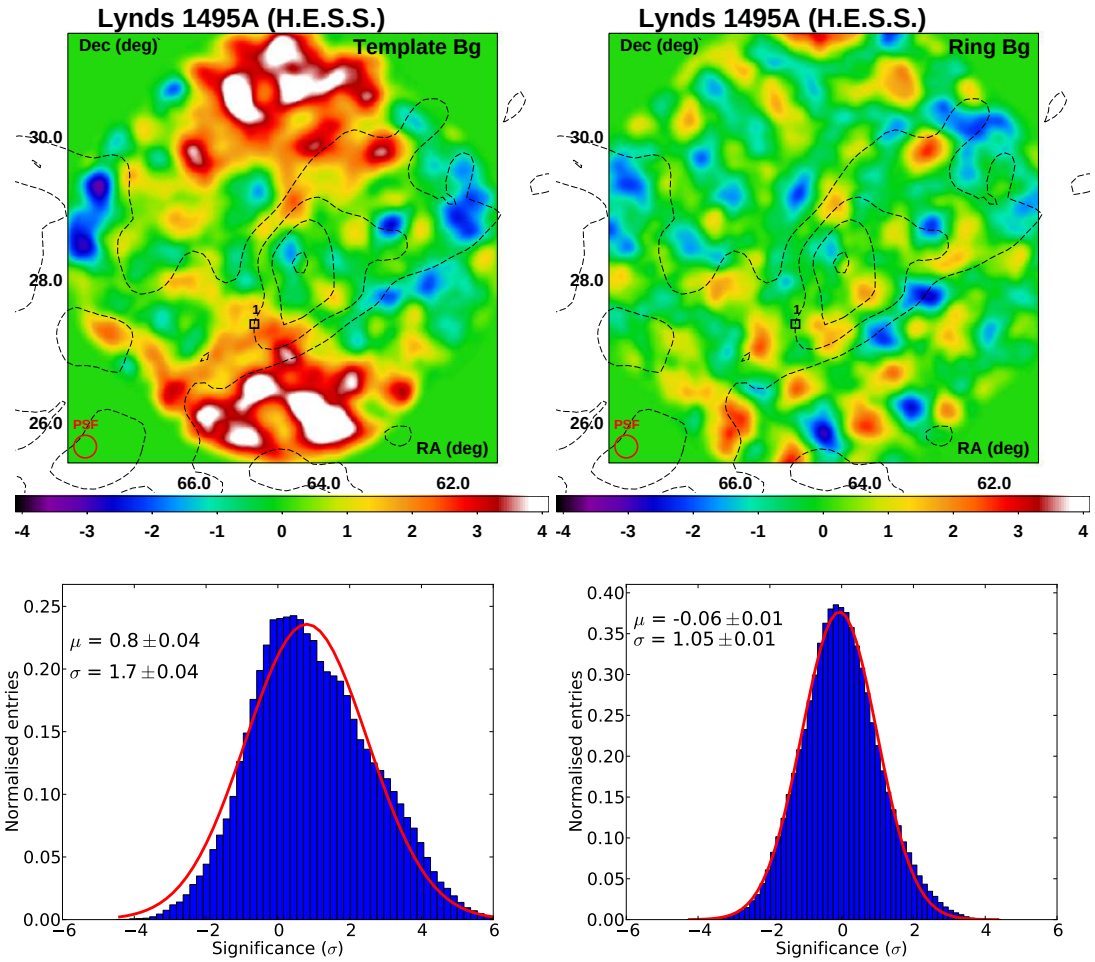

FIGURE 7.5 The 6° × 6° VHE γ-ray significance images of the Lynds 1495A subcloud. Depicted are the CO contours (Dame et al., 2001) from 10 to 25 K in steps of 5 K (dashed line) and one bright star (1), see text for more information) from Perryman et al. (1997). The red circle represents the 68 %-containment PSF of this analysis (0.16°). The skymaps are calculated by integration of events within a radius of 0.22° and smoothed with a Gaussian σ of the size of the PSF. Below each skymap is the respective significance distribution with μ and σ of a standard normalised-Gaussian distribution. **LEFT:** VHE γ-ray significance skymap obtained with the TBg model. **RIGHT:** VHE γ-ray significance skymap obtained with the RingBg method.

7.3.3 ORION A

In Figure 7.6, the H.E.S.S. significance skymaps around Orion A are shown. Overlaid are the CO(1-0) contours from Dame et al. (2001) as black dashed lines ranging from 30 to 70 K in steps of 20 K. The H.E.S.S. FoV includes seven bright stars listed in Perryman et al. (1997): HIP 26235 (1, 4.98^{mag}), HIP 26237 (2, 4.98^{mag}), HIP 26241 (3, 2.75^{mag}), HIP 26199 (1, 4.78^{mag}), HIP 26237 (5, 4.58^{mag}), HIP 26563 (6, 4.77^{mag}), and HIP 25923 (7, 4.62^{mag}). Four *Fermi*–LAT sources are found around the densest part of Orion A (Nolan et al., 2012). They are all marked as confused with three of them being unassociated, namely 2FGL J0534.8-0548c, 2FGL J0538.5-0534c, and 2FGL J0534.9-0450c. The source 2FGL J0530.8-0517c is an FSRQ and close to its position, extended emission is observed in both skymaps. The analysis of this region at the position 82.666°, −5.055° with a source radius of 0.2° resulted in 2.9 σ with the RingBg method and 56 excess events derived with $\alpha_{\mathrm{RingBg}} = 0.169$.

No significant signal is seen from Orion A, neither from the core nor from the remainder of the cloud structure. There are *holes* (sharp dips of $< -4\,\sigma$) in the skymaps around the centre of Orion A and there is a gradient in north-south direction visible in the TBg skymap. This could hint that the radial symmetry in the FoV is broken, thus affecting the background normalisation of the TBg model. Possible reasons could be the presence of a faint source or systematic effects due to the bright stars in the FoV. This gradient is not observed in the skymap produced with the RingBg method.

However, at the position of the bright stars (1 to 5) no enhancement in significance is observed although expected with the TBg method given their brightness. Conversely, they led to dips in significance at their positions in the skymaps produced with the RingBg method.

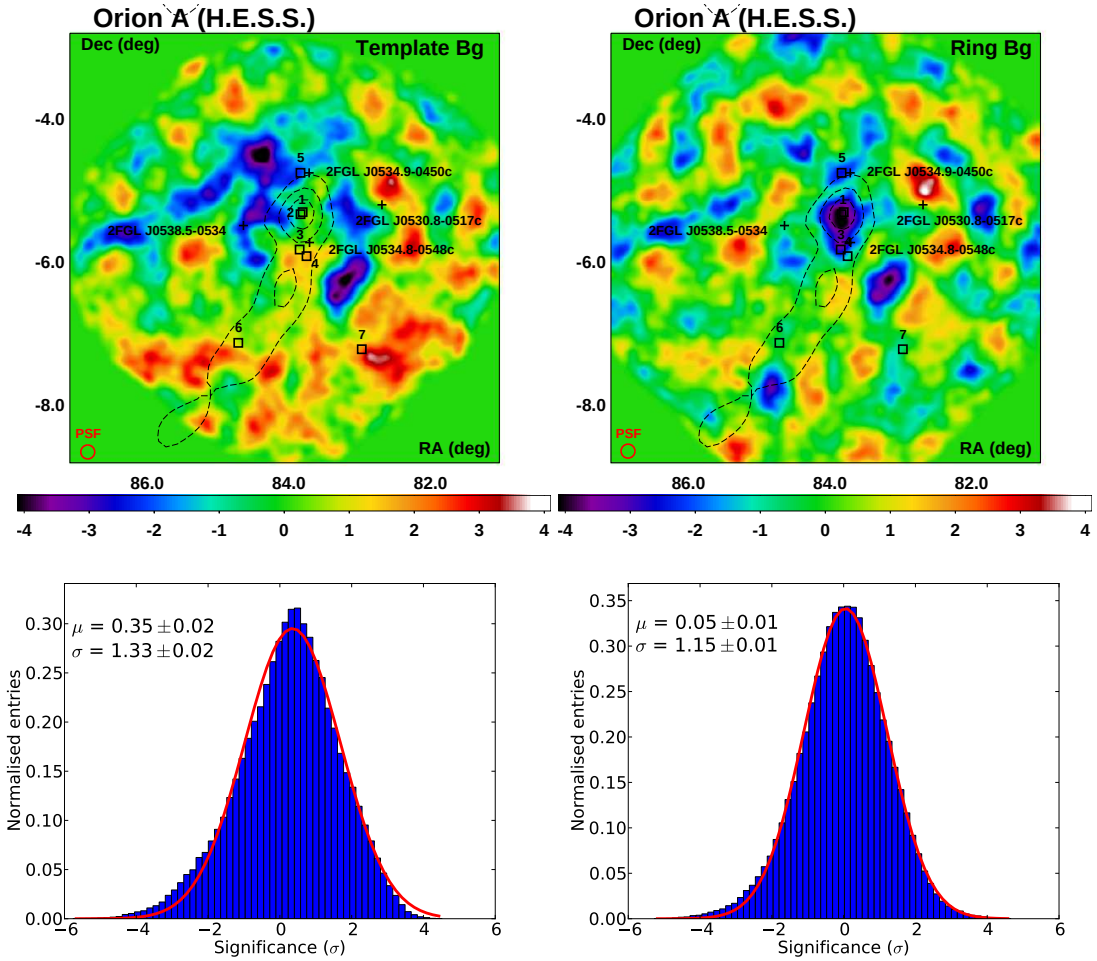

FIGURE 7.6 The 6° × 6° VHE γ-ray significance images of the Orion A cloud. Depicted are the CO contours (Dame et al., 2001) from 30 to 70 K in steps of 20 K (dashed line), GeV sources from Nolan et al. (2012), and bright stars (1 to 7, see text for more information) from Perryman et al. (1997). The red circle represents the 68 %-containment PSF of this analysis (~ 0.1°). The skymaps are calculated by integration of events within a radius of 0.22° and smoothed with a Gaussian σ of the size of the PSF. Below each skymap is the respective significance distribution with μ and σ of a standard normalised-Gaussian distribution. **LEFT:** VHE γ-ray significance skymap obtained with the TBg model. **RIGHT:** VHE γ-ray significance skymap obtained with the RingBg method.

7.3.4 PERSEUS CLOUD

The exposure around the dense part (i.e. the target position) of the Perseus cloud (black contours of 20, 30, 40 K from Dame et al. (2001)) is not homogeneous because all observations wobbled west and south were either aborted or failed the run selection criteria. In Figure 7.7, the TBg skymap exhibits a large emission region towards the north end of the FoV. This is very likely a systematic effect caused by the camera acceptance at these high zenith angles. Similar as for the Lynds 1495A FoV, there appears to be a gradient in north-south direction. The analysis with the RingBg method did not show any gradient in the FoV and the significance distribution is that of the null-hypothesis.

There is an excess at the position (53.350°, 32.155°) with a peak significance of $3.7\,\sigma$ in the TBg skymap. At this location, a radio source is found, NVSS J033311+321405 (Condon et al., 1998), which is undetected in HE or VHE γ-ray energies. The point-source analysis with a source radius $\theta = 0.11°$ using both the TBg model and the RingBg method did not result in an increase in significance: 9 excess events at $1\,\sigma$ ($\alpha_{\mathrm{TBg}} = 0.050$) and 3 excess events at $0.3\,\sigma$ ($\alpha_{\mathrm{RingBg}} = 0.056$). The hint for a second emission region towards the south-east edge of the FoV in both skymaps is not included in all FoVs of the runs. Because this data set is small with just 4.2 hrs of exposure, a re-analysis using only about half of the data will not provide any significant statement.

The *Fermi*–LAT sources reported in Nolan et al. (2012) 2FGL J0337.0+3200c (FSRQ), 2FGL J0333.7+2918 (an active galaxy), and 2FGL J0341.8+3148c (not identified) are not detected at TeV energies.

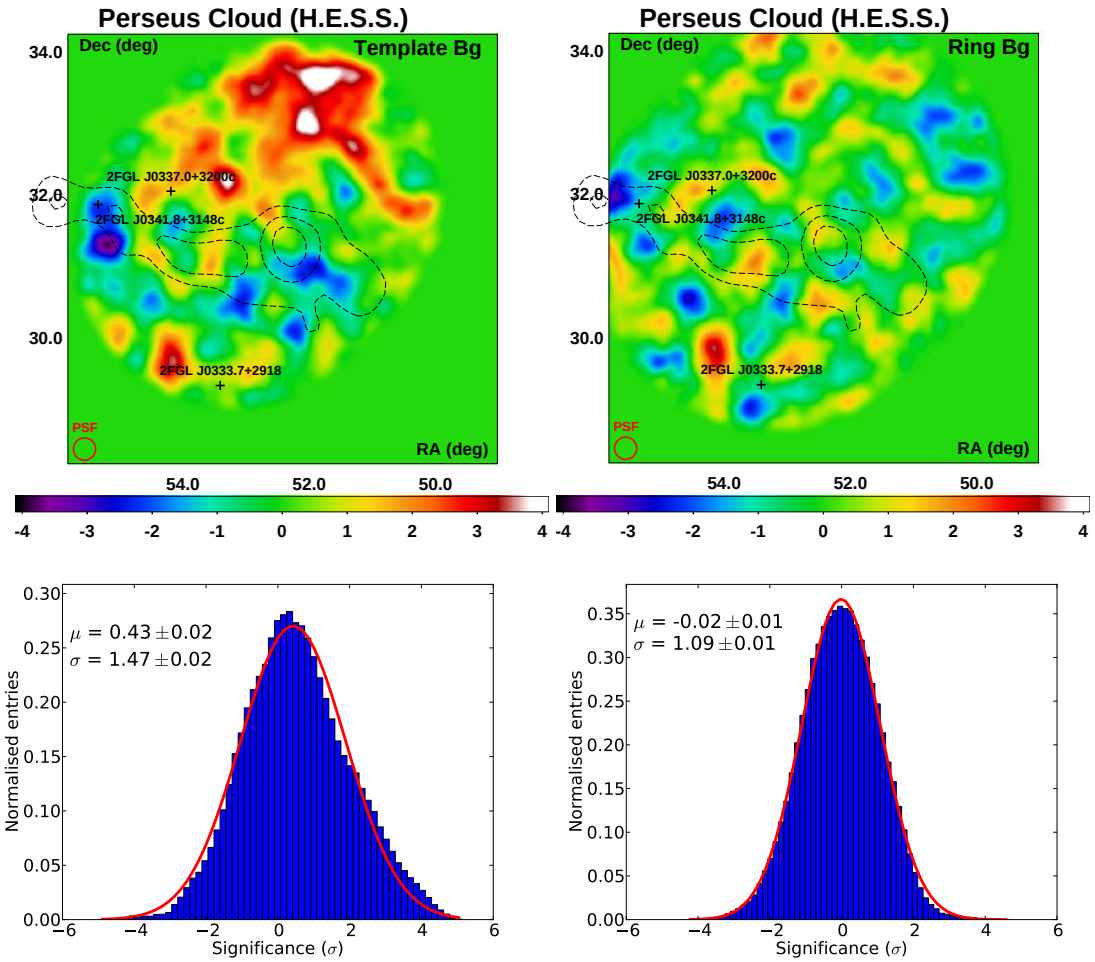

FIGURE 7.7 The 6° × 6° VHE γ-ray significance images of the Perseus-cloud core. Depicted are the CO contours (Dame et al., 2001) from 20 to 40 K in steps of 10 K (dashed line) and three *Fermi*–LAT sources from Nolan et al. (2012). The red circle represents the 68 %-containment PSF of this analysis (0.15°). The skymaps are calculated by integration of events within a radius of 0.22° and smoothed with a Gaussian σ of the size of the PSF. Below each skymap is the respective significance distribution with μ and σ of a standard normalised-Gaussian distribution. **LEFT:** VHE γ-ray significance skymap obtained with the TBg model. **RIGHT:** VHE γ-ray significance skymap obtained with the RingBg method.

7.3.5 ρ–OPHIUCHUS B

In the FoV of ρ–Oph B no hint for VHE γ-ray emission towards the cloud could be found (see Figure 7.8). Consistently, no hint for TeV emission in the skymaps produced with the RingBg method could be found.

There are bright stars in the FoV reported in Perryman et al. (1997), namely HIP 80473 (1, 4.57^{mag}), HIP 80079 (2, 4.55^{mag}), HIP 80815 (3, 4.79^{mag}), HIP 80112 (4, 2.90^{mag}), and HIP 80763 (5, 1.06^{mag}). Five *Fermi*–LAT sources are found in the FoV. Two of those GeV sources (2FGL J1620.5-2320c and 2FGL J1632.6-2328c) are unassociated in Nolan et al. (2012) and remain undetected at TeV energies. The two other sources are 2FGL J1617.6-2526c (active galaxy) and 2FGL J1625.7-2526 (FSRQ and EGRET source 3EG J1626-2519). The third source 2FGL J1627.0-2425c is located at the centre of densest part of the cloud and reported to be an active galaxy in Nolan et al. (2012). It is also an EGRET source (3EG J1627-2419, Hartman et al., 1999). However, this source may also be a residual of the cloud itself (as noted in *simbad.u-strasbg.fr/simbad*, see also Kovalev (2009)) and not an additional source.

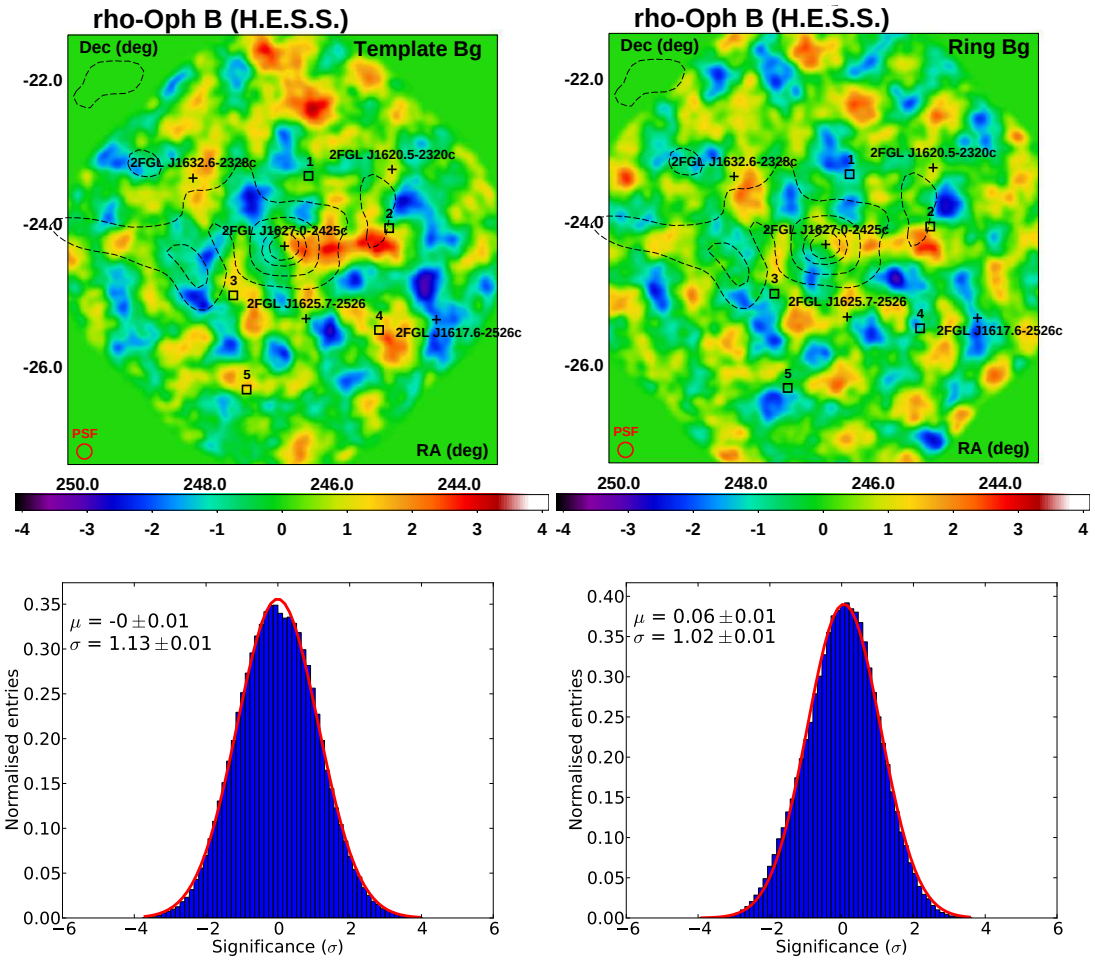

FIGURE 7.8 The 6° × 6° VHE γ-ray significance images of the ρ–Oph B cloud. Depicted are the CO contours (Dame et al., 2001) 10, 20, 30, 35 K (dashed line), bright stars (1 to 5, Perryman et al., 1997) and *Fermi*–LAT sources from Nolan et al. (2012). The red circle represents the 68 %-containment PSF of this analysis (0.1°). The skymaps are calculated by integration of events within a radius of 0.22° and smoothed with a Gaussian σ of the size of the PSF. Below each skymap is the respective significance distribution with μ and σ of a standard normalised-Gaussian distribution. **LEFT:** VHE γ-ray significance skymap obtained with the TBg model. **RIGHT:** VHE γ-ray significance skymap obtained with the RingBg method.

7.4 RESULTS OBTAINED WITH EXTRA-GALACTIC LOOK-UPS OF THE CAMERA ACCEPTANCE

The presented results did not provide an evidence or at least a convincing hint for VHE γ-ray emission towards any of the targeted GB clouds. It may have occurred that the analyses may have cancelled out a possible faint diffuse and possibly largely extended emission. For the TBg model, the calculated acceptances may not be source-free and therefore the background normalisation could be incorrect. In the analysis with the RingBg method, these regions will lead to an overestimate of the background. Therefore, both background-estimation methods may have diluted any hypothetical faint emission beyond significant detection. In addition, the many bright stars in the FoV may have affected the background estimate. This seems likely as especially the TBg model appears to suffer from problems related to camera acceptance. For example, the gradients across the FoV are normally not seen in the application of this background method unless VHE γ-ray emission regions are not excluded in the calculation of the acceptance. Therefore, in a second analysis of all five GB source regions, the extra-Galactic look-ups of the camera acceptance were used that are normally used for analyses of Galactic sources (Sect. 3.3.8.6)

It has to be pointed out that these look-ups are apparently not applicable to the analysis of data away from the Galactic Plane. A test analysis on the Centaurus A data set with the TBg model resulted in a very extended emission and a north-south gradient across the FoV (Sect. C.2). Therefore, the advantage of the unaffected and unbiased camera acceptance is severely questioned. These analyses are found in Appendix C.3. In the following, a brief summary is given. In principle, the possible emission regions can be analysed with the RrBg method; however, this is only possible if observations did not point at the test region. The advantage would be the acceptance-independent background estimate. However, none of the test regions discussed above and in the following could be positively confirmed.

RESULTS WITH THE RING BACKGROUND METHOD

The re-analyses of the GB regions with the RingBg method and the acceptance look-ups were consistent with the results presented above. No promising hint for VHE γ-ray emission was found.

RESULTS WITH THE TEMPLATE BACKGROUND MODEL

LYNDS 1495A AND THE PERSEUS CLOUD No convincing hint for VHE γ-ray emission is seen in the FoV of Lynds 1495A using the TBg model. As described in Section 7.3.2, an enhancement in significance is observed towards the northern and southern edges of the FoV. A similar result is obtained for the Perseus region. In Figure C.12, a second compact region with a significance peak of almost $4\,\sigma$ is found, which cannot be verified by any other background-estimation method or analysis.

LUPUS 3 AND ρ–OPH B Extended VHE γ-ray emission is seen in the FoVs of Lupus 3 and ρ–Oph B towards the respective clouds (Figs. C.7 and C.13). The emission towards the centre of ρ–Oph B seems to correlate with a *Fermi*–LAT source (see also Figure C.5). As before, these emission regions cannot be reproduced with the RingBg method.

ORION A Strong extended TeV emission is found towards the brightest stars of Orion A (Fig C.9). This emission is seen at the location of the brightest star of Orion A (stars 3 and 4) and therefore could be related to the effect of the stars in combination with the TBg model. This is supported since the RingBg method produced significant dips at the respective star positions (Fig. C.10).

Because the effect of the stars correlates with their brightness and with the image size allowed in the analysis, a harder cut on the image size was used to check the emission in question (image size > 160 p.e.; ζ_{hard} analysis; see also Section 3.3.5). The strong emission around the stars 3 and 4 disappeared, but a $3\,\sigma$-emission region is seen towards the densest part of Orion A where two stars are located (1 and 2), see Figure C.11. However these stars are not as bright as the stars 3 and 4 and because this emission appears to be spatially correlated with the GeV skymap above 10 GeV (Fig. C.3), the observed hint may not be due to the stars.

7.5 SPECTRAL ANALYSIS

The spectral analysis to derive flux upper limits on the GB cloud regions was done using the TBS method, for which the Hillas standard cuts and the gamma/hadron separation on the MRSW were used (Chapter 4). Thus, the spectral information can be obtained for the assumed large source sizes (especially for Lynds 1495A where the reflected-region background method fails) but as a drawback, the sensitivity is reduced compared to the TMVA-based analysis chain. The regions defined in Table 7.2 were taken as the test positions. The data selected for the spectral reconstruction with TBS consisted only of four-telescope data, thus reducing the available livetime on some sources, but improving the quality of the data set.

In Table 7.5, the results of the analysis with TBS are summarised for the individual clouds. Consistently with the non-detections reported in Section 7.3, four of the five GB clouds have not been detected significantly with TBS. Only in the case of Orion A, a $6.7\,\sigma$ excess is observed and thus a spectrum could be reconstructed. A similar effect as for the TBg skymaps due the bright stars might have led to the strong γ-ray signal since the underlying background determination is based on the standard TBg model.

7.5.1 ORION A

The emission reconstructed with TBS is best-described by a power law with a normalisation at 1 TeV of $\Phi_0 = (1.32 \pm 0.53) \times 10^{-8}\,\mathrm{TeV}^{-1}\,\mathrm{m}^{-2}\,\mathrm{s}^{-1}$ and an index of $\Gamma = 3.63 \pm 0.39$ between 0.25 TeV and 20.0 TeV, which results in an integral flux above 0.25 TeV of $(10.8 \pm 1.6)\,\%$ of that of the Crab Nebula above the same threshold (see Table 7.6 and

TABLE 7.5 Analysis results of the GB regions with TBS. Stated are the energy ranges, for which the TBS-background normalisation α_{TBS} could be calculated. The gamma-like events N_{g} and the hadron-like events N_{h} used to calculate the excess N_{excess} are given as well as the respective statistical significance S (Eq. 3.22) and the livetime t.

Cloud	E_{min} TeV	E_{max} TeV	N_{g}	N_{h}	α_{TBS}	N_{excess}	S σ	t hrs
Lupus 3	0.25	7.94	590	6145	0.101	−33	−1.3	2.2
Lynds 1495A	1.0	63.1	8147	80144	0.107	−419	−4.3	5.0
Orion A	0.25	20.0	3816	45279	0.075	405	6.6	8.1
Perseus cloud	1.26	20.0	404	2300	0.164	28	1.3	1.4
ρ–Oph B	0.25	20.0	5508	58101	0.094	19	0.3	11.5

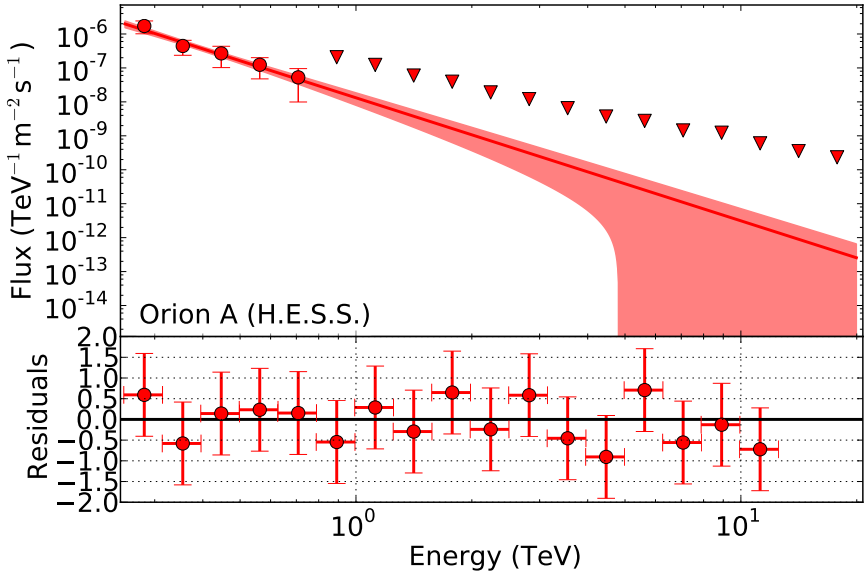

FIGURE 7.9 Forward-folded spectrum of Orion A using the TBS method. Shown are the flux points directly obtained by scaling residuals from the forward folding (bottom panel) to the estimated flux. The flux points depicted have a statistical significance of at least $2\,\sigma$. The upper limits on the differential flux are obtained through the likelihood method in von Seggern (2014) and are at the 95 % confidence level. Data points without a residual indicate bins of non-Gaussian statistics.

Figure 7.9). The TBS-introduced systematic errors are 0.8 % on the integral flux and 0.31 on the power-law index.

As in the case of the skymaps produced with the TBg model, it cannot be ruled out that the VHE γ-ray excess spectrally reconstructed with TBS is due to the bright stars. The nominal H.E.S.S. sensitivity for Orion A-like observations is $\sim$ 10.3 %, thus the observed flux is at the required level and therefore sufficiently high. However, since bright stars not only reduce the acceptance, but also the event rate (especially of the hadrons) at

TABLE 7.6 Spectral parameters for Orion A derived with TBS. The best-fit parameters of the power law are determined with TBS for n_{dof} degrees of freedom. The integral flux is calculated above an energy threshold of 0.25 TeV.

Cloud	$\Phi_0(1\,\mathrm{TeV})$ $10^{-8}\,\mathrm{TeV}^{-1}\mathrm{m}^{-2}\mathrm{s}^{-1}$	Γ	n_{dof}	$F_{E>0.25\,\mathrm{TeV}}$ $10^{-7}\,\mathrm{m}^{-2}\mathrm{s}^{-1}$
Orion A	1.32±0.53	3.63±0.39	17	1.89±0.28

TABLE 7.7 Analysed data sets of ζ–Tauri and a region close to the Orion A cloud with the TBg model implemented in TBS.

Cloud	E_{min} TeV	E_{max} TeV	N_{g}	N_{h}	α_{TBS}	N_{excess}	S σ	t hrs
ζ–Tauri	0.50	39.8	229	2503	0.074	44	3.0	9.7
84.845°,−5.416°	0.25	6.31	177	2119	0.078	12	0.9	7.9

the star's position, the background of the Orion A region may be underestimated (Sect. 3.3.8.5. This could explain the observed excess with TBS, too.

Two analyses were conducted to test the susceptibility of the TBS method to bright stars in a possible source region. On the one hand, the star ζ–Tauri (a bright star in the FoV of the Crab Nebula with 2.97^{mag} in the Johnson V band) was analysed. On the other hand, an apparently empty region in the Orion A FoV was analysed to test for any systematic effects or issues related to the calculation of the background normalisation. This region was chosen $\sim 1^\circ$ east of the H.E.S.S. target position at the coordinates (84.845°,−5.416°; J2000).

Both sources were analysed assuming a point-like source radius of 0.11°. The analysis results are tabulated in Table 7.7 and 7.8. As expected, a positive excess is reconstructed at the position of ζ–Tauri at a $3\,\sigma$ level. However, the spectrum reconstructed with TBS is rather hard ($\Gamma = 2.22 \pm 0.32$) and does not resemble the spectrum derived for the Orion A region. The selected empty region in the Orion A FoV from which no γ-ray emission is observed, shows a $1\,\sigma$ excess and an even harder spectral index ($\Gamma = 1.27 \pm 0.80$).

Although this may not be considered a systematic test of the TBS method, a source-free region or a region containing a star did not lead and perhaps does not necessarily have to lead to a soft spectrum observed for the Orion A cloud.

TABLE 7.8 Results of the spectral reconstruction with TBS of the two test regions ζ–Tauri and in the Orion A FoV.

Test position	$\Phi_0(1\,\mathrm{TeV})$ $10^{-9}\,\mathrm{TeV}^{-1}\mathrm{m}^{-2}\mathrm{s}^{-1}$	Γ	n_{dof}
ζ–Tauri	6.34±2.28	2.22±0.32	15
84.845°,−5.416°	1.50±1.61	1.27±0.80	10

7.6 Cosmic-ray enhancement factor

Although no firm detection of VHE γ-ray emission has been established, the TeV data can be used to constrain the expected flux and CR density towards the cloud structures. Aharonian (1991) proposed that the VHE γ-ray flux could be determined on the basis of the cloud properties and the CR enhancement factor k:

$$F(>E) \approx 2.9 \times 10^{-9} \left(\frac{E}{1\,\mathrm{TeV}}\right)^{-1.6} \left(\frac{M}{10^5\,M_\odot}\right) \left(\frac{d}{1\,\mathrm{kpc}}\right)^{-2} k(>E)\,\mathrm{m}^{-2}\,\mathrm{s}^{-1}\,, \tag{7.1}$$

where E is the lower energy boundary from which on the flux is integrated and k the CR enhancement factor above the same energy threshold and in units of the local CR density (about 1 particle per cm^{-3}). Hence, given a flux measurement or an upper limit, the CR enhancement factor or an upper limit on it can be determined through inversion of Equation 7.1. Here, a value $k \approx 1$ means the absence of a CR accelerator within the cloud.

The upper limit on the excess counts N_{UL} for Lupus 3, Lynds 1495A, the Perseus-cloud core, and ρ–Oph B are calculated at a 95 % confidence interval using the likelihood method described in von Seggern (2014). The spectra of these four sources are spectrally reconstructed to estimate the integral flux F above an energy threshold E and the predicted counts N_{pred} for a fixed power-law index of $\Gamma = 2.6$ of the differential energy spectrum (matching the integral-flux shape of $\Gamma = 1.6$ in Equation 7.1). Given these three quantities, the 95 % upper limit on the flux can be estimated:

$$F_{\mathrm{UL}}(>E) = F(>E)\,\frac{N_{\mathrm{UL}}(>E)}{N_{\mathrm{pred}}(>E)}\,. \tag{7.2}$$

In Table 7.9, the respective values of the four aforementioned clouds are summarised together with the upper limit on k. The results of the actual spectral reconstruction are found in Appendix C.4.

For Orion A, the CR-enhancement factor is directly calculated to be $k \approx 9$ using the cloud properties and the determined values listed in Table 7.2 and 7.6. However, in Aharonian (1991) an integral CR spectrum of $\Gamma = 1.6$ is assumed (Eq. 7.1), which differs significantly from that derived for the γ-ray spectrum with TBS (integral spectrum of $\Gamma = 2.63$). In this case, Equation 7.1 would have to be corrected for the much softer spectrum (e.g. done in Maxted et al., 2013). Because the difference in the indices is considerably large ($\Delta\Gamma \approx 1$) and the presence of the γ-ray source has still to be verified and understood, the estimated CR enhancement has to be taken with caution.

TABLE 7.9 The CR-enhancement factor for the GB sources lacking a significant excess (see Table 7.5). Stated are the expected excess from the forward folding N_{pred} assuming $\Gamma = 2.6$, the resulting integral flux $F(> E_{\mathrm{min}})$ above the threshold E_{min}, the 95 % counts upper limit N_{UL} derived with the method proposed in von Seggern (2014), the integral flux upper limit (95 %) F_{UL} (Eq. 7.2), and the inferred upper limit on the CR-enhancement factor k_{UL} (Eq. 7.1).

Cloud	N_{pred}	$F(> E_{\mathrm{min}})$ $\mathrm{m^{-2}\,s^{-1}}$	N_{UL}	F_{UL} $\mathrm{m^{-2}\,s^{-1}}$	k_{UL}
Lupus 3	0.005	5.7×10^{-12}	25	2.9×10^{-8}	8
Lynds 1495A	0.004	6.3×10^{-13}	29	4.6×10^{-9}	32
Perseus Core	19	1.0×10^{-8}	71	3.7×10^{-8}	58
ρ–Oph B	0.02	5.7×10^{-12}	172	4.3×10^{-8}	3

7.7 SUMMARY AND OUTLOOK

In this chapter, H.E.S.S. data on five regions of the GB were analysed. In a combination of two background-estimation methods (TBg and RingBg), no hint for VHE γ-ray emission was found towards either of the clouds. However, the FoVs include bright stars and possibly faint emission that can affect the camera acceptance and therefore the background estimate. To circumvent this, look-ups of the acceptances made out of extra-Galactic data were used and to check the FoVs for possible emission (see Appendix C.3).

In the case of Lupus 3 and ρ–Oph B extended emission is found located towards the respective clouds. Especially for the emission around ρ–Oph B, a spatial correlation with a *Fermi*–LAT and an EGRET source is found. Also Orion A appears to shine bright in TeV γ rays and moreover, a spectrum could be reconstructed with the TBS method. A harder cut on the image size leaves a $3\,\sigma$ hint for emission in Orion A that correlates with the smoothed *Fermi*–LAT skymap above 10 GeV. However, the emission is located towards the bright Orion A stars and therefore is a challenge to current background-estimation methods, thus none of these sources can be confirmed. Additionally, the extra-Galactic look-ups used suffer from yet not-understood systematics (of the background estimates or the acceptance for hadrons). This is discussed in Appendix C.2.

The detection and confirmation of VHE γ-ray emission towards the GB clouds could hint at a nearby VHE particle accelerator illuminating the clouds in a hadronic scenario. Known VHE γ-ray sources are not found within the TeV-emission regions in question. VHE γ-ray emission from Orion A could be an indication that SFRs, young high-mass stars, or stellar binaries (without a compact object) could constitute a new VHE γ-ray source class.

The spectral results (upper limits on the flux and the flux determined for Orion A) on the five sources obtained with TBS and were used to determine constraints on the CR enhancement towards the clouds (Tables 7.9 and 7.10).

A possible VHE γ-ray source like Orion A with its bright stars may also constitute a limitation of current background-estimation methods and the IACTs. Therefore, non-

TABLE 7.10 Summary of the spectral results on the GB clouds observed with H.E.S.S. and analysed with TBS.

Cloud	E_{min} TeV	$F(> E_{\mathrm{min}})$ $10^{-8}\,\mathrm{m}^{-2}\,\mathrm{s}^{-1}$	k
Lupus 3	0.25	< 2.9	< 8
Lynds 1495A	1.00	< 4.6	< 32
Orion A	0.25	18.8 ± 4.0	9
Perseus Core	1.26	< 3.7	< 58
ρ–Oph B	0.25	< 4.3	< 3

IACTs could provide further insight if a sufficiently low energy threshold is provided because of the soft spectrum motivated by *Fermi*–LAT results in general for the GB and specifically by the results on Orion A with the TBS method. Another approach may be observations with IACTs not equipped with PMTs: FACT (The First G-APD Cherenkov Telescope Anderhub et al., 2009) is equipped with Geiger-mode avalanche photodiodes (instead of PMTs used for state-of-the-art IACTs) and therefore allowing observations even under moon light (Knoetig et al., 2013).

Chapter 8

Concluding Remarks

This thesis consisted of four parts that were combined in an effort to shed light on the long-standing question if GCRs are accelerated in SCs up to TeV energies and beyond. The results on HESS J1646–458 and its large source region, which could not be analysed with the RrBg method, motivated the search for an alternative method and resulted in the development of TBS. The spectral results on HESS J1614–518 and the GB were then produced with TBS.

The detailed summaries and the specific outlooks are given in the respective chapters of TBS (Chapter 4), Westerlund 1 (Chapter 5), HESS J1614–518 (Chapter 6), and the GB (Chapter 7). In the following, the main results are summarised and the implications w.r.t. the question of SCs being possible GCR accelerators are discussed.

Template Background Spectrum (TBS)

Current IACTs like H.E.S.S., MAGIC, or VERITAS are in operation for about a decade and so, a deep exposure is obtained for a significant fraction of the sky, especially the Galactic Plane. This deep exposure in combination with constant advances in the data analysis to improve the sensitivity have led to the discovery of very extended VHE γ-ray sources up to $\sim 2^\circ$ in diameter and regions with large-scale diffuse γ-ray emission. These sources fill a large fraction of the FoV and thereby state-of-the-art methods to estimate the background for a spectral reconstruction are not more applicable. In these cases, additional data are required and mostly also a source-specific adjustment of the analysis method, which cannot be used in the analysis of a similar source.

In this thesis, a new method was developed to determine the background in a spectral analysis of large sources and for sources in complex FoVs, where many sources or diffuse emission or both are present, but without the need of additional data. This method is based on the TBg model, which is very often used to determine the background in skymaps in VHE γ-ray astronomy, but not considered to be a viable background-estimation method for spectra. The basic idea is the generation of an energy, zenith angle, and angular-offset-dependent look-up of the TBg normalisation from the very same data set and that this background normalisation accounts for relative differences between γ rays and the background.

The new method has been tested on H.E.S.S. data on sources in different FoVs (a clear

region with only the source present and a crowded one like the Galactic-Centre region) and with different properties, e.g. size (0.2° to 2° in diameter) and flux (0.7 % to ~ 100 % of that of the Crab Nebula). A good agreement with the results reported by the H.E.S.S. collaboration is found. After the *On*/*Off*-background method and the RrBg method, TBS is the third general method to estimate the background in a spectral reconstruction, but the first one that does not need *Off* data.

The systematic uncertainties appear to be treated appropriately because two forward-folding methods implemented in the TBS framework (χ^2 minimisation and $\mathcal{L}$ maximisation) give consistent results, although they are sensitive to different characteristics of the analysis. Only for the largest sources systematic errors dominate since they naturally provide sufficient data from the source region, but fewer data to calculate the background normalisation. This results in a higher fraction of extrapolated data in TBS, which constitutes the largest contribution to the overall systematic error. However, the uncertainties on the spectral results determined in the likelihood approach are comparable to those of the RrBg method and the *On*/*Off*-background method. Having said that, larger errors are then only introduced into the calculated excess counts and flux points.

Further improvements on the interpolation and extrapolation methods, a more sophisticated gamma/hadron separation, and a perhaps less conservative error estimation will likely enhance the performance of TBS. In addition, a set of template-correction look-ups made out of extra-Galactic data might noticeably reduce the above mentioned uncertainties, but possible systematic effects noticed in the analysis of the GB with such look-ups for the TBg model may affect the TBS method, too. Thus, these effects require further studies on the background. Besides these future improvements, the Monte Carlo data set has to be expanded to use different analysis configurations and to analyse high zenith-angle observations. Moreover, the inclusion of TBS into an existing analysis framework such as the H.E.S.S. analysis package, or into that of other current and future IACTs is aimed for.

For the future CTA telescope array with its superior sensitivity, it is likely that not only new VHE γ-ray sources will be detected, but also that the extents of current VHE γ-ray sources will increase and also that perhaps a considerable larger amount of diffuse emission might be present in the Galactic Plane. In these cases, much larger exclusion regions will have to be used, which will hamper the use of the RrBg method and motivate the use of the TBS method.

WESTERLUND 1, PISMIS 22, AND THE GOULD BELT

Stellar clusters, especially the massive ones, harbour a lot of high-mass stars that drive strong and dense winds, providing a large mechanical energy reservoir. In a scenario, in which these winds add up to a collective SC wind, acceleration of CRs to very-high energies is suggestive. However, most firmly associated Galactic VHE γ-ray sources are related to some stage of stellar evolution and therefore, SCs naturally provide many possible and viable source scenarios that do not necessarily relate to the opening question and the motivated acceleration scenario. Observations of SCs and SFRs that are compar-

atively young and therefore ideally without a known classical TeV γ-ray source (e.g. a SNR or a pulsar), may provide an unbiased view on γ-ray emission from SCs and young associations of high-mass stars. Five regions of the Gould Belt, a large-scale elliptical structure traced by large molecular clouds and SFRs, were targeted with H.E.S.S.

WESTERLUND 1 AND HESS J1646–458 Wd 1 is the current record holder in terms of the cluster mass and high-mass stars in the Milky Way. Its observation with the H.E.S.S. telescope system were therefore very well motivated. The TeV γ-ray source HESS J1646–458 towards Wd 1 discovered with H.E.S.S. is with a diameter of $\sim 2^\circ$ the largest source in the TeV sky. It is suggestive that this TeV γ-ay emission has its origin in the SC because the centroid of the emission is located at the nominal cluster position. In addition, there is clear evidence that the SC Wd 1 has shaped the ambient medium by producing a large void visible in the HI radio data and supporting the collective cluster-wind scenario. Because of the size of HESS J1646–458 many other possible counterparts are found besides the cluster itself. However, only Wd 1 provides a sufficient kinetic energy budget and a scenario to explain the observed source size if this source were produced by a single astrophysical object. On the other hand, (dominant) contributions of other (perhaps yet undetected) sources in the FoV adding up to the observed TeV γ-ray emission cannot be ruled out.

Further H.E.S.S. $\sim$ 70 hrs of data (i.e. the double amount of the current live time) would help study the morphology and possible spectral variations across this source. In this case, TBS may be a promising analysis method to reconstruct the spectral shape(s), because the RrBg method cannot be used and the *On*/*Off*-background method would require additional $\sim$ 70 hrs of observations. Also, a combined spectral and morphological analysis ad study using more than 5 years of *Fermi*–LAT data will certainly provide new insights.

PISMIS 22 AND HESS J1614–518 Pismis 22 is an old and perhaps inconspicuous SC embedded in the extended TeV γ-ray emission region HESS J1614–518. This is one of the brightest unidentified TeV sources and perhaps the TeV source with the largest observed TeV-to-X-ray flux ratio. Unlike for HESS J1646–458, where a couple of objects and acceleration scenarios could be possible and where also the SC has left its imprint on the ambient medium, no viable counterparts are found for HESS J1614–518 and this source remains unidentified. A collective cluster-wind scenario may account for the required energetics, but the lack of detected high-mass stars in Pismis 22 does not support this scenario. A possible SNR scenario lacks support from observations in other wavelengths. The available X-ray data are insufficient as they do not cover the entire source. A possible relic PWN or a PWN of a yet undetected pulsar cannot be ruled out, but is challenged by the TeV morphology.

As in the case of HESS J1646–458, a comparable amount of additional exposure on this source with H.E.S.S. would be needed, too. Especially, because this source appears to be changing with energy. In addition, observations with XMM–*Newton* or *Chandra* that map the entire source region would be needed.

THE GOULD BELT The analysis of H.E.S.S. data on the Gould Belt, remains inconclusive. Based on the standard analysis methods, no evidence for VHE γ-ray emission is found in any of the FoVs; these non-detections are consistent with the results of the *Fermi*–LAT data from Yang et al. (2013). Approaches using extra-Galactic data in the background determination are very well motivated and resulted in the detection of extended VHE γ-ray emission towards three of the clouds (namely Lupus 3, Orion A, and ρ–Oph B), but appear to affected by some yet not-understood effects. These effects might be related to the presence of bright stars or systematics in the camera acceptance and in the background-estimations methods (TBg model and RingBg method). From an analysis point of view, the data sets used to generate the extra-Galactic camera-acceptance look-ups ought to be reviewed and checked for run-by-run variations, which could explain the observed systematics.

The possible Orion A source was spectrally reconstructed with TBS. The observed spectrum is very soft ($\Gamma = 3.7$), which is in accordance with the soft spectra motivated by the *Fermi*–LAT results for the GB. The flux is reasonably high to be detected with H.E.S.S. (perhaps ruling out a source *faked* by the analysis and actually too faint to be detected). However, similar as for the standard TBg model used for the skymaps, this method may also be affected by the bright stars in Orion A.

The exposure on most of the Gould Belt, targets is about 10 hrs. Therefore additional observations with H.E.S.S. (preferably with the five-telescope configuration) at a larger wobble offset would be required. The soft spectra should lead to a measurable signal with CT5. On the other hand, sources that contain bright stars may be the limit of current back-ground-estimation methods for IACTs. Observations with non-IACTs or IACTs not-equipped with PMTs may be considered as well.

STELLAR CLUSTERS AND STAR-FORMING REGIONS AS GALACTIC COSMIC-RAY ACCELERATORS ?

In summary, the H.E.S.S. observations towards Westerlund 1 and Pismis 22 have revealed extended VHE γ-ray emission centred around the respective SCs. In the case of Wd 1, the size of the TeV source offers a couple of acceleration mechanisms and scenarios. Also for Pismis 22 and HESS J1614–518 different scenarios were put forward, but most of them lack the support from other wavelengths. Thus, there is evidence that SCs may be particle accelerators onto the VHE regime, but this potentially new source class still awaits its firm detection and association.

Young high-mass stars and young SFRs may also provide acceleration of particles leading to TeV γ-ray emission; this is especially motivated by the results on Orion A. However, the systematic effects (and perhaps the underlying physics) involved in the background, in the detector response, or in the background estimation appear not to be sufficiently well understood and a notable amount of effort (and observations) might/may be needed before any significant conclusion can be drawn. A positive discovery of TeV γ rays and if this is not the result of a nearby accelerator illuminating the clouds, would provide evidence for γ-rays produced in young SFRs and young stellar associations.

Chapter 9

Publication List

Refereed journal articles

1. **Discovery of extended VHE γ-ray emission from the vicinity of the young massive stellar cluster Westerlund 1**
   Authors: A. Abramowski, ..., **M. V. Fernandes** et al.
   Journal: Astronomy & Astrophysics, Volume 537
   Publication Date: January 2012
   Contribution: See Chapter 5.

2. **Dark matter subhaloes as gamma-ray sources and candidates in the first Fermi-LAT catalogue**
   Authors: H.-S. Zechlin, **M. V. Fernandes**, D. Elsässer, and D. Horns
   Journal: Astronomy & Astrophysics, Volume 538
   Publication Date: February 2012
   Contribution: Analysis of the *Fermi*–LAT data and thereby development of the respective analysis scripts (analysis chain and to determine the positional uncertainty).

3. **A new method of reconstructing VHE γ-ray spectra: the Template Background Spectrum**
   Authors: **M. V. Fernandes**, D. Horns, K. Kosack, M. Raue, and G. Rowell
   Journal: Astronomy & Astrophysics
   Publication Date: 23.03.2014 (accepted)
   Contribution: The idea and the concept, the statistical considerations, the coding and programming of the entire analysis framework of TBS. The analysis of H.E.S.S. data with the TBS method and the cross-check analyses with the H.E.S.S. analysis package (see also Chapter 4). The draft is written by me and incorporates comments and suggestions from the co-authors and a few members of the H.E.S.S. collaboration.

4. About 45 H.E.S.S. collaboration papers where I have contributed in form of discussions at various collaboration and work-group meetings and also through comments at different stages of the manuscripts

CONFERENCE PROCEEDINGS

1. **H.E.S.S. Observations of Massive Stellar Clusters**
   Authors: S. Ohm, ..., **M. V. Fernandes** et al.
   Journal: High Energy Phenomena in Massive Stars ASP Conference Series, Volume 422
   Publication Date: May 2010

2. **H.E.S.S. observations of the massive stellar cluster Westerlund 1**
   Authors: S. Ohm, **M. V. Fernandes** et al.
   Journal: Proceedings of the 25th Texas Symposium on Relativistic Astrophysics. Published online
   Publication Date: 2010

3. **Spectral reconstruction of extended VHE γ-ray sources with the template background**
   Authors: **M. V. Fernandes**, D. Horns, and M. Raue
   Journal: HIGH ENERGY GAMMA-RAY ASTRONOMY: 5th International Meeting on High Energy Gamma-Ray Astronomy
   Publication Date: December 2012

The Appendix

Appendix A

Auxiliary Information to Chapter 4

In this section of the appendix, additional information is given for Chapter 4. The framework of TBS is described in Appendix A.2. Some of the histograms that were used to calculate α in Figure 4.2 and used in the discussion on Section 4.2.3 are shown below (Appendix A.1). In Appendix A.3, the bilinear interpolation of the IR data (shown for the effective area) is presented and is referred to in Section 4.5.1. In Appendix A.4, a discussion on alternative energy thresholds is given. The correlation of the best-fit spectral parameters of the forward-folding method using the likelihood approach (determined and discussed in Section 4.5.2) are shown in Appendix A.5.

A.1 Histograms

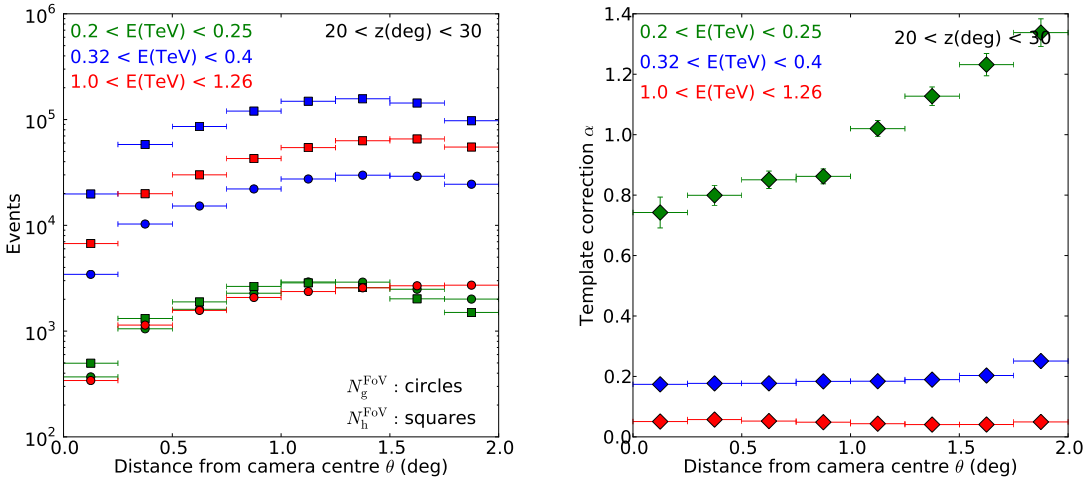

Figure A.1 Template correction calculated from H.E.S.S. data on Centaurus A (Aharonian et al., 2009c) at a fixed zenith-angle range of 20° to 30° for different energy intervals: 0.2 TeV to 0.25 TeV (green markers), 0.32 TeV to 0.4 TeV (blue markers), and 1.0 TeV to 1.3 TeV (red markers). **Left:** Histograms of the gamma-like (circle markers) and hadron-like events (square markers) used to calculate α. **Right:** The template correction α.

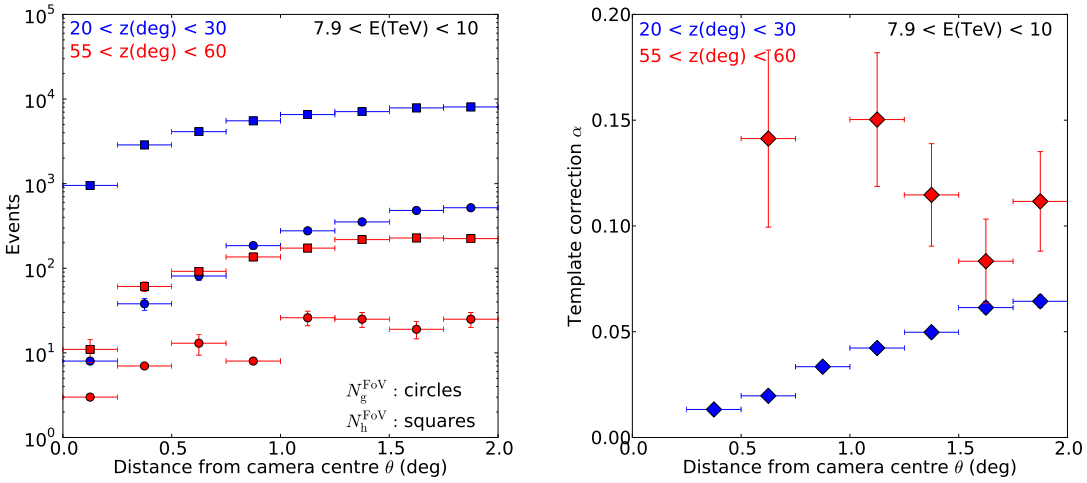

FIGURE A.2 Template correction calculated from H.E.S.S. data on Centaurus A (Aharonian et al., 2009c) at a fixed energy range of 7.9 TeV to 10 TeV for different zenith-angle intervals: 20° to 30° (blue markers) and 50° to 55° (red markers). **LEFT:** Histograms of the gamma-like (circle markers) and hadron-like events (square markers) used to calculate α. **RIGHT:** The template correction α.

A.2 TBS FRAMEWORK

In Figure A.3, the developed framework of TBS is depicted. The analysis chain consists of three parts: the calculation of the IR data for every run, the calculation of the template correction, and the determination of the excess events from the signal region. Prior to this analysis chain, the H.E.S.S. MC data were converted into the `FITS` format with HAP and then reprocessed to produce the effective areas, energy thresholds, and energy-resolution matrices for TBS. This was done with `MFMakeMCdata.py`.

The analysis chain is started with `MFTemplateAnalysis.py` and requires a configuration file (including path to files, analysis and plotting options), a runlist, and a list of exclusion regions. Then subsequently the following `python` scripts are called and executed:

1. `get_run_info.py`: this script reads in the provided files. It calculates and gathers basic information of every run (e.g. muon correction, livetime, stats, wobble offsets, zenith angle) and the interpolated IR (effective area, energy threshold, energy-resolution matrix) per run and writes the results into a `FITS` file

2. subchain to calculate the LuT:

   (a) `get_cam_data.py`: accounts for the exclusion regions; and the gamma-like and hadron-like events from the data in the FoV post energy-threshold cut are selected ($N^{\mathrm{FoV}}_{\mathrm{g,h}}$) and filled into bins of (E, z, θ)

   (b) `get_tempcorr.py`: calculates the template correction α and the reference corrections for every (E, z, θ) bin

   (c) `do_tc_FITS.py`: calculates the statistical errors $\sigma\,(\alpha(E, z, \theta))$ and writes the results into `FITS` files.

3. calculation of the excess events from the signal region

   (a) `get_obs_data.py`: accounts for the exclusion regions; and the gamma-like and hadron-like events from the signal region post energy-threshold cut are selected ($N^{\mathrm{S}}_{\mathrm{g,h}}$) and filled into bins of (E, z, θ)

   (b) `cor_obs_data.py`: applies the template correction the hadron-like data in every energy and zenith-angle bin: $\beta_{\mathrm{eff}}(\Delta E, \Delta z, \theta)$ bin through interpolation or extrapolation

   (c) `cat_obs_data.py`: concatenates the data from separate $(\Delta E, \Delta z)$ bins into bins of ΔE

   (d) `do_on_FITS.py`: calculates the effective correction $\beta_{\mathrm{eff}}\,(\Delta E)$ and the respective error $\sigma\,(\beta_{\mathrm{eff}}\,(\Delta E))$ and writes the results into a `FITS` file

   (e) `calc_summary.py`: calculates the excess, the statistical significance and some other quantities per energy bin and writes the results into a `FITS` file

(f) `reco_hadrons.py` (optional): if hadrons within an energy bin were left without a correction, they are corrected if a respective $\beta_{\text{eff}}(\Delta E)$ is available; the previous output file is then modified.

At the end of this analysis chain, all information and quantities are available to determine the spectrum through a forward folding. This is done by the script `MFMakeTBS.py`, which calls the scripts `do_logl_pl.py` and `do_logl_ple.py` for the use of the likelihood analysis for the spectral shapes power law and power law with an exponential cutoff, respectively. It is also possible to use the χ^2 minimisation routine with `do_chi2_pl.py` and `do_chi2_ple.py`. For the forward folding, the previous output results are read in and after choosing initial starting values of the spectral shape, `pyminuit` and `Minuit` are used to determine the best-fit spectrum.

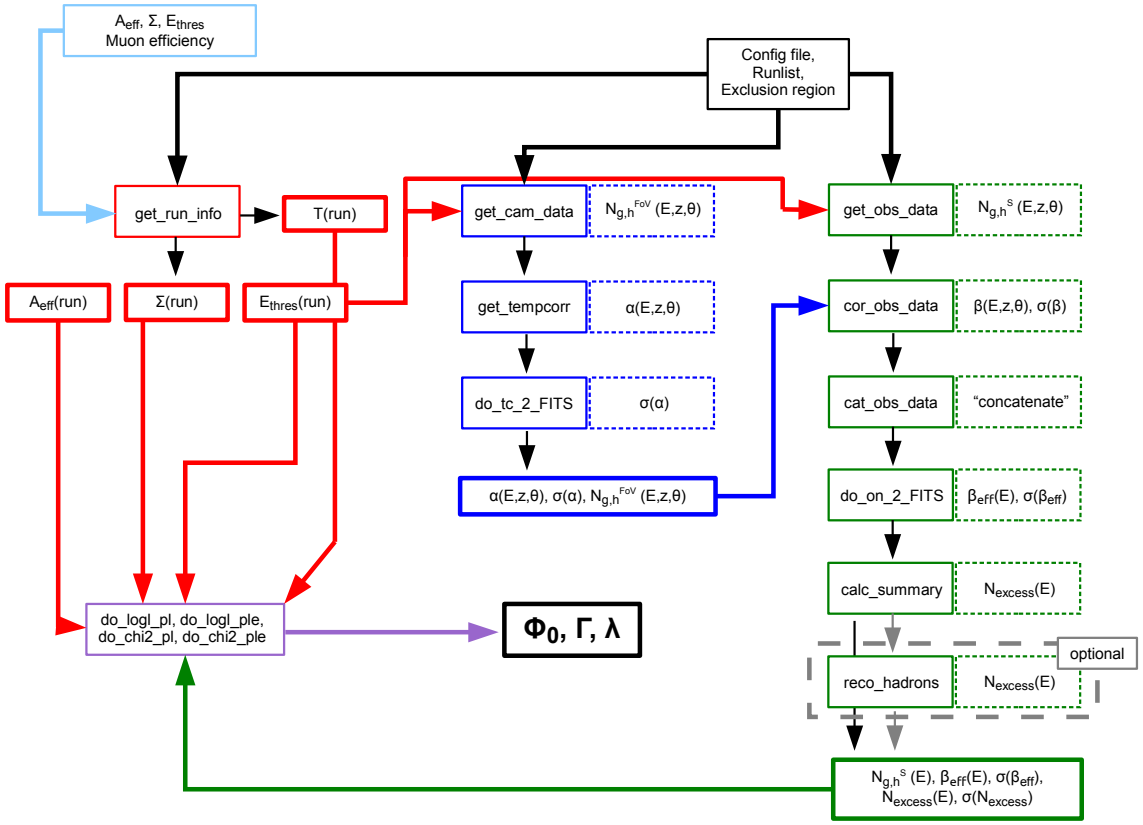

FIGURE A.3 Framework of TBS. Depicted are the different steps in the analysis chain of TBS (`MFTemplateAnalysis.py`), especially the three main parts: the determination of the MC data for very observation (red boxes and arrows), the calculation of the look-up table of the template correction (blue boxes and arrows), and the correction of the data from the source region (greed boxes and arrows). See text for further information.

A.3 Bilinear interpolation

For the forward folding, the pre-calculated IR data (effective area, energy resolution, and energy threshold) have to be processed to match the observational properties of the respective run. This is done in a bilinear-interpolation task and presented in the following on the example of the effective area.

For every observation run with its mean reconstructed zenith angle z_{obs} and its wobble offset ω_{obs}, the respective run effective $A_{\mathrm{eff}}(E, z_{\mathrm{obs}}, \omega_{\mathrm{obs}})$ has to be determined. In general, the z_{obs} and ω_{obs} will not be matching the simulated configuration of the zenith angle and wobble offset z_{sim} and ω_{sim} but z_{obs} and ω_{obs} will fall between the simulated quantities (otherwise these runs are not used). Given this, the requested $A_{\mathrm{eff}}(E', z_{\mathrm{obs}}, \omega_{\mathrm{obs}})$ matching the observation run is estimated through a bilinear interpolation of four sets of muon-corrected effective areas:

- $A_{\mathrm{eff},1}(E', z_{\mathrm{sim},1}, \omega_{\mathrm{sim},1})$,
- $A_{\mathrm{eff},2}(E', z_{\mathrm{sim},1}, \omega_{\mathrm{sim},2})$,
- $A_{\mathrm{eff},3}(E', z_{\mathrm{sim},2}, \omega_{\mathrm{sim},1})$, and
- $A_{\mathrm{eff},4}(E', z_{\mathrm{sim},2}, \omega_{\mathrm{sim},2})$,

for which $\omega_{\mathrm{sim},1} < \omega_{\mathrm{obs}} < \omega_{\mathrm{sim},2}$ and $z_{\mathrm{sim},1} < z_{\mathrm{obs}} < z_{\mathrm{sim},2}$ hold. The result of the bilinear interpolation is then

$$A_{\mathrm{eff}}(z_{\mathrm{obs}}, \omega_{\mathrm{obs}}) = \frac{\omega_{\mathrm{sim},2} - \omega_{\mathrm{obs}}}{\omega_{\mathrm{sim},2} - \omega_{\mathrm{sim},1}} \tilde{A}_1 + \frac{\omega_{\mathrm{sim},1} - \omega_{\mathrm{obs}}}{\omega_{\mathrm{sim},2} - \omega_{\mathrm{sim},1}} \tilde{A}_2 \,, \tag{A.1}$$

where $\tilde{A}_1$ and $\tilde{A}_2$ are linear interpolations in the zenith-angle plane:

$$\tilde{A}_1(z_{\mathrm{obs}}, \omega_{\mathrm{sim}}) = \frac{z_{\mathrm{sim},2} - z_{\mathrm{obs}}}{z_{\mathrm{sim},2} - z_{\mathrm{sim},1}} A_{\mathrm{eff},1} + \frac{z_{\mathrm{sim},1} - z_{\mathrm{obs}}}{z_{\mathrm{sim},2} - z_{\mathrm{sim},1}} A_{\mathrm{eff},3} \tag{A.2}$$

$$\tilde{A}_2(z_{\mathrm{obs}}, \omega_{\mathrm{sim}}) = \frac{z_{\mathrm{sim},2} - z_{\mathrm{obs}}}{z_{\mathrm{sim},2} - z_{\mathrm{sim},1}} A_{\mathrm{eff},2} + \frac{z_{\mathrm{sim},1} - z_{\mathrm{obs}}}{z_{\mathrm{sim},2} - z_{\mathrm{sim},1}} A_{\mathrm{eff},4} \,. \tag{A.3}$$

A.4 Alternative definitions of the energy threshold

Different approaches and methods were tested in order to define the *a priori* energy threshold, but did not suffice as they mostly led to a too large value, which limits covered energy range and therefore the sensitivity of TBS. Among these were methods based on

1. the energy bias,
2. the effective area, and
3. the energy resolution.

TBS is more sensitive towards the spread of the energy bias and for this, its mean may be a more appropriate approach than the median. Using the mean of the energy bias led to a higher energy threshold (in general, the next-highest bin w.r.t. to that chosen by the median value), which is not desired. Also, the root mean square (RMS) of the binned relative energy bias was considered as it is more sensitive to the spread of the distribution. However, it is not trivial to define a selection criterion based on the RMS as the RMS is nearly constant around $\sim$ 20 % and only approaches smaller RMS values at energies above 1 TeV even for small zenith angles, which is an unacceptable high value decreasing the sensitivity of TBS drastically.

The effective area corrected with the energy-resolution matrix was also considered as a threshold-defining parameter. For this, criteria were tested where the energy threshold was defined as the energy bin in which the effective area reached 10 % to 20 % of its maximum value or when it absolutely reached 10^5 m^2. However, especially zenith angles above 50°, these definitions lead to high energy thresholds (around 1 TeV at an offset of 0.5°, for example) based on the effective areas produced for TBS (see also Figure 4.7) and therefore, these methods were not applied.

It was also investigated if the muon-corrected energy-resolution matrix could serve as a template to determine the energy threshold. In Figure 4.6 (which represents the energy resolution for a Crab Nebula-like observation) it can be seen, that the energy reconstruction fails at lower energies (transition from the diagonal to the straight). One could use the spread of the diagonal after the transition point to define an energy threshold. However, depending on the criterion (e.g. the sum of the entries along a column to be less than 2), the thresholds derived are too high and hamper the analysis of high-zenith angle data and of extended sources (as the diagonal in the energy-resolution matrix is not as sharp as for point-like data).

In summary, the definition of the energy threshold through the median of energy bias (Sect. 4.5.1.3) suits a spectral analysis best since a lower energy threshold is desired. Other tested definitions are too conservative and lead to very high energy thresholds.

A.5 Correlation plots

In general, the individual spectral parameters of a spectral shape are not independent from one another, but correlated. Therefore, a correlation plot mapping the $1\,\sigma$ and $2\,\sigma$ of the forward folding are a better display if spectral results are comparable with one another. In the following, the correlation plots obtained in the likelihood maximisation in TBS are shown for all six studied sources in Section 4.5.2. These sources are

- the Crab Nebula,
- Centaurus A,
- HESS J1745–290,
- HESS J1507–622,
- Vela X, and
- Vela Junior.

A.5.1 Crab Nebula

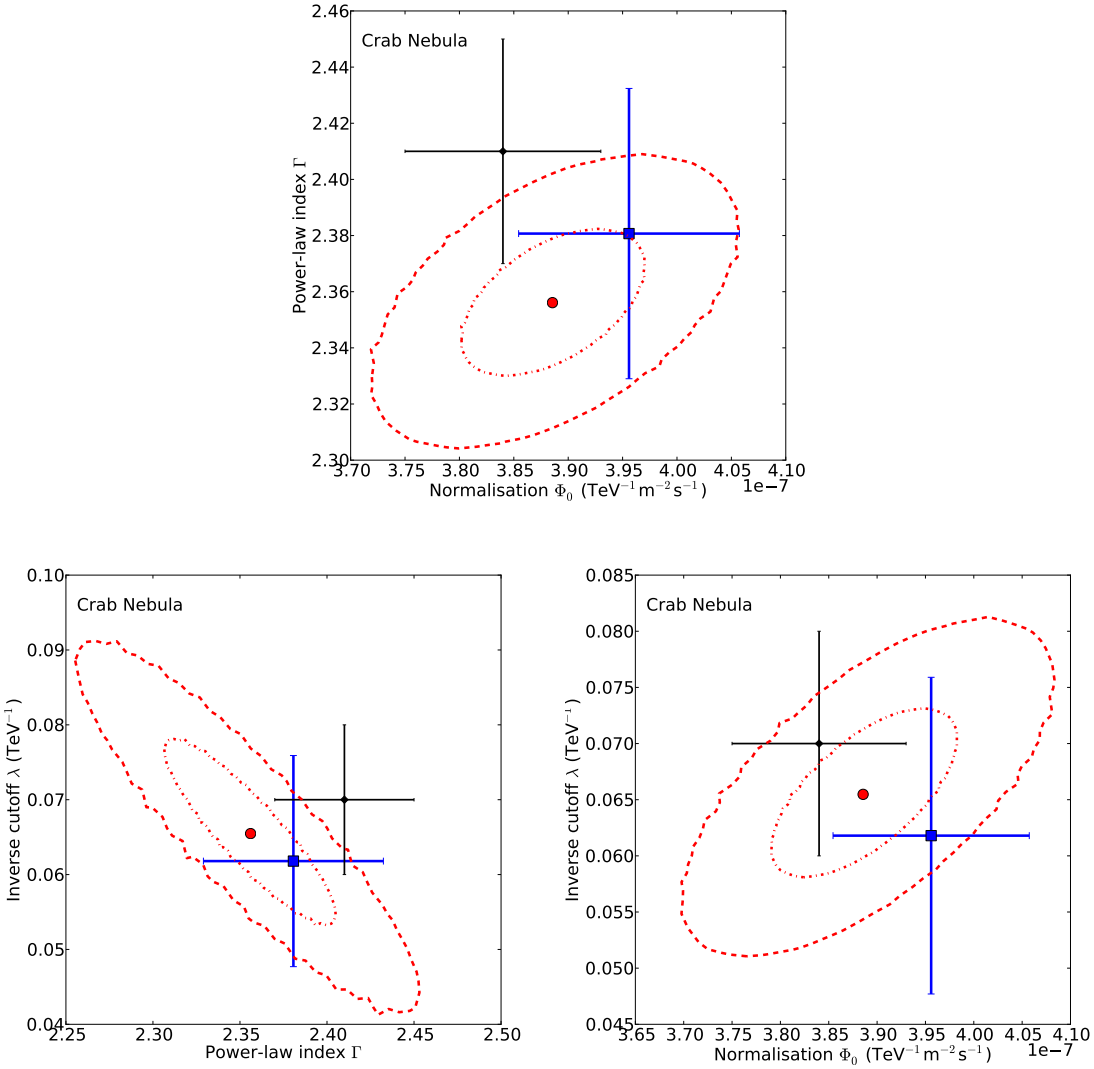

Figure A.4 Correlation plots for the TBS analysis of the Crab Nebula. Depicted are the best-fit results obtained with TBS (red circle), the cross check (blue square), and from (Aharonian et al., 2006a, black diamond). The short-dashed and the normal dashed lines depict the 1 σ and 2 σ uncertainty contours of TBS. **Top:** Correlation plot of power-law index vs. flux normalisation. **Bottom left:** Correlation plot of inverse cutoff vs. power-law index. **Bottom right:** Correlation plot of inverse cutoff vs. flux normalisation.

A.5.2 CENTAURUS A

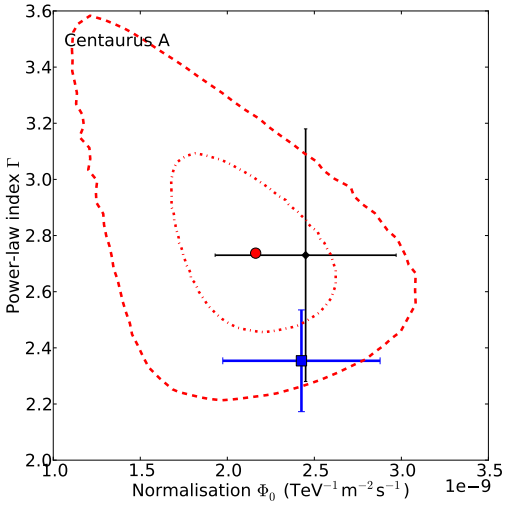

FIGURE A.5 Correlation plots for the TBS analysis of Centaurus A. Depicted are the best-fit results obtained with TBS (red circle), the cross check (blue square), and from (Aharonian et al., 2009c, black diamond). The short-dashed and the normal dashed lines depict the $1\,\sigma$ and $2\,\sigma$ uncertainty contours of TBS. Correlation plot of power-law index vs. flux normalisation.

A.5.3 HESS J1745–290

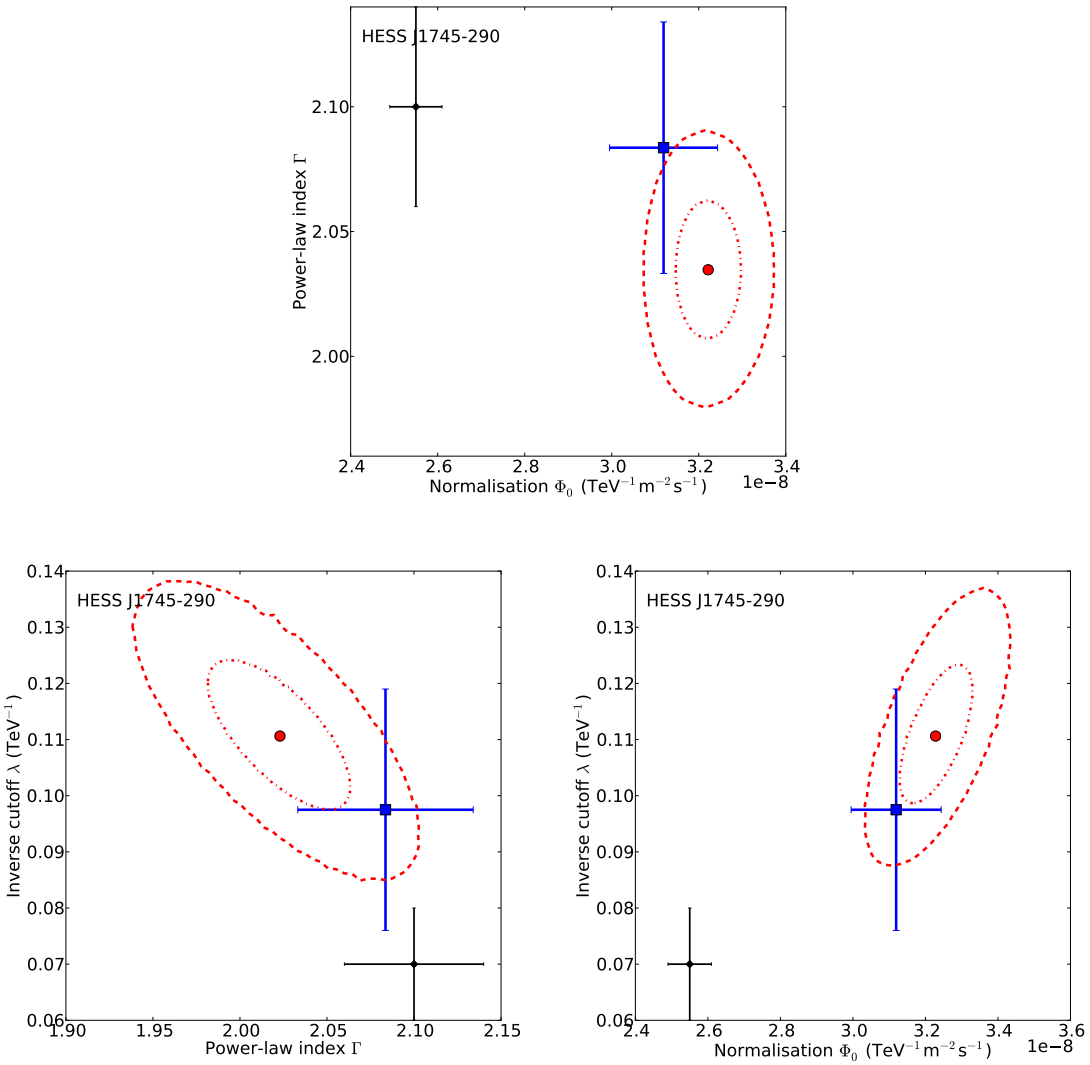

Figure A.6 Correlation plots for the TBS analysis of HESS J1745–290. Depicted are the best-fit results obtained with TBS (red circle), the cross check (blue square), and from (Aharonian et al., 2009b, black diamond). The short-dashed and the normal dashed lines depict the 1 σ and 2 σ uncertainty contours of TBS. **Top:** Correlation plot of power-law index vs. flux normalisation. **Bottom left:** Correlation plot of inverse cutoff vs. power-law index. **Bottom right:** Correlation plot of inverse cutoff vs. flux normalisation.

A.5.4 HESS J1507–622

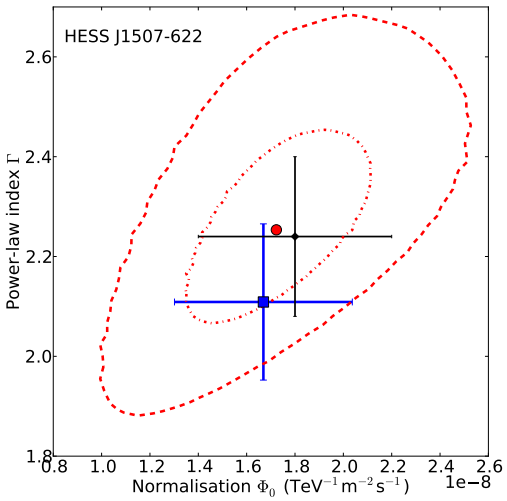

Figure A.7 Correlation plots for the TBS analysis of Centaurus A. Depicted are the best-fit results obtained with TBS (red circle), the cross check (blue square), and from (Acero et al., 2011, black diamond). The short-dashed and the normal dashed lines depict the $1\,\sigma$ and $2\,\sigma$ uncertainty contours of TBS. Correlation plot of power-law index vs. flux normalisation.

A.5.5 VELA X

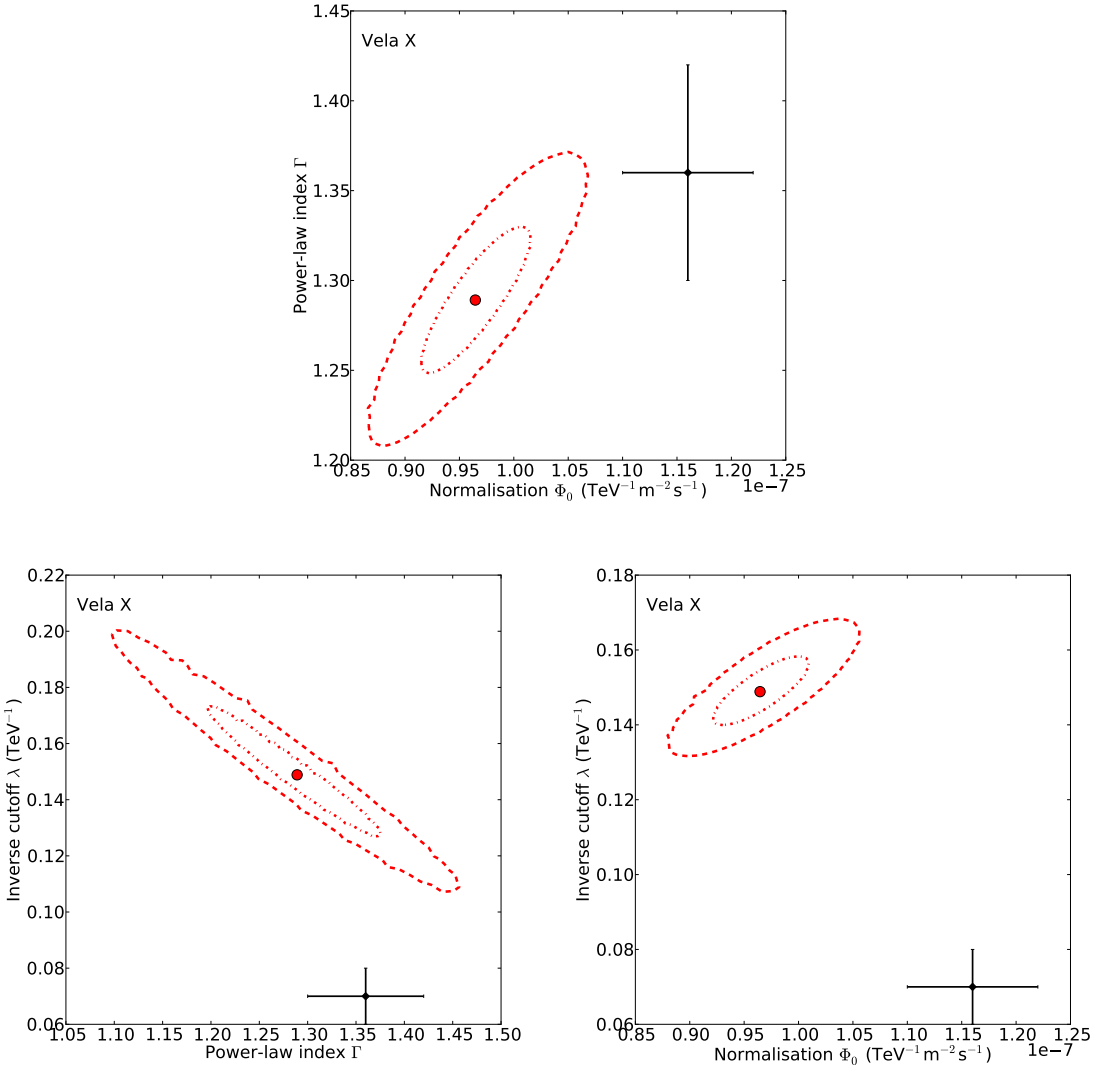

FIGURE A.8 Correlation plots for the TBS analysis of Vela X. Depicted are the best-fit results obtained with TBS (red circle) and from (Abramowski et al., 2012b, black diamond). The short-dashed and the normal dashed lines depict the $1\,\sigma$ and $2\,\sigma$ uncertainty contours of TBS. **TOP:** Correlation plot of power-law index vs. flux normalisation. **BOTTOM LEFT:** Correlation plot of inverse cutoff vs. power-law index. **BOTTOM RIGHT:** Correlation plot of inverse cutoff vs. flux normalisation.

A.5.6 VELA JUNIOR

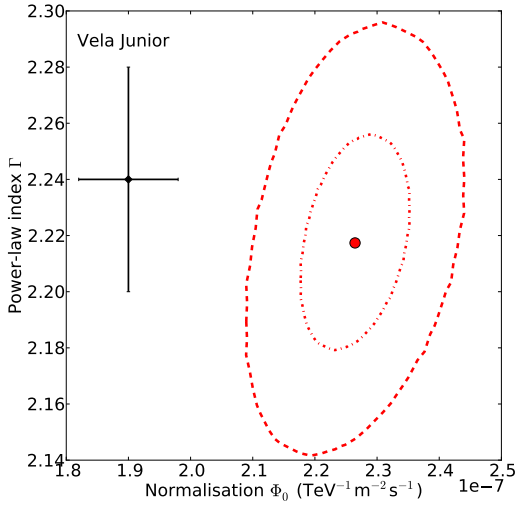

FIGURE A.9 Correlation plots for the TBS analysis of Vela Junior. Depicted are the best-fit results obtained with TBS (red circle) and from (Aharonian et al., 2005b, black diamond).The short-dashed and the normal dashed lines depict the 1 σ and 2 σ uncertainty contours of TBS. Correlation plot of power-law index vs. flux normalisation.

Appendix B

Auxiliary Information to Chapter 6

In this section of the appendix additional information is given for Chapter 6.

B.1 Differential energy spectra

The differential energy spectra of H.E.S.S. for two assumed spectral shapes as obtained by scaling the residuals of the forward folding to the expected flux. In general, the flux points exhibit at least a statistical significance of $2\,\sigma$, otherwise a $2\,\sigma$ upper limits is calculated using the likelihood method introduced in von Seggern (2014). The residuals are depicted below each spectrum, but in the case where Gaussian statistics were not provided, no uncertainty was determined for the excess. These residuals indicate the fit range when using the alternative χ^2 minimisation.

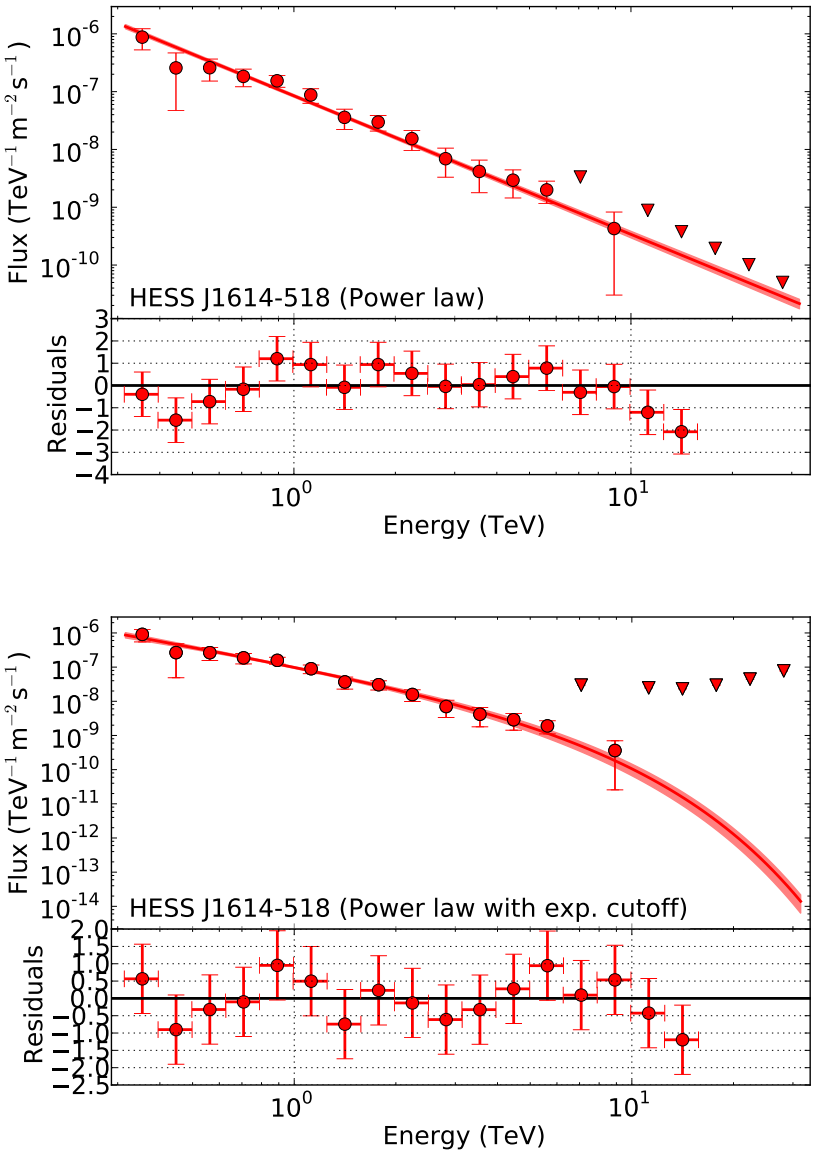

FIGURE B.1 Differential energy spectra depicted as the 1 σ butterflies of the forward-folding in TBS of the entire source HESS J1614−518 (red area). **TOP:** Fit of a simple power law. **BOTTOM:** Fit of a simple power law with an exponential cutoff.

B.2 RADIAL VELOCITIES

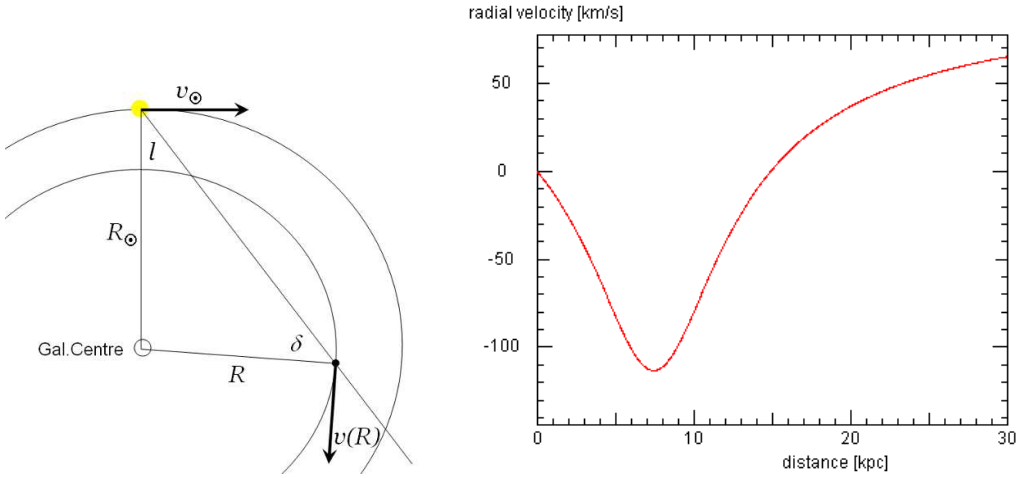

FIGURE B.2 Determination of the radial velocity and the distance **LEFT:** Sketch how the radial velocity is determined through simple geometrical consideration. **RIGHT:** The radial velocity versus distance towards HESS J1614–518. Both images are adopted from *astro.u-strasbg.fr/~koppen/Haystack/rotation.html*

The Milky Way is a rotating spiral-arm galaxy and because the Sun is not in its centre, astrophysical objects (e.g. stars, clouds) along the line of sight appear to be moving towards or from the Sun (or the Earth). The motion of matter can be determined by measuring the Doppler effect on the HI emission at 21 cm.

Given the Galactic rotation model and the distance of the Sun to the Galactic Centre, these velocities can be used to estimate the distance w.r.t. the Sun. The distance to the Galactic Centre can be estimated through direct (e.g. parallax of single stars/stellar cluster or stellar orbits around Sgr A*) and indirect (measuring the apparent magnitude of specific stars and stellar clusters and determining the absolute magnitude) measurements or through kinematic/rotation models, in which account for the motion stars and matter in the disk. An overview of these various techniques and methods is given in Gillessen et al. (2013).

On the left-hand side of Figure B.2 a sketch is drawn to show how the radial velocity is used to determine the distance of objects.

$$v_{\text{radial}} = v(R)\,\sin\delta - v_\odot\,\sin l\,, \tag{B.1}$$

where $v(R)$ is the rotational speed, $v_\odot$ the speed of the Sun, and l the Galactic longitude. The distance object-Galactic Centre R and the distance Sun-Galactic Centre $R_\odot$ are related through $R\sin\delta = R_\odot \sin l$.

For the distance determination in Chapter 6, the right-hand plot in Figure B.2 was used to estimate the distance of the discussed objects. This radial velocity versus distance plot was produced using a web applet[i] with the parameters $v_\odot = 220\,\mathrm{km\,s^{-1}}$, $R_\odot$=8.5 kpc and $l = 331.5°$ (i.e. the nominal Galactic longitude towards HESS J1614–518).

[i] *astro.u-strasbg.fr/~koppen/Haystack/rotation.html*

B.3 STARBURST 99 PARAMETERS

The kinetic energy provided over the cluster life time was determined using the Starburst99 cluster-evolution model (Leitherer et al., 2010). The simulations were run on a server accessible over *stsci.edu/science/starburst99/docs/default.htm*. The default parameters were used implying a Kroupa initial-mass function (Kroupa, 2001) and stellar-wind models for massive stars from Maeder (1990). Altogether, three models were computed for initial cluster masses of $10^2\,M_\odot$,$10^3\,M_\odot$, and $10^4\,M_\odot$ up to a cluster life time of 40 Myrs (see Section 6.3.1).

```
MODEL DESIGNATION: p22_m1000
MODEL GENERATED ON 20130822  AT 171405.2


CONTINUOUS STAR FORMATION (>0) OR FIXED MASS (<=):
-1
TOTAL STELLAR MASS (IF "FIXED MASS" IS CHOSEN):
0.100E+04
SFR(T=0) IF "CONT SF" IS CHOSEN:
      1.00
NUMBER OF INTERVALS FOR THE IMF:
 2
IMF EXPONENTS :
      1.30       2.30
MASS LIMITS FOR IMF [SOLAR MASSES]:
      0.10       0.50      100.00
SUPERNOVA CUT-OFF MASS:
      8.00
BLACK HOLE CUT-OFF MASS:
    120.00
METALLICITY + TRACKS:
GENEVA STD:  11=0.001; 12=0.004; 13=0.008; 14=0.020; 15=0.040
GENEVA HIGH: 21=0.001; 22=0.004; 23=0.008; 24=0.020; 25=0.040
PADOVA STD: 31=0.0004; 32=0.004; 33=0.008; 34=0.020; 35=0.050
PADOVA AGB: 41=0.0004; 42=0.004; 43=0.008; 44=0.020; 45=0.050
44
WIND MODEL (0=MAEDER; 1=EMPIRICAL; 2=THEOR.; 3=ELSON):
 0
INITIAL TIME:
0.100E+05
TIME SCALE: LINEAR (=0) OR LOGARITHMIC (=1)
 1
TIME STEP [1.e6 YEARS] (IF JTIME=0) OR
NUMBER OF STEPS       (IF JTIME=1):
   1000
LAST GRID POINT:
0.403E+08
SMALL (=0) OR LARGE (=1) MASS GRID;
ISOCHRONE ON  LARGE GRID (=2) OR FULL ISOCHRONE (=3):
 3
LMIN, LMAX (ALL = 0):
    2   818
TIME STEP FOR PRINTING OUT THE SYNTHETIC SPECTRA:
0.200E+07
MODEL ATMOSPHERE: 1=PLA, 2=LEJ, 3=LEJ+SCH, 4=LEJ+SMI, 5=PAU+SMI
 5
METALLICITY OF THE HIGH RESOLUTION MODELS
(1=0.001, 2=0.008, 3=0.020, 4=0.040):
 3
METALLICITY OF THE UV LINE SPECTRUM: (1=SOLAR, 2=LMC/SMC)
 1
RSG FEATURE: MICROTURB. VELOCITY (1-6), SOLAR/NON-SOLAR ABUNDANCE (0,1)
 3,0
OUTPUT FILES (NO<0, YES >=0):
 1  1  1  1  1  1  1  1  1  1  1  1  1  1  1
```

Appendix C

Auxiliary Information to Chapter 7

In this chapter of the appendix, additional information on the Gould Belt is presented, but in general discussed and referred to in Chapter 7.

C.1 *Fermi*–LAT view on the Gould Belt

The *Fermi*–LAT HE skymaps above 100 MeV and above 10 GeV were selected for the period 239557417 s to 410136591 s in MET (04.08.2008 to 31.12.2013) including front and back-converted events of the IRF `P7REP_SOURCE_V15` and a radius of 20° around the nominal target position listed in Table 7.2.

The skymaps were produced following the recommended instructions[i] and for a smaller radius of 5° around the source position, i.e. double the size of the H.E.S.S. FoV. In all skymaps, the bin width is 0.1°. The skymaps of γ-ray energies above 100 MeV are smoothed with a Gaussian with $\sigma = 0.3°$ that undersamples the strongly energy-dependent PSF of *Fermi*–LAT (Sect. 3.1.2), but is used to reduce statistical noise in the skymaps. The skymaps above 10 GeV are smoothed with a larger Gaussian of $\sigma = 0.6°$ (about twice the PSF around 10 GeV) to trace extended features and because the event rates above this threshold are relatively low for *Fermi*–LAT and would otherwise leave large parts of the skymaps empty. For a better visibility of the entire cloud structure in the MeV to GeV band, the GeV sources are only depicted in the skymaps of energies above 10 GeV.

[i] Autumn 2013; *fermi.gsfc.nasa.gov/ssc/data/analysis/scitools/likelihood_tutorial.html*.

C.1.1 LUPUS 3 CLOUD

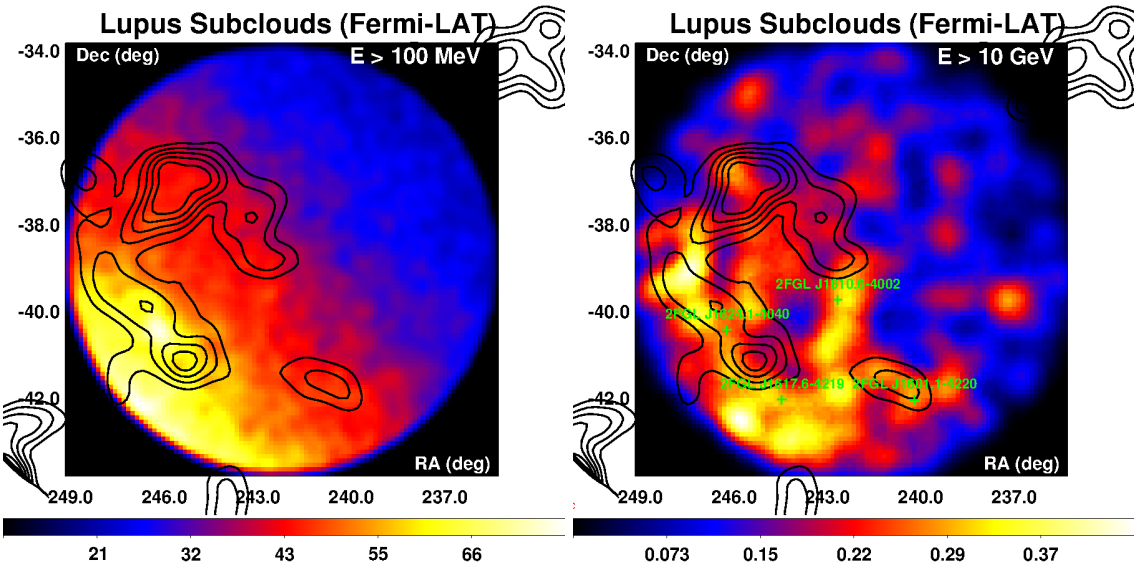

FIGURE C.1 The HE γ-ray skymaps obtained from *Fermi*–LAT data for the Lupus 3 region. The solid lines depict the CO contours from 6 to 18 K in steps of 3 K (Dame et al., 2001). **LEFT:** The skymap with events above 100 MeV and smoothed with a Gaussian width $\sigma = 0.3°$. **RIGHT:** The skymap with events above 10 GeV and smoothed with a Gaussian width $\sigma = 0.6°$. Depicted are the *Fermi*–LAT sources from Nolan et al. (2012).

The Lupus subclouds depicted in Figure C.1 are not directly visible in the *Fermi*–LAT skymaps. Although the Lupus clouds are about 10° above the Galactic Centre, any emission from these clouds is outshone by the bright HE emission from the Galactic-Centre region and the diffuse emission along the Galactic Plane. At energies above 10 GeV, the statistics are too sparse to identify the Lupus subclouds in the HE γ-ray data.

There are four 2FGL sources reported in Nolan et al. (2012). Three of them are unidentified and unassociated, namely 2FGL J1624.1–4040, 2FGL J1601.1–4220, and 2FGL J1617.6–4219. The fourth source 2FGL J1610.6–4002 is identified as a FSRQ and associated with PMN J1610-3958 (Landt et al., 2001).

C.1.2 TAURUS REGION (LYNDS 1495A)

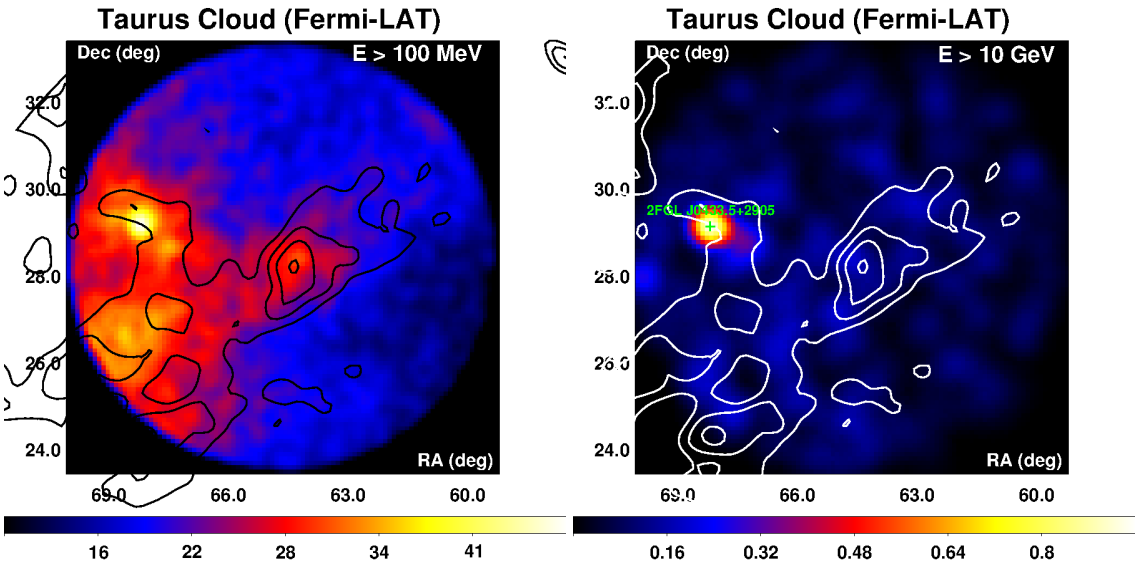

FIGURE C.2 The HE γ-ray skymaps obtained from *Fermi*–LAT data of the Taurus region (Lynds 1495A). The solid lines depict the CO contours from 10 to 25 K in steps of 5 K (Dame et al., 2001). **LEFT:** The skymap with events above 100 MeV and smoothed with a Gaussian width $\sigma = 0.3°$. **RIGHT:** The skymap with events above 10 GeV and smoothed with a Gaussian width $\sigma = 0.6°$. Depicted is one *Fermi*–LAT source from Nolan et al. (2012).

The Taurus region depicted in Figure C.2 is clearly seen in the HE energy map above 100 MeV. At higher energies, the FoV is relatively empty and only γ-ray bright around the 2FGL source 2FGL J0433.5+2905 (Nolan et al., 2012), which is the BL Lac-type blazar MITG2 J043337+2905 (Langston et al., 1990). The compact region in the centre of the FoV (Lynds 1495A) does not show any hint of HE γ-ray emission.

C.1.3 ORION A

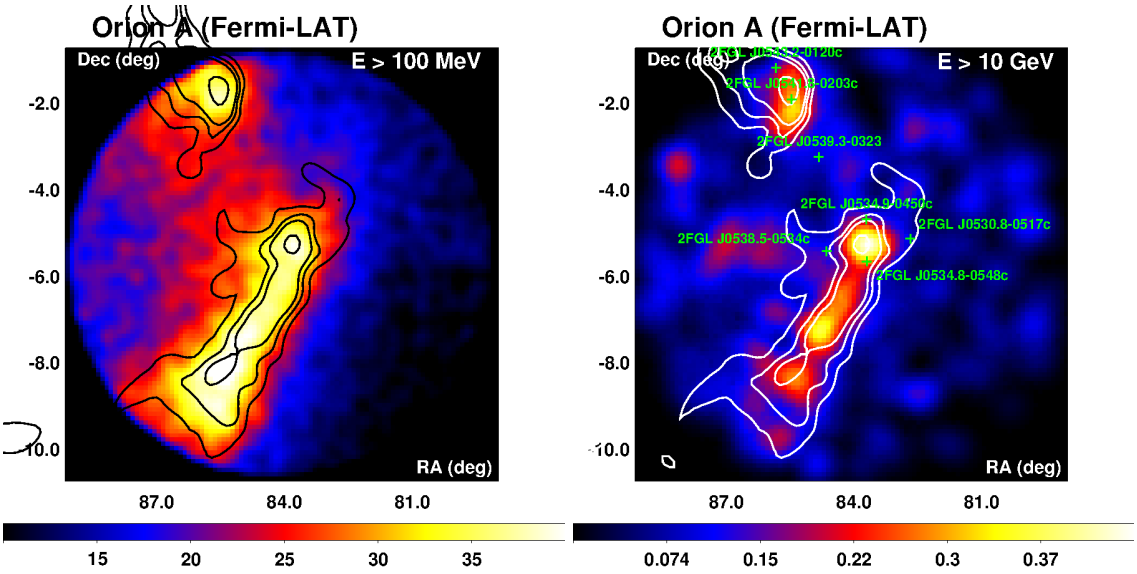

FIGURE C.3 The HE γ-ray skymaps obtained from *Fermi*–LAT data of the Orion A region. The solid lines depict the CO contours 10, 20, 30, 70 K (Dame et al., 2001). **LEFT:** The skymap with events above 100 MeV and smoothed with a Gaussian width $\sigma = 0.3°$. **RIGHT:** The skymap with events above 10 GeV and smoothed with a Gaussian width $\sigma = 0.6°$. Depicted are the *Fermi*–LAT sources from Nolan et al. (2012).

The Orion A region is bright in the γ-ray regime above 100 MeV. The observed HE emission traces the cloud structure very well (Fig. C.3). Above 10 GeV the smoothed skymap still shows a bright GeV feature in the compact centre of Orion A (i.e. the H.E.S.S. target). Around this compact emission region, four *Fermi*–LAT sources are found. The sources 2FGL J0534.8-0548c, 2FGL J0538.5-0534c, and 2FGL J0534.9-0450c are unassociated and flagged as possibly confused (c) with the Galactic diffuse emission. The source 2FGL J0530.8-0517c is also flagged as confused, but associated with the FSRQ PMN J0529-0519 (Healey et al., 2008).

C.1.4 PERSEUS CLOUD

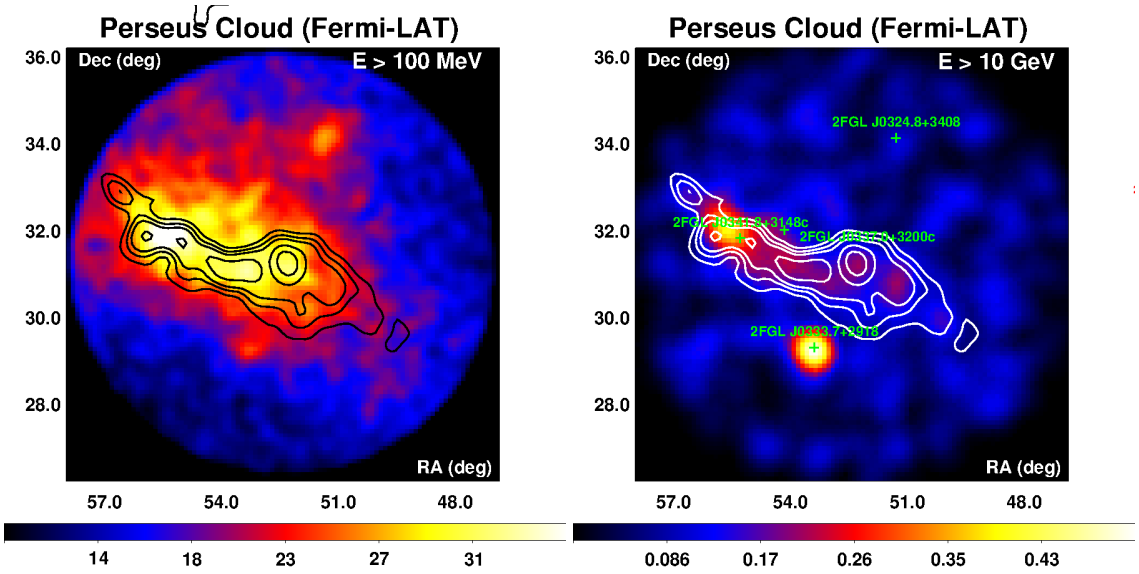

FIGURE C.4 The HE γ-ray skymaps obtained from *Fermi*–LAT data for the Perseus region. The solid lines depict the CO contours 10, 15, 20, 30, 40 K (Dame et al., 2001). **LEFT:** The skymap with events above 100 MeV and smoothed with a Gaussian width $\sigma = 0.3°$. **RIGHT:** The skymap with events above 10 GeV and smoothed with a Gaussian width $\sigma = 0.6°$. Depicted are the *Fermi*–LAT sources from Nolan et al. (2012).

The Perseus cloud depicted in Figure C.4 is bright in γ rays above 100 MeV At energies above 10 GeV, the smoothed skymap shows two bright spots spatially correlated with two reported 2FGL sources, but also a weak trace of HE γ-ray emission within the clouds. In Nolan et al. (2012), the two bright GeV sources are 2FGL J0337.0+3200c (associated the FSRQ NRAO 140; Lanyi et al., 2010) and the unidentified 2FGL J0341.8+3148c. The other sources, which are not bright at energies above 10 GeV, are 2FGL J0333.7+2918 and 2FGL J0324.8+3408, which are associated with the active galaxy TXS 0330+291 (Douglas et al., 1996) and the Seyfert 1 galaxy 1H 0323+342 (Healey et al., 2007), respectively.

C.1.5 ρ–OPHIUCHUS B

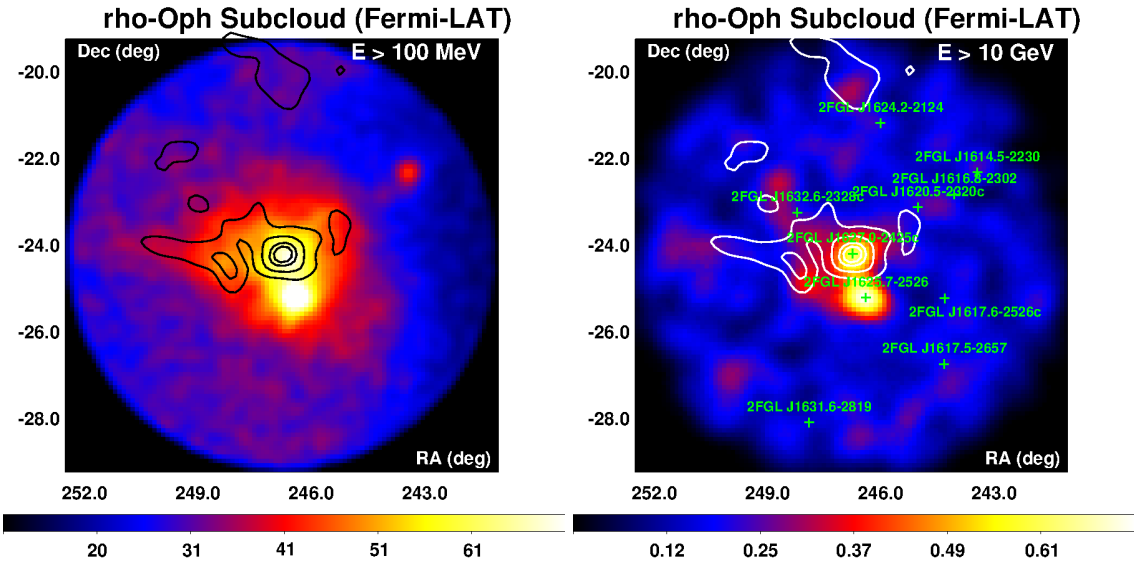

FIGURE C.5 The HE γ-ray skymaps obtained from *Fermi*–LAT data for the ρ–Oph B region. The solid lines depict the CO contours 10, 20, 30, 35 K(Dame et al., 2001). **LEFT:** The skymap with events above 100 MeV and smoothed with a Gaussian width $\sigma = 0.3°$. **RIGHT:** The skymap with events above 10 GeV and smoothed with a Gaussian width $\sigma = 0.6°$. Depicted are the *Fermi*–LAT sources from Nolan et al. (2012).

The region around the ρ–Oph B cloud is very bright in HE γ rays above 100 MeV. Also, at energies above 10 GeV, the centre part of the cloud is bright and next to it, a second bright source is to be seen; the other GeV sources in the FoV are rather dim (Nolan et al., 2012).

At the centre of the cloud, the GeV source 2FGL J1627.0-2425c is reported as an active galactic nucleus. However, since this source is located at the densest part of the cloud, it may also be a residual of the cloud itself as noted in *simbad.u-strasbg.fr/simbad* and discussed in Kovalev (2009). The second bright source 2FGL J1625.7-2526 is associated with the FSRQ PKS 1622-253 (Ekers, 1969).

C.2 ANALYSIS OF CENTAURUS A WITH EXTRA-GALACTIC LOOK-UPS OF THE CAMERA ACCEPTANCE

In this section, H.E.S.S. data on Centaurus A were used to test the extra-Galactic acceptance look-ups in combination with the TBg model and the RingBg model and the gamma/hadron separation using the ζ_{std} cuts. For this, available H.E.S.S. data consisting of 375 four-telescope runs between 2004 and 2010 resulting in 159 hrs of high-quality data were analysed. With the TBg model and the acceptance correction from the same data, Centaurus A is detected at a 6.1 σ level.

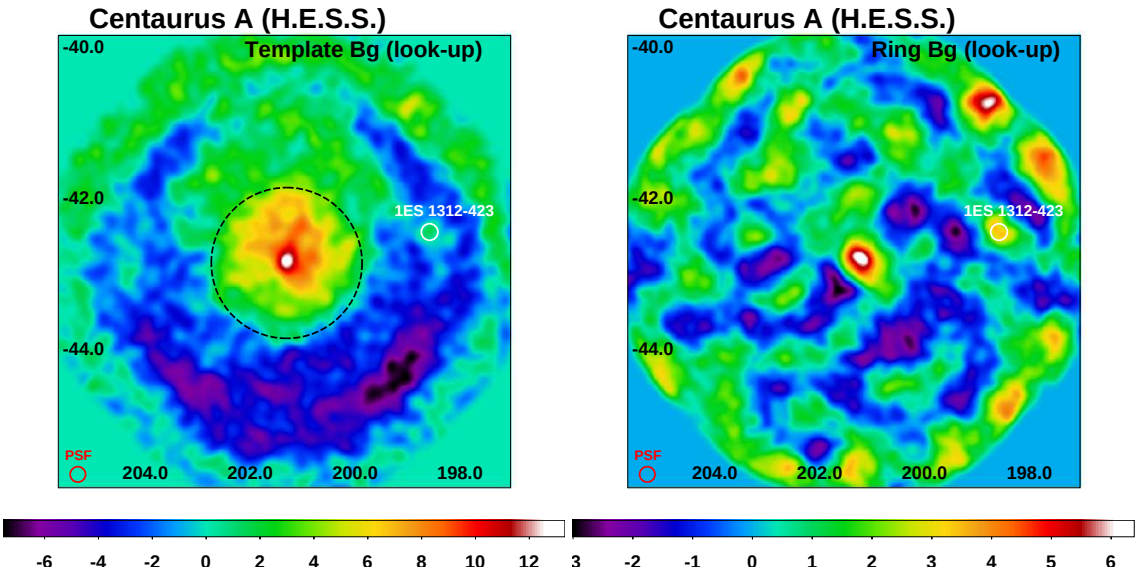

FIGURE C.6 Significance skymap of the Centaurus A (in the centre) FoV to demonstrate the effect extra-Galactic acceptance look-ups. The skymaps are calculated by integration of events within a circle of 0.1° and smoothed with a Gaussian of the PSF size. The source 1ES 1312–423 is a faint extra-Galactic point source detected with *Fermi*–LAT and H.E.S.S. (Abramowski et al., 2013). The PSF radius is $\sim$ 0.10°. **LEFT:** Significance skymap using the TBg model. The black-dashed circle is for comparison purposes and has a radius of 1°. **RIGHT:** Significance skymap using the RingBg method.

In Figure C.6, the significance skymap is shown as obtained with the TBg model (left) and the RingBg method (right) by integrating events within 0.1° and smoothing the skymap with a Gaussian of the size of the PSF (0.10°) As a results of the TBg analysis, Centaurus A is detected with more than double of the statistical significance than for the analysis with the acceptance correction from data. Moreover, there is a significance plateau with a radius of $\sim$ 1° of $6 \ldots 8\,\sigma$, a gradient from north to south and at the edge of the FoV, the manifestation of the camera-edge effect. The analysis with the RingBg method results in the expected point-like excess at the position of Centaurus A.

Because the RingBg method resulted in the expected point source without a large-scale extended emission, this is a clear indication that the extra-Galactic acceptance look-ups for hadrons underestimate the response for hadron-like events and therefore affect the TBg model that uses these hadron acceptances. There are many possible approaches to explain these results or make some scenarios unlikely.

As the gamma-like and hadron-like events are treated identically in the production of the acceptance look-ups (same data sets, same quality selections and criteria, identical binning in zenith angle and azimuth angle) and because the analysis in HAP uses the same routine to use these acceptance look-ups in the analysis, this makes a trivial *bug* in the analysis and application to the data that would only affect the hadron-like events unlikely.

The separate analysis of data below and above 1 TeV with the TBg model and the extra-Galactic acceptance look-ups resulted in the same feature and thus making an energy-dependent feature unlikely.

Possible explanations may be unknown systematic effects related to hadron-like data, e.g. a change in the response of the H.E.S.S. detector for such events, variations in the sky, which become dominant when accumulating data to produce the look-ups, or the need of optical-efficiency correction (in general not done for skymap production) for look-ups as data spanning almost 10 yrs are used. It is also possible that the assumption of radial symmetry of the H.E.S.S. FoV is not valid anymore when the relative statistical errors on the data used in the look-ups are below $\sim$ 1 % and possible asymmetries become dominant.

The following checks could involve different systematic studies, but may provide a solution:

- re-visit the runs and check for possible faint γ-ray excess and problems in the acceptances: selected runs probably contain recently detected sources,
- exclusion of (faint) sources and bright stars: size of exclusion radii and significance threshold,
- cumulative effects of different excluded regions and broken pixels,
- radial symmetry of the camera acceptance: up to what level and under what observing conditions as well as possible effects of exclusion regions; since statistical errors in the look-up are far below 1 %, a higher systematic error would limit the look-ups,
- energy dependence may have to be accounted for before filling the look-ups,
- intervals in zenith angle and azimuth angle: the camera acceptance varies strongly at high zenith angles, which may require a very fine binning of the look-ups,
- dependency of the optical efficiency,
- variations in the hadron-like regime: apparently, only the TBg model appears to be affected; this could mean that variations occur in the events classified as hadrons,

perhaps linked the specific gamma/hadron separation or to correlation with observation parameters, e.g. the azimuth angle .

These further and possibly very detailed studies were not part of this thesis and require work and effort at various stages of the analysis chain of H.E.S.S. data in HAP, but also a systematic study of the background and the response of the camera.

In case, the observed effects are due to the systematics errors intrinsic to the camera acceptance and only become dominant because a large amount of data is used to create these look-ups (Sect. 3.3.8.6), a possible solution would be the application of an *adaptive* look-up, for which only a subset of the look-up is used such that the statistical errors are not significantly below the assumed systematic errors. In Section 3.3.7, it was presented that the systematic errors on the camera acceptance appear to be at most 3 % up to moderate zenith angles, but larger for zenith angles above $\sim 55^{\circ}$.

C.3 CROSS-CHECK ANALYSES

In this section, the skymaps of the GB data obtained with the RingBg method are presented. Additionally, the results of the TBg model analysis and RingBg method analysis using look-ups of the camera acceptance are presented and discussed in main part of Section 7.3.

C.3.1 LUPUS 3

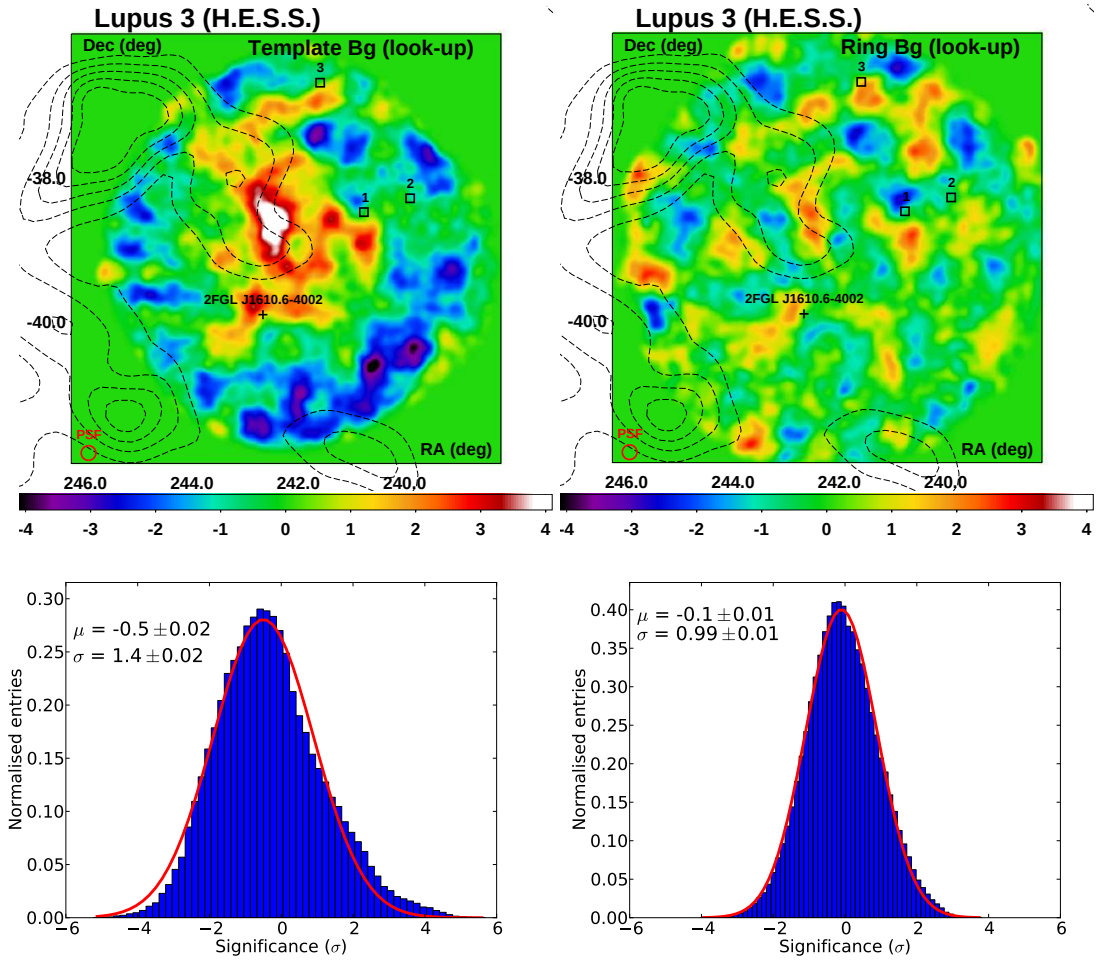

FIGURE C.7 The 6° × 6° VHE γ-ray significance images of the Lupus 3 cloud. The acceptance correction was done using extra-Galactic data, but otherwise these skymaps are identical to those in Figure 7.4. **LEFT:** VHE γ-ray significance skymap obtained with the TplBg model. **RIGHT:** VHE γ-ray significance skymap obtained with the RingBg method. See Section 7.3.1 for more information.

C.3.2 LYNDS 1495A

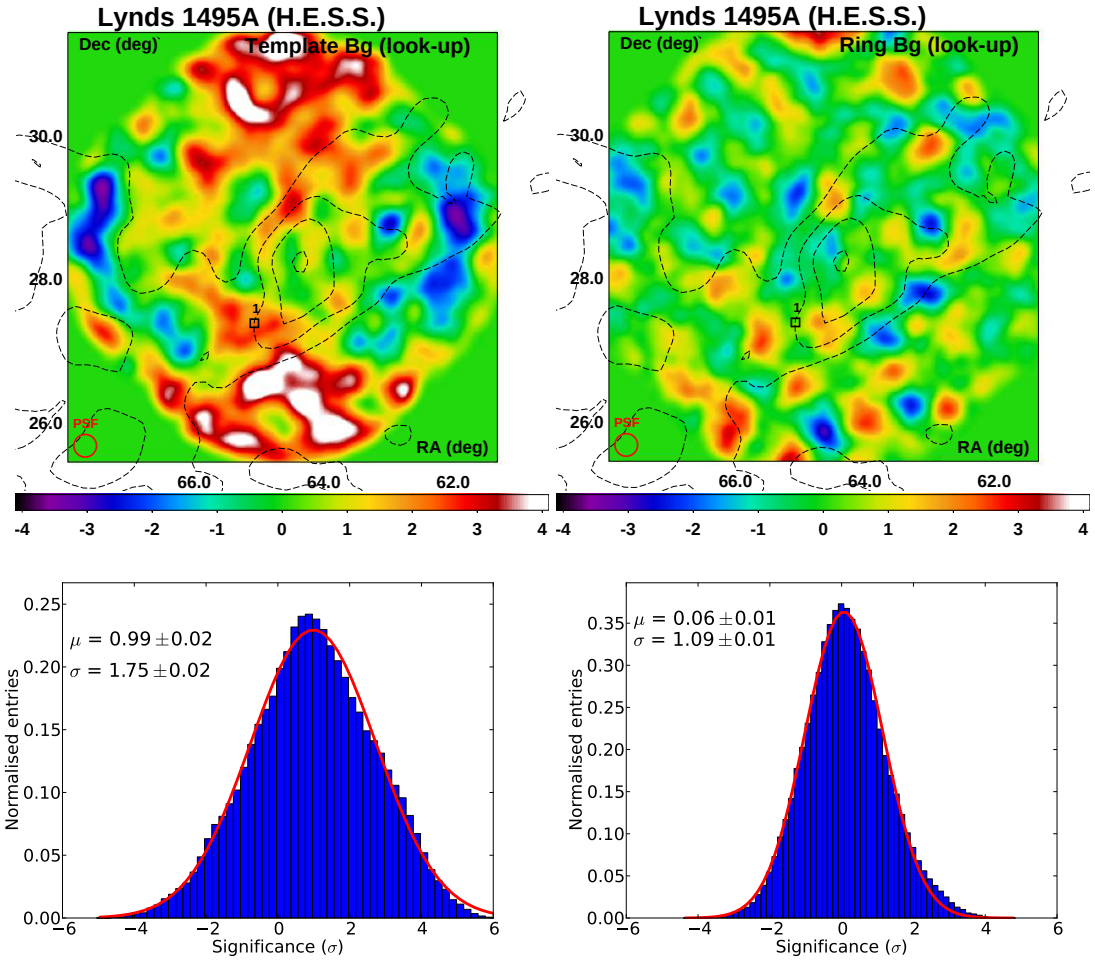

FIGURE C.8 The 6° × 6° VHE γ-ray significance images of the Lynds 1495A subcloud. The acceptance correction was done using extra-Galactic data, but otherwise these skymaps are identical to those in Figure 7.5. **LEFT:** VHE γ-ray significance skymap obtained with the TplBg model. **RIGHT:** VHE γ-ray significance skymap obtained with the RingBg method. See Section 7.3.2 for more information.

C.3.3 ORION A

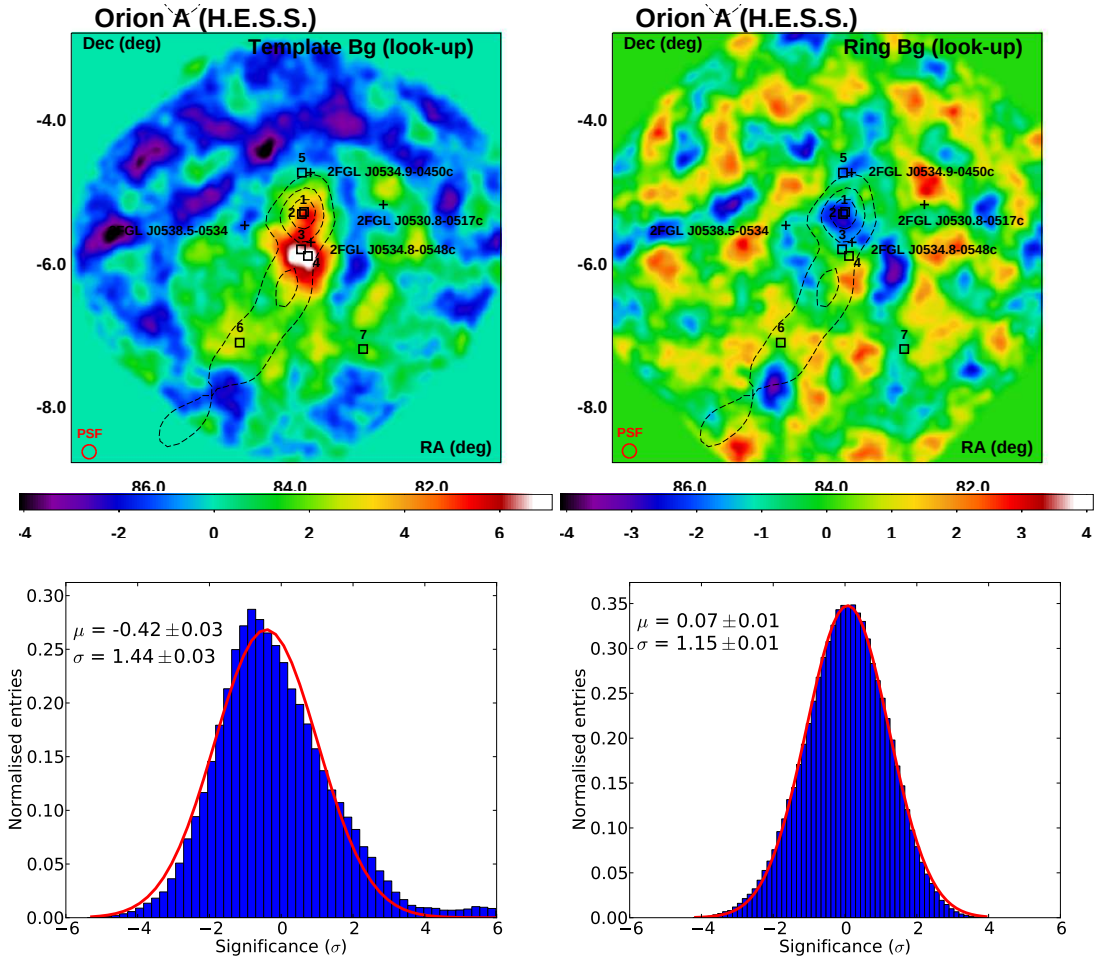

FIGURE C.9 The 6° × 6° VHE γ-ray significance images of the Orion A cloud. The acceptance correction was done using extra-Galactic data, but otherwise these skymaps are identical to those in Figure 7.6. **LEFT:** VHE γ-ray significance skymap obtained with the TplBg model. **RIGHT:** VHE γ-ray significance skymap obtained with the RingBg method. See Section 7.3.3 for more information.

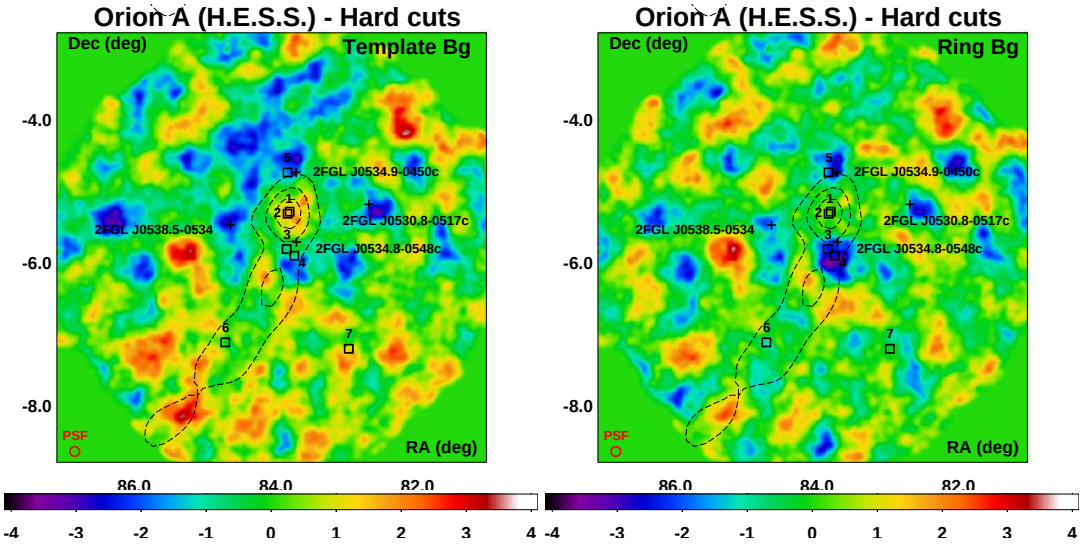

FIGURE C.10 The 6° × 6° VHE γ-ray significance images of the Orion A cloud. The ζ_{hard}-cuts analysis was used, but otherwise these skymaps are identical to those in Figure 7.6. **LEFT:** VHE γ-ray significance skymap obtained with the TplBg model. **RIGHT:** VHE γ-ray significance skymap obtained with the RingBg method. See Section 7.3.3 for more information.

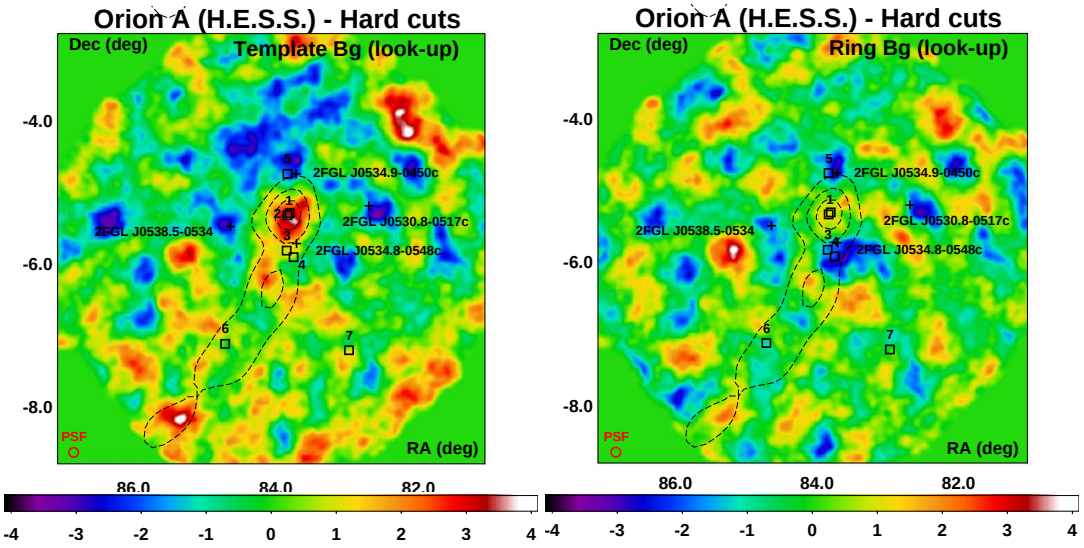

FIGURE C.11 The 6° × 6° VHE γ-ray significance images of the Orion A cloud. The acceptance correction was done using extra-Galactic data and the ζ_{hard}-cuts analysis, but otherwise these skymaps are identical to those in Figure 7.6. **LEFT:** VHE γ-ray significance skymap obtained with the TplBg model. **RIGHT:** VHE γ-ray significance skymap obtained with the RingBg method. See Section 7.3.3 for more information.

C.3.4 PERSEUS CLOUD

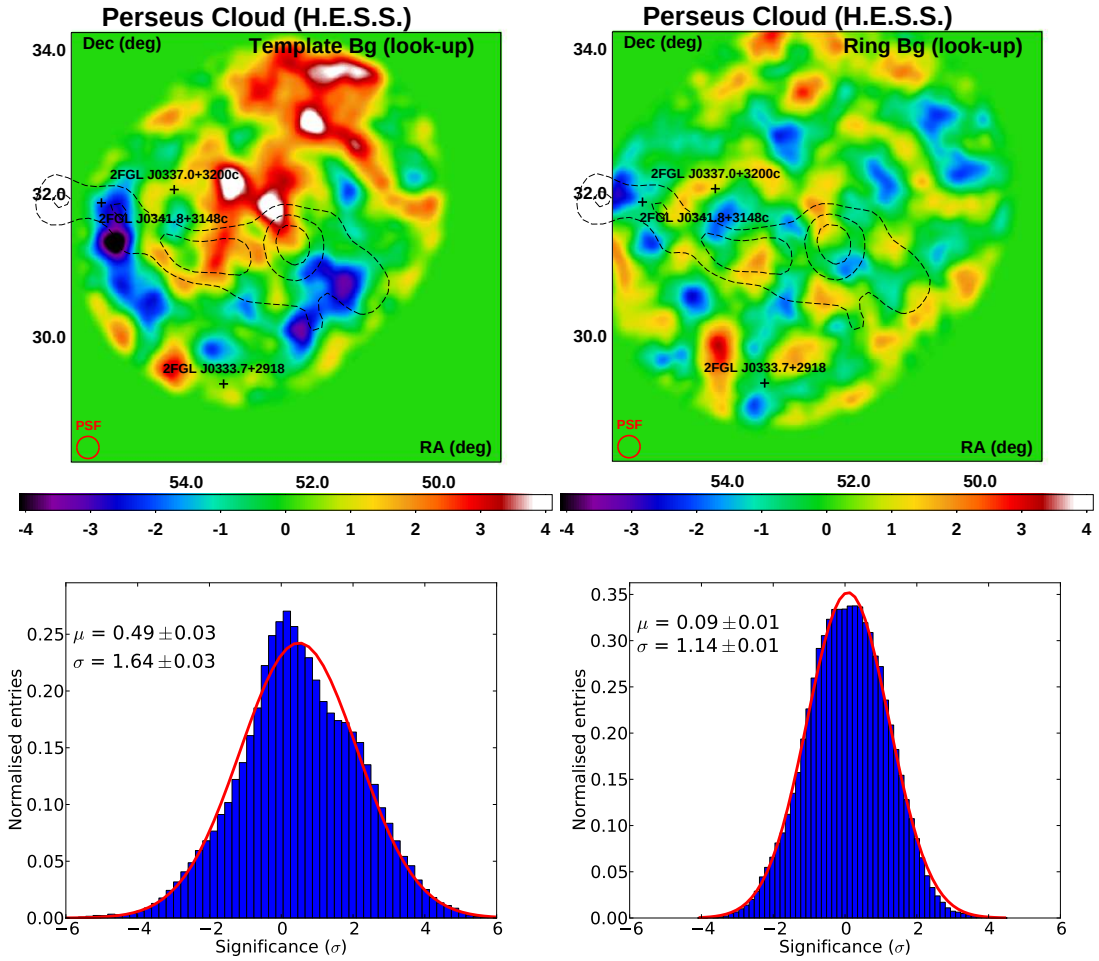

FIGURE C.12 The 6° × 6° VHE γ-ray significance images of the Perseus-cloud core. The acceptance correction was done using extra-Galactic data, but otherwise these skymaps are identical to those in Figure 7.7. **LEFT:** VHE γ-ray significance skymap obtained with the TplBg model. **RIGHT:** VHE γ-ray significance skymap obtained with the RingBg method. See Section 7.3.4 for more information.

C.3.5 ρ–OPHIUCHUS B

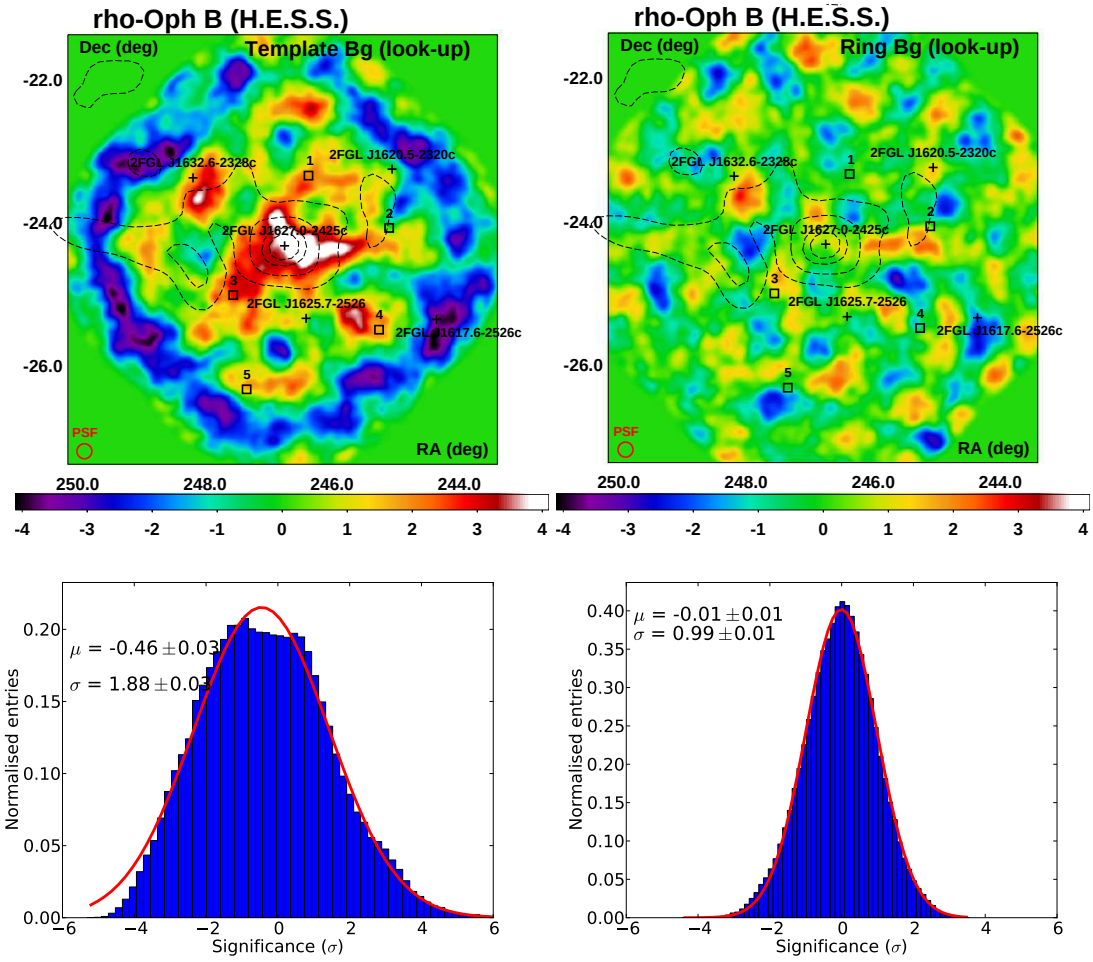

FIGURE C.13 The 6° × 6° VHE γ-ray significance images of the ρ–Oph B cloud. The acceptance correction was done using extra-Galactic data, but otherwise these skymaps are identical to those in Figure 7.8. **LEFT:** VHE γ-ray significance skymap obtained with the TplBg model. **RIGHT:** VHE γ-ray significance skymap obtained with the RingBg method. See Section 7.3.5 for more information.

C.4 RESULTS OF THE SPECTRAL RECONSTRUCTION USED TO DETERMINE THE EXCESS UPPER LIMITS

This section includes the results of the forward folding used to determine the expected excess counts N_{pred} and the integral flux (Table C.1). With these, the upper limit on the excess counts and the corresponding upper limit on the integral flux are determined and used to estimate the CR-enhancement factor.

TABLE C.1 Spectral parameters for the five Gould Belt regions as obtained with the Template Background Spectrum for a simple power law (Eq. 4.15). Note: $\Phi_0 = 10^{-12}\,\mathrm{TeV}^{-1}\mathrm{m}^{-2}\mathrm{s}^{-1}$ is the lower limit of the parameter and lowering this bound does not noticeably change the results presented in Section 7.6.

Cloud	E_{min} TeV	E_{max} TeV	$\Phi_0(1\,\mathrm{TeV})$ $10^{-8}\,\mathrm{TeV}^{-1}\mathrm{m}^{-2}\mathrm{s}^{-1}$	Γ	n_{dof}
Lupus 3	0.25	7.94	$1.00 \times 10^{-4} \pm 1.24$	2.6 (fixed)	13
Lynds 1495A	1.0	63.1	$1.00 \times 10^{-4} \pm 0.30$	2.6 (fixed)	16
Orion A	0.25	20.0	1.32 ± 0.53	3.63 ± 0.39	17
Perseus cloud	1.26	20.0	2.31 ± 2.69	2.6 (fixed)	10
ρ–Oph B	0.25	20.0	$1.00 \times 10^{-4} \pm 2.12$	2.6 (fixed)	17

BIBLIOGRAPHY

Abdo, A. A., Ackermann, M., Ajello, M., et al. 2010a, *Fermi Large Area Telescope First Source Catalog*, ApJS, 188, 405

Abdo, A. A., Ackermann, M., Ajello, M., et al. 2010b, *Fermi Large Area Telescope Observation of a Gamma-ray Source at the Position of Eta Carinae*, ApJ, 723, 649

Abdo, A. A., Ackermann, M., Ajello, M., et al. 2009, *Fermi large area telescope observations of the cosmic-ray induced gamma-ray emission of the Earth's atmosphere*, Phys. Rev. D, 80, 122004

Abramowski, A., Acero, F., Aharonian, F., et al. 2013, *HESS and Fermi-LAT discovery of gamma-rays from the blazar 1ES 1312-423*, MNRAS, 434, 1889

Abramowski, A., Acero, F., Aharonian, F., et al. 2012a, *Identification of HESS J1303-631 as a pulsar wind nebula through gamma-ray, X-ray, and radio observations*, A&A, 548, A46

Abramowski, A., Acero, F., Aharonian, F., et al. 2012b, *Probing the extent of the non-thermal emission from the Vela X region at TeV energies with H.E.S.S.*, A&A, 548, A38

Abramowski, A., Acero, F., Aharonian, F., et al. 2012c, *Discovery of extended VHE gamma-ray emission from the vicinity of the young massive stellar cluster Westerlund 1*, A&A, 537, A114

Abramowski, A., Acero, F., Aharonian, F., et al. 2012d, *HESS observations of the Carina nebula and its enigmatic colliding wind binary Eta Carinae*, MNRAS, 424, 128

Abramowski, A., Acero, F., Aharonian, F., et al. 2011, *Revisiting the Westerlund 2 field with the HESS telescope array*, A&A, 525, A46

Acero, F., Ackermann, M., Ajello, M., et al. 2013, *Constraints on the Galactic Population of TeV Pulsar Wind Nebulae Using Fermi Large Area Telescope Observations*, ApJ, 773, 77

Acero, F., Aharonian, F., Akhperjanian, A. G., et al. 2010, *First detection of VHE gamma-rays from SN 1006 by HESS*, A&A, 516, A62

Acero, F., Aharonian, F., Akhperjanian, A. G., et al. 2011, *Discovery and follow-up studies of the extended, off-plane, VHE gamma-ray source HESS J1507-622*, A&A, 525, A45

Ackermann, M., Ajello, M., Albert, A., et al. 2012, *The Fermi Large Area Telescope on Orbit: Event Classification, Instrument Response Functions, and Calibration*, ApJS, 203, 4

Ackermann, M., Ajello, M., Allafort, A., et al. 2013a, *Determination of the Point-spread Function for the Fermi Large Area Telescope from On-orbit Data and Limits on Pair Halos of Active Galactic Nuclei*, ApJ, 765, 54

Ackermann, M., Ajello, M., Allafort, A., et al. 2013b, *Detection of the Characteristic Pion-Decay Signature in Supernova Remnants*, Science, 339, 807

Aharonian, F., Akhperjanian, A. G., Anton, G., et al. 2009a, *Detection of very high energy radiation from HESS J1908+063 confirms the Milagro unidentified source MGRO J1908+06*, A&A, 499, 723

Aharonian, F., Akhperjanian, A. G., Anton, G., et al. 2009b, *Spectrum and variability of the Galactic center VHE gamma-ray source HESS J1745-290*, A&A, 503, 817

Aharonian, F., Akhperjanian, A. G., Anton, G., et al. 2009c, *Discovery of Very High Energy Gamma-Ray Emission from Centaurus a with H.E.S.S.*, ApJ, 695, L40

Aharonian, F., Akhperjanian, A. G., Aye, K.-M., et al. 2005a, *A New Population of Very High Energy Gamma-Ray Sources in the Milky Way*, Science, 307, 1938

Aharonian, F., Akhperjanian, A. G., Aye, K.-M., et al. 2004, *Calibration of cameras of the H.E.S.S. detector*, Astroparticle Physics, 22, 109

Aharonian, F., Akhperjanian, A. G., Bazer-Bachi, A. R., et al. 2008, *Discovery of very high energy gamma-ray emission coincident with molecular clouds in the W 28 (G6.4-0.1) field*, A&A, 481, 401

Aharonian, F., Akhperjanian, A. G., Bazer-Bachi, A. R., et al. 2006a, *Observations of the Crab nebula with HESS*, A&A, 457, 899

Aharonian, F., Akhperjanian, A. G., Bazer-Bachi, A. R., et al. 2005b, *Detection of TeV gamma-ray emission from the shell-type supernova remnant RX J0852.0-4622 with HESS*, A&A, 437, L7

Aharonian, F., Akhperjanian, A. G., Bazer-Bachi, A. R., et al. 2006b, *The H.E.S.S. Survey of the Inner Galaxy in Very High Energy Gamma Rays*, ApJ, 636, 777

Aharonian, F., Akhperjanian, A. G., Bazer-Bachi, A. R., et al. 2006c, *3.9 day orbital modulation in the TeV gamma-ray flux and spectrum from the X-ray binary LS 5039*, A&A, 460, 743

Aharonian, F., Akhperjanian, A. G., Bazer-Bachi, A. R., et al. 2006d, *Energy dependent gamma-ray morphology in the pulsar wind nebula HESS J1825-137*, A&A, 460, 365

Aharonian, F., Arqueros, F., Badran, H., et al. 1991, *The AIROBICC Project: A New Air Cerenkov Detector Matrix for the Observation of UHE Cosmic Rays*, International Cosmic Ray Conference, 4, 468

Aharonian, F., Horns, D., Rowell, G., & Santangelo, A. 2005c, *H.E.S.S. Observations of the Gould Belt: A Survey of Nearby Off-Plane Molecular Clouds*, H.E.S.S. internal observation proposal

Aharonian, F. A. 1991, *Very high and ultra-high-energy gamma-rays from giant molecular clouds*, Ap&SS, 180, 305

Aharonian, F. A. 2004, *Very high energy cosmic gamma radiation : a crucial window on the extreme Universe*

Aleksić, J., Alvarez, E. A., Antonelli, L. A., et al. 2012, *Performance of the MAGIC stereo system obtained with Crab Nebula data*, Astroparticle Physics, 35, 435

Anderhub, H., Backes, M., Biland, A., et al. 2009, *A novel camera type for very high energy gamma-ray astronomy based on Geiger-mode avalanche photodiodes*, Journal of Instrumentation, 4, 10010

Andrae, R., Schulze-Hartung, T., & Melchior, P. 2010, *Dos and don'ts of reduced chi-squared*, ArXiv e-prints

Arnaud, K. A. 1996, *XSPEC: The First Ten Years*, in Astronomical Society of the Pacific Conference Series, Vol. 101, Astronomical Data Analysis Software and Systems V, ed. G. H. Jacoby & J. Barnes, 17

Atwood, W. B., Abdo, A. A., Ackermann, M., et al. 2009, *The Large Area Telescope on the Fermi Gamma-Ray Space Telescope Mission*, ApJ, 697, 1071

Atwood, W. B., Bagagli, R., Baldini, L., et al. 2007, *Design and initial tests of the Tracker-converter of the Gamma-ray Large Area Space Telescope*, Astroparticle Physics, 28, 422

Axford, W. I., Leer, E., & Skadron, G. 1977, *The acceleration of cosmic rays by shock waves*, International Cosmic Ray Conference, 11, 132

Baillon, P., Behr, L., Danagoulian, S., et al. 1991, *Observation of the Crab in Multi TeV Gamma Rays by the THEMISTOCLE experiment*, International Cosmic Ray Conference, 1, 220

Bauleo, P. M. & Rodríguez Martino, J. 2009, *The dawn of the particle astronomy era in ultra-high-energy cosmic rays*, Nature, 458, 847

Becherini, Y., Djannati-Ataï, A., Marandon, V., Punch, M., & Pita, S. 2011, *A new analysis strategy for detection of faint gamma-ray sources with Imaging Atmospheric Cherenkov Telescopes*, Astroparticle Physics, 34, 858

Bell, A. R. 1978, *The acceleration of cosmic rays in shock fronts. I*, MNRAS, 182, 147

Benaglia, P. & Romero, G. E. 2003, *Gamma-ray emission from Wolf-Rayet binaries*, A&A, 399, 1121

Berge, D., Funk, S., & Hinton, J. 2007, *Background modelling in very-high-energy gamma-ray astronomy*, A&A, 466, 1219

Bevington, P. R. 1969, *Data reduction and error analysis for the physical sciences*

Bignami, G. F., Boella, G., Burger, J. J., et al. 1975, *The COS-B experiment for gamma-ray astronomy*, Space Science Instrumentation, 1, 245

Bird, A. J., Barlow, E. J., Bassani, L., et al. 2004, *The First IBIS/ISGRI Soft Gamma-Ray Galactic Plane Survey Catalog*, ApJ, 607, L33

Bird, D. J., Corbato, S. C., Dai, H. Y., et al. 1995, *Detection of a cosmic ray with measured energy well beyond the expected spectral cutoff due to cosmic microwave radiation*, ApJ, 441, 144

Blandford, R. D. & Ostriker, J. P. 1978, *Particle acceleration by astrophysical shocks*, ApJ, 221, L29

Blasi, P. 2013, *The origin of galactic cosmic rays*, A&A Rev., 21, 70

Bolz, O. 2004, *Absolute energy calibration of the imaging Cherenkov telescopes of the H.E.S.S. experiment and results of the first observations of the supernova remnant RX J1713.7–3946*, PhD thesis, Ruprecht-Karls-University of Heidelberg, Germany

Budnev, N. M., Besson, D., Chvalaev, O. A., et al. 2010, *The Tunka-133 EAS Chrenkov array - status, first results and plans*, ArXiv e-prints

Burrows, D. N., Hill, J. E., Nousek, J. A., et al. 2004, *The Swift X-Ray Telescope*, in Society of Photo-Optical Instrumentation Engineers (SPIE) Conference Series, Vol. 5165, X-Ray and Gamma-Ray Instrumentation for Astronomy XIII, ed. K. A. Flanagan & O. H. W. Siegmund, 201–216

Cameron, R. A., Kurfess, J. D., Johnson, W. N., et al. 1992, *Operation and performance of the OSSE instrument*, in NASA Conference Publication, Vol. 3137, NASA Conference Publication, ed. C. R. Shrader, N. Gehrels, & B. Dennis, 3–14

Carrigan, S. 2007, *Pulsar Wind Nebulae with H.E.S.S.: Establishing a Connection between high-power Pulsars and very-high-energy gamma-ray Sources*, PhD thesis, Ruprecht-Karls-University of Heidelberg, Germany

Carrigan, S., Deil, C., & Gast, H. 2012, *New methods implemented in hap for the Galactic Plane Survey: Adaptive ring background method Automatically generated exclusion maps Flux maps* , H.E.S.S. internal note

Chaves, R. C. G. 2009, *HESS Exclusion regions*, H.E.S.S. internal note

Chaves, R. C. G., Renaud, M., Lemoine-Goumard, M., & Goret, P. 2008, *HESS J1848-018: Discovery Of VHE gamma-ray Emission From The Direction Of W 43*, in American Institute of Physics Conference Series, Vol. 1085, American Institute of Physics Conference Series, ed. F. A. Aharonian, W. Hofmann, & F. Rieger, 372–375

Chevalier, R. A. 1982, *Self-similar solutions for the interaction of stellar ejecta with an external medium*, ApJ, 258, 790

Church, M. J., Gibiec, A., & Bałucińska-Church, M. 2014, *The nature of the island and banana states in atoll sources and a unified model for low-mass X-ray binaries*, MNRAS

Clark, J. S., Negueruela, I., Crowther, P. A., & Goodwin, S. P. 2005, *On the massive stellar population of the super star cluster Westerlund 1*, A&A, 434, 949

Condon, J. J., Cotton, W. D., Greisen, E. W., et al. 1998, *The NRAO VLA Sky Survey*, AJ, 115, 1693

Conti, P. S. 1978, *Mass loss in early-type stars*, ARA&A, 16, 371

Cornils, R., Gillessen, S., Jung, I., et al. 2003, *The optical system of the H.E.S.S. imaging atmospheric Cherenkov telescopes. Part II: mirror alignment and point spread function*, Astroparticle Physics, 20, 129

Crowther, P. A. 2007, *Physical Properties of Wolf-Rayet Stars*, ARA&A, 45, 177

Dame, T. M., Hartmann, D., & Thaddeus, P. 2001, *The Milky Way in Molecular Clouds: A New Complete CO Survey*, ApJ, 547, 792

Daum, A., Hermann, G., Hess, M., et al. 1997, *First results on the performance of the HEGRA IACT array*, Astroparticle Physics, 8, 1

Davies, J. M. & Cotton, E. S. 1957, *Design of the quartermaster solar furnace*, Solar Energy, 1, 16

de Jager, O. C., Ferreira, S. E. S., Djannati-Ataï, A., et al. 2009, *Unidentified Gamma-Ray Sources as Ancient Pulsar Wind Nebulae*, ArXiv e-prints

de la Calle Pérez, I. & Biller, S. D. 2006, *Extending the sensitivity of air Cerenkov telescopes*, Astroparticle Physics, 26, 69

de los Reyes, R., Hahn, J., Bernloehr, K., et al. 2013, *Influence of aerosols from biomass burning on the spectral analysis of Cherenkov telescopes*, ArXiv e-prints

de Naurois, M. & Rolland, L. 2009, *A high performance likelihood reconstruction of gamma-rays for imaging atmospheric Cherenkov telescopes*, Astroparticle Physics, 32, 231

de Oña Wilhelmi, E. 2011, *Latest Results on Pulsar Wind Nebulae on the TeV Energy Regime*, in American Institute of Physics Conference Series, Vol. 1357, American Institute of Physics Conference Series, ed. M. Burgay, N. D'Amico, P. Esposito, A. Pellizzoni, & A. Possenti, 213–220

Denherder, J. W., Aarts, H., Bennett, K., et al. 1992, *COMPTEL: Instrument description and performance*, in NASA Conference Publication, Vol. 3137, NASA Conference Publication, ed. C. R. Shrader, N. Gehrels, & B. Dennis, 85–94

Derdeyn, S. M., Ehrmann, C. H., Fichtel, C. E., Kniffen, D. A., & Ross, R. W. 1972, *SAS-B digitized spark chamber gamma ray telescope.*, Nuclear Instruments and Methods, 98, 557

Dickey, J. M. & Lockman, F. J. 1990, *H I in the Galaxy*, ARA&A, 28, 215

Doro, M. & CTA Consortium. 2011, *CTA – A project for a new generation of Cherenkov telescopes*, Nuclear Instruments and Methods in Physics Research A, 630, 285

Douglas, J. N., Bash, F. N., Bozyan, F. A., Torrence, G. W., & Wolfe, C. 1996, *The Texas Survey of Radio Sources Covering -35.5 degrees < declination < 71.5 degrees at 365 MHz*, AJ, 111, 1945

Drury, L. O. . 2012, *Origin of cosmic rays*, Astroparticle Physics, 39, 52

Dwarkadas, V. V. 2008, *Turbulence in wind-blown bubbles around massive stars*, Physica Scripta Volume T, 132, 014024

Dyakonov, M. N., Knurenko, S. P., Kolosov, V. A., et al. 1973, *The Results of the First Stage Observations at the Yakutsk EAS Complex Array. II. The Lateral Distribution of EAS Cernekov Light of Large Sizes at Sea Level.*, International Cosmic Ray Conference, 4, 2389

Eichler, D. & Usov, V. 1993, *Particle acceleration and nonthermal radio emission in binaries of early-type stars*, ApJ, 402, 271

Eidelman, S., Hayes, K., Olive, K., et al. 2004, *Review of Particle Physics*, Physics Letters B, 592, 1+

Ekers, J. A. 1969, *The Parkes catalogue of radio sources, declination zone +20 to -90 .*, Australian Journal of Physics Astrophysical Supplement, 7, 3

Federmann, G. 2003, *Viktor Hess und die Entdeckung der Kosmischen Strahlung*, Diplomarbeit, University of Vienna

Fermi, E. 1949, *On the Origin of the Cosmic Radiation*, Physical Review, 75, 1169

Fernandes, M. V. 2009, *Untersuchung hochenergetischer Gamma-Strahlung von Westerlund 1 und weiteren Sternhaufen*, Diplomarbeit, University of Hamburg

Fishman, G. J. 1992, *BATSE - The burst and transient source experiment on the Gamma Ray Observatory*, ed. C. Ho, R. I. Epstein, & E. E. Fenimore, 265–272

Fontaine, G., Baillon, P., Behr, L., et al. 1990, *Aims and status of the Themistocle physics experiment*, Nuclear Physics B Proceedings Supplements, 14, 79

Frew, D. J. & Parker, Q. A. 2010, *Planetary Nebulae: Observational Properties, Mimics and Diagnostics*, PASA, 27, 129

Funk, S., Hinton, J., Hermann, G., et al. 2005, *The Central Trigger System of the H.E.S.S. Telescope Array*, in American Institute of Physics Conference Series, Vol. 745, High Energy Gamma-Ray Astronomy, ed. F. A. Aharonian, H. J. Völk, & D. Horns, 753–757

Gaensler, B. M. & Slane, P. O. 2006, *The Evolution and Structure of Pulsar Wind Nebulae*, ARA&A, 44, 17

Gaisser, T. K. 2012, *Spectrum of cosmic-ray nucleons, kaon production, and the atmospheric muon charge ratio*, Astroparticle Physics, 35, 801

Gast, H. 2012, *A new lookup scheme for hap*, H.E.S.S. internal note

Giacconi, R., Murray, S., Gursky, H., et al. 1974, *The Third UHURU Catalog of X-Ray Sources*, ApJS, 27, 37

Giebels, B. 2013, *Status and recent results from H.E.S.S*, ArXiv e-prints

Gierliński, M. & Done, C. 2002, *The X-ray spectrum of the atoll source 4U 1608-52*, MNRAS, 337, 1373

Gillessen, S., Eisenhauer, F., Fritz, T. K., et al. 2013, *The distance to the Galactic Center*, in IAU Symposium, Vol. 289, IAU Symposium, ed. R. de Grijs, 29–35

Ginzburg, V. L. & Syrovatskii, S. I. 1964, *The Origin of Cosmic Rays*

Gould, B. A. & Galle, J. G. 1874, *Observations of Flora at Cordoba*, Astronomische Nachrichten, 84, 313

Green, A. J., Cram, L. E., Large, M. I., & Ye, T. 1999, *The Molonglo Galactic Plane Survey. I. Overview and Images*, ApJS, 122, 207

Greisen, K. 1966, *End to the Cosmic-Ray Spectrum?*, Physical Review Letters, 16, 748

Grenier, I. A. 2004, *The Gould Belt, star formation, and the local interstellar medium*, ArXiv Astrophysics e-prints

Grove, J. E. & Johnson, W. N. 2010, *The calorimeter of the Fermi Large Area Telescope*, in Society of Photo-Optical Instrumentation Engineers (SPIE) Conference Series, Vol. 7732, Society of Photo-Optical Instrumentation Engineers (SPIE) Conference Series

Guillout, P., Sterzik, M. F., Schmitt, J. H. M. M., Motch, C., & Neuhaeuser, R. 1998, *Discovery of a late-type stellar population associated with the Gould Belt*, A&A, 337, 113

Hampf, D. 2012, *Study for the wide-angle air Cherenkov detector HiSCORE and time gradient event reconstruction for the H.E.S.S. experiment*, PhD thesis, University of Hamburg, Germany

Hartman, R. C., Bertsch, D. L., Bloom, S. D., et al. 1999, *The Third EGRET Catalog of High-Energy Gamma-Ray Sources*, ApJS, 123, 79

Healey, S. E., Romani, R. W., Cotter, G., et al. 2008, *CGRaBS: An All-Sky Survey of Gamma-Ray Blazar Candidates*, ApJS, 175, 97

Healey, S. E., Romani, R. W., Taylor, G. B., et al. 2007, *CRATES: An All-Sky Survey of Flat-Spectrum Radio Sources*, ApJS, 171, 61

Heitler, W. 1954, *Quantum theory of radiation*

Herschel, Sir, J. F. W. 1847, *Results of astronomical observations made during the years 1834, 5, 6, 7, 8, at the Cape of Good Hope; being the completion of a telescopic survey of the whole surface of the visible heavens, commenced in 1825*

Hess, V. F. 1912, *Über Beobachtungen der durchdringenden Strahlung bei sieben Freiballonfahrten*, Physikalische Zeitschrift, 13, 1084

Higdon, J. C. & Lingenfelter, R. E. 2003, *The Superbubble Origin of ^{22}Ne in Cosmic Rays*, ApJ, 590, 822

Hillas, A. M. 1984, *The Origin of Ultra-High-Energy Cosmic Rays*, ARA&A, 22, 425

Hillas, A. M. 1985, *Cerenkov light images of EAS produced by primary gamma*, in International Cosmic Ray Conference, Vol. 3, International Cosmic Ray Conference, ed. F. C. Jones, 445–448

Hillas, A. M. 2005, *TOPICAL REVIEW: Can diffusive shock acceleration in supernova remnants account for high-energy galactic cosmic rays?*, Journal of Physics G Nuclear Physics, 31, 95

Hillas, A. M. 2006, *Cosmic Rays: Recent Progress and some Current Questions*, ArXiv Astrophysics e-prints

Hillas, A. M. 2013, *Evolution of ground-based gamma-ray astronomy from the early days to the Cherenkov Telescope Arrays*, Astroparticle Physics, 43, 19

Hinton, J. A. 2004, *The status of the HESS project*, New A Rev., 48, 331

Hinton, J. A. 2009, *Ground-based gamma-ray astronomy with Cherenkov telescopes*, New Journal of Physics, 11, 055005

Hinton, J. A. & Hofmann, W. 2009, *Teraelectronvolt Astronomy*, ARA&A, 47, 523

Hofmann, W., Jung, I., Konopelko, A., et al. 1999, *Comparison of techniques to reconstruct VHE gamma-ray showers from multiple stereoscopic Cherenkov images*, Astroparticle Physics, 12, 135

Jansen, F., Lumb, D., Altieri, B., et al. 2001, *XMM-Newton observatory. I. The spacecraft and operations*, A&A, 365, L1

Kanbach, G., Bertsch, D. L., Fichtel, C. E., et al. 1988, *The project EGRET (Energetic Gamma-Ray Experiment Telescope) on NASA's Gamma-Ray Observatory (GRO)*, Space Sci. Rev., 49, 69

Kargaltsev, O., Rangelov, B., & Pavlov, G. G. 2013, *Gamma-ray and X-ray Properties of Pulsar Wind Nebulae and Unidentified Galactic TeV Sources*, ArXiv e-prints

Klapdor-Kleingrothaus, H. V. & Zuber, K. 1997, *Teilchenastrophysik.*

Klebesadel, R. W., Strong, I. B., & Olson, R. A. 1973, *Observations of Gamma-Ray Bursts of Cosmic Origin*, ApJ, 182, L85

Knoetig, M. L., Biland, A., Bretz, T., et al. 2013, *FACT - Long-term stability and observations during strong Moon light*, ArXiv e-prints

Koo, B.-C., Kang, J.-h., & Salter, C. J. 2006, *A Missing Supernova Remnant Revealed by the 21 cm Line of Atomic Hydrogen*, ApJ, 643, L49

Kosack, K. P. 2005, *Very High Energy Gamma Rays from the Galactic Center*, PhD thesis, University of Washington, U.S.A.

Kothes, R. & Dougherty, S. M. 2007, *The distance and neutral environment of the massive stellar cluster Westerlund 1*, A&A, 468, 993

Kovalev, Y. Y. 2009, *Identification of the Early Fermi/LAT Gamma-Ray Bright Objects with Extragalactic VLBI Sources*, ApJ, 707, L56

Koyama, K., Tsunemi, H., Dotani, T., et al. 2007, *X-Ray Imaging Spectrometer (XIS) on Board Suzaku*, PASJ, 59, 23

Kraushaar, W., Clark, G. W., Garmire, G., et al. 1965, *Explorer XI Experiment on Cosmic Gamma Rays.*, ApJ, 141, 845

Kraushaar, W. L. & Clark, G. W. 1962, *Search for Primary Cosmic Gamma Rays with the Satellite Explorer XI*, Physical Review Letters, 8, 106

Kraushaar, W. L., Clark, G. W., Garmire, G. P., et al. 1972, *High-Energy Cosmic Gamma-Ray Observations from the OSO-3 Satellite*, ApJ, 177, 341

Krayzel, F., Maurin, G., Brunetti, L., et al. 2013, *Improved sensitivity of H.E.S.S.-II through the fifth telescope focus system*, ArXiv e-prints

Kroupa, P. 2001, *On the variation of the initial mass function*, MNRAS, 322, 231

Krymskii, G. F. 1977, *A regular mechanism for the acceleration of charged particles on the front of a shock wave*, Akademiia Nauk SSSR Doklady, 234, 1306

Landi, R., Bassani, L., Malizia, A., et al. 2006, *Swift XRT Follow-up Observations of TeV Sources of the HESS Inner Galaxy Survey*, ApJ, 651, 190

Landi, R., Masetti, N., Bassani, L., et al. 2007, *HESS J1614-518: detection of X-ray emitting stars by Swift/XRT possibly associated with an open cluster*, The Astronomer's Telegram, 1047, 1

Landt, H., Padovani, P., Perlman, E. S., et al. 2001, *The Deep X-Ray Radio Blazar Survey (DXRBS) - II. New identifications*, MNRAS, 323, 757

Langston, G. I., Heflin, M. B., Conner, S. R., et al. 1990, *The second MIT-Green Bank 5 GHz survey*, ApJS, 72, 621

Lanyi, G. E., Boboltz, D. A., Charlot, P., et al. 2010, *The Celestial Reference Frame at 24 and 43 GHz. I. Astrometry*, AJ, 139, 1695

Leitherer, C., Ortiz Otálvaro, P. A., Bresolin, F., et al. 2010, *A Library of Theoretical Ultraviolet Spectra of Massive, Hot Stars for Evolutionary Synthesis*, ApJS, 189, 309

Li, T.-P. & Ma, Y.-Q. 1983, *Analysis methods for results in gamma-ray astronomy*, ApJ, 272, 317

Lopez, J. A. & Meaburn, J. 1983, *The structure and dynamics of the bi-polar nebula MZ-3*, MNRAS, 204, 203

Lorenz, E. 2004, *Status of the 17 m MAGIC telescope*, New A Rev., 48, 339

Maeder, A. 1990, *Tables for massive star evolution at various metallicities*, A&AS, 84, 139

Manchester, R. N., Hobbs, G. B., Teoh, A., & Hobbs, M. 2005, *The Australia Telescope National Facility Pulsar Catalogue*, AJ, 129, 1993

Matsumoto, H., Uchiyama, H., Sawada, M., et al. 2008, *Discovery of Extended X-Ray Emission from an Unidentified TeV Source, HESS J1614-518, Using the Suzaku Satellite*, PASJ, 60, 163

Matsumoto, H., Ueno, M., Bamba, A., et al. 2007, *Suzaku Observations of HESS J1616-508: Evidence for a Dark Particle Accelerator*, PASJ, 59, 199

Mattana, F., Falanga, M., Götz, D., et al. 2009, *The Evolution of the gamma- and X-Ray Luminosities of Pulsar Wind Nebulae*, ApJ, 694, 12

Mattox, J. R., Bertsch, D. L., Chiang, J., et al. 1996, *The Likelihood Analysis of EGRET Data*, ApJ, 461, 396

Maxted, N. I., Rowell, G. P., Dawson, B. R., et al. 2013, *Dense Gas Towards the RX J1713.7-3946 Supernova Remnant*, PASA, 30, 55

McClure-Griffiths, N. M., Dickey, J. M., Gaensler, B. M., et al. 2005, *The Southern Galactic Plane Survey: H I Observations and Analysis*, ApJS, 158, 178

Meegan, C., Lichti, G., Bhat, P. N., et al. 2009, *THE fermi gamma-ray burst monitor*, ApJ, 702, 791

Menzel, D. N. 1922, *Five new planetary nebulae.*, Harvard College Observatory Bulletin, 777, 0

Mereghetti, S. 2008, *The strongest cosmic magnets: soft gamma-ray repeaters and anomalous X-ray pulsars*, A&A Rev., 15, 225

Meyer, M., Horns, D., & Zechlin, H.-S. 2010, *The Crab Nebula as a standard candle in very high-energy astrophysics*, A&A, 523, A2

Meynet, G., Georgy, C., Hirschi, R., et al. 2011, *Red Supergiants, Luminous Blue Variables and Wolf-Rayet stars: the single massive star perspective*, Bulletin de la Societe Royale des Sciences de Liege, 80, 266

Mücke, A. & Pohl, M. 2002, *Non-Thermal High-Energy Emission from WR Binaries?*, in Astronomical Society of the Pacific Conference Series, Vol. 260, Interacting Winds from Massive Stars, ed. A. F. J. Moffat & N. St-Louis, 355

Nakamura, K. 2010, *Review of Particle Physics*, Journal of Physics G Nuclear Physics, 37, 075021

Neronov, A., Semikoz, D. V., & Taylor, A. M. 2012, *Low-Energy Break in the Spectrum of Galactic Cosmic Rays*, Physical Review Letters, 108, 051105

Neugebauer, G., Habing, H. J., van Duinen, R., et al. 1984, *The Infrared Astronomical Satellite (IRAS) mission*, ApJ, 278, L1

Nolan, P. L., Abdo, A. A., Ackermann, M., et al. 2012, *Fermi Large Area Telescope Second Source Catalog*, ApJS, 199, 31

Ohm, S. 2010, *Advanced gamma/hadron separation technique and application to particular gamma-ray sources with H.E.S.S.*, PhD thesis, Ruprecht-Karls-University of Heidelberg, Germany

Ohm, S., Horns, D., Reimer, O., et al. 2010, *H.E.S.S. Observations of Massive Stellar Clusters*, in Astronomical Society of the Pacific Conference Series, Vol. 422, High Energy Phenomena in Massive Stars, ed. J. Martí, P. L. Luque-Escamilla, & J. A. Combi, 265

Ohm, S., van Eldik, C., & Egberts, K. 2009, *Gamma/hadron separation in very-high-energy gamma-ray astronomy using a multivariate analysis method*, Astroparticle Physics, 31, 383

Oskinova, L. M. 2005, *Evolution of X-ray emission from young massive star clusters*, MNRAS, 361, 679

Palmer, D., Barthelmy, S. D., Barbier, L., et al. 2007, *4U 1608-522 in X-ray outburst*, The Astronomer's Telegram, 1113, 1

Paneque, D., X, Y, & Z. 2013, *The First Fermi-LAT Catalog of Sources Above 10 GeV*, ArXiv e-prints

Parizot, E., Marcowith, A., van der Swaluw, E., Bykov, A. M., & Tatischeff, V. 2004, *Superbubbles and energetic particles in the Galaxy. I. Collective effects of particle acceleration*, A&A, 424, 747

Peille, P. 2012, *Study of H.E.S.S. background systematics*, H.E.S.S. internal note

Perryman, M. A. C., Lindegren, L., Kovalevsky, J., et al. 1997, *The HIPPARCOS Catalogue*, A&A, 323, L49

Piatti, A. E., Clariá, J. J., & Bica, E. 2000, *Photometric and integrated spectral study of the young open clusters Pismis 22, NGC 6178, NGC 6216 and Ruprecht 130*, A&A, 360, 529

Piron, F., Djannati-Atai, A., Punch, M., et al. 2001, *Temporal and spectral gamma-ray properties of <ASTROBJ>Mkn 421</ASTROBJ> above 250 GeV from CAT observations between 1996 and 2000*, A&A, 374, 895

Prinja, R. K., Barlow, M. J., & Howarth, I. D. 1990, *Terminal velocities for a large sample of O stars, B supergiants, and Wolf-Rayet stars*, ApJ, 361, 607

Remillard, R., Morgan, E., & ASM Team at MIT, N. 2005, *Superburst in 4U1608-52*, The Astronomer's Telegram, 482, 1

Reynolds, S. P. 2008, *Supernova Remnants at High Energy*, ARA&A, 46, 89

Rowell, G. P. 2003, *A new template background estimate for source searching in TeV gamma-ray astronomy*, A&A, 410, 389

Rowell, G. P., Horns, D., Fukui, Y., & Moriguchi, Y. 2008, *A Closer Look at the Unidentified TeV Source HESS J1614-518*, in American Institute of Physics Conference Series, Vol. 1085, American Institute of Physics Conference Series, ed. F. A. Aharonian, W. Hofmann, & F. Rieger, 241–244

Russeil, D., Adami, C., Amram, P., et al. 2005, *A deep H(alpha) survey of the Milky Way. VI. The l = 332deg area*, A&A, 429, 497

Sakai, M., Yajima, Y., & Matsumoto, H. 2011, *Nature of the Unidentified TeV Source HESS J1614-518, Revealed by Suzaku and XMM-Newton Observations*, PASJ, 63, 879

Salpeter, E. E. 1955, *The Luminosity Function and Stellar Evolution.*, ApJ, 121, 161

Santander-García, M., Corradi, R. L. M., Balick, B., & Mampaso, A. 2004, *Menzel 3: Dissecting the ant*, A&A, 426, 185

Schmeja, S. & Kimeswenger, S. 2001, *Planetary nebula or symbiotic Mira? Near infrared colours mark the difference*, A&A, 377, L18

Shklovskii, I. S. 1953, *Radioastronomiia.*

Silich, S., Tenorio-Tagle, G., & Añorve-Zeferino, G. A. 2005, *On the X-Ray Emission from Massive Star Clusters and Their Evolving Superbubbles*, ApJ, 635, 1116

Sinnis, G. 2009, *Air shower detectors in gamma-ray astronomy*, New Journal of Physics, 11, 055007

Smith, N. 2003, Spatial distribution of near-infrared and optical emission properties in the bipolar nebula Menzel 3, MNRAS, 342, 383

Smith, N. 2014, *Mass Loss: Its Effect on the Evolution and Fate of High-Mass Stars*, ArXiv e-prints

Stegmann, C. 2012, *Highlights from H.E.S.S.*, in American Institute of Physics Conference Series, Vol. 1505, American Institute of Physics Conference Series, ed. F. A. Aharonian, W. Hofmann, & F. M. Rieger, 194–201

Tarana, A., Bazzano, A., Ubertini, P., & Zdziarski, A. A. 2007, *INTEGRAL Spectral Variability Study of the Atoll 4U 1820-30: First Detection of Hard X-Ray Emission*, ApJ, 654, 494

Tavani, M., Barbiellini, G., Argan, A., et al. 2009, *The AGILE Mission*, A&A, 502, 995

Thompson, D. J. 2008, *Gamma ray astrophysics: the EGRET results*, Reports on Progress in Physics, 71, 116901

Tluczykont, M., Hampf, D., Horns, D., et al. 2014, *The HiSCORE concept for gamma-ray and cosmic-ray astrophysics beyond 10 TeV*, Astroparticle Physics, 56, 42

Čerenkov, P. A. 1937, *Visible Radiation Produced by Electrons Moving in a Medium with Velocities Exceeding that of Light*, Physical Review, 52, 378

van der Hucht, K. A. 2001, *The VIIth catalogue of galactic Wolf-Rayet stars*, New A Rev., 45, 135

van Eldik, C., Bolz, O., Braun, I., & et al. 2008, *Localising the H.E.S.S. Galactic Centre point source*, International Cosmic Ray Conference, 2, 589

Vink, J. S., de Koter, A., & Lamers, H. J. G. L. M. 2001, *Mass-loss predictions for O and B stars as a function of metallicity*, A&A, 369, 574

von Seggern, J. E. 2014, *Constraining Weakly Interacting Slim Particles with a Massive Star and in the Laboratory*, PhD thesis, DESY/University of Hamburg, Germany

Wachter, S., Hoard, D. W., Bailyn, C. D., Corbel, S., & Kaaret, P. 2002, *A Closer Look at the Soft X-Ray Transient X1608-52: Long-Term Optical and X-Ray Observations*, ApJ, 568, 901

Watson, M. G., Auguères, J.-L., Ballet, J., et al. 2001, *The XMM-Newton Serendipitous Survey. I. The role of XMM-Newton Survey Science Centre*, A&A, 365, L51

Weaver, R., McCray, R., Castor, J., Shapiro, P., & Moore, R. 1977, *Interstellar bubbles. II - Structure and evolution*, ApJ, 218, 377

Webber, W. R. 1998, *A New Estimate of the Local Interstellar Energy Density and Ionization Rate of Galactic Cosmic Cosmic Rays*, ApJ, 506, 329

Weekes, T. C. 1988, *Very high energy gamma-ray astronomy*, Phys. Rep., 160, 1

Weekes, T. C., Badran, H., Biller, S. D., et al. 2002, *VERITAS: the Very Energetic Radiation Imaging Telescope Array System*, Astroparticle Physics, 17, 221

Weekes, T. C., Cawley, M. F., Fegan, D. J., et al. 1989, *Observation of TeV gamma rays from the Crab nebula using the atmospheric Cerenkov imaging technique*, ApJ, 342, 379

Wells, D. C., Greisen, E. W., & Harten, R. H. 1981, *FITS - a Flexible Image Transport System*, A&AS, 44, 363

Westerlund, B. 1961, *A Heavily Reddened Cluster in ARA*, PASP, 73, 51

Wilks, P. 1938, *The Large-Sample Distribution of the Likelihood Ratio for Testing Composite Hypotheses*, The Annals of Mathematical Statistics, 9, 60

Winstein, B. & Zurek, K. M. 2009, *Cosmic light matter probes heavy dark matter*, Physics, 2, 37

Winston, R. 1970, *Light Collection within the Framework of Geometrical Optics*, Journal of the Optical Society of America (1917-1983), 60, 245

Woosley, S. E., Heger, A., & Weaver, T. A. 2002, *The evolution and explosion of massive stars*, Reviews of Modern Physics, 74, 1015

Woosley, S. E. & Weaver, T. A. 1986, *The physics of supernova explosions*, ARA&A, 24, 205

Yang, R.-z., de Oña Wilhelmi, E., & Aharonian, F. 2013, *Probing Cosmic Rays in Nearby Giant Molecular Clouds with the Fermi Large Area Telescope*, ArXiv e-prints

Zatsepin, G. T. & Kuz'min, V. A. 1966, *Upper Limit of the Spectrum of Cosmic Rays*, Soviet Journal of Experimental and Theoretical Physics Letters, 4, 78

Zavrtanik, D. 2000, *The Pierre Auger Observatory*, Nuclear Physics B Proceedings Supplements, 85, 324

Zhang, Y. & Liu, X.-W. 2006, *The Fe/Ni ratio in the Ant Nebula Mz 3*, in IAU Symposium, Vol. 234, Planetary Nebulae in our Galaxy and Beyond, ed. M. J. Barlow & R. H. Méndez, 547–548